

NEW ASPECTS OF
SUPERNOVA NEUTRINO FLAVOR CONVERSIONS:
IN THE STANDARD MODEL AND BEYOND

A Thesis

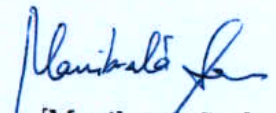
Submitted to the
Tata Institute of Fundamental Research, Mumbai
for the degree of Doctor of Philosophy
in Physics

by
Manibrata Sen

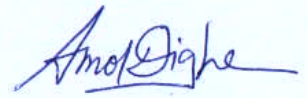
DEPARTMENT OF THEORETICAL PHYSICS
TATA INSTITUTE OF FUNDAMENTAL RESEARCH
MUMBAI
August 2018

DECLARATION

This thesis is a presentation of my original research work. Whatever contributions of others are involved, every effort is made to indicate this clearly, with due reference to the literature, and acknowledgement of collaborative research and discussions. The work was done under the supervision of Professor Amol Dighe, and the co-supervision of Dr. Basudeb Dasgupta, at the Tata Institute of Fundamental Research, Mumbai.

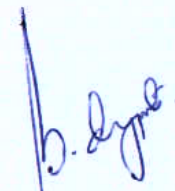

[Manibrata Sen]

In my capacity as supervisor of the candidate's thesis, I certify that the above statements are true to the best of my knowledge.


[Amol Dighe]

Date: 13/08/18

In my capacity as co-supervisor of the candidate's thesis, I certify that the above statements are true to the best of my knowledge.


[Basudeb Dasgupta]

Date: 13/08/18

*There is a tide in the affairs of men,
Which, taken at the flood, leads on to fortune;
Omitted, all the voyage of their life
Is bound in shallows and in miseries.
On such a full sea are we now afloat,
And we must take the current when it serves,
Or lose our ventures.*

– Julius Cæsar, Act IV, Scene III .

ACKNOWLEDGEMENTS

As I conclude this remarkable journey, I feel indebted to an endless list of people who have been associated with this journey for more than half a decade.

First and foremost, I would like to express my heartiest gratitude to Amol for his guidance through all these years. His infinite reservoir of patience (I am yet to see him lose his temper), and his ever-reassuring smile, particularly when ideas did not work out (or even if they did, the results did not make sense) never fail to amaze me. Discussions with him were always refreshing and enjoyable.

No appropriate adjective can suffice to express my gratitude to Basu, who has been a constant source of guidance and support. The kind of enthusiasm with which he works is infectious, and I had a great time collaborating with him. He has been ever so generous - be it with his advice or his Max Planck grant. Thank you for bearing with my silliest of mistakes, and instilling a sense of confidence in me even when things seemed to fall apart.

I would also thank my collaborator, Alessandro, for a very pleasant experience of working together. I also acknowledge the financial support received from the Max-Planck-Partnergroup "Astroparticle Physics" of the Max-Planck-Gesellschaft, and the Sarojini Damodaran Fellowship, and of course, TIFR.

It has been a great privilege to be a part of the Department of Theoretical Physics at TIFR. I have had the good fortune of attending some really good courses by Sreerup, Amol, Gautam, Shiraz, Tuhin, Rajdeep, Basu and Vikram. Lunch table discussions initiated by Tuhin, where we were "forced" to read up papers on ArXiv, really helped in broadening my horizon of knowledge. I must also thank the wonderful people working at the office, and the computer section of the department - Raju ji, Pawar ji, Aniket, Kapil and Ajay - they have left no stone unturned in helping us in every possible way they can. Be it a software installation, a laptop breakdown, requirement of an official document, or any official paperwork - they have always been there to take the burden off our shoulders.

Life in TIFR would have been extremely dull, if it were not for such wonderful friends that I made here. The list is pretty long, so I would name those who have bribed me to keep

their names in the acknowledgement. Moniruzzaman, Chandrodoy and Arpit – you made an excruciatingly rigorous coursework seem bearable. Tousik and Anirban – you were the best coffee-mates one can ask for, those endless coffee-time discussions will be missed. Disha – thank you for being there, no matter what. Indranil, Sudip, Soham and Suman – thank you for being such wonderful juniors, Nairit, Soureek and Debjyoti, for being such great seniors. All those extended lengths of late night *adda*, movies and table tennis will be sorely missed. Gourab da: thank you for being the dotting elder brother that you are to me, life in TIFR would have been a sheer impossibility without you. I would also like to thank all my seniors, colleagues and juniors at C-338 for keeping the working atmosphere extremely homely.

I would take this opportunity to dedicate this thesis to my near and dear ones. Subham and Dibya – you two have been a life-saver, always available over Skype and Hangout, any time of the day. Oishee – no words to describe your contribution — you have always been there, supporting me through my highs and lows, taking out time of your busy schedule to listen, whenever I needed someone to let my anguish out.

I will refrain from expressing “thanks” to my parents, for no words of gratitude can ably be used for that purpose. I am what I am because of you. This thesis is for you.

FOREWORD

The Standard Model (SM) of particle physics has proved to be extremely successful over the past few decades, holding its own against numerous experiments. However, one of the areas where it falls short is explaining the masses of neutrinos and hence neutrino oscillations. Neutrinos are massless within the SM, hence they should not oscillate. Therefore, the data from solar and atmospheric neutrinos also presented the first robust evidence of physics beyond the SM. Our understanding of neutrino physics has improved immensely since then. The determination of neutrino properties is one of the major goals of neutrino phenomenology. Most of the current experiments focus on the precise determination of oscillation parameters, and deduce bounds on possible subdominant oscillation effects, caused by standard or non-standard neutrino interactions. Results from these experiments could open hitherto unexplored avenues of physics beyond the SM.

Neutrinos from astrophysical sources, such as core-collapse supernovae, binary star mergers, or active galactic nuclei, etc., can help us immensely in our understanding of the governing dynamics of these sources. During the explosion of core-collapse supernova (SN), almost all the gravitational binding energy of the star is emitted within a few seconds in the form of neutrinos. These neutrinos, being weakly interacting, escape from the SN much before the shockwave explodes the star. Hence, neutrinos can arrive a few hours before the emitted photons, and can be used as an early SN warning system. A sufficiently high-statistics signal from a future galactic supernova can shed light on the mechanism of the collapse and explosion of a massive star. The extreme conditions through which the neutrinos travel to the Earth would have a dramatic effect on their flavor evolution. This provides us with a rare opportunity to study neutrino propagation through a dense media, which can be relevant even in the early universe. Furthermore, it has been known for quite some time that synthesis of nuclei heavier than iron can take place inside a SN core. This can take place through rapid neutron capture, and hence goes by the name of r-process nucleosynthesis. This process is quite sensitive to the neutrino flavor composition inside a SN. A careful study of neutrino flavor evolution within a SN is required for making correct predictions about the abundances of these heavy elements. Moreover, such enormous number of neutrino events

in future detectors can also be used to look for the existence of non-standard interactions of neutrinos. A SN explosion, therefore, provides a nice astrophysical laboratory to study such effects. Indeed the extreme conditions inside a SN would act to amplify even tiny amounts of such non-standard interactions.

Flavor conversions of SN neutrinos have spurred intense research and debate about the fascinating physics of neutrino flavor transformations during the collapse of a massive star. The early studies in this field considered matter enhanced resonant flavor conversions as the only source of large flavor changes. In this paradigm, neutrinos experience a refractive potential, as they undergo elastic forward scattering with the background matter. These Mikheyev-Smirnov-Wolfenstein (MSW) matter effects aid in yielding large flavor conversions even for tiny vacuum mixing. However, later it was realized that deep within the SN regions, the neutrino density itself is so high that neutrino-neutrino interactions can cause large self-induced collective flavor oscillations. These can occur independently of the MSW effect and need only the vacuum mixing as a perturbing seed. Broadly, these self-induced flavor conversions are expected to either produce swaps in the neutrino spectra, converting regions of ν_e spectra to $\nu_{\mu,\tau}$, or to cause an averaging of flavor information, leading to decoherence. This rich and surprising phenomenology of collective oscillations remains a subject of active research and we are still far from having a complete picture.

More recently, it was shown that the ν - ν potential would lead to more rapid flavor conversions even for (almost) massless neutrinos, requiring a nonzero mass perhaps only as an initial perturbation. These rapid flavor conversions, dubbed as “fast conversions”, would, therefore, be independent of the yet unknown neutrino mass ordering and lead to complete flavor equilibrium for both mass orderings. It was postulated that the necessary condition to achieve these fast conversions is the presence of sufficient anisotropy in the angular emission spectrum of the different neutrino flavors. This is something one can indeed expect near the neutrino emission surface deep inside a SN. Due to different interaction cross-sections with matter, the non-electron flavors $\nu_{\mu,\tau}$ decouple from matter deeper than $\bar{\nu}_e$, and the latter deeper than ν_e . Therefore, near the SN core, the $\nu_{\mu,\tau}$ zenith-angle distribution would be more forward-peaked than that of $\bar{\nu}_e$, which in turn would be more forward-peaked than the ν_e distribution. It is this anisotropy in the neutrino-antineutrino emission that is believed to cause fast conversions. This field of fast flavor conversions is a relatively new field, with

only a handful of papers focussing on the presence and growth rate of these conversions.

In this thesis, we aim to study these non-linear flavor oscillations of neutrinos, emphasizing fast flavor conversions. We discuss fast flavor conversions of SN neutrinos, taking into account the recent developments showing the importance of anisotropic angular emission of different flavors of neutrinos and antineutrinos. In particular, we systematically study the possibility for obtaining fast conversions for evolution in space or time, and find that inward-going neutrinos increase the rate of fast conversions. We present an analytical treatment of the simplest system that exhibits fast conversions, and show that the conversions can be understood as the dynamics of a particle rolling down in a quartic potential. Furthermore, we also study the impact of non-standard self-interactions (NSSI) of neutrinos on the slower as well as fast collective flavor conversions. We find that NSSI can give rise to many features in the neutrino spectra that are not possible in the SM. Hence they will be important when trying to analyze a future SN neutrino signal.

We hope that the work in this thesis can contribute towards a better understanding of SN dynamics and interpretation of a future galactic SN neutrino signal.

Contents

1	Neutrino oscillations: an introduction	1
1.1	Neutrino oscillations in vacuum	3
1.1.1	Two flavor formalism	4
1.2	Neutrino oscillations in matter	5
1.2.1	Constant matter density	6
1.2.2	Varying matter density	8
1.3	Current status of three-flavor neutrino oscillations	9
1.4	Neutrinos from a core-collapse supernova	12
1.4.1	Explosion mechanism and neutrino emission	12
1.4.2	Supernova neutrino spectra	16
1.4.3	Oscillations of supernova neutrinos	18
1.4.4	Supernova neutrino observables and detectors	24
1.5	Outline of the thesis	26
2	Formalism: oscillations of dense neutrino streams	29
2.1	The density matrix formalism	29
2.2	Equations of motion	31
2.2.1	Polarization vector formalism	33
2.3	Collective flavor oscillations: A brief recap	35
2.3.1	Single energy flavor evolution	35
2.3.2	Multi-energy spectral splits	37
2.4	Linearized stability analysis	40
3	Fast Flavor Conversions Near a Supernova core	47

3.1	Introduction	47
3.2	Stability Analysis close to the SN core	48
3.2.1	Stationary Solutions with Evolution in Space	52
3.2.2	Homogeneous Solutions with Evolution in Time	55
3.2.3	Evolution in both Space and Time	58
3.3	Numerical solutions with SN Fluxes	59
3.4	Summarized Results	62
4	An Analytical Understanding of Fast Flavor Conversions	65
4.1	Introduction	65
4.2	Fast oscillations in the intersecting 4-beam model	66
4.2.1	Bipolar limit	68
4.2.2	Fast oscillations beyond the bipolar limit	69
4.3	Full EoMs for Fast Conversions	72
4.3.1	Conserved quantities in the limit $\omega/\mu = 0$ and $\alpha = 0$	73
4.4	Particle in a quartic potential	75
4.5	Varying neutrino density	78
4.6	Asymmetric fast oscillations	80
4.7	Summarized Results	81
5	Non-standard neutrino self-interactions (NSSI) and collective oscillations	83
5.1	Introduction	83
5.2	Flavor evolution in presence of NSSI	85
5.2.1	The flavor pendulum	87
5.2.2	Constant neutrino-neutrino potential	88
5.2.3	Flavor conversions with a varying neutrino potential in a supernova	92
5.3	Effects of NSSI on spectral swaps	93
5.3.1	FP-NSSI scenario: pinching of spectral swaps	94
5.3.2	FV-NSSI scenario: flavor lepton number violation	95
5.4	Collective effects during neutronization burst	97
5.5	Summarized Results	102
6	Analytical aspects of NSSI in a supernova and fast flavor conversions	105

6.1	Introduction	105
6.2	Linear Stability analysis with NSSI	107
6.2.1	Analytical understanding of the evolution of a two-box spectrum . . .	110
6.3	Fast flavor oscillations: the 4-beam model	112
6.3.1	Linearized analysis of the model	113
6.3.2	Interplay of fast and slow oscillations and NSSI	117
6.4	Summarized Results	120
7	Conclusion	123
A	Analytical aspects of NSSI and fast flavor conversions	127
A.1	The eigenvalues of the Hamiltonian in the 4-beam model	127
A.1.1	L-R Symmetric solution (Q_+, \bar{Q}_+)	127
A.1.2	L-R Symmetry breaking solution (Q_-, \bar{Q}_-)	129
B	Collisions and flavor conversions	131
B.1	What role does collision play?	131
B.1.1	Flavor evolution in presence of collisions	134

Chapter 1

Neutrino oscillations: an introduction

The neutrino was first postulated by Wolfgang Pauli in 1930 to explain the energy-momentum conservation in radioactive beta decays [1]. It is an extremely light, uncharged lepton, which can interact only via the weak interaction and gravity. A large number of these weakly-interacting particles have been left over from the Big-Bang almost 13.8 billion years ago [2]. Neutrinos are also constantly produced from nuclear reactions in the Sun, collisions of cosmic rays with nuclei in the upper atmosphere, particle accelerators, nuclear reactors, etc. In fact, every second hundreds of billions of neutrinos, produced from the Sun, pass through our bodies. However, they interact so weakly with matter that they have been popularly alluded as the ‘ghost particles’. The Standard Model (SM) of particle physics predicts three “flavors” of neutrinos: electron neutrino (ν_e), muon neutrino (ν_μ), and tau neutrino (ν_τ), in association with their charged lepton counterparts [3]. The invisible decay of the Z boson, measured at the Large Electron Positron (LEP) collider also gives $N_\nu = 2.984 \pm 0.008$, thereby confirming that there are three active light neutrinos [4].

It is now a well-known fact that neutrinos can oscillate from one flavor to another. This idea of neutrino oscillations was first suggested by Pontecorvo (1957) [5] and later by Maki, Nakagawa and Sakata (1962) [6]. Neutrino oscillations are a quantum-mechanical phenomena, and occur due to the fact that for neutrinos, flavor and mass eigenstates are different. Neutrinos are produced via weak interactions as one of the three flavor eigenstates ν_e , ν_μ and ν_τ and their propagation may be described in terms of mass eigenstates ν_1 , ν_2 and ν_3 [3]. During propagation, the mass eigenstates acquire non-trivial relative phases as a result of

different neutrino masses, and this leads to flavor oscillations. Furthermore, since the neutrinos interact through weak interactions, they can scatter off the electrons and nucleons in the background matter. This can give rise to an effective potential for the neutrinos, which in turn can lead to matter enhanced resonant flavor oscillations. This is the well-known Mikheyev-Smirnov-Wolfenstein (MSW) resonance [7, 8] and can give rise to large flavor conversions in ordinary matter. Over the years, different experiments related to neutrinos from the Sun [9–14], the atmosphere [15–18], reactors [12, 19–21] and accelerators [22–24] have provided us with compelling evidences for the existence of neutrino oscillations.

Neutrinos also play a dominant role in the dynamics of a core-collapse supernova (SN). The extreme conditions created by a stellar collapse can provide a unique opportunity to study neutrino flavor propagation through highly dense matter (see, e.g., [25] for a review). The signatures of neutrino flavor conversions deep inside a star can be imprinted on the neutrino spectra observed from a galactic SN. This can be used to infer yet unknown neutrino properties, as well as understand stellar dynamics.

The main focus of this thesis will be the study of neutrino flavor oscillations in a SN. The phenomenon of neutrino oscillations has to be taken into account when studying neutrino propagation through matter, and therefore becomes particularly relevant in dense media, like a core-collapse supernova (SN) or the early universe. In the first half of this thesis, we assume that neutrinos have Standard Model (SM) couplings and study flavor conversions in dense media. This can help us learn more about SN explosion dynamics and nucleosynthesis. In the second half of this thesis, we assume that neutrinos can have non-SM couplings, which can play an important role in the flavor propagation.

In this chapter, we present a brief review of our current understanding of neutrino phenomenology. We will introduce the basics of neutrino oscillations theory, both in vacuum and in matter. We report on the current status of three-flavor neutrino oscillation parameters. Finally, we will give a brief overview of the phenomenology of neutrinos streaming out of a core-collapse SN.

1.1 Neutrino oscillations in vacuum

There are three neutrino flavors ν_e , ν_μ and ν_τ , produced along with their charged lepton counterparts e , μ and τ [3]. The flavor eigenstates ν_α ($\alpha = e, \mu, \tau$) are related to the mass eigenstates ν_i ($i = 1, 2, 3$) by ¹

$$|\nu_\alpha\rangle = \sum_i U_{\alpha i}^* |\nu_i\rangle, \quad (1.1.1)$$

where U is called the Pontecorvo-Maki-Nakagawa-Sakata (PMNS) matrix [5, 6]. In the 3-flavor framework, this unitary mixing matrix can be parameterized as [3]

$$U = \begin{pmatrix} c_{12}c_{13} & s_{12}c_{13} & s_{13}e^{-i\delta} \\ -s_{12}c_{23} - c_{12}s_{23}s_{13}e^{i\delta} & c_{12}c_{23} - s_{12}s_{23}s_{13}e^{i\delta} & s_{23}c_{13} \\ s_{12}s_{23} - c_{12}c_{23}s_{13}e^{i\delta} & -c_{12}s_{23} - s_{12}c_{23}s_{13}e^{i\delta} & c_{23}c_{13} \end{pmatrix} \times \text{diag}\left(1, e^{i\frac{\alpha_{21}}{2}}, e^{i\frac{\alpha_{31}}{2}}\right), \quad (1.1.2)$$

where $c_{ij} \equiv \cos\vartheta_{ij}$, $s_{ij} \equiv \sin\vartheta_{ij}$, the angles $\vartheta_{ij} = [0, \pi/2]$. The Dirac CP-violating phase is $\delta = [0, 2\pi]$, whereas α_{21} , α_{31} are the two Majorana CP violation phases. The antineutrinos $\bar{\nu}_e$, $\bar{\nu}_\mu$ and $\bar{\nu}_\tau$ are related to their mass eigenstates by U , i.e., $|\bar{\nu}_\alpha\rangle = \sum_i U_{\alpha i} |\bar{\nu}_i\rangle$.

Suppose at $t = 0$, the initial neutrino flavor is ν_α . This may be written as a linear combination of the three mass states, i.e., $|\nu_\alpha(0)\rangle = \sum_i U_{\alpha i}^* |\nu_i\rangle$. After propagating for a time t , the mass eigenstates acquire a phase, and hence

$$|\nu_\alpha(t)\rangle = \sum_i U_{\alpha i}^* e^{-iE_i t} |\nu_i\rangle, \quad (1.1.3)$$

where $E_i = \sqrt{|\mathbf{p}_i|^2 + m_i^2}$ is the energy, \mathbf{p}_i is the momentum, and m_i is the mass of $|\nu_i\rangle$. The probability of obtaining another flavor ν_β after a time t is given by

$$P_{\alpha\beta} = |\langle\nu_\beta|\nu_\alpha\rangle|^2 = \left| \sum_i U_{\beta i} U_{\alpha i}^* e^{-iE_i t} \right|^2. \quad (1.1.4)$$

In the ultra-relativistic limit, $|\mathbf{p}_i| \gg m_i$, hence we can approximate

$$E_i = \sqrt{|\mathbf{p}_i|^2 + m_i^2} \simeq |\mathbf{p}_i| + \frac{m_i^2}{2|\mathbf{p}_i|}. \quad (1.1.5)$$

Further terms are of $\mathcal{O}(m_i^4/|\mathbf{p}_i^3|)$ and can be neglected. The second term can be further expanded as

$$\frac{m_i^2}{2|\mathbf{p}_i|} = \frac{m_i^2}{2E_i} \left(1 + \frac{m_i^2}{2E_i^2}\right). \quad (1.1.6)$$

¹We follow closely the discussion in [26].

Since the neutrinos are ultra-relativistic, one can again neglect terms of $\mathcal{O}(m_i^4/E_i^3)$. Thus, for all practical purposes, the mass eigenstates have the same energy, i.e., $E_i \simeq E$, since the error involved in this approximation is also $\mathcal{O}(m_i^4/E_i^3)$, and can be neglected.

This allows us to rewrite Eq. (1.1.4) as

$$P_{\alpha\beta} = \sum_i |U_{\beta i}|^2 |U_{\alpha i}|^2 + 2 \operatorname{Re} \left[\sum_{i>j} U_{\beta i} U_{\alpha i}^* U_{\beta j}^* U_{\alpha j} e^{-i \frac{\Delta m_{ij}^2}{2E} t} \right], \quad (1.1.7)$$

in terms of the neutrino mass-squared differences $\Delta m_{ij}^2 = m_i^2 - m_j^2$.

Using the unitarity property of U , one can write Eq. (1.1.7) as

$$\begin{aligned} P_{\alpha\beta} &= \delta_{\alpha\beta} - 4 \operatorname{Re} \left[\sum_{i>j} U_{\beta i} U_{\alpha i}^* U_{\beta j}^* U_{\alpha j} \right] \sin^2 \left(\frac{\Delta m_{ij}^2}{4E} t \right) \\ &\quad + 2 \operatorname{Im} \left[\sum_{i>j} U_{\beta i} U_{\alpha i}^* U_{\beta j}^* U_{\alpha j} \right] \sin \left(\frac{\Delta m_{ij}^2}{2E} t \right). \end{aligned} \quad (1.1.8)$$

The oscillation probabilities with $\alpha = \beta$ are called the survival probabilities, while the ones with $\alpha \neq \beta$ are called the transition probabilities. Clearly, for survival probabilities, the quartic terms involving U s are real, and Eq. (1.1.8) simplifies to

$$P_{\alpha\alpha} = 1 - 4 \sum_{i>j} |U_{\alpha i}|^2 |U_{\alpha j}|^2 \sin^2 \left(\frac{\Delta m_{ij}^2}{4E} t \right). \quad (1.1.9)$$

Such an oscillating dependence of the flavor composition on t gives rise to neutrino flavor oscillations [27]. Clearly, when the neutrinos are massless, $\Delta m_{ij}^2 = 0$, and there are no oscillations. For ultra-relativistic neutrinos, one may substitute $t \approx L$ in the above equations, where L is the distance between the source and the detector.

1.1.1 Two flavor formalism

In this section, we illustrate the idea of neutrino oscillations using a two flavor scenario, say ν_e and ν_μ . This can be obtained, for e.g., by setting $\vartheta_{23}, \vartheta_{13} \rightarrow 0$ in Eq. (1.1.2). The mixing matrix connecting the mass and flavor basis is given by

$$U = \begin{pmatrix} \cos \vartheta_0 & \sin \vartheta_0 \\ -\sin \vartheta_0 & \cos \vartheta_0 \end{pmatrix}, \quad (1.1.10)$$

where ϑ_0 is the mixing angle. Using this, the transition probability in two flavors is given by

$$P_{\nu_e \rightarrow \nu_\mu} = P_{\nu_\mu \rightarrow \nu_e} = \sin^2 2\vartheta_0 \sin^2 \left(\frac{\Delta m^2}{4E} L \right). \quad (1.1.11)$$

From unitarity, the survival probabilities are given by

$$P_{\nu_e \rightarrow \nu_e} = P_{\nu_\mu \rightarrow \nu_\mu} = 1 - P_{\nu_e \rightarrow \nu_\mu}. \quad (1.1.12)$$

It is important to remember that since the complex phase can be rotated away in a two flavor framework, the expressions for antineutrinos are same as that for neutrinos.

Two crucial points may be obtained from the expression of the transition probability in Eq.(1.1.11). Firstly, the amplitude of oscillations is a function of the mixing angle ϑ_0 , while the frequency of oscillations is a function of Δm^2 . Therefore, neutrino oscillations require both mass and mixing to happen. However, since the dependence is on Δm^2 , we cannot access the information about individual mass from oscillation data. Secondly, for oscillations to be observed, the phase factor $(\Delta m^2 L)/(4E) \simeq \pi$. This allows us to define the oscillation length as

$$L_{\text{osc}} = \frac{4\pi E}{\Delta m^2} \simeq 2.48 \frac{E \text{ (MeV)}}{\Delta m^2 \text{ (eV}^2\text{)}} \text{ (in m)}. \quad (1.1.13)$$

If $L \ll L_{\text{osc}}$, the phase factor is too small, and oscillation does not develop. On the other hand, if $L \gg L_{\text{osc}}$, the phase is large, leading to rapid oscillations, which get averaged at the detector. Therefore, the oscillation probability at the detector becomes

$$\overline{P_{\nu_e \rightarrow \nu_\mu}} = \frac{1}{2} \sin^2 2\vartheta_0, \quad (1.1.14)$$

and the oscillation information is washed out.

1.2 Neutrino oscillations in matter

Till now, we have only considered neutrino oscillations in vacuum. However, in most realistic scenarios, neutrinos traverse through a medium before being detected. Hence it is important to treat neutrino oscillations in matter.

Neutrinos interact with the background matter through the SM weak interactions. The dominant contribution comes from coherent forward elastic scattering with electrons and nucleons in the medium. These processes involve only a single power of the Fermi coupling G_F , and hence dominate over non-elastic and loop processes, which involve larger powers of G_F [7]. Ordinary matter consists of e , p and n , but no μ and τ . Hence, forward scattering

processes involve charged current (CC) interactions of ν_e with e , and equal neutral current interactions of all neutrino flavors with n , p and e .

The effect of such coherent processes on neutrinos is equivalent to neutrino propagation in an effective potential [7, 28]. The effective potential due to CC interactions with ν_e is given by [29]

$$V_{\text{CC}}(r) = \sqrt{2}G_F n_e(r), \quad (1.2.1)$$

where $n_e(r)$ is the local electron density in the medium. Similarly, for NC interactions of $\nu_{e,\mu,\tau}$ with nucleons, the effective potential is given by [29]

$$V_{\text{NC}}(r) = -\frac{G_F n_n(r)}{\sqrt{2}}, \quad (1.2.2)$$

where $n_n(r)$ is the local nucleon density in the medium. Note that the NC interactions being flavor-blind, this potential is the same for all flavors and hence can be rotated away as an overall phase. For $\bar{\nu}$, both these effective potentials acquire a relative minus sign.

As a result of this matter effect, the resultant Hamiltonian (after dropping the identical NC terms) for evolution in matter is given by [28]

$$i d_t \begin{pmatrix} \nu_e \\ \nu_\mu \end{pmatrix} = \begin{pmatrix} -\frac{\Delta m^2}{4E} \cos 2\vartheta_0 + \frac{V_{\text{CC}}}{2} & \frac{\Delta m^2}{4E} \sin 2\vartheta_0 \\ \frac{\Delta m^2}{4E} \sin 2\vartheta_0 & \frac{\Delta m^2}{4E} \cos 2\vartheta_0 - \frac{V_{\text{CC}}}{2} \end{pmatrix} \begin{pmatrix} \nu_e \\ \nu_\mu \end{pmatrix} \quad (1.2.3)$$

This general EoM applies for both constant as well as varying matter density. In general, this equation is not easy to solve analytically. However, it can be solved analytically under certain conditions. In the following sections, we will briefly outline the treatment for a constant and varying matter profile.

1.2.1 Constant matter density

The assumption of a constant matter density vastly simplifies the problem and makes it analytically tractable. The idea is to solve the problem in the basis of instantaneous matter eigenstates, ν_i^m , in which the Hamiltonian is diagonalizable. Clearly, for a varying matter profile, these eigenstates will be a function of time, but for a constant matter profile, they just provide a separate basis. The flavor states are related to the matter states by [28]

$$\begin{pmatrix} \nu_e \\ \nu_\mu \end{pmatrix} = U(\vartheta_m) \begin{pmatrix} \nu_1^m \\ \nu_2^m \end{pmatrix} = \begin{pmatrix} \cos \vartheta_m & \sin \vartheta_m \\ -\sin \vartheta_m & \cos \vartheta_m \end{pmatrix} \begin{pmatrix} \nu_1^m \\ \nu_2^m \end{pmatrix}, \quad (1.2.4)$$

where ϑ_m is the effective mixing angle in matter. The diagonalization of the Hamiltonian gives the mixing angle

$$\tan 2\vartheta_m = \frac{\sin 2\vartheta_0}{\cos 2\vartheta_0 - \frac{2EV_{CC}}{\Delta m^2}}, \quad (1.2.5)$$

and the effective mass-squared difference in matter

$$\Delta m_m^2 = \sqrt{(\Delta m^2 \cos 2\vartheta_0 - 2EV_{CC})^2 + (\Delta m^2 \sin 2\vartheta_0)^2}. \quad (1.2.6)$$

In terms of these, the effective squared masses in matter m_{1m}^2 , m_{2m}^2 are given by

$$m_{1m,2m}^2 = \frac{1}{2} (m_1^2 + m_2^2 + 2EV_{CC} \pm \Delta m_m^2). \quad (1.2.7)$$

In the top panel of Fig. 1.1, we show the behavior of ϑ_m and $m_{1m,2m}^2$ as a function of the electron density n_e , plotted in arbitrary units. One can see that for n_e much less than the resonant electron density n_e^R , the effective mixing angle in matter is equal to that in vacuum, while for $n_e = n_e^R$, the value of ϑ_m passes through 45° , eventually going to 90° for large electron densities. In the bottom panel of Fig. 1.1, we plot the behavior of the effective squared masses as a function of the electron density.

Clearly, with these redefinitions, the evolution in a medium with constant matter density reduces to that of vacuum, with the vacuum parameters replaced by their corresponding matter mixing angle and masses. The oscillation probability is given by [28]

$$P_{\nu_e \rightarrow \nu_\mu} = \sin^2 2\vartheta_m \sin^2 \left(\frac{\omega_m L}{2} \right) \quad (1.2.8)$$

where

$$\sin 2\vartheta_m = \frac{\omega \sin 2\vartheta_0}{\sqrt{(\omega \cos 2\vartheta_0 - V_{CC})^2 + (\omega \sin 2\vartheta_0)^2}}, \quad (1.2.9)$$

and $\omega_{(m)} = \frac{\Delta m_{(m)}^2}{2E}$.

Eq. (1.2.8) demonstrates that the oscillation probability can undergo a resonance when $\sin^2 2\vartheta_m = 1$. This is the MSW (Mikheyev-Smirnov-Wolfenstein) resonance condition and is satisfied when [7, 8]

$$\omega \cos 2\vartheta_0 = V_{CC}. \quad (1.2.10)$$

This condition, satisfied either by neutrinos or antineutrinos, depending on the mass hierarchy, leads to maximal mixing in matter, i.e. $\vartheta_m = \pi/4$, and can cause large flavor conversions even when ϑ_0 is small.

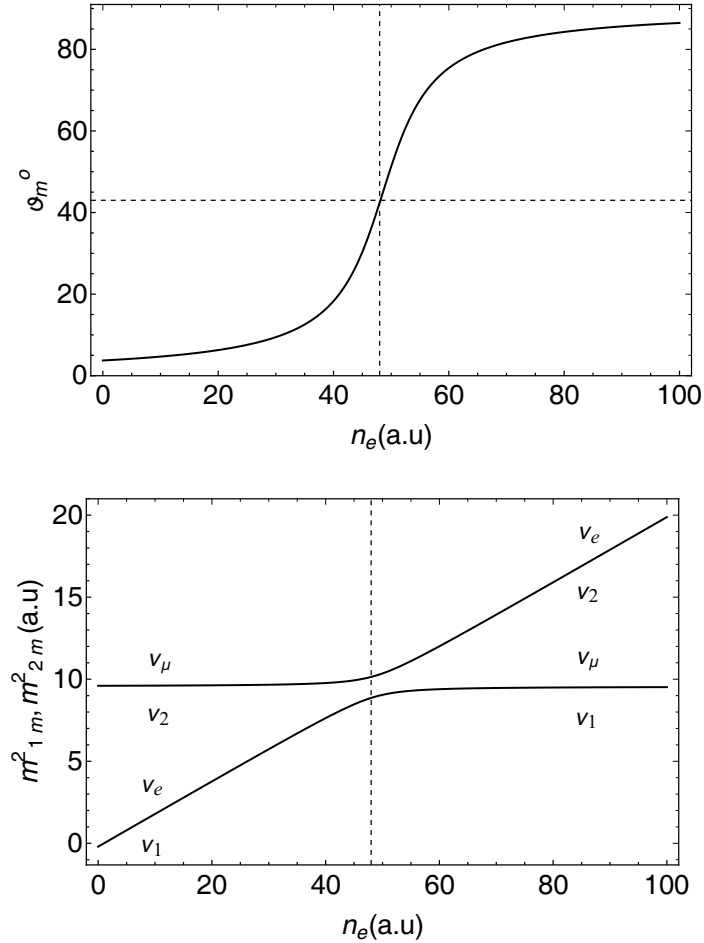


Figure 1.1: Effective mixing angle ϑ_m (top) and effective squared-masses $m_{1m, 2m}^2$ (bottom) in matter as functions of the electron number density $n_e(r) \propto r$. The other parameters used are $\Delta m^2 = 5 \times 10^{-5} \text{ eV}^2$, $\sin^2 2\vartheta = 0.1$ and $E = 1 \text{ MeV}$. The vertical dashed line indicates the resonant electron density n_e^R .

1.2.2 Varying matter density

A more realistic scenario is when the neutrinos travel through a varying matter density profile. In this case, the matter basis, and hence the unitary transformation connecting the matter and flavor basis, become time-dependent. As a result, the evolution equations become

$$i d_t \begin{pmatrix} \nu_e \\ \nu_\mu \end{pmatrix} = U(\vartheta_m) d_t \begin{pmatrix} \nu_1^m \\ \nu_2^m \end{pmatrix} + d_t(U(\vartheta_m)) \begin{pmatrix} \nu_1^m \\ \nu_2^m \end{pmatrix}. \quad (1.2.11)$$

Using this, one arrives at

$$i d_t \begin{pmatrix} \nu_1^m \\ \nu_2^m \end{pmatrix} = \begin{pmatrix} \omega_m & -i \frac{d\vartheta_m}{dt} \\ i \frac{d\vartheta_m}{dt} & -\omega_m \end{pmatrix} \begin{pmatrix} \nu_1^m \\ \nu_2^m \end{pmatrix}. \quad (1.2.12)$$

Clearly, the Hamiltonian is not diagonal, and the $\nu_{\{1,2\}}^m$ are not energy eigenstates. Hence, they mix with each other, depending on the size of the off-diagonal element.

One can parameterize the relative size of the off-diagonal element with respect to the diagonal element via the adiabaticity parameter [30]

$$\gamma \equiv \frac{|\omega_m|}{|d\vartheta_m/dt|} = \left| \frac{4 (\Delta m_m^2)^3}{\Delta m \sin 2\vartheta_0} \left(\frac{dV_{CC}}{dt} \right)^{-1} \right|. \quad (1.2.13)$$

The resonance is said to be adiabatic if $\gamma \gg 1$ at all points of the neutrino trajectory, and in that case, transitions between matter eigenstates are suppressed. However, if $\gamma \lesssim 1$, the resonance is non-adiabatic, and flavor transitions are sizeable. Large flavor transitions can be obtained when γ is minimized. Near an MSW resonance, the value of γ :

$$\gamma_{\text{res}} = \frac{\Delta m^2 \sin^2 2\vartheta_0}{2E \cos 2\vartheta_0} \left| \frac{1}{V_{CC}} \frac{dV_{CC}}{dt} \right|_{\text{res}}^{-1}. \quad (1.2.14)$$

Correspondingly, the probability of one instantaneous matter eigenstate converting to the other is [30]

$$P_{\text{res}} = \frac{\exp\left(-\frac{\pi}{2}\gamma_{\text{res}}F\right) - \exp\left(-\frac{\pi}{2\sin^2\vartheta_0}\gamma_{\text{res}}F\right)}{1 - \exp\left(-\frac{\pi}{2\sin^2\vartheta_0}\gamma_{\text{res}}F\right)}, \quad (1.2.15)$$

where F is a parameter which depends on the density profile.

It is important to note that a similar matter-like potential $V \sim \sqrt{2}G_F n_\nu$ is generated due to interaction with the ambient neutrinos and antineutrinos in the medium [31,32]. However, since this is proportional to the surrounding neutrino density, it is usually negligible in most circumstances, for example, propagating inside the Sun or in the Earth. However, this potential plays a very important role in the propagation of SN neutrinos, as this makes the whole problem non-linear. We will deal with this issue in detail in later chapters.

1.3 Current status of three-flavor neutrino oscillations

Clearly, from the previous discussions, studying neutrino oscillation physics in detail requires knowledge of six parameters: Δm_{21}^2 , Δm_{31}^2 , ϑ_{12} , ϑ_{23} , ϑ_{13} , δ . Much of our understanding

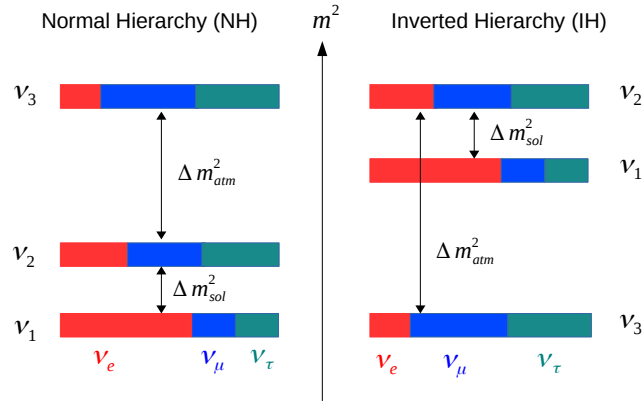


Figure 1.2: The two different neutrino mass-orderings are shown. The relative fraction of the ν_e (red), ν_μ (blue) and ν_τ (green) in the individual mass eigenstates are also shown for both the mass orderings. Left: Normal mass hierarchy. Right: Inverted mass hierarchy.

of the three-flavor neutrino oscillation framework have been confirmed by experiments using atmospheric, solar, reactor and accelerator neutrinos, which have helped to determine five of these unknown parameters with great precision. While we have knowledge of the Δm_{21}^2 , $|\Delta m_{31}^2|$, ϑ_{12} , ϑ_{23} , and ϑ_{13} , what remain to be determined are the CP violating phase δ and the sign of m_{31}^2 . Typically, depending on the sign of Δm_{31}^2 , two mass orderings are defined, as shown in Fig.1.2. If $m_3 > m_1$, the mass ordering is called the normal mass hierarchy (NH), while if $m_1 > m_3$, it is called the inverted mass hierarchy (IH).

The most stringent bounds on ϑ_{23} come from atmospheric neutrino measurements by Super-Kamiokande [15, 16], whereas the magnitude of the atmospheric mass-squared difference $|\Delta m_{\text{atm}}^2| \equiv |\Delta m_{31}^2|$ is best constrained by accelerator experiments, for e.g., MINOS [33]. These give the following best fit with 1σ errors [34, 35]:

$$\begin{aligned} \sin^2 \vartheta_{23} &= 0.441_{-0.021}^{+0.027} \text{ (NH)}, & \sin^2 \vartheta_{23} &= 0.587_{-0.024}^{+0.020} \text{ (IH)}. \\ |\Delta m_{31}^2| &= 2.52_{-0.040}^{+0.039} \times 10^{-3} \text{ eV}^2 \text{ (NH)}, & |\Delta m_{32}^2| &= 2.51_{-0.041}^{+0.038} \times 10^{-3} \text{ eV}^2 \text{ (IH)}. \end{aligned}$$

Future experiments like JUNO [36], and INO [37] will shed light on the sign of Δm_{31}^2 , thereby resolving the neutrino mass-hierarchy determination problem. Latest global fits from the Bari group [38] including the T2K [39] and NO ν A [40] data indicate a $\sim 3\sigma$ preference in favor of NH.

Limits on the solar neutrino parameters were given by the KamLAND reactor experiment [12], as well as SNO [13,41], Super-Kamiokande [15,42], Borexino [43], and Gallex [44] experiments. While KamLAND constrains the solar mass-squared difference $\Delta m_{\odot}^2 \equiv \Delta m_{21}^2$ [12], the solar mixing angle ϑ_{12} is mainly constrained by solar experiments. The best fit with 1σ errors are given by [34,35]

$$\begin{aligned}\sin^2 \vartheta_{12} &= 0.306_{-0.012}^{+0.012} \text{ (NH)}, & \sin^2 \vartheta_{12} &= 0.306_{-0.012}^{+0.012} \text{ (IH)}. \\ \Delta m_{21}^2 &= 7.50_{-0.17}^{+0.19} \times 10^{-5} \text{ eV}^2 \text{ (NH)}, & \Delta m_{21}^2 &= 7.50_{-0.17}^{+0.19} \times 10^{-5} \text{ eV}^2 \text{ (IH)}.\end{aligned}$$

The reactor mixing angle has now been well-determined by reactor neutrino experiments and is quoted as [19,20]

$$\sin^2 \vartheta_{13} = 0.02166_{-0.00075}^{+0.00075} \text{ (NH)}, \quad \sin^2 \vartheta_{13} = 0.02179_{-0.00076}^{+0.00076} \text{ (IH)}.$$

Long-baseline neutrino oscillation data play an important role in determining the CP violating phase δ . The best fit with 1σ errors are quoted as [34,35]

$$\delta = 261_{-59}^{+51} \text{ (NH)}, \quad \delta = 277_{-46}^{+40} \text{ (IH)}.$$

However, note that latest values of δ measured by T2K and NO ν A do not overlap within 1σ . Latest data from T2K excludes the CP conserving value ($\delta = 0^\circ, 180^\circ$) at 2σ confidence [45]. NO ν A, on the other hand, quotes the 1σ confidence interval for δ as $[0^\circ, 21.6^\circ] \cup [163.8^\circ, 360^\circ]$ [46]. Therefore, we still do not know the value of δ .

The absolute neutrino mass is unknown, but cosmology puts an upper bound on the sum of neutrino masses to be $\sum_i m_{\nu_i} \leq 0.17 \text{ eV}$ [47]. Finally, note that the experiments studying neutrino flavor oscillations cannot provide information on the Dirac or Majorana nature of neutrinos. Establishing the nature of massive neutrinos is one of the most challenging problems of neutrino physics. The experiments currently having the capability to establish the Majorana nature of neutrinos are those searching for the neutrinoless double beta-decay [48,49].

1.4 Neutrinos from a core-collapse supernova

1.4.1 Explosion mechanism and neutrino emission

In this section, we will present a brief overview of the theory of a core-collapse SN, and the associated neutrino emission². For detailed reviews of the same, focusing on different aspects, see Refs. [25, 50–56]. The end stage of hydrostatic burning of a massive star ($8 M_{\odot} - 20 M_{\odot}$) leaves behind concentric shells of elements (starting with hydrogen on the outermost layer and ending mostly in iron), as end-products. Typically, hydrostatic burning concludes with the formation of iron, as iron has the highest average binding energy per nucleon, and production of heavier elements require energy to be supplied than released. As the iron shell, formed from silicon burning, grows to a mass larger than the Chandrasekhar mass limit $\sim 1.44 M_{\odot}$, electron degeneracy pressure fails to support it any longer and a collapse is initiated ($t = 0$ s). In the initial stages of the collapse ($t \sim 10$ ms), electron capture, as well as β -decay of nuclei, lead to further reduction in degeneracy pressure and this accelerates the collapse. Neutrinos are also emitted through these processes. At a time of around $t \sim 100$ ms, when the surrounding densities are $\rho \equiv \rho_{\text{trap}} \approx 10^{12}$ g/cm³, neutrinos get trapped in the core, as their diffusion time becomes larger than the collapse time. The collapse proceeds until nuclear densities $\rho_{\text{nuc}} \approx 10^{14}$ g/cm³ are reached, when the core stiffens. This decelerates the infall of the core, which bounces in response to the increased nuclear matter pressure. This creates a shock wave into the outer core. The outer core, on the other hand, is not in acoustic communication with the inner core and keeps falling at a supersonic speed.

This “bounce and shock formation” [57] is ultimately responsible for a SN explosion, however, the exact details of it still remain a matter of active research. The “prompt explosion” scenario is one where the shock wave is energetic enough to drive the explosion [58, 59]. However, hydrodynamic simulations suggest that the shock wave uses its energy in the dissociation of heavy nuclei into nucleons [60]. The free protons, thus formed, have a larger rate of electron capture, which leads to the production of a large burst of neutrinos. This phase, dubbed as the “neutronization burst”, is quite a robust feature of all simulations [61, 62]. These neutrinos produced quickly leave the star, carrying away much of the energy of the

²The discussion in this section follows from [50].

shock wave. In the process, the shock weakens and finally stalls, turning into an “accretion shock” at a radius between 100 km and 200 km [61, 62].

As the shock stalls, the compact proto-neutron star (PNS) at the center begins to grow by accretion of infalling stellar material. Most of the neutrinos and antineutrinos that were trapped initially due to the high density start free-streaming from the “neutrinosphere”, which acts like the surface of last scattering [63]. These neutrinos carry away a major fraction of the gravitational binding energy of the star, which leads to the cooling of the PNS (“Kelvin-Helmholtz cooling phase”) [64]. It is believed that the neutrinos deposit their energy in the region behind the shock front through charged current capture of ν_e and $\bar{\nu}_e$ on n and p [65]. In the “delayed neutrino-heating” explosion mechanism [61, 62], this neutrino heating drives the shock-wave outward, leading to a successful explosion. However, this scenario is highly sensitive to the neutrino flavor information and hence requires a precise understanding of the phenomenon of neutrino flavor oscillations.

Thus, to sum it up, there are four distinct phases of neutrino emission from a core-collapse SN [50, 56]:

(i) In the initial collapse phase, when the core bounce has not yet taken place, small amounts of ν_e are mainly emitted due to beta decay and electron capture.

(ii) During the “neutronization burst” phase which occurs typically $\mathcal{O}(25)$ ms after core-bounce, this ν_e flux rises steeply. During this period, smaller amounts of $\bar{\nu}_e$, as well as the other flavors (ν_μ , $\bar{\nu}_\mu$, ν_τ , $\bar{\nu}_\tau$) are also emitted, but these are negligible compared to the ν_e flux.

(iii) This is followed by the “accretion phase”, which lasts for a period of $\mathcal{O}(1)$ s. As the shockwave stagnates, matter accretes onto the core for a few 100 ms. During this phase, the star cools by radiating neutrinos and antineutrinos of all flavors. Typically, there is an excess of ν_e over other species, with a clear hierarchy in average energies $\langle E_{\nu_{\mu,\tau}} \rangle > \langle E_{\bar{\nu}_e} \rangle > \langle E_{\nu_e} \rangle$.

(iv) Finally, one enters the “Kelvin-Helmholtz cooling phase”, where the PNS at the center cools by radiating away neutrinos for a period of $\mathcal{O}(10)$ s. The hierarchy of average energy of neutrino flavors in this phase is found to be milder.

In Fig. 1.3, we highlight the luminosities and the average energies of the emitted neutrinos

during these four phases [66, 67]. The left column indicates the initial collapse and the neutronization burst phase, while the middle and the right column indicates the accretion phase and the cooling phase respectively.

One can make a quick back-of-the-envelope estimate about the flux and the average energies of neutrinos emitted from a core-collapse SN. Typically for a PNS of mass $M_{\text{PNS}} \approx 1.4 M_{\odot}$ and a radius $R_{\text{PNS}} \approx 15$ km, the nucleon mean kinetic energy can be estimated from the virial theorem by

$$\langle E_n \rangle = \frac{1}{2} \frac{G_N M_{\text{PNS}} m_n}{R_{\text{PNS}}} \approx 25 \text{ MeV},$$

where G_N is the Newton's gravitational constant. The average energy of the emitted neutrinos $\langle E_{\nu} \rangle$ is roughly of the same order of magnitude as $\langle E_n \rangle$. During a collapse, almost 99% of the entire gravitational binding energy of the star is emitted in the form of neutrinos. This energy is equally divided among the three neutrino flavors and their antiparticles. The energy released during a collapse is given by

$$E_g \approx \frac{3}{5} \frac{G_N M_{\text{PNS}}^2}{R_{\text{PNS}}} \approx 10^{59} \text{ MeV}.$$

Therefore, one expects that an approximate $E_g / \langle E_n \rangle \sim 10^{58}$ neutrinos are emitted from the SN. These are emitted during a timescale of ~ 10 s, which is the typical diffusion timescale of neutrinos within the core.

Regarding the different species of neutrino flavor emitted, one has to keep in mind that non-electron flavors like ν_{μ}, ν_{τ} have smaller opacities, i.e, they decouple *earlier*. They do not have enough energy to undergo CC interactions of the form $\bar{\nu}_{\mu} + p \rightarrow n + \mu^{+}$ because the leptons are heavier. Hence they decouple at higher temperatures and have higher energy. The average energies of ν_e and $\bar{\nu}_e$ are governed by the reactions $\nu_e + n \rightarrow p + e^{-}$ and $\bar{\nu}_e + p \rightarrow n + e^{+}$. Since there are more neutrons than protons, the interaction rate of ν_e is more than that of $\bar{\nu}_e$, hence average energies of $\bar{\nu}_e$ are larger than that of ν_e . Hence typical average energy hierarchy goes as $\langle E_{\nu_e} \rangle < \langle E_{\bar{\nu}_e} \rangle < \langle E_{\nu_{\mu,\tau}} \rangle$. Also, since the scattering cross-section of neutrinos on nucleons $\sigma \propto (G_F^2 E_{\nu}^2)$, the neutrinosphere - the surface of free-streaming for neutrinos, is also *energy dependent*, and *flavor dependent*.³

³The scattering of neutrinos with nuclei does not allow for much exchange of energies [68]. It is possible that while undergoing collisions, the neutrinos can change directions without any change in energy. Hence the concept of an energysphere (beyond which there is no exchange of energy) is different from a transportsphere

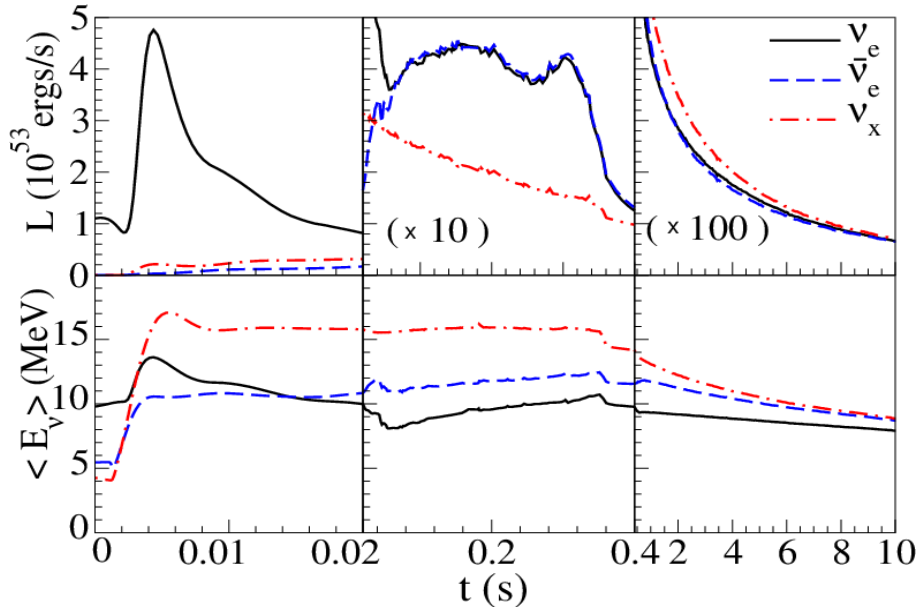


Figure 1.3: Snapshot of the luminosities and the average energies of the emitted neutrinos in the different phases [66]. This figure has been taken from [67]. Left: Initial cooling and neutronization burst phase. Middle: Accretion phase. Right: Cooling phase.

For more quantitative claims about the neutrino fluxes and average energies, one has to resort to numerical simulations. These simulations employ detailed neutrino transport, incorporating all the relevant weak interaction processes. The neutrino luminosities are typically time-dependent, being very high $\sim 10^{54}$ ergs/s during the neutronization epoch, and gradually decreasing with time. Moreover, the relative neutrino number fluxes are also seen to change with time.

The hydrodynamics simulations of the SN do not always result in successful explosions by this delayed neutrino-heating mechanism. While some of the low mass ($8 M_{\odot} - 12 M_{\odot}$) stars explode [69, 70], explosions might be inhibited in heavier mass stars [71]. Typically, the neutrino heating is not sufficient to trigger the shockwave, hence the shock falls back and no explosion takes place. Simulations in 2D can generate explosions sometimes by including convection inside the PNS just below the neutrinosphere [55, 71]. One of the effects of convection is to enhance the early neutrino luminosities, thereby increasing the energy deposition behind the shock. In 3D, it is more difficult to generate explosions using

(beyond which the neutrinos can free stream). However, for most part of this thesis, we will not distinguish between the two, and identify the region of free-streaming as a neutrinosphere.

only convection [72], since turbulent energy cascade in 3D occurs from larger scales to smaller scales, which is the opposite of what happens in 2D [73]. An important parameter in these studies of neutrino-driven explosion is the compactness parameter, which characterizes the difference in various stellar density profiles [74]. It is defined as the ratio of a chosen mass shell to the radius that encloses the mass. Low mass progenitors ($M < 12 M_{\odot}$) have low compactness, and are easier to explode [74]. However, this compactness is a non-monotonic function of the progenitor mass, and hence can be very different for stars of nearly the same mass [74,75]. Therefore, non explosions of certain massive progenitors may be a result of this non-monotonicity rather than a numerical artefact. Non-radial hydrodynamic instabilities can also become relevant in the explosion mechanism of the SN. Large scale convective overturns can occur in the PNS, just below the shockwave in the accretion shock phase. The delayed explosion mechanism can also be assisted by such standing accretion shock instability (SASI) [69,76], which causes violent convective motions below the shock wave, thereby aiding in regenerating the shockwave by added energy deposition. However, throughout this thesis, we neglect such convective instabilities, and assume that the delayed explosion mechanism is realized inside a star.

1.4.2 Supernova neutrino spectra

A detailed measurement of the neutrino signal from a galactic SN could yield important information about the masses, and mixing of the neutrinos, as well as the SN explosion mechanism [25,77]. Furthermore, a detailed understanding of neutrino flavor conversions is necessary for a proper interpretation of a neutrino signal from a SN [78].

The neutrinos free-stream from the neutrinosphere, and pass through the SN envelope, going through a huge range of ordinary matter densities, varying from $\sim 10^{11}$ g/cc near the core to nearly vacuum in the interstellar space. During the neutrino propagation, flavor conversions are affected not only by the matter density, but also the surrounding neutrino density. This is because near the neutrinosphere, the neutrino density itself is so high that neutrinos start interacting with other neutrinos. Thus, for SN neutrinos, enhanced flavor conversion can happen in two ways: either due to ordinary matter, which introduces a potential $\sqrt{2}G_F n_e(\mathbf{r})$ for a background electron density $n_e(\mathbf{r})$, or due to the potential created

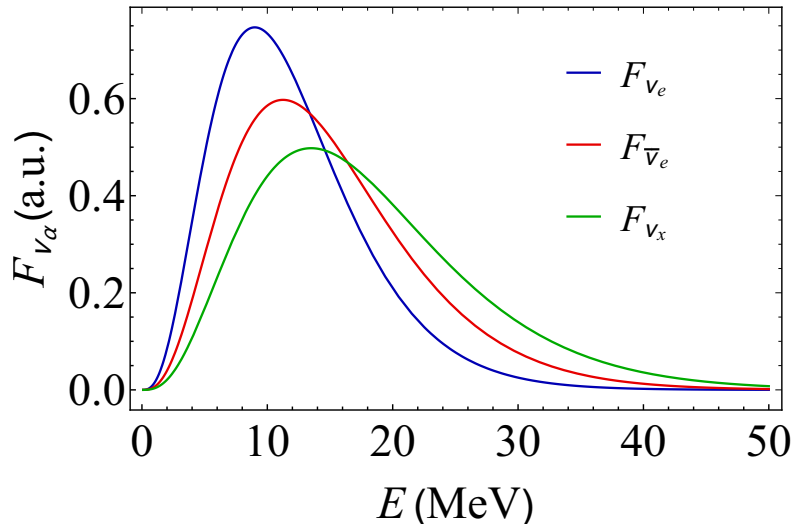


Figure 1.4: The alpha-fit neutrino spectra shown for $\alpha = 3$, $\langle E_{\nu_e} \rangle = 12$ MeV, $\langle E_{\bar{\nu}_e} \rangle = 15$ MeV and $\langle E_{\nu_x} \rangle = 18$ MeV [79]. Here ν_x refers to ν_μ , ν_τ or any linear combination of both. All the plots are scaled by a factor of 10, keeping the relative normalization intact, and hence shown in arbitrary units.

by ambient neutrinos and antineutrinos $\propto \sqrt{2}G_F (n_\nu(\mathbf{r}) + n_{\bar{\nu}}(\mathbf{r}))$ for a background neutrino density $n_\nu(\mathbf{r})$ [31, 32].

A SN acts like an approximate blackbody, which cools by emission of neutrinos. Keeping this in mind, SN simulations typically fit the neutrino spectra with a “quasi-thermal” spectra, the so-called “alpha-fit” [79]:

$$F_{\nu_\alpha}(E) = \frac{1}{\langle E_\nu \rangle} \frac{(\alpha + 1)^{(\alpha+1)}}{\Gamma(\alpha + 1)} \left(\frac{E}{\langle E_\nu \rangle} \right)^\alpha \exp \left[-(\alpha + 1) \frac{E}{\langle E_\nu \rangle} \right], \quad (1.4.1)$$

where $F_{\nu_\alpha}(E)$ is normalized to unity. Here, $\langle E_\nu \rangle$ denotes the average energy of the neutrinos, $\Gamma(z)$ is the Euler gamma function, and α is a dimensionless parameter which relates to the width of the spectra, given by

$$\frac{1}{1 + \alpha} = \frac{\langle E^2 \rangle - \langle E \rangle^2}{\langle E \rangle^2}.$$

These spectral parameters can be different for the different neutrino emission phases, and depend on the particulars of simulation, such as the treatment of neutrino transport, and inputs from nuclear physics. Typically $\alpha = 2$ corresponds to a Maxwell-Boltzmann spectrum, $\alpha > 2$ to a pinched spectrum, where the high and low energy tails are suppressed, and $\alpha < 2$

to a broadened spectrum. Usual simulations quote values of α such that $2 \leq \alpha \leq 5$ [79]. Typically, one expects that $\langle E_{\nu_e} \rangle \approx 10 - 12$ MeV, while the $\bar{\nu}_e$ energies are slightly larger, i.e., $\langle E_{\bar{\nu}_e} \rangle \approx 12 - 15$ MeV [79]. Interactions for ν_μ, ν_τ and their antiparticles are almost identical, and their average energies are higher: $\langle E_{\nu_{\mu,\tau}} \rangle \approx 15 - 18$ MeV [79]. The hierarchy in average energies of different flavors is essentially due to the different neutrino interaction cross-sections, as explained in the previous section. An illustration of the quasi-thermal alpha-fit spectra is shown in Fig. 1.4.

The total flux of neutrinos streaming out of the neutrinosphere is a function of the luminosity and is given by

$$\Phi_{\nu_\alpha}(E) = \frac{L_\nu}{\langle E_\nu \rangle} F_{\nu_\alpha}(E), \quad (1.4.2)$$

where L_ν is the corresponding neutrino luminosity.

1.4.3 Oscillations of supernova neutrinos

The question we want to address is the following: how do the final spectra emerging from the SN, after flavor conversions, look like? To answer this question, we need to understand the physics of flavor conversions of SN neutrinos.

1.4.3.1 MSW flavor conversions

For a long time, it was believed that the major mode of flavor conversions in a SN was due to resonant flavor conversions by the Mikheyev-Smirnov-Wolfenstein (MSW) effect [30, 77]. Within this paradigm, large flavor conversions happen when the $\Delta m_\nu^2 \cos 2\vartheta / (2E_\nu) = \pm \sqrt{2} G_F n_e$, where the plus and minus signs refer to neutrinos and antineutrinos respectively. For the solar neutrino mass-squared difference Δm_\odot^2 , it is called the ‘‘L-resonance’’ (low density), as it occurs at matter densities of about $\rho_L \approx (10 - 100)$ g/cc. Since we know that $\Delta m_\odot^2 > 0$, the L-resonance takes place only for neutrinos. For the atmospheric mass-squared difference Δm_{atm}^2 , the resonance is called ‘‘H-resonance’’ (high density), and occurs at matter densities of about $\rho_H \approx (10^3 - 10^4)$ g/cc. The H-resonance takes place for neutrinos in the normal hierarchy ($\Delta m_{\text{atm}}^2 > 0$), and for antineutrinos in the inverted hierarchy ($\Delta m_{\text{atm}}^2 < 0$). For a typical SN density profile, these resonances are shown in Fig. 1.5. It is now known that

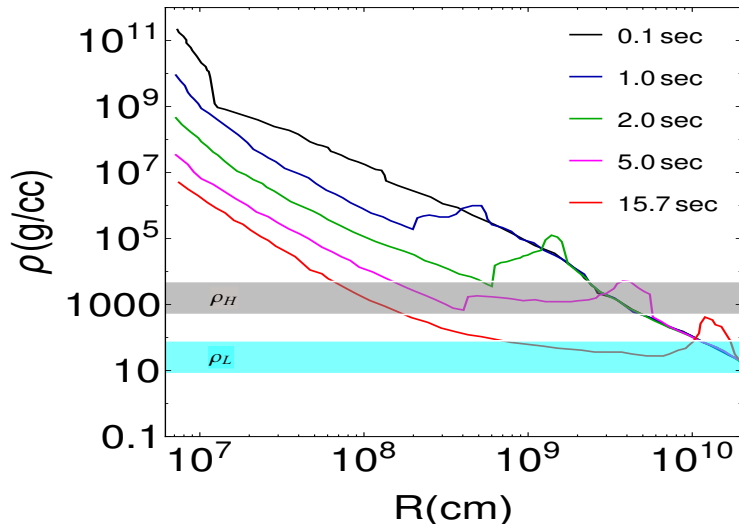


Figure 1.5: A snapshot of a SN density profile at the indicated times, taken from a $15 M_{\odot}$ progenitor [87]. The density region ρ_H corresponds to the H-resonance with the atmospheric mass difference, while ρ_L corresponds to the L-resonance with the solar mass difference. The width of the bands are due to the range of expected energies of SN neutrinos.

both these resonances are adiabatic, since both the mixing angles are reasonably large [34,35]. Such resonant flavor conversions in a SN has already been studied in details to probe neutrino properties and SN dynamics [77, 80–86]. From Fig. 1.5, we see that typical SN post-bounce matter density profiles are non-monotonic, time-dependent, and show a discontinuity at the position of the shock-front. This discontinuity is due to the shockwave leaving behind a rarefaction region, with a sharp drop in density. The final ν_e flux after an MSW resonance is given by [77]

$$F_{\nu_e} = p(E)F_{\nu_e}^0(E) + (1 - p(E))F_{\nu_x}^0(E), \quad (1.4.3)$$

where $p(E)$ denotes the energy dependent ν_e survival probability and F^0 indicates the initial fluxes leaving the SN core. Typically, for a static SN profile, ignoring turbulence effects, one finds $(p, \bar{p}) \approx (0, \cos^2 \vartheta_{12})$ for NH, and $(p, \bar{p}) \approx (\sin^2 \vartheta_{12}, 0)$ for IH, where \bar{p} refers to the $\bar{\nu}_e$ survival probability [77].

1.4.3.2 Self-induced bipolar neutrino oscillations

However, this above picture assumes that the effect of the neutrino potential within a SN is negligible, which is found not to be the case [88–92]. Deep inside a SN, the neutrino

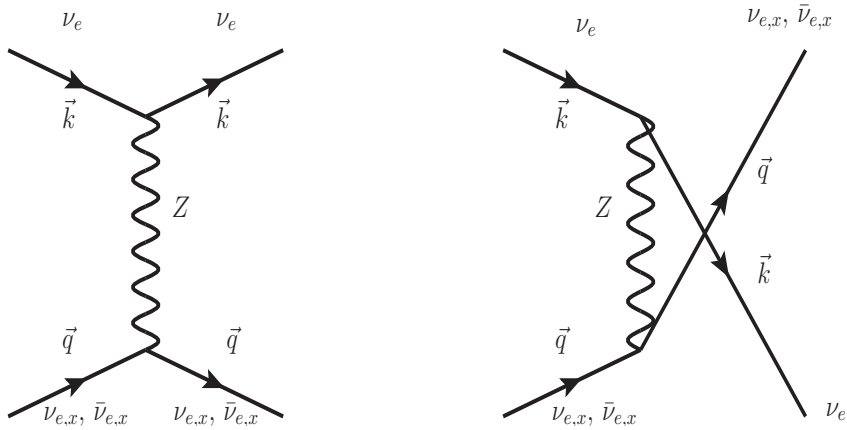


Figure 1.6: Neutral current interaction processes which contribute to the self-interactions of ν_e . Similar processes also hold for $\bar{\nu}_e$ and ν_x .

density is so high $\sim 10^{31}/\text{cc}$, that neutrino-neutrino interactions are significant. These interactions give rise to an MSW-like potential $\propto \sqrt{2}G_F(n_\nu(\mathbf{r}) + n_{\bar{\nu}}(\mathbf{r}))$ for a background neutrino density $n_\nu(\mathbf{r})$ [31]. As a result, each neutrino interacts with all other neutrinos in the medium, thereby making the problem of flavor evolution non-linear. Neutral current interactions preserve flavor, so the processes which contribute to these self-interactions are of the scatterings of the type $\nu_e(\mathbf{p}) + \nu_x(\mathbf{k}) \leftrightarrow \nu_x(\mathbf{p}) + \nu_e(\mathbf{k})$, and $\nu_e(\mathbf{p}) + \bar{\nu}_e(\mathbf{k}) \leftrightarrow \nu_x(\mathbf{p}) + \bar{\nu}_x(\mathbf{k})$, as shown in Fig. 1.6. Here $\nu_x \equiv \nu_\mu, \nu_\tau$, or any linear combination of both, since all non-electron flavors have identical interactions within the SN, and for phenomenological purposes, can be considered the same. Hence, unlike the matter potential, this neutrino potential is not flavor diagonal, and has significant contributions in the off-diagonal components as well [89, 90]. Such flavor evolution has been studied extensively using the density matrix formalism [88–96]. It was shown that due to these non-linear neutrino-neutrino interactions, a dense ensemble of neutrinos and antineutrinos exhibit collective oscillations. The simplest example would be a mono-energetic ensemble of ν_e and $\bar{\nu}_e$, partly oscillating to ν_x and $\bar{\nu}_x$, leaving the net flavor content unchanged [89, 90, 97]. The system behaves like a collection of coupled oscillators in flavor space [97, 98]. Depending on the neutrino-neutrino coupling, these coupled oscillators can either oscillate harmonically, or have run-away solutions, which would indicate large self-induced flavor conversions [97, 98].

Such nonlinear flavor conversions in a SN have been studied extensively in the literature (see Refs. [25, 78, 99, 100] for a discussion of the recent developments and the open issues).

In [97], two stages of collective effects were recognized: (i) “synchronized” oscillations, where neutrinos of all energies oscillate with a single frequency but small amplitude—due to the small mixing angle in matter [101], and (ii) “bipolar” oscillations. For mono-energetic neutrinos, these bipolar can lead to a complete flavor conversion for IH even for small mixing angle. In the case of NH, no bipolar oscillations take place. This analysis was restricted to two flavors: ν_e and ν_x , with an excess of ν_e over $\bar{\nu}_e$. Bipolar oscillations were shown to be equivalent to an inverted pendulum in flavor space, where swinging of the pendulum from an unstable inverted position was shown to be equivalent to run-away flavor oscillations [97, 98].

The bipolar oscillations further culminate in spectral splits. For a single spectral split, all ν_e beyond a certain critical energy would convert to ν_x , while below this energy, the ν_e s would emerge in their original flavor [91]. An analytical understanding of the phenomenon was offered [102, 103] using a simple box spectrum in the variable $\omega \equiv \pm \Delta m^2 / (2E)$, where the positive (negative) sign stands for neutrinos (antineutrinos). Multiple spectral splits observed in the simulations [104, 105] were explained analytically [106] in terms of the development of spectral swaps in g_ω , where

$$\begin{aligned} g_\omega &\propto F_{\nu_e}(\omega) - F_{\nu_x}(\omega) && \text{for } \omega > 0, \\ &\propto F_{\bar{\nu}_x}(\omega) - F_{\bar{\nu}_e}(\omega) && \text{for } \omega < 0. \end{aligned} \quad (1.4.4)$$

It was shown that in IH (NH), any positive (negative) crossing of the g_ω -spectra is unstable, thereby causing bipolar oscillations leading to a spectral swap. The three-flavor mixing effects can be largely understood in terms of stepwise two flavor effects. However, decoupling of the third flavor need not always be straightforward, and interesting effects can arise due to that [95, 107–109].

Most of the above analyses were carried out in the two-flavor framework with a single angle approximation, i.e., all neutrinos were emitted from the neutrinosphere with the same initial angle [91]. Multi-angle effects were shown to cause smearing of features in bipolar oscillations, leading to smoothening of spectral splits [104]. However, such multi-angle decoherence can be suppressed for sufficient neutrino-antineutrino asymmetry, which can exist in the deleptonization flux in a realistic supernova [94]. The inclusion of multi-angle effects can also result in the suppression of bipolar oscillations in presence of matter [91, 104, 110–113].

We are still far from having a complete analytical picture of the flavor instabilities that lead

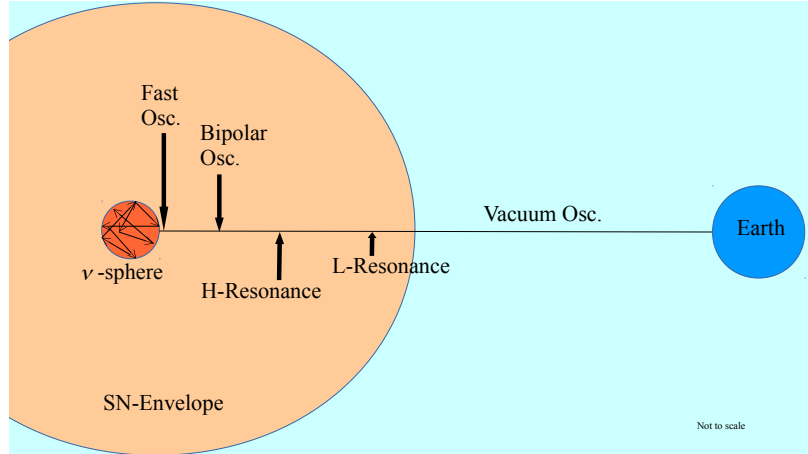


Figure 1.7: A schematic picture of a SN envelope with the different length scales involved.

to spectral swaps. However, one can get an understanding of the onset of these instabilities using a linearized stability analysis [96, 100, 114]. For an isotropic gas of neutrinos and antineutrinos, the rate of development of these instabilities is proportional to $\sqrt{\omega\mu}$, where $\mu = \sqrt{2}G_F n_\nu$ is the rate of interaction with ambient neutrinos, proportional to the number density of the neutrinos n_ν .

1.4.3.3 Fast flavor oscillations

All the above studies considered flavor independent angular emissions of neutrinos from the neutrinosphere. However, if this assumption does not hold, then new instabilities can arise even deeper inside the star, which would result in faster flavor conversions with a rate proportional to μ , producing flavor equilibrium among the different neutrino fluxes at $r \sim \mathcal{O}(1)$ m from the SN surface [115]. These conversions could occur even for massless neutrinos, requiring a nonzero ω perhaps only as an initial perturbation, thereby being independent of the yet unknown neutrino mass ordering. It was speculated that the necessary condition to achieve these fast conversions is the presence of sufficient anisotropy in the angular emission spectrum of the different neutrino flavors. This is something one can indeed expect near the neutrinosphere deep inside a SN. Due to different interaction cross-sections with matter, the non-electron flavors $\nu_{\mu,\tau}$ decouple from matter deeper than $\bar{\nu}_e$, and the latter deeper than ν_e . Therefore, near the SN core, the $\nu_{\mu,\tau}$ zenith-angle distribution would be more forward-peaked than that of $\bar{\nu}_e$, which in turn would be more forward-peaked than the ν_e

distribution. This would give rise to flavor dependent emission angular distribution for the neutrino flavors, which is required for fast conversions. Such fast conversions would imply that flavor conversions can occur even earlier than before. A schematic picture of different length scales associated with neutrino flavor conversions within a SN envelope is shown in Fig. (1.7). These effects were not found in previous numerical studies of self-induced flavor conversion because they focused on a region relatively far away from the neutrinosphere, where the angular distributions of the different ν species become similar. Although flavor-dependent angular distributions of neutrinos were considered in [116, 117], fast conversions were not obtained because these works considered different angular distributions for ν_e and $\nu_{\mu,\tau}$, while keeping those of ν_e and $\bar{\nu}_e$ similar.

In [111], a linear stability analysis was applied to demonstrate the presence of these large flavor conversions due to flavor dependent neutrino angular distributions. Although [111] showed the presence of fast conversions, the results were derived using a highly discretized versions of the neutrino angular distributions, which were known to lead to spurious flavor conversions [113]. More recently, these results were vindicated in [118] by employing larger number of angular modes. Fast conversions were further studied in [119], where a stability analysis with non-trivial continuous ν angular distributions was performed, at large distances from the core. Here, it was shown that if there are more $\bar{\nu}_e$ than ν_e , or if the emission distribution of $\bar{\nu}_e$ are wider, fast conversions can take place. This condition is unphysical in a SN, as there are typically more ν_e than $\bar{\nu}_e$. However, fast conversions can also take place in conditions prevalent within a SN. Indeed, it will be shown in this thesis that fast conversions can happen for parameters more relevant to a SN.

One may wonder how these results get affected in the presence of non-standard interactions. There are stringent bounds on non-standard interactions (NSI) of neutrinos with charged fermions [120–125]. But non-standard self-interactions (NSSI) of neutrinos have very loose direct constraints and can be as large as in the SM, if not larger [126–129]. This is primarily because neutrino-neutrino interactions have not been directly observed yet, and hence it is very difficult to put bounds on them. The framework for analyzing the effect of NSSI on collective oscillations was first developed in [130], which showed that flavor-violating NSSI can cause complete flavor conversions even in the absence of any mixing.

1.4.4 Supernova neutrino observables and detectors

A detailed understanding of neutrino flavor conversions within a SN can help in possible interpretations of a neutrino signal from a galactic or extra-galactic SN. The ν_e neutronization burst signal is found to be quite robust, and almost independent of the progenitor mass and the nuclear equation of state [131]. Hence, it is a particularly interesting probe of flavor conversions. The neutronization burst can be utilized to discern the neutrino mass-ordering since the signal is suppressed by $\sin^2 \vartheta_{13} \simeq 0.02$ in NH and $\sin^2 \vartheta_{12} \simeq 0.3$ in IH [77, 81, 82, 85, 131]. The detection of the neutronization burst can also be used to constrain non-standard neutrino physics, such as oscillations of active neutrinos into light sterile neutrinos [132], violation of Lorentz invariance [133], neutrino decay [134], etc. All these scenarios would lead to a suppression of the neutronization burst in either hierarchy. The rise time of a galactic SN $\bar{\nu}_e$ light curve, observable in large underground detectors, can also provide a diagnostic tool for the neutrino mass hierarchy [135].

Earth-matter effects on neutrino oscillations as the neutrinos pass through the Earth mantle have also been investigated [77, 83, 84]. The sensitivity of the oscillations to shock-wave propagation [136–140] and to turbulence in the density of the stellar envelope [141–143] has also been studied. Resonant neutrino conversions in a SN can be used to probe neutrino mixing and SN dynamics [80]. Attempts have also been made at extracting SN and neutrino parameters from experimental data [144]. More recent studies have tried to reconstruct the neutrino spectra at various detectors [145–148]. A new model-independent analysis strategy for the next galactic SN signal which can distinguish flavor equalization due to fast flavor conversions from the MSW scenario during the SN accretion phase has been proposed in [149].

The only recorded neutrino burst from a supernova came from SN1987A, which occurred in the Large Magellanic Cloud, at a distance of about 50 kpc from the solar system [150]. A few hours before the optical discovery of SN1987A, a small number of neutrino events (about 20 events in total) with energy ~ 10 MeV was observed around the same time in Kamiokande-II [151], IMB [152] and Baksan [153]. Owing to the extremely low statistics, only weak bounds can be placed on the neutrino relative luminosities during different times. However, the observed few events were compatible with the general features of a core-collapse SN described in the earlier sections.

After SN1987A, a lot of detectors have been constructed with the primary or secondary aim of SN neutrino detection. Suitable detectors should be sensitive to products of neutrino interactions in the $\mathcal{O} \sim 10$ MeV range. SN neutrinos can undergo CC as well as NC reactions with the detector materials. Most of the detectors during SN1987A, as well as most of the current detectors are sensitive to $\bar{\nu}_e$, primarily through the inverse beta decay (IBD) process: $\bar{\nu}_e + p \rightarrow n + e^+$ [154]. Detection is via the energy loss of the positron, either through Cherenkov radiation in water, for e.g., Super-Kamiokande [155], and the recently proposed Hyper-Kamiokande [156], or through liquid scintillator detectors, for e.g., LVD [157], Borexino [158], KamLAND [159], and the proposed JUNO [36], and LENA [160]. Recently, Super Kamiokande has approved Gd mixing with water to increase neutron capture efficiency, which will help in reducing background immensely [161].

Long string detectors, for e.g., Icecube [162] and the next generation PINGU [163], can also detect SN neutrino burst as a diffuse signal [162, 164]. Icecube cannot determine the flavor, energy, and direction of individual neutrinos from a SN, rather the signal appears as a correlated rise in the background noise. However, for a near galactic SN, one can expect large statistics in Icecube. This can allow for a clear distinction between the accretion and cooling phases during a core-collapse [165]. Furthermore, an estimation of the progenitor mass from the shape of the neutrino light curve can also be obtained from Icecube data [165]. It may also be possible to observe the neutrino spectral modulation due to turbulence, and forward and reverse shockwave during the cooling phase [165].

For detection of ν_e , the most promising detector material is liquid Argon. Liquid Ar has a high cross-section for the CC interaction channel : $\nu_e + \text{Ar} \rightarrow e^- + \text{K}^*$, from which the e^- track can be constructed in a time projection chamber (TPC) [166]. This channel is particularly useful for detection of the ν_e burst during the neutronization epoch. The upcoming DUNE [167], and MicroBooNE [168] will be using this liquid Ar TPC technology for detection of ν_e .

The detection of the non-electron flavors, ν_μ and ν_τ , are more difficult, as they do not have enough energy to undergo CC interactions in a detector. They can be detected via NC interactions, which are flavor-blind. Elastic NC scatterings on protons is a viable channel which can be used for detection of these non-electron flavors [145]. Such NC interactions

are sensitive to neutrinos having an energy of $\mathcal{O} \sim 20$ MeV. Hence, the advantage of $\nu_{\mu,\tau}$ over ν_e and $\bar{\nu}_e$ in NC interactions is that the former are more energetic than the latter, and hence form a significant part of the neutrino signal. These are observable in scintillator detectors.

Finally, note that elastic scattering on electrons, $\nu + e^- \rightarrow \nu + e^-$ is sensitive to all neutrino flavors [169] and can occur in all detectors. The interaction cross-section of this channel is larger for the electron flavor neutrinos than the non-electron flavor ones. The advantage of this interaction channel is that the angular distribution of the scattered electrons are forward peaked, and this information can be used to locate the SN. However, this interaction channel is plagued by backgrounds of the primary interaction channel in each detector, and hence is more difficult to track. The addition of Gd to water in Super Kamiokande is expected to reduce the backgrounds due to IBD [161], and improve the directional property.

1.5 Outline of the thesis

Our present work explores some of these new aspects of flavor oscillations of SN neutrinos: the first half of this thesis focuses on fast flavor conversions *near* the SN core, while the second half studies the effect of NSSI of neutrinos on flavor conversions. In Chapter 2, we discuss the mathematical formalism required to study neutrino flavor propagating in a dense media. To check for fast conversions, in Chapter 3, we perform the linear stability analyses for a flat source geometry that more appropriately models the SN emission region, using physically more plausible conditions, where the ν_e are in excess of $\bar{\nu}_e$, but the angular distributions are different. We carefully specify the possible fast instabilities for evolution in space or time, and show the impact of inward-going neutrinos. We verify these linear stability predictions, for several cases, using numerical calculations of the fully nonlinear evolution. In Chapter 4, we explore this further by studying analytically the simplest system that shows fast flavor conversions: a set of four beams of neutrinos and antineutrinos intersecting each other at an angle θ . We demonstrate analytically that its dynamics is equivalent to that of a particle in a quartic potential. Fast oscillations correspond to the inversion of this potential, leading to an instability. This gives us a clearer understanding of the phenomenon of fast flavor conversions.

We also perform an exploratory study of the effects of NSSI on flavor conversions of SN neutrinos in Chapter 5. We find that the presence of NSSI makes us reconsider many of the standard results of flavor evolutions of dense neutrino streams. A smoking gun effect of the presence of NSSI is that a spectral crossing is no longer necessary for the development of spectral swaps. This could give rise to collective oscillations during the neutronization epoch, which are absent otherwise. As a result, distinct splits in the neutrino spectra during this epoch can be a signal of NSSI. Finally, in Chapter 6, we also explore the effects of NSSI on the long-time flavor evolution of the four-beam model by solving the fully non-linear equations of motion numerically. We demonstrate that the fast oscillations are modulated by the slow oscillations. Finally, in Chapter 7, we discuss our results and conclude.

We believe that many of these results will have important observable consequences for the neutrino signal from a future galactic SN.

Chapter 2

Formalism: oscillations of dense neutrino streams

In this chapter, we present a formalism for studying neutrino flavor oscillations in a dense media. We outline the density matrix formalism, and then introduce the polarization vector notation. We also discuss the linear stability analysis (LSA), used primarily to check for the presence of an instability in the system. We present the LSA formalism used to study flavor conversions far away from a SN core. The results of this chapter will be used in all the subsequent chapters.

2.1 The density matrix formalism

The previous chapter describes the flavor evolution of neutrino beams, in vacuum or in a medium, in terms of the Schrödinger equation. However, this formalism is inadequate when one has to treat an ensemble of neutrinos, which undergoes mixing as well as scattering in a medium. This becomes relevant while studying neutrino flavor evolution in a SN, or in the early universe, where the density of neutrinos is very high and one needs to deal with an ensemble, instead of single particle states. Apart from the refractive effects caused due to background matter, as well as the ambient neutrinos, one also needs to model collisions, which can destroy the coherence of the evolution, and affect the oscillations.

A proper treatment of these neutrino flavor conversions may be modeled using the density matrix formalism, which can account for mixed states and possible loss of coherence due to collisions. We closely follow the derivation of [170]. See Refs. [171–174] for related derivation, and [175] for recent developments.

Consider a left-handed massless neutrino field $\nu_L(\mathbf{x})$, which can be expanded in the momentum basis as

$$\nu_L(\mathbf{x}) = \int d\mathbf{p} (a_{\mathbf{p}} u_{\mathbf{p}} + b_{\mathbf{p}}^\dagger v_{-\mathbf{p}}) e^{i\mathbf{p}\cdot\mathbf{x}}, \quad (2.1.1)$$

where $d\mathbf{p} = d^3\mathbf{p}/(2\pi)^3$, and the Dirac spinors $u_{\mathbf{p}}$ and $v_{-\mathbf{p}}$ refer to the massless negative-helicity neutrinos and positive helicity antineutrinos respectively. Here $a_{\mathbf{p}}$ is an annihilation operator for the neutrinos of momentum \mathbf{p} and $b_{\mathbf{p}}^\dagger$ is a creation operator for the antineutrinos. For an ensemble of n neutrinos, these operators are column vectors, which satisfy the anticommutation relation

$$\{a_i(\mathbf{p}), a_j^\dagger(\mathbf{p})\} = \{b_i(\mathbf{p}), b_j^\dagger(\mathbf{p})\} = \delta_{ij} (2\pi)^3, \quad (2.1.2)$$

where i, j range from 1 to n .

From all the possible bilinears of $a_{\mathbf{p}}$ and $b_{\mathbf{p}}^\dagger$, the only ones which do not violate lepton number, and whose expectation values do not oscillate rapidly around zero, are the “density-operators” $a_{\mathbf{p}}^\dagger a_{\mathbf{p}}$ and $b_{\mathbf{p}}^\dagger b_{\mathbf{p}}$. Therefore, an ensemble of neutrinos and antineutrinos can be characterized by the $n \times n$ “matrix of density” $\rho_{\mathbf{p}, \mathbf{x}, t}$ and $\bar{\rho}_{\mathbf{p}, \mathbf{x}, t}$, defined for neutrinos and antineutrinos, respectively, as

$$\begin{aligned} \langle a_j^\dagger(\mathbf{p}) a_i(\mathbf{p}) \rangle &= (2\pi)^3 (\rho_{\mathbf{p}, \mathbf{x}, t})_{ij} \\ \langle b_i^\dagger(\mathbf{p}) b_j(\mathbf{p}) \rangle &= (2\pi)^3 (\bar{\rho}_{\mathbf{p}, \mathbf{x}, t})_{ij} \end{aligned}$$

where $\langle \rangle$ indicates an expectation value taken with respect to the initial states of the ensemble. Note that the order of indices in the definition of $\bar{\rho}$ is reversed. This guarantees that the $\bar{\rho}$ transforms in the same way as ρ under a unitary transformation $\nu_L = U^\dagger \nu_L U$. For a three flavor neutrino ensemble, the density matrix can be written as

$$\rho_{\mathbf{p}, \mathbf{x}, t} = \begin{pmatrix} \rho_{ee} & \rho_{e\mu} & \rho_{e\tau} \\ \rho_{e\mu} & \rho_{\mu\mu} & \rho_{\mu\tau} \\ \rho_{\tau e} & \rho_{\tau\mu} & \rho_{\tau\tau} \end{pmatrix}. \quad (2.1.3)$$

A similar expression holds for $\bar{\rho}$, with the ρ_{ij} replaced by $\bar{\rho}_{ij}$.

Using the above definition of density matrix, one can define a matrix of occupation numbers,

$$\varrho_{\mathbf{p}, \mathbf{x}, t} = n_{\nu_{\mathbf{p}, \mathbf{x}, t}} \rho_{\mathbf{p}, \mathbf{x}, t} \quad (2.1.4)$$

where $n_{\nu_{\mathbf{p}, \mathbf{x}, t}}$ is the number density of neutrinos with momentum \mathbf{p} at a position \mathbf{x} and time t . The diagonal entries of this matrix are the particle and antiparticle occupation numbers for the corresponding neutrino species, while the off-diagonal elements encode phase information related to oscillations. Throughout this thesis, we will work with the occupation number matrices, instead of the density matrices.

2.2 Equations of motion

In the absence of external forces acting on neutrinos, the dynamics of the occupation number matrices is dictated by the following equations of motion (EoMs) [170]:

$$\partial_t \varrho_{\mathbf{p}, \mathbf{x}, t} + \mathbf{v}_{\mathbf{p}} \cdot \nabla_{\mathbf{x}} \varrho_{\mathbf{p}, \mathbf{x}, t} = -i[\mathcal{H}_{\mathbf{p}, \mathbf{x}, t}, \varrho_{\mathbf{p}, \mathbf{x}, t}] + \mathcal{C}[\varrho_{\mathbf{p}, \mathbf{x}, t}] \quad , \quad (2.2.1)$$

with the Liouville operator on the left-hand side. To lighten the notation, we shall drop the subscripts \mathbf{x} and t henceforth. The matrix $\mathcal{H}_{\mathbf{p}}$ is the Hamiltonian

$$\mathcal{H}_{\mathbf{p}} = \mathcal{H}_{\text{vac}} + \mathcal{H}_{\text{MSW}} + \mathcal{H}_{\nu\nu} \quad , \quad (2.2.2)$$

containing the vacuum, matter and self-interaction terms, that leads to the evolution of $\varrho_{\mathbf{p}}$ over space and time.

The first term of Eq. (2.2.1) represents the matrix of vacuum oscillation frequency,

$$\mathcal{H}_{\text{vac}} = U \frac{M^2}{2\mathbf{p}} U^\dagger \quad (2.2.3)$$

where U is the mixing matrix and M^2 is the squared neutrino mass matrix given by $M^2 = \text{diag}(m_1^2, m_2^2, m_3^2)$. Typically, for oscillation physics, one can phase away a common term proportional to the identity matrix, and parameterize M^2 in terms of the solar and the atmospheric mass squared differences. Simplifying to an effective two-flavor scenario, the matrix of vacuum oscillation frequency is $\mathcal{H}_{\text{vac}} = \text{diag}(-\omega/2, +\omega/2)$ in the mass basis, where

$\omega = \Delta m^2/2p \approx \Delta m^2/2E$ for relativistic neutrinos of energy E . The sign \pm in front of the Δm^2 refers to NH (+) and IH (−), respectively. Depending on whether the solar or the atmospheric mass-squared difference is used, one can associate it with $\omega_L = \Delta m_\odot^2/(2E)$ and $\omega_H = \Delta m_{\text{atm}}^2/(2E)$.

The vacuum energy can be affected due to the propagation of neutrinos in a medium. Neutrinos forward scatter with the medium, which in turn gives rise to a refractive effect in the potential proportional to the Fermi constant G_F . For typical energies of $\mathcal{O}(10)$ MeV of SN neutrinos, the electron neutrinos can undergo both neutral current (NC) as well as charged current (CC) interactions with the medium, whereas the other flavors only undergo NC interactions. Since the NC interactions are same for all flavors, they contribute an overall forward scattering phase and can be rotated away. Hence the only relevant process is due to the CC interactions of electron neutrinos with the medium. This gives rise to the well known MSW effect, as discussed in the previous chapter. The matter effect in Eq. (2.2.2), due to the net background electron density $n_e(\mathbf{x})$, is represented by

$$\mathcal{H}_{\text{MSW}} = \lambda \text{diag}(1, 0, 0) \quad (2.2.4)$$

in the weak interaction basis, where $\lambda = \sqrt{2}G_F n_e(\mathbf{x})$ [29]. In the two-flavor basis, this can be written as $\mathcal{H}_{\text{MSW}} = \lambda \text{diag}(1, 0)$.

Apart from this, neutrino-neutrino interactions are dominant deep inside a SN, as discussed in 1.4.3.2. This makes an additional contribution $\mathcal{H}_{\nu\nu}$ to the energy shift due to refractive effects [31], given by

$$\mathcal{H}_{\nu\nu} = \sqrt{2}G_F \int \frac{d^3\mathbf{q}}{(2\pi)^3} (\varrho_{\mathbf{q}} - \bar{\varrho}_{\mathbf{q}})(1 - \mathbf{v}_{\mathbf{p}} \cdot \mathbf{v}_{\mathbf{q}}) . \quad (2.2.5)$$

This occurs due to neutrinos forward scattering off each other in a dense medium, and hence this potential is proportional to ϱ itself, making the problem non-linear. Since ϱ has non-zero off-diagonal entries, this leads to off-diagonal refractive indices. Furthermore, due to the anisotropy of the neutrino background, this potential is proportional to $(1 - \mathbf{v}_{\mathbf{p}} \cdot \mathbf{v}_{\mathbf{q}})$, where $\mathbf{v}_{\mathbf{p}}$ is the velocity of the test neutrino, and $\mathbf{v}_{\mathbf{q}}$ is the background neutrino velocity. This leads to “multi-angle effects”, i.e., neutrinos experience different potentials due to other neutrinos moving on different trajectories. This effect vanishes for an isotropic medium, however, in an anisotropic medium, this can cause flavor decoherence, leading to flavor equilibrium among the different neutrino species.

The last term on right-hand-side in Eq. (2.2.1), i.e. $\mathcal{C}[\varrho_{\mathbf{p},\mathbf{x},t}]$, represents a collision term acting on neutrino flavor evolution. This term is proportional to G_F^2 , and is responsible for destroying the coherence of the neutrino ensemble. We shall neglect all collision terms in all the chapters of this thesis, as this is still an ongoing work. However, we will comment on the effects of collisions on flavor conversions in Appendix B.

As a final remark, note that for antineutrinos, the EoMs are the same but with the replacement $\mathcal{H}_{\text{vac}} \rightarrow -\mathcal{H}_{\text{vac}}$, thus it is convenient to think of antineutrinos of energy E as neutrinos of energy $-E$, making their EoMs formally identical.

2.2.1 Polarization vector formalism

In most of the cases, the three flavor neutrino framework can be approximated by a two-flavor scenario. This is because, within a SN, ν_μ and ν_τ have identical interactions, and behave similarly. Hence the system can be described by two flavors: ν_e and ν_x , where ν_x can be ν_μ , ν_τ or a linear combination of both. The advantage of this is that all terms in the Hamiltonian can be written in terms of 2×2 Hermitian matrices, and can be expanded in the Pauli basis as follows [93]:

$$\begin{aligned}\mathcal{H}_{\text{vac}} &= \frac{1}{2}(\omega_0\mathbb{I} + \omega\mathbf{B} \cdot \boldsymbol{\sigma}), \\ \mathcal{H}_{\text{MSW}} &= \frac{1}{2}(\lambda\mathbb{I} + \lambda\mathbf{L} \cdot \boldsymbol{\sigma}), \\ \varrho_{\mathbf{p}} &= \frac{1}{2}(f_{\mathbf{p}}\mathbb{I} + \mathbf{P}_{\mathbf{p}} \cdot \boldsymbol{\sigma}), \\ \bar{\varrho}_{\mathbf{p}} &= \frac{1}{2}(\bar{f}_{\mathbf{p}}\mathbb{I} + \bar{\mathbf{P}}_{\mathbf{p}} \cdot \boldsymbol{\sigma}),\end{aligned}\tag{2.2.6}$$

where $\mathbf{P}_{\mathbf{p}}$ and $\bar{\mathbf{P}}_{\mathbf{p}}$ may be interpreted as the polarization vectors for neutrinos and anti-neutrinos, respectively. The coordinate system is chosen such that the polarization vector pointing in the $+z$ indicates ν_e whereas that in the $-z$ direction indicates ν_x . The neutrino density is given by integrating the momentum distribution function $f_{\mathbf{p}}$ over all momentum modes, i.e., $n_\nu \equiv \int d^3\mathbf{p} f_{\mathbf{p}}$ and $n_{\bar{\nu}} \equiv \int d^3\mathbf{p} \bar{f}_{\mathbf{p}}$. The normalization is such that $|\bar{\mathbf{P}}_{\mathbf{p}}| = 1$. The vacuum Hamiltonian may be interpreted as an external magnetic field, given by $\mathbf{B} = (\sin 2\vartheta_0, 0, -\cos 2\vartheta_0)$, where ϑ_0 is the vacuum mixing angle between the two flavors. The MSW potential \mathcal{H}_{MSW} is characterized by its magnitude λ and a unit vector $\mathbf{L} = (0, 0, 1)$.

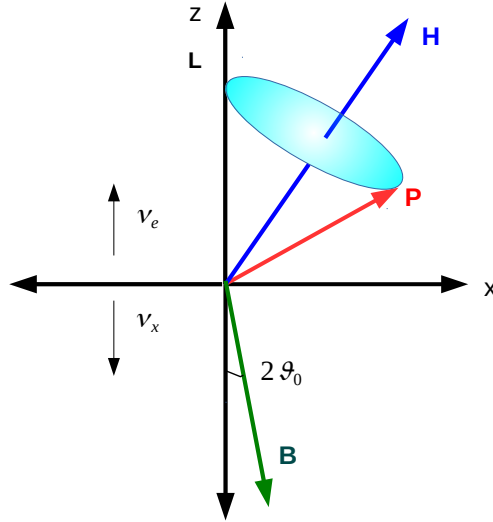


Figure 2.1: The polarization vector picture. The vector \mathbf{P} precesses around the net Hamiltonian vector, denoted by \mathbf{H} . These precessions correspond to oscillations.

Finally, the neutrino-neutrino interaction strength is normalized by $\mu = \sqrt{2}G_F n_\nu$ for a net neutrino density n_ν .

This simplifies the EoMs to

$$(\partial_t + \mathbf{v}_\mathbf{p} \cdot \nabla_\mathbf{x}) \mathbf{P}_\mathbf{p} = [\omega_\mathbf{p} \mathbf{B} + \lambda \mathbf{L} + \mu \int d\mathbf{p}' (1 - \mathbf{v}_\mathbf{p} \cdot \mathbf{v}'_\mathbf{p})(\mathbf{P}'_\mathbf{p} - \bar{\mathbf{P}}'_\mathbf{p})] \times \mathbf{P}_\mathbf{p}, \quad (2.2.7)$$

$$(\partial_t + \mathbf{v}_\mathbf{p} \cdot \nabla_\mathbf{x}) \bar{\mathbf{P}}_\mathbf{p} = [-\omega_\mathbf{p} \mathbf{B} + \lambda \mathbf{L} + \mu \int d\mathbf{p}' (1 - \mathbf{v}_\mathbf{p} \cdot \mathbf{v}'_\mathbf{p})(\mathbf{P}'_\mathbf{p} - \bar{\mathbf{P}}'_\mathbf{p})] \times \bar{\mathbf{P}}_\mathbf{p}. \quad (2.2.8)$$

These are the fully non-linear EoMs, in the polarization picture, for a multi-angle evolution of neutrinos. As mentioned before, for a single-angle evolution, the $(1 - \mathbf{v} \cdot \mathbf{v}')$ term drops out of the integral and the equations become simpler. Using the formalism developed here, one can study the different types of collective behaviors that arise in a dense gas of neutrinos.

Let us focus on Eqs. (2.2.7-2.2.8) in the limit $\mu \rightarrow 0$. In this limit, the net Hamiltonian vector is denoted by \mathbf{H} . The equations are analogous to that of a polarization vector \mathbf{P} precessing around the net Hamiltonian vector, given by \mathbf{H} , as shown in Fig. 2.1. The flavor direction, given by \mathbf{L} , is along the z-axis, whereas \mathbf{B} is confined to the x-z plane, and makes an angle $2\vartheta_0$ with the z-axis. The precession of \mathbf{P} around \mathbf{H} indicates flavor oscillations.

2.3 Collective flavor oscillations: A brief recap

2.3.1 Single energy flavor evolution

Eqs. (2.2.7-2.2.8) are a set of non-linear coupled partial differential equations, involving 3 spatial dimensions, 3 momentum dimensions and 1 dimension of time, and hence is very difficult to solve analytically. In fact, solving the entire problem numerically is a challenging task, and we need to resort to simplifications. One such simplification is the single-angle approximation, where neutrinos and antineutrinos are emitted from the neutrinosphere with a single angle. As a further approximation, one can neglect spatial evolution of the neutrino beams, and consider only propagation along the time direction. This simplifies the EoMs to

$$\partial_t \mathbf{P}_{\mathbf{p}} = [\omega_{\mathbf{p}} \mathbf{B} + \lambda \mathbf{L} + \mu (\mathbf{P} - \bar{\mathbf{P}})] \times \mathbf{P}_{\mathbf{p}}, \quad (2.3.1)$$

$$\partial_t \bar{\mathbf{P}}_{\mathbf{p}} = [-\omega_{\mathbf{p}} \mathbf{B} + \lambda \mathbf{L} + \mu (\mathbf{P} - \bar{\mathbf{P}})] \times \bar{\mathbf{P}}_{\mathbf{p}}, \quad (2.3.2)$$

where $\mathbf{P} = \int d\mathbf{p} \mathbf{P}_{\mathbf{p}}$ and $\bar{\mathbf{P}} = \int d\mathbf{p} \bar{\mathbf{P}}_{\mathbf{p}}$. In this section, we will use the above equations to demonstrate the intriguing aspects of collective oscillations. To begin with, we confine ourselves to a gas of equal densities of ν_e and $\bar{\nu}_e$ with a small effective mixing angle $\vartheta \ll 1$, inverted mass-ordering, and a large self-interaction term $\mu \gg \omega$. We neglect matter effects and set $\lambda = 0$. The flavor evolution is governed by the z-component of the polarization vectors, P_z and \bar{P}_z respectively. For a mono-energetic neutrino ensemble, the flavor evolution for a constant neutrino density is shown in Fig. 2.2. We notice that initially, both the P_z and \bar{P}_z remain fixed in their initial state. After a while, they flip completely, but return to their initial position, causing periodic conversions of ν_e and $\bar{\nu}_e$ to ν_x and $\bar{\nu}_x$. In this whole process, the net flavor lepton number is always conserved. Note that the above case was in the inverted mass ordering. On the other hand, for normal mass ordering, the system is completely stable and there are no flavor conversions.

These ‘‘bipolar oscillations’’, involving pair conversions of $\nu_e \bar{\nu}_e \leftrightarrow \nu_x \bar{\nu}_x$ are collective in nature, i.e., all neutrino energies oscillate at the same frequency, and occur with a frequency $\sim \sqrt{\omega\mu}$. This system is mathematically equivalent to a pendulum in flavor space [91, 97], similar to how the ordinary neutrino oscillations in vacuum or matter are equivalent to a

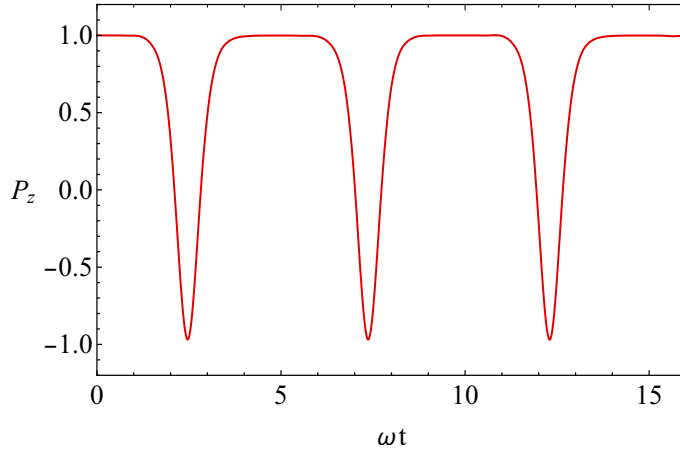


Figure 2.2: Flavor evolution of P_z in inverted mass ordering for the system of equations Eqs. (2.2.7-2.2.8). The parameters chosen for this plot are $\vartheta_0 = 0.01$, $\omega = 0.3 \text{ km}^{-1}$, corresponding to the atmospheric mass squared difference and neutrino energy 10 MeV, and $\mu = 10 \text{ km}^{-1}$.

precessing spin [93, 176, 177]. Depending on the neutrino mass ordering, the gravitational force for this flavor pendulum acts upwards or downwards, thereby making certain flavor configurations unstable, akin to an inverted pendulum. Bipolar oscillations correspond to the pendulum starting in an unstable inverted position, slightly offset by a small mixing angle, and swinging through the lowest position to the other side. The time-period of this flavor pendulum depends logarithmically on the vacuum mixing angle [97]. Naively, one can associate these type of flavor conversions with an instability in flavor space, as will be explored in the next section.

In order to model a more realistic SN environment with a toy model, one needs to have a varying neutrino density, which is declining with distance. We consider a toy neutrino potential, as shown in Fig. 2.3 (left panel),

$$\mu(r) = 10^2 \left(\frac{r_{\text{NS}}}{r} \right)^4 \text{ km}^{-1}, \quad (2.3.3)$$

where $r_{\text{NS}} = 10 \text{ km}$ is the radius of the neutrinosphere. The corresponding evolution for P_z and \bar{P}_z are shown in the right panel of Fig. 2.3. Clearly, the oscillations decline as a function of radii, leading to complete flavor conversion. Using the flavor pendulum analogy, one can show that reduction of $\mu(r)$ leads to a reduction in the energy of the pendulum, thereby reducing the amplitude in each swing.

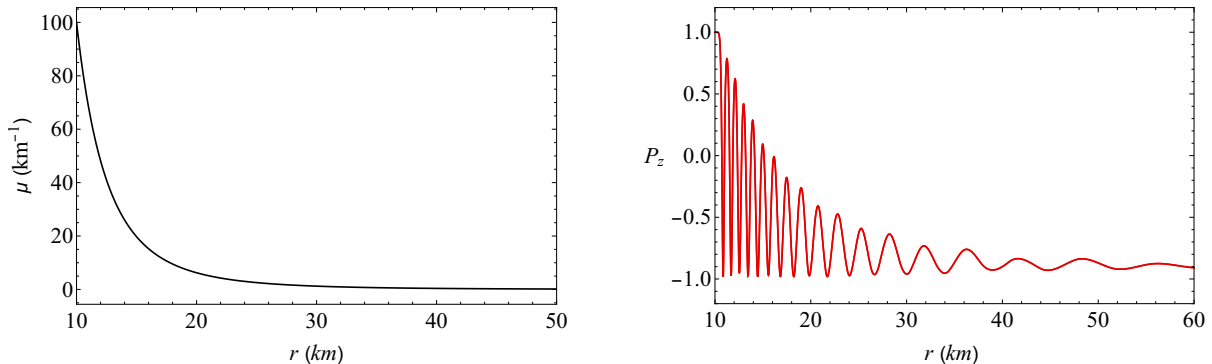


Figure 2.3: Left: The varying neutrino potential given by Eq. (2.3.3). Right: Flavor evolution of P_z in inverted mass ordering for the system of equations Eqs. (2.2.7-2.2.8) for a varying neutrino potential given by Eq. (2.3.3). The other parameters chosen for this plot are chosen for this plot are $\vartheta_0 = 0.01$, $\omega = 0.3 \text{ km}^{-1}$, corresponding to the atmospheric mass squared difference and neutrino energy 10 MeV.

Finally, a comment regarding the matter effect. It can also be shown that the presence of a finite non-zero λ can be treated by transforming to a frame rotating around \mathbf{L} . In such a frame, the mixing angle is matter suppressed, thereby leading to a logarithmic delay [97] in the onset of oscillations.

2.3.2 Multi-energy spectral splits

The previous section dealt with non-linear flavor conversions for a simple toy model of mono-energetic neutrinos and antineutrinos. However in a SN, neutrinos and antineutrinos are emitted with a continuous energy distribution, given by Eq. (1.4.1). The flavor evolution for a spectrum of ν_e and ν_x is shown in Fig. 2.4. The left panel corresponds to inverted mass hierarchy (IH), while the right panel corresponds to normal mass hierarchy (NH). One can see that the bipolar oscillations eventually give rise to spectral splits [91]. In IH, all ν_e and ν_x within a certain energy range are swapped, whereas in NH, the swapping occurs beyond a certain energy. Such a flavor exchange is called a “swap”, whereas the sharp boundaries at either side of the swaps are called “splits”.

During the cooling phase, multiple spectral splits were observed in the simulations both in the neutrino and antineutrino channel [104, 105]. An analytical explanation of this effect

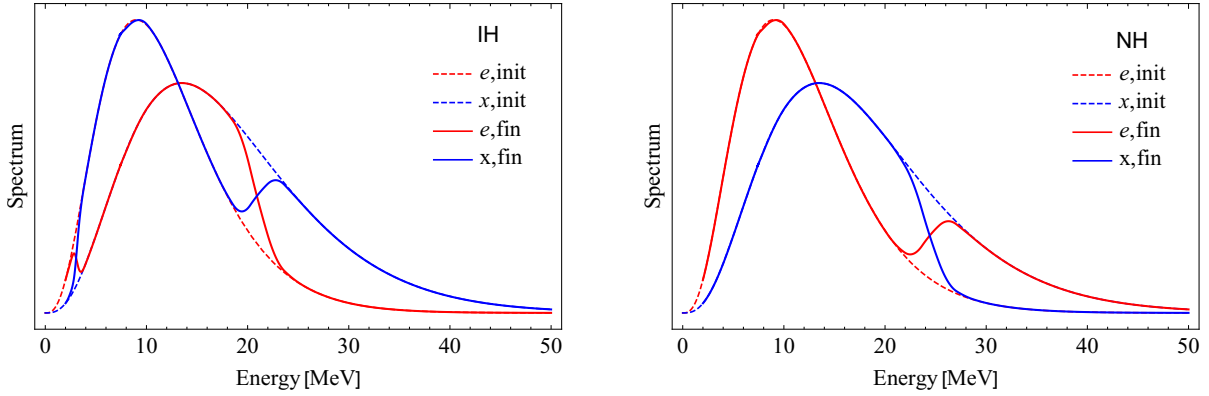


Figure 2.4: SN neutrino spectra before (dashed lines) and after (solid lines) collective bipolar oscillations, indicating the presence of distinct spectral splits. The ν_e spectra is shown in red, while the ν_x spectra is shown in blue. For this neutrino spectra, we consider $\alpha = 3$, $\langle E_{\nu_e} \rangle = 12$ MeV, $\langle E_{\bar{\nu}_e} \rangle = 15$ MeV and $\langle E_{\nu_x} \rangle = 18$ MeV. The flavor evolution assumes the single-angle emission of neutrinos.

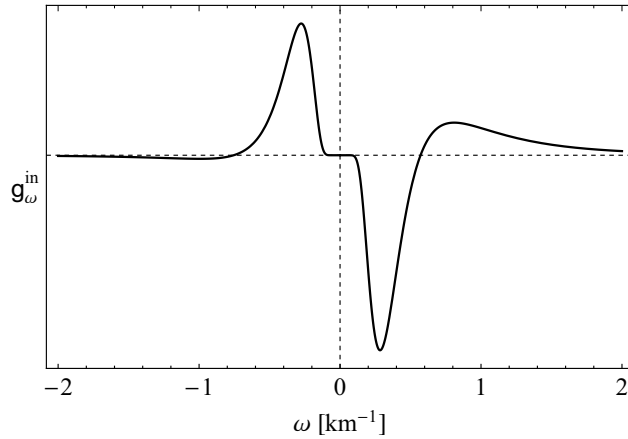


Figure 2.5: The difference spectrum g_ω^{in} for the initial spectra considered in Fig. 2.4. Notice that there is a positive crossing at $\omega \approx -0.8 \text{ km}^{-1}$ and $\omega \approx 0.6 \text{ km}^{-1}$, and a negative crossing at $\omega \approx 0 \text{ km}^{-1}$.

was offered in [106], in terms of the development of spectral swaps in the difference spectrum g_ω , defined as (see Eq. (1.4.4))

$$\begin{aligned}
 g_\omega &\propto F_{\nu_e}(\omega) - F_{\nu_x}(\omega) && \text{for } \omega > 0, \\
 &\propto F_{\bar{\nu}_x}(\omega) - F_{\bar{\nu}_e}(\omega) && \text{for } \omega < 0.
 \end{aligned} \tag{2.3.4}$$

For the initial spectra considered in Fig. 2.4, we show the difference spectrum g_ω in Fig. 2.5. Notice that g_ω has a number of “spectral crossings”. A crossing is defined as “positive”

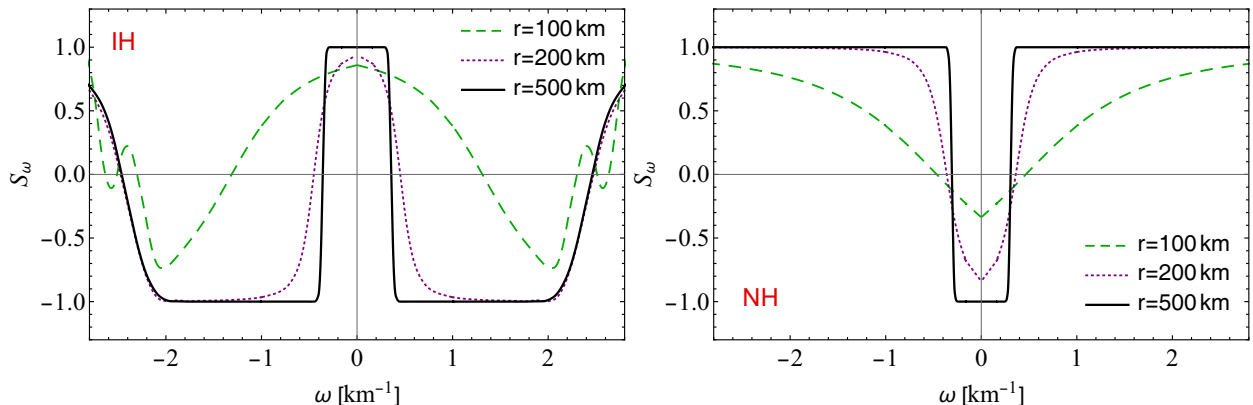


Figure 2.6: The development of the swap factor S_ω with distance r from the neutrinosphere. Left: Inverted hierarchy. Right: Normal hierarchy.

(“negative”) if g_ω changes sign from negative (positive) to positive (negative). The effects of collective oscillations are best described in terms of the “swap factor” given by

$$g_\omega^{\text{fin}} = S_\omega g_\omega^{\text{in}}, \quad (2.3.5)$$

where g_ω^{in} is the initial difference spectrum, and g_ω^{fin} is the final spectrum after collective oscillations. In Fig. 2.6, we show the development of S_ω , as a function of the distance from the neutrinosphere, for IH (left panel) and NH (right panel). Note that in IH (NH), any positive (negative) crossing of the g_ω -spectra is unstable, thereby causing bipolar oscillations leading to a spectral swap.

This development of a swap around a spectral crossing is related to the conservation of flavor lepton number during bipolar oscillations [106]. The EoMs imply that $\mathbf{B} \cdot (\mathbf{P} - \bar{\mathbf{P}}) = \int d\omega g_\omega$ is conserved, and hence zero across the swap. As a result, swaps can only develop around a spectral crossing.

However, multi-angle matter effects were shown to cause smearing of these spectral splits in the accretion phase [104]. Furthermore, three flavor effects were shown to cause additional splits, and could be mostly interpreted in terms of stepwise two-flavor splits [107, 108].

Therefore, it is clear that in order to solve the set of non-linear equations, one needs to take resort to numerical simulations. However, one can get some intuitive insights into the onset of these oscillations by treating this as an instability in flavor space, and applying a

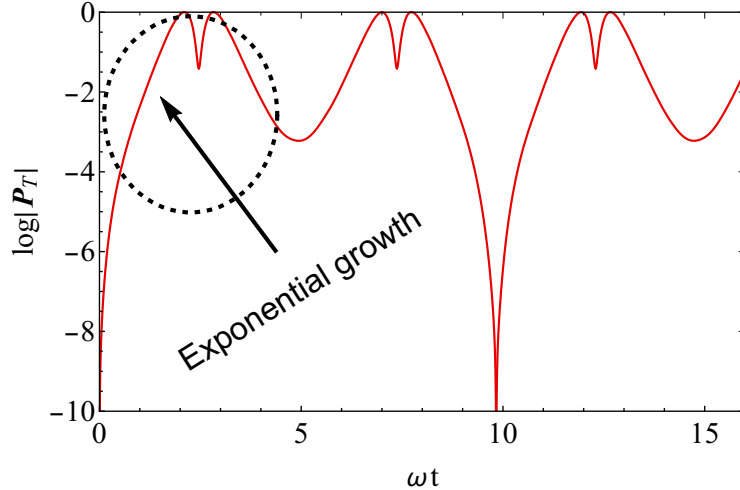


Figure 2.7: Plot showing the growth of the off-diagonal element $|\mathbf{P}_T|$ for the parameters chosen in Fig. 2.2.

stability analysis. This technique, developed in [96] within the context of SN neutrinos, will be the next topic of discussion.

2.4 Linearized stability analysis

The non-linearity of the equations of motion (EoMs) makes the analytic understanding of long time behavior of collective oscillations intractable. However, it is possible to analytically study the onset of these oscillations if one interprets the problem as an instability in propagating flavor waves. To motivate this point, let us first focus on the off-diagonal of the occupation number matrix. In terms of the polarization vector picture, this can also be denoted by $|\mathbf{P}_T| = \sqrt{P_x^2 + P_y^2}$. In Fig. 2.7, we plot the quantity $\log |\mathbf{P}_T|$ for the parameters chosen in Fig. 2.2. Notice that it starts as a very small quantity. This is because, deep inside the SN, the matter density is so high that flavor and mass eigenstates are almost identical. However, note that there is a period of rapid exponential growth in $|\mathbf{P}_T|$, which indicates the onset of collective oscillations. This exponential growth during onset can be calculated using a linear stability analysis [96, 114]. Such an analysis typically leads to an eigenvalue equation, whose exponentially growing eigenvalues correspond to an instability, and indicate the onset [96].

To begin with, we confine ourselves to a spherically symmetric setup, where neutrinos are emitted from a fiducial neutrinosphere of radius R , as shown in Fig. 2.8. Following [96], we label them by the variable $u = \sin^2 \vartheta_R$, where ϑ_R is the emission angle of the neutrinos. The radial velocity for a mode u at the radius r is $v_{r,u} = \sqrt{1 - uR^2/r^2}$. The transverse velocity is given by $v_{r,u}^T = u^{1/2}R/r$. In the following section, we will assume that the solutions are stationary, and hence the time-derivate drops out of the equation.

In terms of the flux matrices F [96, 114]

$$F_{\omega,u,\varphi} d\omega du = 2\pi r^2 v_{r,u} \varrho_{\mathbf{p}} \frac{d^3 \mathbf{p}}{(2\pi)^3}, \quad (2.4.1)$$

the EoMs become

$$i\partial_r F_{\omega,u,\varphi} = [\mathcal{H}_{\omega,u,\varphi}, F_{\omega,u,\varphi}], \quad (2.4.2)$$

where

$$H_{\omega,u,\varphi} = (\omega + \lambda_r) v_{r,u}^{-1} + \mu_R \frac{R^2}{r^2} \int d\Gamma' \frac{1 - v_{r,u} v_{r,u'} - \mathbf{v}_{r,u}^T \cdot \mathbf{v}_{r,u'}^T}{v_{r,u} v_{r,u'}} F_{\omega,u',\varphi'}, \quad (2.4.3)$$

and φ is the azimuthal angle. Here $\int d\Gamma = \int_{-\infty}^{\infty} d\omega \int_0^1 du \int_0^{2\pi} d\varphi$, and negative values of ω represent antineutrinos. In addition, we have $\mathbf{v}_{r,u}^T \cdot \mathbf{v}_{r,u'}^T = \sqrt{u u'} (R^2/r^2) \cos(\varphi - \varphi')$. If axial symmetry is enforced, this term drops out of the EoMs [114].

The quantities λ_r (matter potential at a radius r) and μ_R (neutrino-neutrino potential at the neutrinosphere) are defined as

$$\begin{aligned} \lambda_r &= \sqrt{2} G_F n_e(r), \\ \mu_R &= \frac{\sqrt{2} G_F [F_{\omega,u,\varphi}^{\bar{e}}(R) - F_{\omega,u,\varphi}^{\bar{x}}(R)]}{4\pi R^2}, \end{aligned} \quad (2.4.4)$$

where $F_{\omega,u,\varphi}^{\bar{e}}(r)$ represents the $\bar{\nu}_e \bar{\nu}_e$ flavor-diagonal element of the 2×2 matrix $F_{\omega,u,\varphi}(r)$, at a radius r , for $\omega < 0$, i.e., for antineutrinos.

The flux matrices $F_{\omega,u,\varphi}$ in Eq. (2.4.3) have been rescaled such that at $t = 0$,

$$\int d\Gamma [F_{\omega,u,\varphi}^{\bar{e}}(R) - F_{\omega,u,\varphi}^{\bar{x}}(R)] = 1.$$

These $F_{\omega,u,\varphi}$ may now be written in the form

$$F_{\omega,u,\varphi} = \frac{\text{Tr}(F_{\omega,u,\varphi})}{2} + \frac{g_{\omega,u,\varphi}}{2} \begin{pmatrix} s_{\omega,u,\varphi} & S_{\omega,u,\varphi} \\ S_{\omega,u,\varphi}^* & -s_{\omega,u,\varphi} \end{pmatrix}, \quad (2.4.5)$$

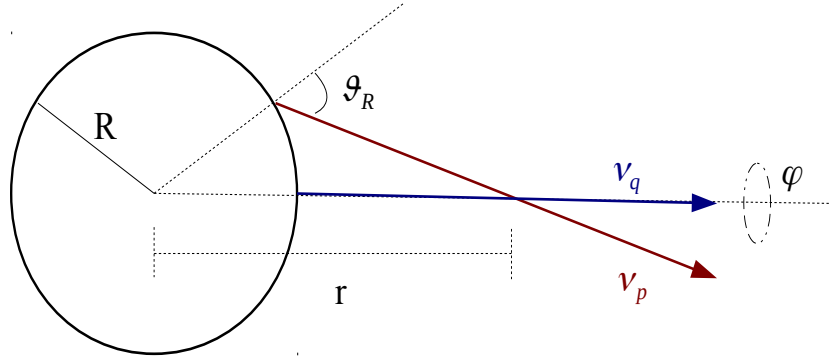


Figure 2.8: Neutrinos with a momentum \mathbf{p} emitted from the neutrinosphere of radius R . The emission angle is denoted by ϑ_R . These neutrinos interact with other neutrinos of momentum \mathbf{q} at a distance r from the neutrinosphere.

where

$$g_{\omega,u,\varphi} = \begin{cases} F_{\omega,u,\varphi}^e - F_{\omega,u,\varphi}^x & \text{for } \omega > 0 \\ F_{\omega,u,\varphi}^{\bar{x}} - F_{\omega,u,\varphi}^{\bar{e}} & \text{for } \omega < 0 \end{cases} \quad (2.4.6)$$

is the difference in spectra of the two flavors and $S_{\omega,u,\varphi}$ is the off-diagonal parameter that we will use to characterize flavor conversions. In this entire analysis, we neglect all collisional processes which change the total number of neutrinos. Hence $\text{Tr}(F_{\omega,u,\varphi})$ is conserved and can be dropped from the EoMs.

At $t = 0$, we have $s = 1$ and $S = 0$ in Eq. (2.4.5). As flavor evolution begins, S starts developing a non-zero value. Since $s^2 + |S|^2 = 1$, a small amplitude expansion may be performed with the approximation $s \approx 1$, $|S| \ll 1$, and where terms of $\mathcal{O}(|S|^2)$ are dropped. This is equivalent to linearizing the equations in S .

To linear order in $S_{\omega,u,\varphi}$, we get an eigenvalue equation of the form

$$\begin{aligned} i\partial_r S_{\omega,u,\varphi} &= \left[(\omega + \lambda_r) v_{r,u}^{-1} + \mu_R \frac{R^2}{r^2} \times \int d\Gamma' \frac{1 - v_{r,u} v_{r,u'} - \mathbf{v}_{r,u}^T \cdot \mathbf{v}_{r,u'}^T}{v_{r,u} v_{r,u'}} g_{\omega',u',\varphi'} \right] S_{\omega,u,\varphi} \\ &- \mu_R \frac{R^2}{r^2} \int d\Gamma' \frac{1 - v_{r,u} v_{r,u'} - \mathbf{v}_{r,u}^T \cdot \mathbf{v}_{r,u'}^T}{v_{r,u} v_{r,u'}} g_{\omega',u',\varphi'} S_{\omega',u',\varphi'}. \end{aligned} \quad (2.4.7)$$

Far away from the neutrinosphere ($r \gg R$), we can drop terms of $\mathcal{O}(R^2/r^2)$ in Eq. (2.4.7).

In this limit, dropping the constant term λ_r , the EoMs are given by

$$i\partial_r S_{\omega,u,\varphi} = \left[\omega + u\tilde{\lambda}_r + u\tilde{\mu}_r\epsilon \right] S_{\omega,u,\varphi} - \tilde{\mu}_r \int d\Gamma' \left[u + u' - 2\sqrt{u u'} \cos(\varphi - \varphi') \right] g_{\omega',u',\varphi'} S_{\omega',u',\varphi'}, \quad (2.4.8)$$

where

$$\begin{aligned} \tilde{\lambda}_r &= \sqrt{2}G_F n_e(r) \frac{R^2}{2r^2}, \\ \tilde{\mu}_r &= \frac{\sqrt{2}G_F}{4\pi R^2} \frac{R^4}{2r^4} \left[F_{\omega,u,\varphi}^{\bar{e}}(R) - F_{\omega,u,\varphi}^{\bar{x}}(R) \right]. \end{aligned} \quad (2.4.9)$$

Here $\epsilon = \int d\Gamma' g_{\omega',u',\varphi'}$ encodes the net neutrino-antineutrino asymmetry. We also define $\bar{\lambda} = \tilde{\lambda}_r + \epsilon\tilde{\mu}_r$ for notational convenience.

We try to solve Eq. (2.4.8) for exponential solutions of the eigenvalue equation of the form

$$S_{\omega,u,\varphi} = Q_{\omega,u,\varphi} e^{-i\Omega r}, \quad (2.4.10)$$

with $\Omega = \gamma + i\kappa$. Whether flavor conversions take place depends on whether Eq. (2.4.8) has complex solutions for Ω . A positive imaginary solution of Ω , i.e a positive κ , leads to an exponential rise in S , and signals an instability. Typically, since these equations have real coefficients, the solutions of Ω are complex conjugate pairs. Hence every growing solution is accompanied by a decaying solution. However, all we care about is the presence of the growing solution, which leads to run-away solutions in the system.

Using Eq. (2.4.10), one finds that the eigenvector Q satisfies the eigenvalue equation

$$(\omega + u\bar{\lambda} - \Omega) Q_{\omega,u,\varphi} = \tilde{\mu}_r \int d\Gamma' \left[u + u' - 2\sqrt{u u'} \cos(\varphi - \varphi') \right] g_{\omega',u',\varphi'} Q_{\omega',u',\varphi'}. \quad (2.4.11)$$

Observe from Eq. (2.4.11) that the RHS has the form $A + Bu + \sqrt{u}(C \cos \varphi + D \sin \varphi)$, where A , B , C and D are complex numbers. This motivates us to consider the following ansatz for Q :

$$Q_{\omega,u,\varphi} = \frac{A + Bu + \sqrt{u}(C \cos \varphi + D \sin \varphi)}{(\omega + u\bar{\lambda} - \Omega)}. \quad (2.4.12)$$

Inserting Eq. (2.4.12) into Eq. (2.4.11) gives

$$\begin{pmatrix} I_1^{0,0} - 1 & I_2^{0,0} & I_{3/2}^{1,0} & I_{3/2}^{0,1} \\ I_0^{0,0} & I_1^{0,0} - 1 & I_{1/2}^{1,0} & I_{1/2}^{0,1} \\ -2I_{1/2}^{1,0} & -2I_{3/2}^{1,0} & -2I_1^{2,0} - 1 & -2I_1^{1,1} \\ -2I_{1/2}^{0,1} & -2I_{3/2}^{0,1} & -2I_1^{1,1} & -2I_1^{0,2} - 1 \end{pmatrix} \begin{pmatrix} A \\ B \\ C \\ D \end{pmatrix} = 0 \quad (2.4.13)$$

where

$$I_n^{\alpha, \beta} = \tilde{\mu}_r \int d\omega du d\varphi g_{\omega, u, \varphi} \frac{u^n}{\omega + u\bar{\lambda} - \Omega} \cos^\alpha \varphi \sin^\beta \varphi. \quad (2.4.14)$$

Clearly, non-trivial solutions exist *only* if the determinant of the matrix is zero. It is also important to note that for a given angular mode u_0 , the quantity $|Q_{\omega, u, \varphi}|^2$ is a Lorentzian in a range of ω -modes.

In order to determine the eigenvalue Ω , we assume that the neutrinos have an axial symmetry of emission, i.e., $g_{\omega, u, \varphi} \rightarrow g_{\omega, u}/2\pi$. This allows us to do the φ integral, therefore simplifying the determinant immensely,

$$\begin{pmatrix} I_1 - 1 & I_2 & 0 & 0 \\ I_0 & I_1 - 1 & 0 & 0 \\ 0 & 0 & -I_1 - 1 & 0 \\ 0 & 0 & 0 & -I_1 - 1 \end{pmatrix} \begin{pmatrix} A \\ B \\ C \\ D \end{pmatrix} = 0 \quad (2.4.15)$$

From this, one arrives at the following set of characteristic equations:

$$(I_1 - 1)^2 = I_0 I_2, \quad (2.4.16)$$

$$I_1 = -1. \quad (2.4.17)$$

The first equation leads to nonzero solutions for A and B , and corresponds to the axially symmetric solutions, which exist for a non-trivial distribution of zenith angles. They are known as the multi-zenith angle (MZA) instability. The second equation has nonzero solutions for C and D , thereby giving solutions with a nontrivial dependence on the azimuthal angle φ . These are the multi-azimuthal angle (MAA) instability.

A few of comments are in order. Firstly, both the instabilities are only dominant when $\mu_r \sim \bar{\lambda}$, and can be suppressed by large matter effects [96]. Secondly, one can study the growth of temporal solutions, where one check for large growths in time. In such a case, it has been shown that matter effects cannot suppress these instabilities, and only affect the real part of Ω [178]. Furthermore, it was shown that the stability analysis, when applied to discretization of continuous angular distributions, gives rise to ‘‘spurious instabilities’’ [113]. However, recently, it was demonstrated that these spurious modes originate from artificial pole singularities, instead of a branch cut in the Riemann surface. This identification helps

in the removal of the spurious modes [179]. Finally, this method is only useful to predict the exponential growth rate of instabilities in the system. The fully non-linear solutions of simple toy models show an initial onset phase, followed by an exponential rise, before the growth becomes non-linear. However, linear stability only accounts for the growth rate in the initial phase till the non-linearity sets in.

Chapter 3

Fast Flavor Conversions Near a Supernova core

In this chapter, we apply the formalism presented in previous chapter to explore some new aspects of collective oscillations of supernova (SN) neutrinos. In particular, we explore the presence and growth rates of fast flavor conversions in a realistic SN environment. We perform the linear stability analysis (LSA) to study the onset of fast flavor conversion of neutrinos *near* the source of emission. We classify growth rates into spatial and temporal, and conclude this chapter with the solutions of the fully non-linear equations of motion, demonstrating the presence of fast flavor conversions in a realistic SN environment. ¹

3.1 Introduction

As already explained in Chapter 1, in the deepest SN regions, the neutrino density itself is so high that a ν - ν potential, $\mu \sim \sqrt{2}G_F n_\nu$, is also experienced by a propagating neutrino [31]. This potential is flavor off-diagonal and can lead to self-induced flavor oscillations with a frequency $\sim \sqrt{\omega\mu}$. However, more recently, it was pointed out that the ν - ν potential would lead to even faster flavor conversions at a rate $\sim \mu$, in contrast to $\sqrt{\omega\mu}$ above, for a non-

¹The results in this chapter are based on the paper: B. Dasgupta, A. Mirizzi and M. Sen, “*Fast neutrino flavor conversions near the supernova core with realistic flavor-dependent angular distributions*”, Journal of Cosmology and Astrophysics 1702 (2017) no.02, 019 [arXiv: 1609.00528[hep-ph]].

trivial neutrino emission angular spectra [111, 115, 118, 119]. These faster conversions can produce flavor equilibrium among the different neutrino fluxes at $r \sim \mathcal{O}(1)$ m from the SN surface. Such rapid flavor conversions have been dubbed in the literature as “fast flavor conversions”.

Following up previous literature, in [119], a stability analysis showed that if there are more $\bar{\nu}_e$ than ν_e , or if the emission angular distribution of $\bar{\nu}_e$ are wider, then fast conversions occur. However, this situation is physically less motivated since in a SN environment, there is typically an excess of ν_e over $\bar{\nu}_e$. Furthermore, these instabilities only existed for $\mu \simeq \lambda$, and were suppressed for a larger λ . These results were in contrast with those in [118], where fast conversions existed even when $\lambda = 0$, as long as there was some noise in the emission distributions.

In this chapter, we identify that the resolution to these differences [180]. The resolution lies in the observation that [118] focuses on fast flavor evolution in *time*, very close to the SN core using discrete distributions, whereas [119] considers the flavor evolution in *space*, at larger distances and employing continuous distributions. We perform a more detailed study of the conditions for the development of the fast flavor conversions *close* to the SN core. To this purpose, we do the LSA for a flat source geometry that more appropriately models neutrino emission close to the neutrinosphere. We consider physically well-motivated neutrino fluxes, i.e., ν_e have a larger flux and wider angular distribution than $\bar{\nu}_e$, and use continuous distributions to avoid the problem of spurious modes. We carefully specify the possible instabilities for evolution in space or time, and consider the impact of inward-going neutrinos, which can play an important role near the SN core. Finally, we verify these linear stability predictions using numerical calculations of the fully nonlinear evolution, and present nonlinear calculations of fast conversion using SN neutrino fluxes and angular distributions inspired from a SN simulation.

3.2 Stability Analysis close to the SN core

In this section, we perform the LSA for a flat source emitting neutrinos. Since we are focusing on distances $\sim \mathcal{O}(10)$ m from the neutrinosphere, a major simplification happens if flavor

conversions are studied only at small distances from the SN core. Most of the neutrinos are then emitted around a radius $\mathcal{O}(10)$ m from the neutrinosphere. Since the conversions take place very close to this emission region, the curvature of the neutrinosphere is not relevant. We therefore model the source region as a diffuse flat infinite plane, as shown in Fig. 3.1. As discussed in previous chapters, we consider two flavors: ν_e and ν_x , where $x = \mu, \tau$ or a linear combination of both.

Deep inside a SN, due to the cross-section of interaction ν_x decouple from matter deeper than $\bar{\nu}_e$, which in turn decouple earlier than ν_e . Therefore, one expects that close to the SN core the ν_x zenith-angle distribution would be more forward-peaked than that of $\bar{\nu}_e$, which again would be more forward-peaked than the ν_e distribution. This would give rise to flavor dependent emission angular distribution for the neutrino flavors, as shown in Fig. 3.1.

The neutrinos are conveniently labeled by ω , v_z , and φ , that define the Cartesian components of the momenta

$$\mathbf{p} = \left(E\sqrt{1-v_z^2}\cos\varphi, E\sqrt{1-v_z^2}\sin\varphi, Ev_z \right), \quad (3.2.1)$$

where $v_z \equiv \cos\vartheta$ is the component of the neutrino velocity along the z -axis, and ϑ and φ the zenith and azimuthal angles, respectively. Note that v_z can take negative values, i.e., the zenith angle ϑ can take values between 0 and π , representing neutrinos with trajectories that range from radially outward to radially inward into the star.

The advantage of working near the neutrinosphere is that one does not need to resort to the flux matrices, which were introduced to conserve the flux through a sphere of radius r , and directly work with the occupation matrices. The neutrino occupation matrix, defined in Chapter 2 can also be represented as

$$\varrho_{\omega,v_z,\varphi} = \frac{1}{2}\text{Tr}[\varrho_{\omega,v_z,\varphi}]\mathbb{I} + \Phi_{\bar{\nu}}\frac{g_{\omega,v_z,\varphi}}{2} \begin{pmatrix} s_{\omega,v_z,\varphi} & S_{\omega,v_z,\varphi} \\ S_{\omega,v_z,\varphi}^* & -s_{\omega,v_z,\varphi} \end{pmatrix}, \quad (3.2.2)$$

where $v_z = \cos\vartheta$ is the component of the neutrino velocity along the z -axis, and ϑ and φ the zenith and azimuthal angles, respectively.

The normalization of $g_{\omega,v_z,\varphi}$ is given by $\Phi_{\bar{\nu}}$, determined by the condition

$$\Phi_{\bar{\nu}} \int_{-\infty}^0 d\Gamma g_{\omega,v_z,\varphi} = -(\Phi_{\bar{\nu}_e} - \Phi_{\bar{\nu}_x}), \quad (3.2.3)$$

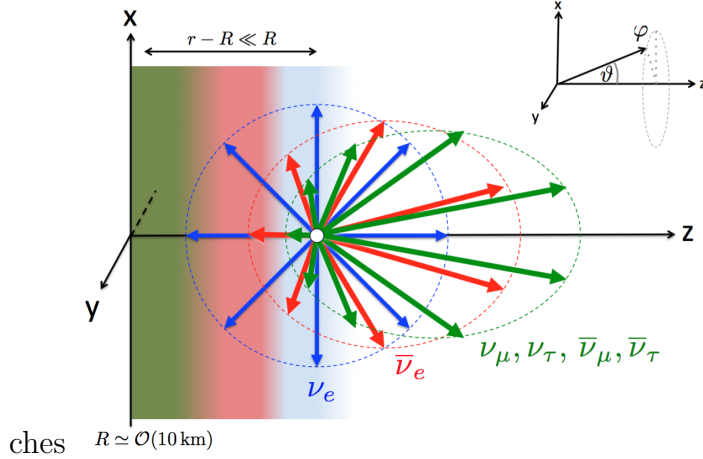


Figure 3.1: Schematic geometry of the model and flavor-dependent zenith-angle distributions of neutrino fluxes. The 3 ellipses are schematic polar plots of the normalized angular distributions of the ν_e (blue), $\bar{\nu}_e$ (red), and ν_x (green) fluxes at the point where the arrows originate.

where $d\Gamma = d\omega dv_z d\varphi / (2\pi)^3$, and $\Phi_{\bar{\nu}_{e,x}}$ are the flavor-dependent total number fluxes averaged over the sphere of radius x . This specific normalization does not matter and all physical quantities depend only on the product $\Phi_\nu g_{\omega,v_z,\varphi}$. Note that in this scheme of normalization, the neutrino-neutrino interaction potential is then given by $\mu = \sqrt{2}G_F\Phi_\nu$. We observe that these differential fluxes $d\Phi_{\nu_\alpha}/d\Gamma$ are predicted in some of the detailed SN simulations, and can be used as initial conditions for subsequent flavor evolution. Also, in order to include neutrinos with trajectories that range from radially outward to radially inward into the star, $v_z \equiv \cos\vartheta$ can take negative values.

Since the total number of neutrinos is conserved, the trace term can be dropped from the EoMs. At the neutrinosphere, neutrinos are emitted as flavor eigenstates, hence $s_{\omega,v_z,\varphi} = 1$, and $S_{\omega,v_z,\varphi} = 0$, leading to no flavor mixing. In absence of collisions, $\text{Tr}[\rho^2]$ is conserved, giving $s_{\omega,v_z,\varphi}^2 + |S_{\omega,v_z,\varphi}|^2 = 1$. The quantity that is relevant for the calculation is the difference of the flux distributions for the two flavors:

$$\begin{aligned}
 g_{\omega,v_z,\varphi} &\propto d\Phi_{\nu_e}/d\Gamma - d\Phi_{\nu_x}/d\Gamma && \text{for neutrinos } (\omega > 0), \\
 &\propto d\Phi_{\bar{\nu}_e}/d\Gamma - d\Phi_{\bar{\nu}_x}/d\Gamma && \text{for antineutrinos } (\omega < 0).
 \end{aligned}
 \tag{3.2.4}$$

Using the formalism outlined in 2.4, one can redo the eigenvalue equation on S for neutrino emission from the flat source. To linear order in $S_{\omega,v_z,\varphi}$, we have the eigenvalue equation

$$\begin{aligned}
i(\partial_t + v_z \partial_z + \vec{v}_T \cdot \vec{\partial}_T) S_{\omega, v_z, \varphi} &= \left[\omega + \lambda + \mu \int d\Gamma' (1 - v_z v'_z - \vec{v}_T \cdot \vec{v}'_T) g_{\omega', v'_z, \varphi'} \right] S_{\omega, v_z, \varphi} \\
&\quad - \mu \int d\Gamma' (1 - v_z v'_z - \vec{v}_T \cdot \vec{v}'_T) g_{\omega', v'_z, \varphi'} S_{\omega', v'_z, \varphi'}, \quad (3.2.5)
\end{aligned}$$

where \vec{v}_T is the velocity vector of the neutrino projected on the x - y -plane. For now, we assume translation invariance of the solutions along the transverse directions and drop the term involving the ∂_T .

Our discussion pertains to a situation where $\mu \gg \Delta m^2/(2E)$ for all relevant neutrino energies E . We can then ignore the vacuum term, and integrate Eq. (3.2.5) $\int d\omega g_{\omega, v_z, \varphi}$ to find that the evolution of $\tilde{S}_{v_z, \varphi} \equiv \int d\omega g_{\omega, v_z, \varphi} S_{\omega, v_z, \varphi}$ depends on spectrum $g_{\omega, v_z, \varphi}$ only through $\tilde{g}_{v_z, \varphi} \equiv \int d\omega g_{\omega, v_z, \varphi}$, i.e., the difference of the flux-weighted angular spectra of the neutrinos and antineutrinos. Explicitly, when $g_{\omega, v_x, \varphi} \propto (d\Phi_{\nu_e}/d\Gamma - d\Phi_{\bar{\nu}_e}/d\Gamma)_{\omega > 0} + (d\Phi_{\bar{\nu}_e}/d\Gamma - d\Phi_{\nu_e}/d\Gamma)_{\omega < 0}$ is integrated over ω , the ν_x and $\bar{\nu}_x$ dependent terms cancel each other. As a result, the ν_x and $\bar{\nu}_x$ distributions do not enter the EoMs as long as they are equal. At this point, one could integrate out ω and study the stability of $\tilde{S}_{v_z, \varphi}$. However, we will study the stability of $S_{\omega, v_z, \varphi}$, keeping our equations general and explicitly retaining ω , setting it to zero only at the end.

In this section, we consider only ν_e and $\bar{\nu}_e$ with the spectrum

$$g_{\omega, v_z, \varphi} = \frac{1}{2\pi} \left[(1+a) f_{\nu_e}(\omega) \Theta(v_z) \Theta(1-v_z) - \frac{1}{(1-b)} f_{\bar{\nu}_e}(\omega) \Theta(v_z-b) \Theta(1-v_z) \right], \quad (3.2.6)$$

which, once integrated over their normalized ω -distributions $f_{\nu_e}(\omega)$ and $f_{\bar{\nu}_e}(\omega)$, encodes the difference of the flux-weighted zenith-angle distributions of ν_e and $\bar{\nu}_e$.

We consider two toy models with different angular distributions, which are shown in the two panels of Fig. 3.2. These models incorporate an important feature of the realistic SN spectra, that the zenith angle distributions for the neutrinos and antineutrinos are not the same. In Model I (left panel), while neutrinos are emitted over the entire forward hemisphere ($0 \leq v_z \leq 1$), the antineutrinos are contained in a narrower forward cone $b \leq v_z \leq 1$, with $b > 0$. Model II (right panel), in addition, also allows for inward going neutrinos and antineutrinos, i.e., $-1 \leq v_z \leq 1$ for neutrinos and $b \leq v_z \leq 1$ for antineutrinos, with $b > -1$.

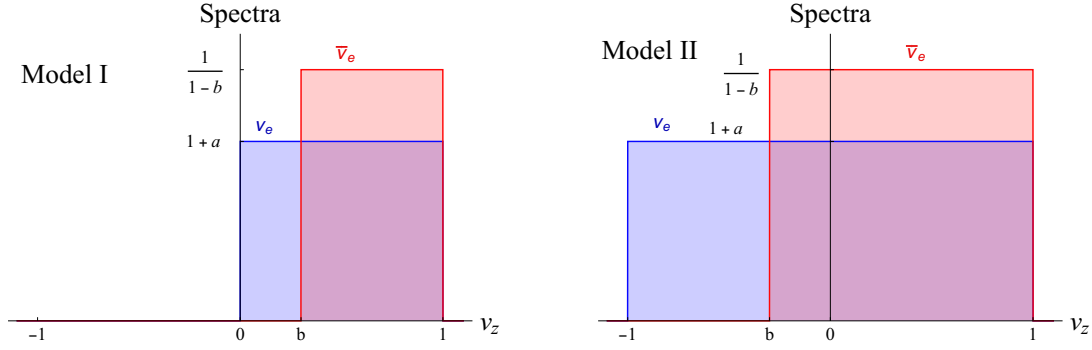


Figure 3.2: Sketches of the schematic zenith angle distributions of ν_e (blue) and $\bar{\nu}_e$ (red), used for the calculations in this section. Left: Model I shows a spectrum that corresponds to no inward going ν_e or $\bar{\nu}_e$ as defined by Eq. (3.2.6). Right: Model II shows a spectrum with inward going ν_e and $\bar{\nu}_e$ as defined by Eq. (3.2.7). The ν_e and $\bar{\nu}_e$ have a flux ratio $1 + a$, i.e., more ν_e than $\bar{\nu}_e$ when $a > 0$, and the $\bar{\nu}_e$ have a more forward-peaked distribution, controlled by the parameter b which we always choose to be larger than the $\min(v_z)$ for ν_e .

Model II can be represented by the spectrum

$$g_{\omega, v_z, \varphi} = \frac{1}{2\pi} \left[\frac{1+a}{2} f_{\nu_e}(\omega) \Theta(1+v_z) \Theta(1-v_z) - \frac{1}{(1-b)} f_{\bar{\nu}_e}(\omega) \Theta(v_z-b) \Theta(1-v_z) \right], \quad (3.2.7)$$

In both the models, the neutrino-antineutrino asymmetry is labeled by a , such that $1 + a$ encodes the ratio of the total neutrino to antineutrino flux. Typically for a SN, $a > 0$. As long as $1/(1-b) > 1 + a$, there is a *crossing* of the two flux-weighted angular spectra. This kind of a “non-trivial” flavor-dependent angular distribution is believed to be crucial for fast conversion.

3.2.1 Stationary Solutions with Evolution in Space

We begin by looking for a steady state or stationary solution, i.e., the occupation matrices do not change with time. In that case it is appropriate to drop the time-derivative in Eq. (3.2.5), and the eigenvalue equation for $S = Qe^{-i\Omega z}$ becomes

$$\left[\omega + \lambda + \mu\epsilon - (\Omega + \mu\epsilon_v) v_z - \mu(\epsilon_c \cos \varphi + \epsilon_s \sin \varphi) \sqrt{1-v_z^2} \right] Q = \mu \int d\Gamma' \left[1 - v_z v'_z - \cos(\varphi - \varphi') \sqrt{(1-v_z^2)(1-v_z'^2)} \right] g_{\omega', v'_z, \varphi'} Q', \quad (3.2.8)$$

where we have defined the integrals over the spectrum,

$$\epsilon = \int d\Gamma g_{\omega, v_z, \varphi} , \quad (3.2.9)$$

$$\epsilon_v = \int d\Gamma v_z g_{\omega, v_z, \varphi} , \quad (3.2.10)$$

$$\epsilon_s = \int d\Gamma \sin \varphi \sqrt{1 - v_z^2} g_{\omega, v_z, \varphi} , \quad (3.2.11)$$

$$\epsilon_c = \int d\Gamma \cos \varphi \sqrt{1 - v_z^2} g_{\omega, v_z, \varphi} , \quad (3.2.12)$$

that encode the total, zenith, and azimuthal asymmetries, respectively. We take the ansatz that

$$Q = \frac{q_1 + q_2 v_z + q_3 \cos \varphi \sqrt{1 - v_z^2} + q_4 \sin \varphi \sqrt{1 - v_z^2}}{\omega + \lambda + \mu \epsilon - (\Omega + \mu \epsilon_v) v_z - \mu (\epsilon_c \cos \varphi + \epsilon_s \sin \varphi) \sqrt{1 - v_z^2}} , \quad (3.2.13)$$

which gives us an eigenvalue equation,

$$\begin{bmatrix} q_1 \\ q_2 \\ q_3 \\ q_4 \end{bmatrix} = \begin{bmatrix} I_{0,0}^{0,0} & I_{1,0}^{0,0} & I_{0,1}^{1,0} & I_{0,1}^{0,1} \\ -I_{1,0}^{0,0} & -I_{2,0}^{0,0} & -I_{1,1}^{1,0} & -I_{1,1}^{0,1} \\ -I_{0,1}^{1,0} & -I_{1,1}^{1,0} & -I_{0,2}^{2,0} & -I_{0,2}^{1,1} \\ -I_{0,1}^{0,1} & -I_{1,1}^{0,1} & -I_{0,2}^{1,1} & -I_{0,2}^{0,2} \end{bmatrix} \begin{bmatrix} q_1 \\ q_2 \\ q_3 \\ q_4 \end{bmatrix} , \quad (3.2.14)$$

in terms of a family of integrals

$$I_{m,n}^{\alpha,\beta} = \mu \int d\Gamma \left[\frac{\cos^\alpha \varphi \sin^\beta \varphi v_z^m (1 - v_z^2)^{n/2}}{\omega + \lambda + \mu \epsilon - (\Omega + \mu \epsilon_v) v_z - \mu (\epsilon_c \cos \varphi + \epsilon_s \sin \varphi) \sqrt{1 - v_z^2}} \right] g_{\omega, v_z, \varphi} . \quad (3.2.15)$$

Note that the integrals are dimensionless, and functions of Ω and other parameters.

The main point here is that whether fast flavor conversions take place depends on whether Eq. (3.2.14) has complex solutions for Ω . The imaginary part of Ω , that we denote as usual as $\kappa = \text{Im}(\Omega)$, leads to an exponential rise in $S_{\omega, v_z, \varphi} \sim e^{\kappa t}$. If $\text{Im}(\Omega)$ happens to be nonzero in the limit of vanishing ω and λ , it can only be proportional to μ , which is the only remaining dimensional scale, signaling an instability whose rate scales directly with μ , in contrast to the usual bipolar instabilities that scale as $\sqrt{\omega \mu}$.

If $g_{\omega, v_z, \varphi}$ is independent of φ , as we have chosen in Eq. (3.2.6), the φ integrals decouple and we can drop the indices α, β in the integrals $I_{m,n}^{\alpha,\beta}$ (setting them to zero), and write

Eq. (3.2.14) as

$$\begin{bmatrix} q_1 \\ q_2 \\ q_3 \\ q_4 \end{bmatrix} = \begin{bmatrix} I_{0,0} & I_{1,0} & 0 & 0 \\ -I_{1,0} & -I_{2,0} & 0 & 0 \\ 0 & 0 & -I_{0,2}/2 & 0 \\ 0 & 0 & 0 & -I_{0,2}/2 \end{bmatrix} \begin{bmatrix} q_1 \\ q_2 \\ q_3 \\ q_4 \end{bmatrix} . \quad (3.2.16)$$

The upper 2×2 block, manifestly independent of φ , gives the azimuthally symmetric solution, whereas the diagonal lower block gives the azimuthal symmetry breaking solution. The eigenvalues for the azimuthally symmetric instabilities are given by

$$(I_{0,0} - 1)(I_{2,0} + 1) - (I_{1,0})^2 = 0 , \quad (3.2.17)$$

while for the azimuthally non-symmetric instabilities one has

$$\left(\frac{I_{0,2}}{2} + 1 \right) = 0 . \quad (3.2.18)$$

These azimuthal symmetry breaking instabilities spontaneously can generate large φ -dependent variations in the flavor composition, even if one starts with almost perfectly symmetric initial condition.

With a choice of the spectrum $g_{\omega, v_z, \varphi}$ given in Eq. (3.2.6), it is possible to perform the integrals $I_{m,n}$ analytically and one can write the eigenvalue equations explicitly. However, these are transcendental equations in Ω and one cannot obtain closed-form solution for Ω using them, in general. Thus we resort to solving Eqs. (3.2.17) and (3.2.18) numerically using MATHEMATICA.

In Fig. 3.3, we show a contour plot of the imaginary part of Ω for different values of a and b which shows that fast conversions do not occur if $b = 0$. The instabilities are azimuthally symmetric, i.e., solutions to Eq. (3.2.17) and we found no solutions to Eq. (3.2.18) with imaginary parts. As discussed before, the parameters a and b , that define the spectrum $g_{\omega, v_z, \varphi}$, are in fact closely related to the total and zenith angle asymmetries between the neutrino flavors, $\epsilon = a$ and $\epsilon_v = (a - b)/2$. For $\lambda = 0$, we found no instabilities in the azimuthally symmetric as well as asymmetric equations. These results are in qualitative agreement with the results obtained in ref. [119]

The most important feature to be noticed here is that there are no instabilities if $b = 0$, i.e., when the neutrino and antineutrino distributions are the same. We have checked explicitly

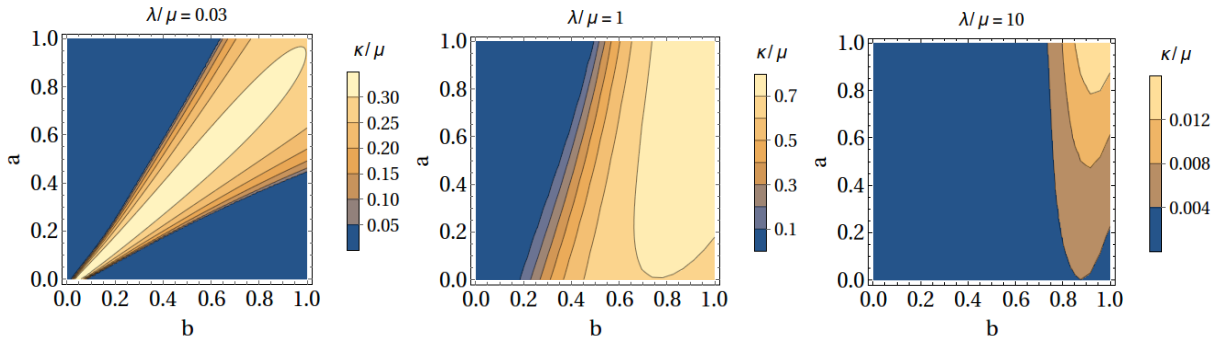


Figure 3.3: Instability rates for different values of a and b , for three different values of $\lambda/\mu = 0.03, 1, \text{ and } 10$, respectively from left to right. Note that a large a corresponds to large total flavor asymmetry ϵ and a zero b corresponds to identical angular distributions for the two flavors, where the instabilities vanish. The instabilities are azimuthally symmetric, and we find no instabilities that break the azimuthal symmetry. For $\lambda = 0$ we find no instabilities, azimuthally symmetric or not, that scale as μ .

that a *necessary* condition to have fast instabilities appears to be a *crossing* between the angular spectra of ν_e and $\bar{\nu}_e$, as shown in Fig. 3.2. Another important feature to be noted is that instabilities exist only if $\lambda \sim \mu$, disappearing for both smaller and larger λ .

3.2.2 Homogeneous Solutions with Evolution in Time

We also consider the possibility that the flavor composition does not vary spatially, but undergoes rapid turnovers in time. This is motivated by the results of the previous section, where we saw that unless $\lambda \sim \mu$, we did not find fast conversions. We will now show that for temporal growths, matter effects *do not matter*.

If we assume that the neutrino flavor composition is relatively homogeneous over the region of interest and only varies with time, we can drop the spatial derivatives in Eq. (3.2.5), and write $S_{\omega, v_z, \varphi} = Q e^{-i\Omega t}$. Thereafter, analogous to the previous section, one obtains the same eigenvalue equation for Q as in Eq. (3.2.14), but with the integrals $I_{m,n}^{\alpha,\beta}$ replaced by a new family of integrals

$$J_{m,n}^{\alpha,\beta} = \mu \int d\Gamma \left[\frac{\cos^\alpha \varphi \sin^\beta \varphi v_z^m (1 - v_z^2)^{n/2}}{\omega + \lambda + \mu\epsilon - \Omega - \mu\epsilon_v v_z - \mu(\epsilon_c \cos \varphi + \epsilon_s \sin \varphi) \sqrt{1 - v_z^2}} \right] \mathcal{G}_{\omega, v_z, \varphi} , \quad (3.2.19)$$

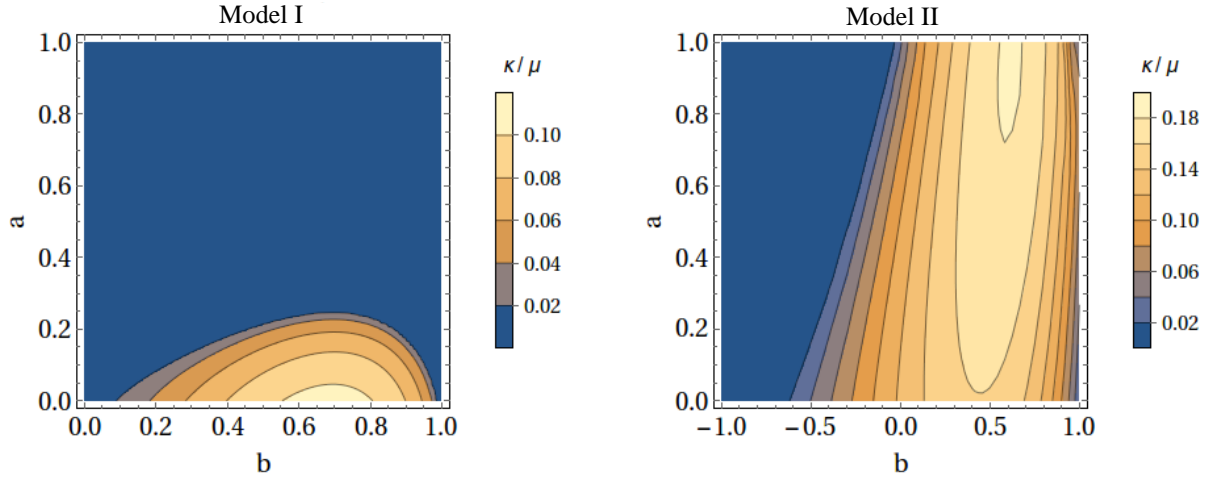


Figure 3.4: Instability rates for different values of a and b , for evolution in time, without including inward going modes (left panel) and including inward going modes (right panel). These instabilities are azimuthally asymmetric, and we found no instabilities if the azimuthal symmetry were to be exact. There is no dependence on λ .

which differ by the replacement $v_z \Omega \rightarrow \Omega$ in the denominator of the integrand of $I_{m,n}^{\alpha,\beta}$.

For a spectrum which is independent of φ , Eq. (3.2.14) simplifies as Eq. (3.2.16). The upper block gives the azimuthally symmetric solution whereas the lower block gives the azimuthal symmetry breaking solution. The eigenvalues for the azimuthally symmetric instabilities are given by

$$(J_{0,0} - 1)(J_{2,0} + 1) - (J_{1,0})^2 = 0 \quad , \quad (3.2.20)$$

while for the azimuthally non-symmetric instabilities one has

$$\left(\frac{J_{0,2}}{2} + 1 \right) = 0 \quad . \quad (3.2.21)$$

The important fact here is that λ does not affect the temporal stability in any way. If there is an unstable solution for $\lambda = 0$, one will find an unstable solution with the same imaginary part for any other value of λ by simply shifting the real part of Ω , i.e., by shifting $\Omega \rightarrow \Omega + \lambda$, as is apparent from Eq. (3.2.19).

In Fig. 3.4 (left panel) we show the instability rates for evolution in time, for Model I, i.e., $g_{\omega,v_z,\varphi}$ is given by Eq. (3.2.6). It is apparent that fast instabilities, which are azimuthal symmetry breaking solutions to Eq. (3.2.21), exist only for small values of a and large values of b . There is no dependence on λ , which can be absorbed into the real part of Ω .

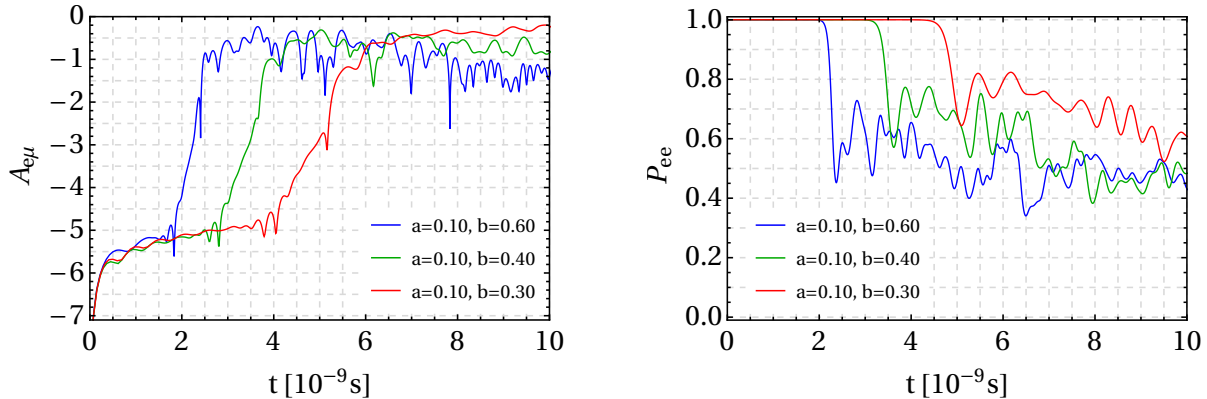


Figure 3.5: Growth of instability for evolution in time, as predicted by numerical solution of the nonlinear evolution of $\bar{\nu}_e$, for representative values of a and b . The left panel shows quantity $A_{e\mu} = \log_{10}|S|$ as a measure of the extent of flavor conversion. The right panel shows the angle-integrated survival probabilities P_{ee} . These instabilities are azimuthally asymmetric and independent of λ .

On the right panel in Fig. 3.4, we show the analogous results, but for Model II, where the ν_e are emitted isotropically along all zenith angles (see right panel of Fig. 3.2). It is clear that, for the same value of a and b , the presence of the backward traveling modes of ν_e greatly amplify the instabilities. This is another important result we arrive at. Closer to the neutrinosphere, the fast instability can be stronger due to the presence of these inward going neutrinos.

We have also numerically solved the fully nonlinear EoMs for the spectrum corresponding to the left panel in Fig. 3.4 (no inward going modes). The EoMs were discretized in v_z and φ , with 100 modes for $0 \leq v_z \leq 1$ and 10 modes in φ , and the ν - ν interaction strength was taken to be $\mu = 4 \times 10^5 \text{ km}^{-1}$. In Fig. 3.5 we show the numerically evaluated angle-integrated amplitudes of the flavor conversions for the $\bar{\nu}_e$,

$$A_{e\mu}(t) = \log_{10}|S(t)| \quad , \quad (3.2.22)$$

for some representative values of a and b . The initial evolution, that asymptotes to a plateau at $A_{e\mu} \simeq 10^{-5}$, is not the fast conversion predicted by linear stability analysis. However, the subsequent evolution, where $A_{e\mu}$ grows approximately linearly, is in excellent agreement with the corresponding growth rates shown in the left panel of Fig. 3.4. We have also performed nonlinear calculations corresponding to the right panel of Fig. 3.4, which show faster growth,

but we do not show them here, as they are otherwise quite similar. In all these cases we find a perfect agreement between the linear and non-linear calculation of $A_{e\mu}$. In particular, we find exponentially growing solutions within $t \sim \mathcal{O}(10^{-8})$ s.

In the right panel of Fig. 3.5, we also show the corresponding angle-integrated survival probability given by $P_{ee}(t)$. As one can clearly see, fast conversions lead to approximate flavor equilibrium, i.e., $P_{ee} \simeq 1/2$. Depending on the details of these fast conversions, however, this equilibration may not necessarily be complete, e.g., if the instability growth rates are small.²

3.2.3 Evolution in both Space and Time

If the occupation matrix evolves in both space and time, the formalism presented above is inadequate. A useful way of studying these solutions is to consider

$$S(\vec{x}, t) = Q e^{-i(\vec{\Omega}_x \cdot \vec{x} + \Omega_t t)} , \quad (3.2.23)$$

and follow the approach in refs. [178, 181] (see also [100, 182]). One can Fourier transform to the momentum space as $Q e^{-i(\vec{\Omega}_x \cdot \vec{x} + \Omega_t t)} \rightarrow \sum_{\vec{k}, p} Q_{\vec{k}, p} e^{-i(\vec{k} \cdot \vec{x} + pt)}$, and study the stability of these Fourier modes. Physically, \vec{k} and p correspond to *inhomogeneities* or *pulsations* with wave-vectors \vec{k} or frequency p , respectively. Here, we do not go into a detailed study along these lines, except to note a few key features:

1. If we are looking at spatial evolution along z , the time-dependence in S will appear as pulsations of frequency $p = \Omega_t$ that affects the linear stability, e.g., in Eq. (3.2.14), through the replacement $\lambda \rightarrow \lambda - p$ in Eq. (3.2.15).
2. If on the other hand we wish to study evolution in time, the spatial oscillations of S along z can be Fourier decomposed into their constituent frequencies labeled by k_z , and one simply shifts

$$\mu\epsilon_v \rightarrow \mu\epsilon_v + k_z , \quad (3.2.24)$$

in Eq. (3.2.19).

3. Fourier modes of the fluctuations along transverse directions x and y will lead to

² I would like to thank Alessandro Mirizzi for the simulations leading to these plots.

analogous shifts

$$\mu\epsilon_{c,s} \rightarrow \mu\epsilon_{c,s} + k_{x,y} , \quad (3.2.25)$$

in the denominator of Eq. (3.2.15) or Eq. (3.2.19).

4. The linear stability analysis can then proceed with these minor replacements, essentially amounting to these redefinitions of the asymmetry parameters. Practically, this may have interesting consequences leading to enhanced fast conversions, e.g., as was shown in refs. [178,181], the pulsations can enhance instabilities by effectively removing the matter effect for the specific pulsating Fourier modes and the evolution of nearby modes via nonlinear coupling of modes. Similarly, inhomogeneity may dynamically mimic a larger zenith or azimuthal angle asymmetry and enhance fast conversions. A detailed exploration of these possibilities is left for a future study.

Another more intuitive way of studying these solutions is to consider the dispersion relations for the flavor instability field S [183]. In this, instabilities arise as gaps in the dispersion relations. Based on this, a categorization of different types of instabilities was presented in [183].

3.3 Numerical solutions with SN Fluxes

Numerical simulations of SN explosions predict flavor-dependent zenith-angle neutrino distributions, as explained earlier. Inspired by SN simulations, a first attempt to characterize self-induced neutrino flavor conversions with flavor-dependent ν distributions was performed in [117, 184]. However, angular distributions for ν_e and $\bar{\nu}_e$ were assumed to be identical in these studies, and only a crossing between electron and non-electron neutrino angular spectra was considered. As a result, even though the flavor conversions were shown to be enhanced with respect to the case with trivial angular distributions, the possibility of fast conversions was missed. In light of the insights obtained in the previous sections, we now consider the possibility of fast conversions by introducing realistic SN angular distributions with different angular distributions for ν_e and $\bar{\nu}_e$.

We consider the normalized angular distributions for different ν species from a one-dimensional SN model for a $25 M_\odot$ progenitor at post-bounce time $t = 0.325$ s and $r = 25$ km,

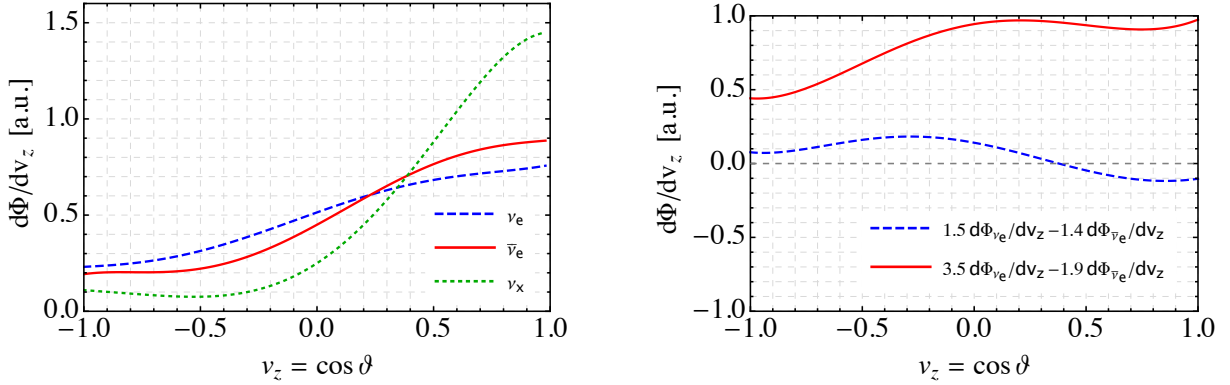


Figure 3.6: Left panel: Normalized flavor-dependent zenith angle distributions of SN neutrinos from a one-dimensional SN model from the Garching group for a $25 M_{\odot}$ progenitor at post-bounce time $t = 0.325$ s and $r = 25$ km [185]. Right panel: Difference of flux-weighted angular spectra of ν_e and $\bar{\nu}_e$, for two choices of flux ratios corresponding to small asymmetry (dashed line) and large asymmetry (solid line), respectively. Note that ν_x and $\bar{\nu}_x$ fluxes are equal and thus drop out.

simulated by the Garching group [185], as shown in Fig. 3.6 (left panel). Notice that while the ν_x distributions are mostly forward-peaked, ν_e and $\bar{\nu}_e$ have a significant fraction of backward going neutrinos.

In this specific simulation, there exists a strongly hierarchical flavor ratio $\Phi_{\nu_e} : \Phi_{\bar{\nu}_e} : \Phi_{\nu_x} = 3.5 : 1.9 : 1$. For such a strong ν_e to $\bar{\nu}_e$ asymmetry, there is no crossing between the zenith-angle spectra of ν_e and $\bar{\nu}_e$ (see right panel in Fig. 3.6) and we do not expect to find any fast conversion. However, it has been recently discovered that multidimensional SN simulations exhibit a phenomenon called lepton-emission self-sustained asymmetry (LESA) [76], i.e., the lepton asymmetries of the neutrino fluxes have strong variance over various directions and this roughly hemispherical asymmetry appears to be self-stabilized. In particular, along some directions flavor asymmetries among the different species can be much milder than in the corresponding 1D simulations (see [186]).

Currently, the ν angular distributions for the multi-dimensional SN models showing the LESA effects are not available in a readily usable form. Therefore, we use the 1D distributions shown in Fig. 3.6, and simply change the relative weights of ν_e and $\bar{\nu}_e$ fluxes within the range predicted by models exhibiting LESA. In particular we take two cases, one with a large asymmetry $\Phi_{\nu_e} : \Phi_{\bar{\nu}_e} : \Phi_{\nu_x} = 3.5 : 1.9 : 1$, and another with a small asymmetry

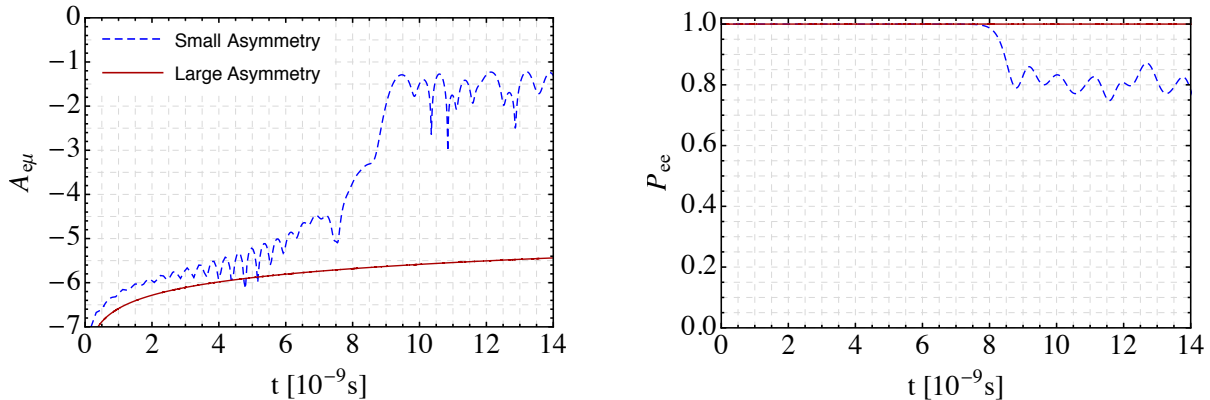


Figure 3.7: Growth of fast instabilities for realistic SN neutrino angular distributions considered in this thesis. The dashed and continuous curves correspond to the flux parameters with small and large lepton asymmetries, as may be expected due to LESA. While large asymmetries suppress the fast conversion, for smaller asymmetries there is $\simeq 20\%$ flavor conversion within a few nanoseconds. The growth of off-diagonal components is shown on the left panel, while the right panel shows the angle-integrated survival probability for $\bar{\nu}_e$.

$\Phi_{\nu_e} : \Phi_{\bar{\nu}_e} : \Phi_{\nu_x} = 1.5 : 1.4 : 1$, roughly corresponding to the direction with lowest asymmetry. In this latter case, one finds a crossing between the zenith-angle spectra of ν_e and $\bar{\nu}_e$, as shown in the right panel of Fig. 3.6. Therefore, fast conversions are expected here.

In Fig. 3.7 (left panel) we show the amplitude of flavor evolution $A_{e\mu}$ for $\bar{\nu}_e$, for these two choices of flux ratios. Note that these calculations include the inward going neutrino modes as shown in Fig. 3.7. The right panel of Fig. 3.7 shows the corresponding angle-integrated survival probabilities $P_{ee}(t)$. One can see that while no fast conversion takes place for the large flux asymmetry, if the flux asymmetry is not very large fast conversion leads to almost $\mathcal{O}(1)$ flavor conversion within a few nanoseconds, in a range of $r - R \sim \mathcal{O}(1)$ m from the boundary leading to approximate flavor equilibrium. This emphasizes the idea that fast flavor conversions require a crossing in the spectra of ν_e and $\bar{\nu}_e$ to take place.³

³ I would like to thank Alessandro Mirizzi for the simulations leading to these plots.

3.4 Summarized Results

In this chapter, we have investigated the possibility of flavor conversions of SN neutrinos, that occur with a fast rate $\sim \mu$, driven by interactions of neutrinos emitted with non-trivial angular distributions. Considering physically well-motivated neutrino fluxes and emission geometry, we have studied the nonlinear flavor evolution for different toy models, and compared it with the linear stability analyses. We have found excellent agreement between the linearized growth rate of fully non-linear solutions, and those predicted by the stability analysis. We have demonstrated that a necessary condition in order to have fast conversions is the presence of a crossing among the angular spectra of ν_e and $\bar{\nu}_e$. Another important result is that the backward going modes strongly enhance fast conversions, and make fast conversions possible for a wider range of flux and angular asymmetries. In particular, rapid flavor turn-overs may occur in time, even if the corresponding spatial evolution is suppressed by the presence of a large matter potential. Considering a moderate hierarchy among the fluxes of different flavors and flavor-dependent ν angular distributions, as predicted from Garching SN simulations, we have shown that fast conversion is possible in realistic scenarios.

The natural region where these effect would show up is just above the core of a SN, where one expects significant differences in the angular distributions of the different ν species. In multi-dimensional SN simulations presenting the LESA phenomenon, it is quite likely that there will be directions along which the flavor asymmetries among the different species are moderate at early post-bounce times and allow for these fast conversions. If these conversions indeed take place, these would produce a tendency towards flavor equilibrium among the different species. Since at the neutrinosphere, the non-electron neutrino flavors are supposed to be more energetic, such rapid $\nu_e \nu_x$ would indicate a large energy gain for the ν_e . This can in turn help in sufficient heating behind the stalled shock wave through charged current ν_e capture processes, since the energy deposition behind the shock wave depends on the ν_e and $\bar{\nu}_e$ luminosity. This can have a strong impact on the revival of the stalled shock-wave by enhanced neutrino reheating. Furthermore, due to the change in the number of ν_e and $\bar{\nu}_e$ due to fast flavor conversions, the ratio of neutron to proton also gets affected deep inside the SN. This can affect r-process nucleosynthesis of heavy elements, which are quite sensitive to the neutron to proton ratio inside the SN.

The possibility of this new form of self-induced flavor conversions represents a new challenge for the simulation of the SN neutrino signal. Indeed, in its most general form, the problem involves tracking the neutrino ensemble, including oscillations and scattering, in an anisotropic and fluctuating environment of an exploding supernova. This is way beyond the scope of current studies. In the next chapter, we will consider a simple system undergoing fast oscillations, and try to understand analytically through a classical analogue of the phenomenon. This will help us get an intuitive understanding of fast oscillations.

Chapter 4

An Analytical Understanding of Fast Flavor Conversions

In the previous chapter, we explored the phenomena of fast flavor conversions, and demonstrated that fast conversions indeed take place near the neutrinosphere, causing rapid neutrino flavor conversions. While the linear stability analysis allows us to predict the onset of these instabilities and study them in the linear regime, an analytical understanding of fast conversions was missing. In this chapter, we present an analytical treatment of the simplest system that exhibits fast conversions, and show that the conversions can be understood as the dynamics of a particle rolling down in a quartic potential governed dominantly by the neutrino potential. We show that subleading effects due to the vacuum terms are needed to seed fast conversions. ¹

4.1 Introduction

Although collective oscillations have been studied extensively numerically, there is still no concrete analytical understanding of collective effects. This is essentially due to the non-linear nature of the problem. However, insights can be gained into collective bipolar oscil-

¹The results in this chapter are based on the paper: B. Dasgupta and M. Sen, “*Fast Neutrino Flavor Conversion as Oscillations in a Quartic Potential*”, Physical Review D97 (2018) no.2, 023017, [arXiv:1709.08671[hep-ph]].

lations from a simple model of a pair of mono-energetic neutrino-antineutrino beam interacting with each other. This system is mathematically equivalent to a pendulum in flavor space [91, 97]. The stability of the pendulum is determined by the neutrino mass hierarchy. For the inverted mass ordering, the system is akin to a pendulum starting in an unstable inverted position, slightly offset by a small mixing angle, and swinging through the lowest position to the other side. This corresponds to bipolar flavor conversions. This simple mechanical analog of the flavor oscillations forms the basis for much of our intuitive understanding of the physics of collective oscillations.

We aim to discover a simple mechanical analog of fast oscillations, similar to how the flavor pendulum explains bipolar flavor oscillations. Towards this goal, we consider the simplest model that shows fast oscillations: a set of four beams of neutrinos and antineutrinos intersecting each other at an angle θ . Under some simplifying assumptions, we show that its dynamics is equivalent to oscillations of a particle in a quartic potential. Using the classical mechanical action, we analytically compute the oscillation period in the inverted quartic potential and find excellent agreement with numerical solutions. Furthermore, we identify three different time scales, as well as conserved quantities associated with fast conversions.

4.2 Fast oscillations in the intersecting 4-beam model

We use the polarization vector formalism outlined in Chapter 2, and apply it to a two-flavor neutrino system. The equation of motion (EoM) for a 2-flavor neutrino of momentum \mathbf{p} is given by,

$$\dot{\mathbf{P}}_{\mathbf{p}} = [\omega_{\mathbf{p}}\mathbf{B} + \mu \int d\Gamma' (1 - \mathbf{v} \cdot \mathbf{v}') \mathbf{P}_{\mathbf{p}'}] \times \mathbf{P}_{\mathbf{p}}, \quad (4.2.1)$$

where $\mathbf{B} = (\sin 2\vartheta_0, 0, -\cos 2\vartheta_0)$ for a vacuum mixing angle ϑ_0 , and $d\Gamma'$ refers to an integral over the 3-momenta of the other neutrinos, as explained in 2.2.1. Here, we have ignored ordinary matter effects, and assumed that collisions are absent. For simplicity, we also assume that the flavor evolution is homogeneous over a length scale much larger than the length scale corresponding to fast conversions. Hence we drop the space derivative, and the only relevant dynamics is its time evolution. Similar equations hold for antineutrinos with the replacement $\bar{\mathbf{P}}_{\omega_{\mathbf{p}}, \mathbf{v}_{\mathbf{p}}} \equiv \mathbf{P}_{-\omega_{\mathbf{p}}, \mathbf{v}_{\mathbf{p}}}$. In the following, we drop the subscript \mathbf{p} for clarity.

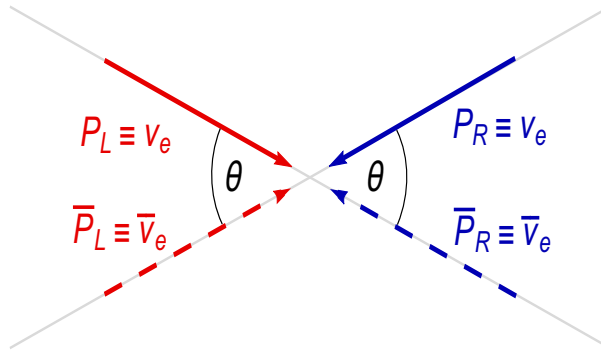


Figure 4.1: Four-beam model: Electron neutrinos (solid) and antineutrinos (dashed) traveling along two beams each, one from the left (red) and another from the right (blue), forward scatter off each other. We study the time evolution of the flavor content of these beams.

The simplest system that shows fast flavor conversions is a system consisting of two right-going and left-going neutrinos and antineutrinos, intersecting each other at an angle θ , as shown in Fig. 4.1 [119]. The neutrino and antineutrino beams are labeled by their corresponding polarization vectors. Following Eq.(4.2.1), the EoMs for the four polarization vectors are given by:

$$\begin{aligned}
 \dot{\mathbf{P}}_L &= \omega \mathbf{B} \times \mathbf{P}_L + \mu [(1+c) \mathbf{P}_R - (1-c) \bar{\mathbf{P}}_L - 2 \bar{\mathbf{P}}_R] \times \mathbf{P}_L, \\
 \dot{\mathbf{P}}_R &= \omega \mathbf{B} \times \mathbf{P}_R + \mu [(1+c) \mathbf{P}_L - (1-c) \bar{\mathbf{P}}_R - 2 \bar{\mathbf{P}}_L] \times \mathbf{P}_R, \\
 \dot{\bar{\mathbf{P}}}_L &= -\omega \mathbf{B} \times \bar{\mathbf{P}}_L + \mu [(1-c) \mathbf{P}_L - (1+c) \bar{\mathbf{P}}_R + 2 \mathbf{P}_R] \times \bar{\mathbf{P}}_L, \\
 \dot{\bar{\mathbf{P}}}_R &= -\omega \mathbf{B} \times \bar{\mathbf{P}}_R + \mu [(1-c) \mathbf{P}_R - (1+c) \bar{\mathbf{P}}_L + 2 \mathbf{P}_L] \times \bar{\mathbf{P}}_R.
 \end{aligned} \tag{4.2.2}$$

The terms involving $\mathbf{v} \cdot \mathbf{v}'$ lead to terms involving $c \equiv \cos \theta$, where θ is the angle shown in Fig. 4.1. Following [97], we define the following linear combination of polarization vectors to understand the flavor evolution more clearly,

$$\mathbf{Q} \equiv \mathbf{P}_L + \mathbf{P}_R + \bar{\mathbf{P}}_L + \bar{\mathbf{P}}_R - \frac{2\omega}{\mu(3-c)} \mathbf{B}, \tag{4.2.3}$$

$$\mathbf{D} \equiv \mathbf{P}_L + \mathbf{P}_R - \bar{\mathbf{P}}_L - \bar{\mathbf{P}}_R. \tag{4.2.4}$$

We additionally define the following combination of polarization vectors

$$\mathbf{X} \equiv \mathbf{P}_L - \mathbf{P}_R + \bar{\mathbf{P}}_L - \bar{\mathbf{P}}_R, \tag{4.2.5}$$

$$\mathbf{Y} \equiv \mathbf{P}_L - \mathbf{P}_R - \bar{\mathbf{P}}_L + \bar{\mathbf{P}}_R. \tag{4.2.6}$$

While the bipolar oscillations were easily described by \mathbf{Q} and \mathbf{D} [97], one needs \mathbf{X} and \mathbf{Y} additionally to describe fast oscillations. In terms of these vectors, the EoMs take the form

$$\dot{\mathbf{Q}} = \frac{\mu}{2}(3-c)\mathbf{D} \times \mathbf{Q} + \frac{\mu}{2}(1+c)\mathbf{X} \times \mathbf{Y}, \quad (4.2.7)$$

$$\dot{\mathbf{D}} = \omega \mathbf{B} \times \mathbf{Q}, \quad (4.2.8)$$

$$\dot{\mathbf{X}} = \left[\omega \left(\frac{3+c}{3-c} \right) \mathbf{B} + \mu c \mathbf{Q} \right] \times \mathbf{Y} + \mu \mathbf{D} \times \mathbf{X}, \quad (4.2.9)$$

$$\dot{\mathbf{Y}} = \left[\omega \left(\frac{2}{3-c} \right) \mathbf{B} - \frac{\mu}{2}(1-c)\mathbf{Q} \right] \times \mathbf{X} + \frac{\mu}{2}(3+c)\mathbf{D} \times \mathbf{Y}. \quad (4.2.10)$$

4.2.1 Bipolar limit

There are two ways in which the above set of equations reduce to the previously well-known equations for the bipolar flavor pendulum.

(i) If $c = -1$, which corresponds to two back-to-back beams of neutrinos and antineutrinos, then Eqs.(4.2.7, 4.2.8) decouple from the rest and simply reproduce the bipolar flavor pendulum. In this limit, Eqs.(4.2.9, 4.2.10) imply that $\mathbf{X} \cdot \mathbf{X} + \mathbf{Y} \cdot \mathbf{Y}$ is constant. Therefore, if \mathbf{X} and \mathbf{Y} are initially zero to begin with, they remain zero throughout.

(ii) For any value of c , if \mathbf{X} and \mathbf{Y} are initially exactly zero, there exists a $L \leftrightarrow R$ exchange symmetry in Eqs.(4.2.5, 4.2.6). In this scenario, these two quantities have no dynamics at all. This is to be expected because the equations of motion do not break this symmetry unless the initial conditions do so. In this case, the first two equations simply reproduce the flavor pendulum that exhibits bipolar oscillations at a frequency $\sim \sqrt{\omega\mu}$. In addition, if the initial neutrino-antineutrino asymmetry α , defined such that $\bar{P}_z = (1 - \alpha)P_z$ is zero, the \mathbf{Q} only evolves in the x - z plane while \mathbf{D} acquires a non-zero component only along the y direction. Here we take $0 \leq \alpha \leq 1$ and $|\mathbf{P}| = 1$, corresponding to an excess of neutrinos over antineutrinos as is expected in a SN. On the other hand, if there is an excess of antineutrinos, it is more convenient to define $P_z = (1 - \bar{\alpha})\bar{P}_z$ with $0 \leq \bar{\alpha} \leq 1$ and $|\bar{\mathbf{P}}| = 1$. More complications may arise if α or $\bar{\alpha} \neq 0$, the pendulum has a spin. In the bipolar scenario, a non-zero neutrino antineutrino asymmetry induces a spin in the pendulum, making it gyrate like a top [97].

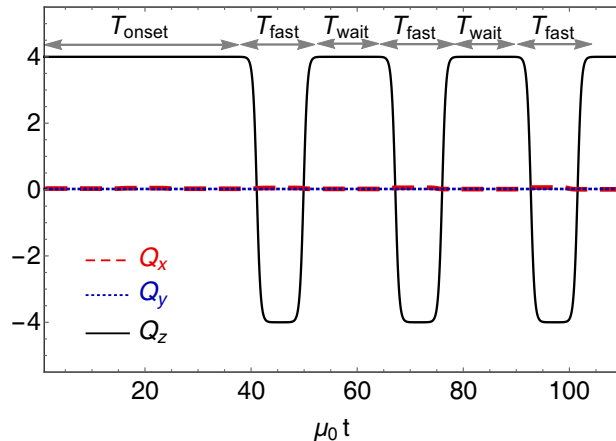


Figure 4.2: Dynamics of the components of \mathbf{Q} . The parameters are chosen to be $\omega/\mu_0 = 10^{-5}$, $\vartheta_0 = 10^{-2}$ and $c = 0.5$. Here $\mu = \mu_0 = 10^5 \text{ km}^{-1}$ is the value of μ at the neutrinosphere. T_{fast} is matched using the estimate in Eq.(4.4.2), which defines T_{onset} and T_{wait} as the periods where $Q_z \geq 0.99 Q_z(t=0)$.

4.2.2 Fast oscillations beyond the bipolar limit

It is thus clear, as was already evident through the linear analysis in [119], that one must break the $L \leftrightarrow R$ symmetry to obtain any oscillations faster than the bipolar oscillations. We will consider initial conditions on the polarization vectors to be

$$\mathbf{P}_{L,R}(0) = (0, 0, 1 \pm \epsilon), \quad (4.2.11)$$

$$\bar{\mathbf{P}}_{L,R}(0) = (0, 0, 1 - \alpha \pm \epsilon), \quad (4.2.12)$$

where ϵ is the small difference between the left and right going modes that breaks the $L \leftrightarrow R$ symmetry. This is a small arbitrary numerical seed chosen in order to break the symmetry. Throughout this chapter, we choose $\epsilon = 10^{-9}$. In general the motion is quite complicated but major simplifications happen if $\alpha = 0$. In this case, for the above initial conditions, one can verify by inspecting Eqs.(4.2.7-4.2.10), that \mathbf{Y} is in the y direction only and \mathbf{X} remains in the x - z plane. This $\alpha = 0$ limit is significantly simpler and we confine our attention to it to illustrate the physics of fast oscillations. However, as we will comment later, many of the obtained insights will be relevant more generally.

Eq.(4.2.1) implies that the magnitudes of each of the 4 polarization vectors $\mathbf{P}_{\mathbf{p}}$ remains

constant. Further, Eq.(4.2.8) provides that

$$\frac{d}{dt} \mathbf{B} \cdot \mathbf{D} = 0. \quad (4.2.13)$$

Hence $\mathbf{B} \cdot \mathbf{D}$ is a constant of motion, as in the bipolar case. This quantity is associated with the conservation of flavor lepton number [97]. Thus, flavor lepton number is conserved even for fast oscillations, as one would expect.

The length of \mathbf{Q} , unlike for bipolar oscillations, is not conserved and changes as

$$\frac{d}{dt} (\mathbf{Q} \cdot \mathbf{Q}) = \mu \frac{(1+c)}{2} [\mathbf{QXY}], \quad (4.2.14)$$

where $[\dots]$ indicates the scalar triple product of the three vectors. The evolution of the components of \mathbf{Q} is shown in Fig. 4.2. We find that the dynamics is mainly captured in Q_z , with $Q_x, Q_y \simeq 0$. Note that there are three timescales associated with the evolution of \mathbf{Q} as illustrated in the figure: T_{onset} , the onset time; T_{fast} , characterizing the time-period of fast oscillations; and T_{wait} , the waiting period in between two oscillations. We will comment more on these in later sections.

Likewise, the quantity $\mathbf{Q} \cdot \mathbf{D}$ varies as

$$\frac{d}{dt} (\mathbf{Q} \cdot \mathbf{D}) = \mu \frac{(1+c)}{2} [\mathbf{DXY}]. \quad (4.2.15)$$

If there is no initial asymmetry, i.e., $\alpha = 0$ and therefore $\mathbf{D}(0) = 0$, the R.H.S. of Eq.(4.2.15) vanishes because \mathbf{D} and $\mathbf{X} \times \mathbf{Y}$ remain orthogonal, as we argued following Eqs.(4.2.7 - 4.2.10). Then, $\mathbf{Q} \cdot \mathbf{D}$ is a constant and remains at its initial value zero. However, for $\alpha \neq 0$, i.e., a non-zero neutrino-antineutrino asymmetry, $\mathbf{Q} \cdot \mathbf{D}$ is no longer constant, unlike for the bipolar flavor pendulum [97]. While a core-collapse SN mostly has an excess of neutrinos over antineutrinos, in the recently discovered lepton-emission self-sustained asymmetry (LESA) phenomenon [76] as well as in binary neutron star mergers [187–189], there can be an excess of antineutrinos over neutrinos, leading to a non-zero value of $\bar{\alpha}$. In Fig. 4.3, we show $\mathbf{Q} \cdot \mathbf{D}$ for $\alpha = 0$ as well as for $\alpha = 0.2$ and $\bar{\alpha} = 0.2$. Defining $\bar{\alpha}$, instead of simply letting α be negative, has the advantage that $\alpha = 0.2$ and $\bar{\alpha} = 0.2$ are related to each other very simply as is apparent from Fig. 4.3. In the limit $\omega \rightarrow 0$, the replacement $\mathbf{P} \leftrightarrow \bar{\mathbf{P}}$ keeps the EoMs unchanged.

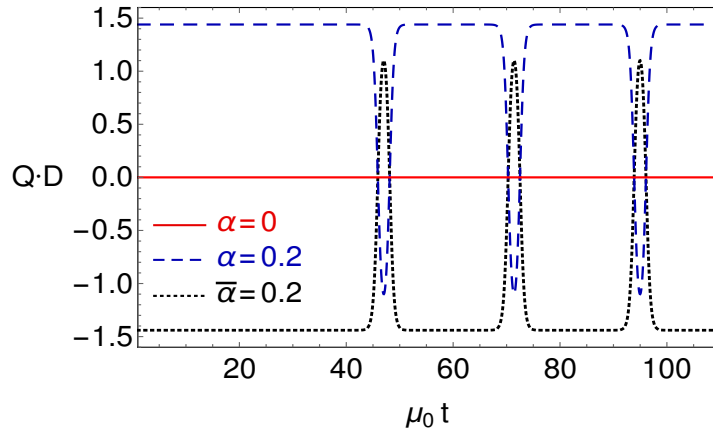


Figure 4.3: Variation of $\mathbf{Q} \cdot \mathbf{D}$ with time for neutrino-antineutrino asymmetry $\alpha = 0$ (solid red), $\alpha = 0.2$ (dashed blue) and $\bar{\alpha} = 0.2$ (dotted black).

As an immediate by-product, one can solve for \mathbf{D} starting from Eq.(4.2.7). Taking a cross product with \mathbf{Q} , one gets

$$\mathbf{D} = \frac{2}{\mu(3-c)} \frac{\mathbf{Q} \times \dot{\mathbf{Q}}}{Q^2} + \frac{\mathbf{Q} \cdot \mathbf{D}}{Q^2} \mathbf{Q} + \frac{(1+c)}{(3-c)} \frac{1}{Q^2} [(\mathbf{Q} \cdot \mathbf{X})\mathbf{Y} - (\mathbf{Q} \cdot \mathbf{Y})\mathbf{X}]. \quad (4.2.16)$$

The first two terms are identical to the \mathbf{D} for the bipolar pendulum [97]. However, note that \mathbf{Q} obeys Eq.(4.2.3), which has extra dynamics from \mathbf{X} and \mathbf{Y} . The last term is the extra one that arises due to fast oscillations. Thus, even when the last term is small, the solution for \mathbf{D} is actually different. Moreover, $\mathbf{Q} \cdot \mathbf{D}$ is not constant if $\alpha \neq 0$, and this expression for \mathbf{D} must be understood as an implicit solution.

Finally, we end this section by showing the evolution of \mathbf{X} and \mathbf{Y} , for $\alpha = 0$ in Fig.4.4. We observe that while \mathbf{X} develops only an x component dominantly and has a subleading z component, the quantity \mathbf{Y} only has a non-zero y component. This can also be inferred by inspecting the EoMs. We have checked that \mathbf{D} remains very small and is always along the y direction, and we do not show it here.

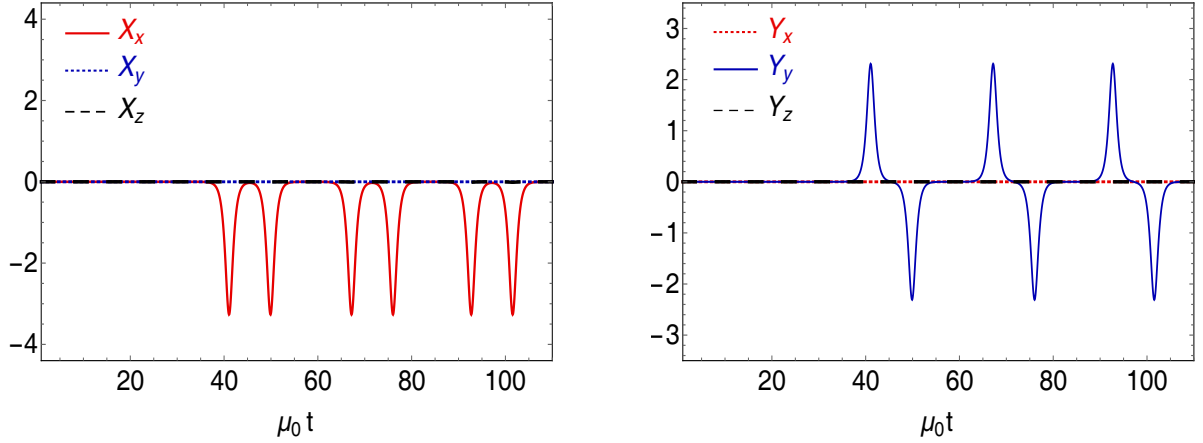


Figure 4.4: Left: Evolution of \mathbf{X} . Right: Evolution of \mathbf{Y} . The parameters used here are $\omega/\mu_0 = 10^{-5}$, $\vartheta_0 = 10^{-2}$ and $c = 0.5$.

4.3 Full EoMs for Fast Conversions

Further simplification can be obtained for Eqs. (4.2.7-4.2.10) in the limit $\omega/\mu \rightarrow 0$, where $\mathbf{D} = \text{constant}$. If in addition $\alpha = 0$, then $\mathbf{D} \sim \omega/\mu$, and can be set to zero at all times for small enough (ω/μ) . This simplifies the equations immensely, thereby giving

$$\dot{\mathbf{Q}} = \frac{\mu}{2}(1+c)\mathbf{X} \times \mathbf{Y}, \quad (4.3.1)$$

$$\dot{\mathbf{X}} = \omega \left(\frac{3+c}{3-c} \right) \mathbf{B} \times \mathbf{Y} + \mu c \mathbf{Q} \times \mathbf{Y}, \quad (4.3.2)$$

$$\dot{\mathbf{Y}} = \omega \left(\frac{2}{3-c} \right) \mathbf{B} \times \mathbf{Y} - \frac{\mu}{2}(1-c)\mathbf{Q} \times \mathbf{X}. \quad (4.3.3)$$

We have kept the terms of $\mathcal{O}(\omega/\mu)$ in Eqs. (4.3.2 - 4.3.3) to indicate the subleading corrections to $\dot{\mathbf{X}}$ and $\dot{\mathbf{Y}}$.

In the limit $\alpha = 0$, one can arrive at the the approximate second-order EoMs for \mathbf{Q} , \mathbf{X} ,

and \mathbf{Y} by taking another time-derivative of Eqs.(4.3.1 - 4.3.3),

$$\begin{aligned} \ddot{\mathbf{Q}} = & \frac{\mu}{2}(1+c) \left[\mu c \left\{ (\mathbf{Y} \cdot \mathbf{Q})\mathbf{Y} - (\mathbf{Y} \cdot \mathbf{Y})\mathbf{Q} \right\} - \frac{\mu}{2}(1-c) \left\{ (\mathbf{X} \cdot \mathbf{X})\mathbf{Q} - (\mathbf{X} \cdot \mathbf{Q})\mathbf{X} \right\} \right. \\ & \left. + \omega \left(\frac{3+c}{3-c} \right) \left\{ (\mathbf{Y} \cdot \mathbf{B})\mathbf{Y} - (\mathbf{Y} \cdot \mathbf{Y})\mathbf{B} \right\} + \omega \left(\frac{2}{3-c} \right) \left\{ (\mathbf{X} \cdot \mathbf{X})\mathbf{B} - (\mathbf{X} \cdot \mathbf{B})\mathbf{X} \right\} \right], \end{aligned} \quad (4.3.4)$$

$$\begin{aligned} \ddot{\mathbf{X}} = & \mu c \left[\frac{\mu}{2}(1+c) \left\{ (\mathbf{Y} \cdot \mathbf{X})\mathbf{Y} - (\mathbf{Y} \cdot \mathbf{Y})\mathbf{X} \right\} - \frac{\mu}{2}(1-c) \left\{ (\mathbf{Q} \cdot \mathbf{X})\mathbf{Q} - (\mathbf{Q} \cdot \mathbf{Q})\mathbf{X} \right\} \right. \\ & \left. + \omega \left(\frac{2}{3-c} \right) \left\{ (\mathbf{Q} \cdot \mathbf{X})\mathbf{B} - (\mathbf{Q} \cdot \mathbf{B})\mathbf{X} \right\} \right] + \omega \left(\frac{3+c}{3-c} \right) \mathbf{B} \times \dot{\mathbf{Y}}, \end{aligned} \quad (4.3.5)$$

$$\begin{aligned} \ddot{\mathbf{Y}} = & -\frac{\mu}{2}(1-c) \left[\frac{\mu}{2}(1+c) \left\{ (\mathbf{X} \cdot \mathbf{X})\mathbf{Y} - (\mathbf{X} \cdot \mathbf{Y})\mathbf{X} \right\} + \mu c \left\{ (\mathbf{Q} \cdot \mathbf{Y})\mathbf{Q} - (\mathbf{Q} \cdot \mathbf{Q})\mathbf{Y} \right\} \right. \\ & \left. + \omega \left(\frac{3+c}{3-c} \right) \left\{ (\mathbf{Q} \cdot \mathbf{Y})\mathbf{B} - (\mathbf{Q} \cdot \mathbf{B})\mathbf{Y} \right\} \right] + \omega \left(\frac{2}{3-c} \right) \mathbf{B} \times \dot{\mathbf{X}}. \end{aligned} \quad (4.3.6)$$

Recall that these equations are based on the assumption that \mathbf{D} is approximately constant and negligible. Also note that the apparently $\mathcal{O}(\mu^2)$ terms on the first line of the above equations contain subleading $\mathcal{O}(\omega\mu)$ terms themselves. We will find that these subleading terms become relevant while determining the onset period, as well as in the interim waiting period.

4.3.1 Conserved quantities in the limit $\omega/\mu = 0$ and $\alpha = 0$

In addition to the above conditionally but exactly conserved quantities, there are some approximately conserved quantities. Setting $\omega/\mu = 0$ simplifies Eqs. (4.3.2 - 4.3.3) to

$$\dot{\mathbf{Q}} = \frac{\mu}{2}(1+c) \mathbf{X} \times \mathbf{Y}, \quad (4.3.7)$$

$$\dot{\mathbf{X}} = \mu c \mathbf{Q} \times \mathbf{Y}, \quad (4.3.8)$$

$$\dot{\mathbf{Y}} = -\frac{\mu}{2}(1-c) \mathbf{Q} \times \mathbf{X}. \quad (4.3.9)$$

In this limit, the following quantities are found to be conserved: $\mathbf{Q} \cdot \mathbf{X}$, $\mathbf{Q} \cdot \mathbf{Y}$, and $\mathbf{X} \cdot \mathbf{Y}$, as well as $2c \mathbf{Q} \cdot \mathbf{Q} + (1+c) \mathbf{X} \cdot \mathbf{X}$ and $(1-c) \mathbf{Q} \cdot \mathbf{Q} + (1+c) \mathbf{Y} \cdot \mathbf{Y}$. These are the extra conditionally conserved quantities of this problem.

Differentiating Eq.(4.3.7), one finds

$$\ddot{\mathbf{Q}} = -\mu^2 c(1-c) \left[|\mathbf{Q}_0|^2 - \mathbf{Q} \cdot \mathbf{Q} \right] \mathbf{Q}, \quad (4.3.10)$$

which is a closed equation for \mathbf{Q} that derives from the Lagrangian

$$\mathcal{L}_{\mathbf{Q}} = \frac{1}{2} |\dot{\mathbf{Q}}|^2 - \mu^2 c(1-c) \left[|\mathbf{Q}_0|^2 - \frac{\mathbf{Q} \cdot \mathbf{Q}}{2} \right] \frac{\mathbf{Q} \cdot \mathbf{Q}}{2}, \quad (4.3.11)$$

where $|\mathbf{Q}_0|$ is the modulus of \mathbf{Q} at time $t = 0$. Using Eq.(4.3.10) one finds the total energy is

$$E = \frac{1}{2} |\dot{\mathbf{Q}}|^2 + \mu^2 c(1-c) \left[|\mathbf{Q}_0|^2 - \frac{\mathbf{Q} \cdot \mathbf{Q}}{2} \right] \frac{\mathbf{Q} \cdot \mathbf{Q}}{2}, \quad (4.3.12)$$

which is an additional constant of motion. Note that \mathbf{Q} is confined to the x - z plane when $\alpha = 0$, and Q_x can be eliminated using E , thereby reducing the problem to the study of only the z component of \mathbf{Q} to understand the flavor evolution shown in Fig.4.2. Clearly, as $Q_x \simeq \mathcal{O}(\vartheta_0)$, the energy E is dominated by Q_z .

Analogous to the closed set of equations and the Lagrangian governing \mathbf{Q} given by Eq.(4.3.10), one can find the closed equation for \mathbf{X} and \mathbf{Y} , each, by neglecting terms of order $\mathcal{O}(\omega^2)$ and $\mathcal{O}(\omega\mu)$ relative to $\mathcal{O}(\mu^2)$,

$$\ddot{\mathbf{X}} = \mu^2 \frac{c(1-c)}{2} \left[|\mathbf{Q}_0|^2 - \frac{(1+c)}{c} (\mathbf{X} \cdot \mathbf{X}) \right] \mathbf{X}, \quad (4.3.13)$$

$$\ddot{\mathbf{Y}} = \mu^2 \frac{c(1-c)}{2} \left[|\mathbf{Q}_0|^2 - 2 \frac{(1+c)}{(1-c)} (\mathbf{Y} \cdot \mathbf{Y}) \right] \mathbf{Y}. \quad (4.3.14)$$

Their corresponding Lagrangians are

$$\mathcal{L}_{\mathbf{X}} = \frac{1}{2} |\dot{\mathbf{X}}|^2 - \mu^2 \left[(1-c^2) \frac{(\mathbf{X} \cdot \mathbf{X})}{2} - \frac{c(1-c)}{2} |\mathbf{Q}_0|^2 \right] \frac{(\mathbf{X} \cdot \mathbf{X})}{2}, \quad (4.3.15)$$

$$\mathcal{L}_{\mathbf{Y}} = \frac{1}{2} |\dot{\mathbf{Y}}|^2 - \mu^2 \left[c(1+c) \frac{(\mathbf{Y} \cdot \mathbf{Y})}{2} - \frac{c(1-c)}{2} |\mathbf{Q}_0|^2 \right] \frac{(\mathbf{Y} \cdot \mathbf{Y})}{2}. \quad (4.3.16)$$

The time evolution of \mathbf{X} and \mathbf{Y} , governed by the above Lagrangians, are already shown in Fig.4.4.

Finally, note that in this $\alpha = 0$ limit, the neglect of the subleading contributions of $\mathcal{O}(\omega\mu)$ and smaller endows a spurious $\mathbf{Q} \rightarrow -\mathbf{Q}$ symmetry to Eq.(4.3.10). As a result, solving Eq.(4.3.10) leads to an evolution of \mathbf{Q} that is exactly symmetric in $Q_z \leftrightarrow -Q_z$ (the onset and waiting times are equal to the fast oscillation time). Numerically however, we find that

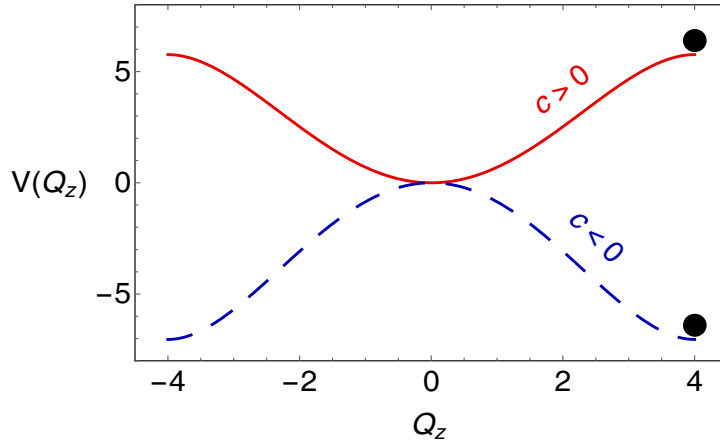


Figure 4.5: Left: The potential $V(Q_z)$ for two different values of $c = 0.1$ (solid red) and $c = -0.1$ (dashed blue).

\mathbf{Q} hovers longer around its initial position at the top, than it does at the bottom of the potential $V(\mathbf{Q})$, as seen in Fig. 4.2. We believe that this slow-down is due to the neglect of subleading friction-like terms that arise at the same order as the terms necessary to seed the fast oscillation.

4.4 Particle in a quartic potential

An interesting feature of this intersecting 4-beam system is that fast conversions exist only for certain angular distributions of the neutrino beams. Using a linear stability analysis, it was shown in [119] that fast conversions exist only for $c \equiv \cos \theta > 0$. The reason for this becomes obvious if one observes the potential term $V(Q_z)$ in $\mathcal{L}_{\mathbf{Q}}$. Classically, this relates to motion of a particle in a quartic potential given by

$$V(Q_z) \approx \mu^2 c(1-c) \left[|\mathbf{Q}_0|^2 - \frac{Q_z^2}{2} \right] \frac{Q_z^2}{2}. \quad (4.4.1)$$

As shown in Fig. 4.5, the potential is an inverted quartic for $c < 0$ and a quartic for $c > 0$. The motion of Q_z is governed by this potential. Given the initial condition $Q_z(0) = 4[1 - (\omega \cos 2\vartheta_0)/(2\mu(3-c))]$, for $c > 0$ the potential causes Q_z to roll down towards the bottom of the potential well and subsequently oscillate in it. In flavor space, these are fast conversions. On the other hand, for $c < 0$ a potential barrier is encountered by Q_z . The value of Q_z therefore remains at its initial value and there are no fast conversions. Note that

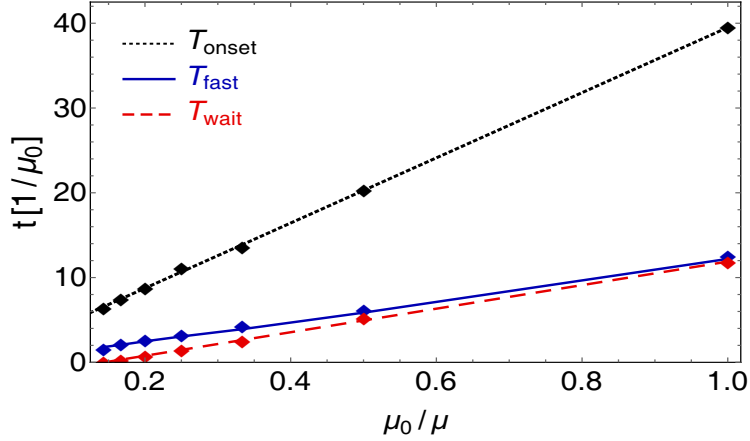


Figure 4.6: Time periods T_{onset} , T_{fast} and T_{wait} and their linear dependence on $1/\mu$. Dots show the numerical data whereas the lines are the best fit through them. While the fit for T_{fast} is given from Eq.(4.4.2), those for T_{onset} and T_{wait} are obtained numerically.

the above initial condition for Q_z is for the inverted mass ordering, where $\omega < 0$. For normal mass ordering, the same initial condition holds with the replacement $\omega \rightarrow -\omega$. However, fast conversions are essentially independent of the mass ordering. In fact, although the triggering of fast conversions is dependent on ω , it does not seem to depend on the sign of ω .

In order to verify whether the above analytical approximations explain the evolution of \mathbf{Q} , we numerically solved Eqs.(4.2.7-4.2.10) and compared with the numerical solution of Eq.(4.3.10). As mentioned before, from the time evolution of \mathbf{Q} shown in Fig.4.2, one observes that there are three timescales: T_{onset} , the onset time; T_{fast} , characterizing the time-period of fast oscillations; and T_{wait} , the waiting period in between two oscillations. We do not expect Eq.(4.3.10) to give the correct solution at initial times up to T_{onset} and in between the oscillations for the periods designated T_{wait} as these are dependent on the subleading terms, which have been dropped in Eq.(4.3.10). To determine these periods numerically, we have considered $Q_z \gtrsim 0.99 Q_z(t=0)$ so that the R.H.S. of Eq.(4.3.10) is very small, i.e., $\lesssim \mathcal{O}(\omega/\mu) = 10^{-5}$. Thus the flavor evolution is governed by the ω -dependent and otherwise sub-dominant terms which we have ignored. On the other hand, in this regime, the solution is already very well understood using linear stability analysis. More interestingly, the evolution of Q_z is very well explained using Eq.(4.3.10) when it is strongly nonlinear, i.e., deviates appreciably from its initial value.

One can compute the time-period of the fast oscillations, T_{fast} , using energy conservation,

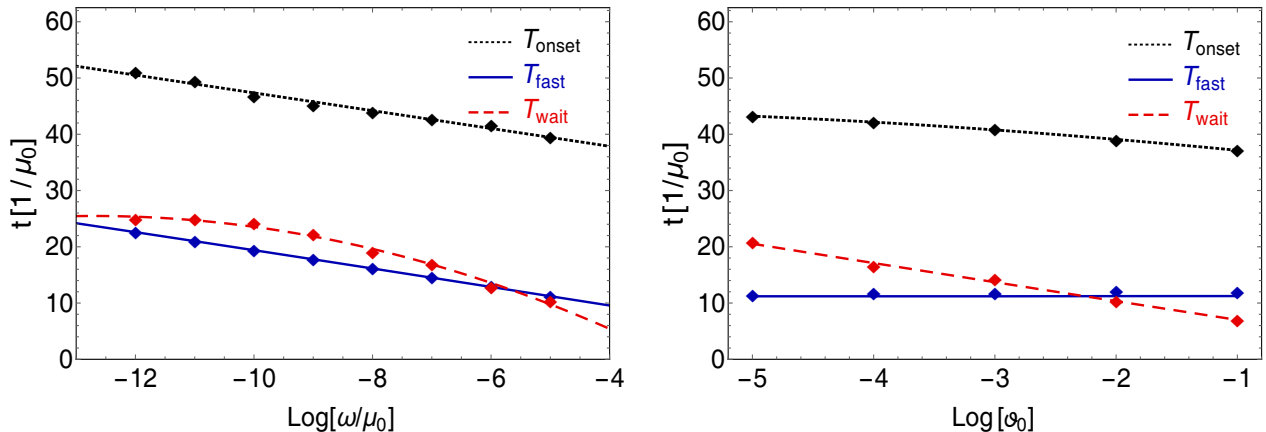


Figure 4.7: Variation of the time periods T_{onset} , T_{fast} and T_{wait} . Dots show the the data generated from simulations whereas the lines are the best fit curves through them. Here $\mu_0 = 10^5 \text{ km}^{-1}$. Left: Variation with ω/μ_0 , for $\mu/\mu_0 = 1$ and $\vartheta_0 = 10^{-2}$. Right: Variation with ϑ_0 , for $\omega/\mu_0 = 10^{-5}$ and $\mu/\mu_0 = 1$.

to get

$$T_{\text{fast}} = 2 \int_{Q_z^{\text{max}}}^{Q_z^{\text{min}}} \frac{dQ_z}{\sqrt{2(E - V(Q_z))}}. \quad (4.4.2)$$

This integral is in fact analytically expressible in terms of an elliptic function. Evaluating the same, we find that it matches quite well with the numerical results shown in Fig. 4.6, if we consider $Q_z^{\text{max}} \approx 0.99 Q_z(t = 0)$. The blue dots represent the fast time-period (excluding the onset and waiting times, as previously noted) obtained from numerical solution of Eqs.(4.2.7-4.2.10), whereas the solid blue line is obtained by evaluating the integral in Eq.(4.4.2).

Similar to how the onset period for the bipolar flavor pendulum depends on ϑ_0 , the time-scales for the fast oscillation, i.e., T_{onset} , T_{fast} , as well as T_{wait} , depend logarithmically on these subleading parameters that seed the oscillations. In Fig. 4.7, we show the variation of T_{onset} , T_{fast} and T_{wait} with ω/μ_0 and ϑ_0 , respectively, where $\mu_0 = 10^5 \text{ km}^{-1}$ is the value of μ at the neutrinosphere. Clearly the time periods vary as μ^{-1} as shown in Fig. 4.6, but with logarithmic corrections proportional to (ω/μ_0) and ϑ_0 .

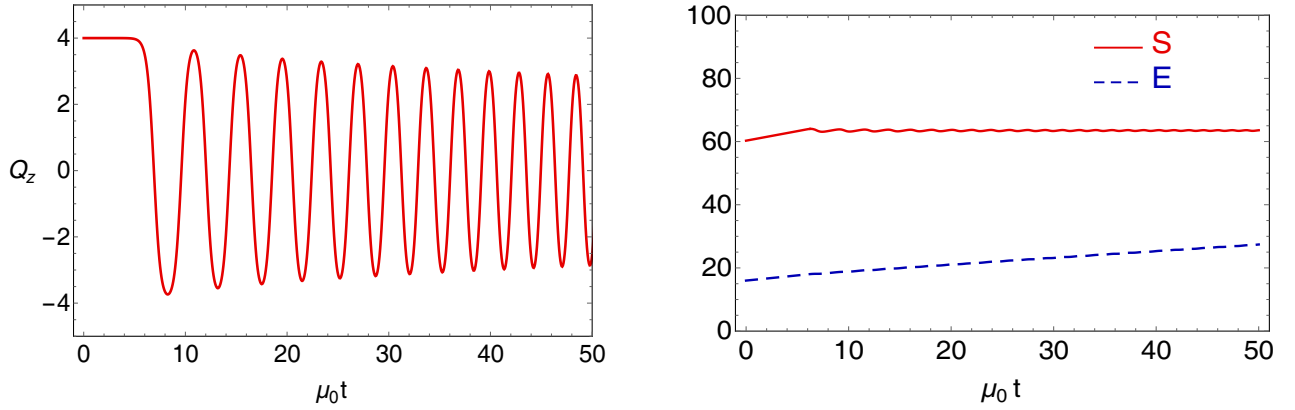


Figure 4.8: Left: Variation of Q_z for a time-varying neutrino-neutrino potential given by $\mu(t) = \mu_0(1 + t/100)$. Right: Plot of the action S and the energy $E(t)$. Note how the energy changes, but action remains constant.

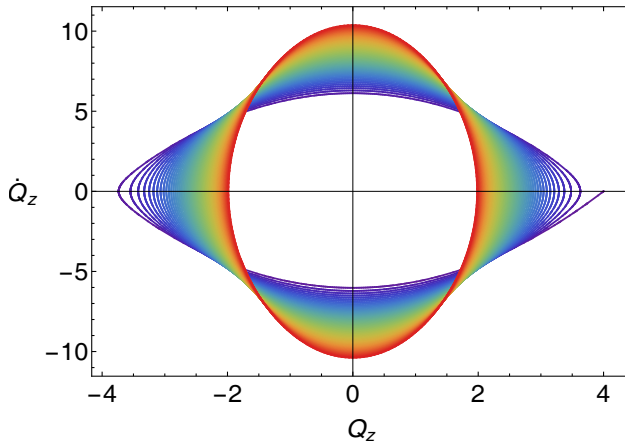


Figure 4.9: Trajectory in phase space for varying μ . Redder colors refer to later times and larger μ .

4.5 Varying neutrino density

In this section, we briefly discuss what happens if μ is not a constant, but rather varies with time as $\mu(t)$. One expects that if $\mu(t)$ is time-dependent, the energy $E(t)$ also becomes time-dependent. Naturally, the time period T_{fast} also changes with time. In Fig. 4.8, we show the evolution of Q_z (left panel) for a time-dependent neutrino potential $\mu(t) = \mu_0(1 + t/100)$.

While this is in general a much more complicated problem, if the rate of change of $\mu(t)$ is much smaller than the frequency of fast oscillations (as chosen above) one can use adiabatic invariance to derive some simple results. In the adiabatic limit, the action variable of the

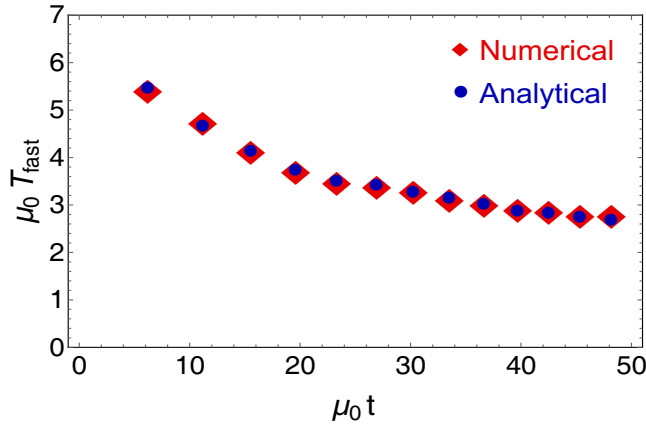


Figure 4.10: Variation of T_{fast} with time.

system

$$S(E, \mu) = \oint p_Q dQ_z = \oint \sqrt{2(E - V(Q_z))} dQ_z, \quad (4.5.1)$$

remains invariant to a good approximation. Here the generalized momentum for the system is $p_Q = \dot{Q}_z$, neglecting $Q_x \simeq 0$. This action $S(E(t), \mu(t))$ remains invariant under adiabatic changes in $\mu(t)$ while energy changes appreciably, as shown in the right panel of Fig. 4.8.

In Fig. 4.9, we show the phase trajectory for the time-varying $\mu(t)$ above. As $\mu(t)$ increases with time, the potential becomes deeper and the oscillation amplitude decreases but the energy increases; the closed trajectory in phase space becomes more oblong along momentum, keeping the enclosed area constant.

It is possible to analytically perform the integral in Eq.(4.5.1), giving a closed expression for the adiabatic invariant S in terms of $E(t)$ and $\mu(t)$. One can then compute an analytical expression for the time-dependent time-period $T_{\text{fast}}(t)$, using

$$T_{\text{fast}}(t) = \frac{\partial}{\partial E} S(E, \mu(t)). \quad (4.5.2)$$

. In Fig. 4.10, we show the time period computed analytically in this manner (blue dots), compared with the same measured from the numerical solutions of the EoMs (red dots). This is based on a single calibration between our analytical estimate of T_{fast} and the numerics that we used to identify $Q_z^{\text{max}} = 0.99 Q_z(t = 0)$ as the boundary where the slower terms become dominant. Subsequently, this agreement at different and changing μ highlights that the agreement is not superfluous or accidental.

The other two time scales, T_{onset} and T_{wait} , are somewhat harder to estimate. We have checked numerically that all of them vary as $1/\mu$, as seen in Fig. 4.6. In addition, we find that T_{onset} depends logarithmically on the “seed” given in Eq.(4.2.7). Solving Eq.(4.3.10) for Q_z , and determining T_{onset} by checking for small deviations of Q_z from its initial value gives,

$$T_{\text{onset}} \propto \frac{1}{\mu\sqrt{2c(1-c)}} \ln \left[\frac{(3-c)\mu_0}{\cos 2\vartheta_0 \omega} \right], \quad (4.5.3)$$

which underestimates T_{onset} by approximately a factor of 2, relative to the numerical value seen in Fig. 4.2. For T_{wait} as well, we find numerically that it depends logarithmically on ϑ_0 and ω , as demonstrated in the previous section.

4.6 Asymmetric fast oscillations

We now turn to the case when the initial neutrino-antineutrino asymmetry is nonzero, i.e., $\alpha \neq 0$. As seen in Sec. 4.3, we notice that one can essentially treat \mathbf{D} as a constant vector in the limit $\omega/\mu \rightarrow 0$. Thus, in Eq.(4.2.7), \mathbf{Q} acquires an extra precession around the \mathbf{D} vector. This precession is essentially around the z axis, and now allows the y component of \mathbf{Q} to evolve as well. The vectors \mathbf{X} and \mathbf{Y} also acquire similar precessions around \mathbf{D} , but each with a different precession frequency. As these frequencies are not all identical, there is no “co-rotating” frame where all the effects of these additional precessions can be completely removed.

Taking a derivative of Eq.(4.2.7), one gets

$$\begin{aligned} \ddot{\mathbf{Q}} = & -\mu^2 c(1-c) \left[|\mathbf{Q}_0|^2 - \mathbf{Q} \cdot \mathbf{Q} \right] \mathbf{Q} + \frac{\mu}{2}(3-c) \mathbf{D} \times \dot{\mathbf{Q}} \\ & + \frac{\mu^2}{2}(1+c) \left[(\mathbf{D} \times \mathbf{X}) \times \mathbf{Y} + \frac{3+c}{2} \mathbf{X} \times (\mathbf{D} \times \mathbf{Y}) \right]. \end{aligned} \quad (4.6.1)$$

The $\mathbf{D} \times \dot{\mathbf{Q}}$ term on the first line represents the action of a approximately constant magnetic field $\mathbf{D} \approx (0, 0, 2\alpha)$ in the z direction. The terms on the second line are approximately equal to $(\mathbf{X} \cdot \mathbf{Y})\mathbf{D}$, which act like a time-varying electric field in the z direction. We may interpret the situation as follows. For $\alpha = 0$, the Q_z already hovers close to its minimum around -4 , but $|\mathbf{Q}|$ is constrained to be ≤ 4 . Now, with $\alpha \neq 0$, the only possible effect of these new terms can be that Q_z becomes larger close to its minimum. This is exactly what is seen in

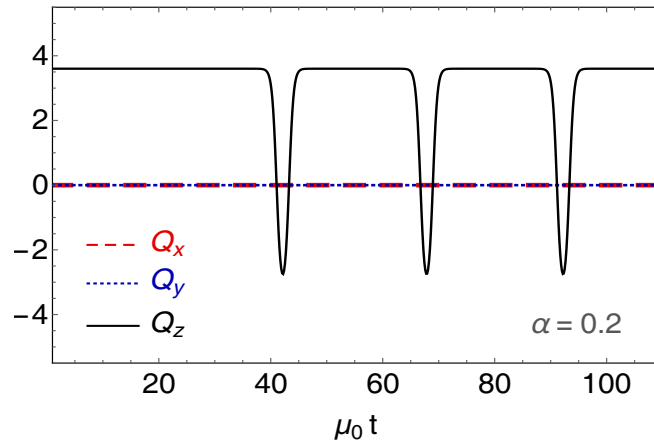


Figure 4.11: Dynamics of the components of \mathbf{Q} for a neutrino-antineutrino asymmetry $\alpha = 0.2$. The parameters are chosen to be $\omega/\mu_0 = 10^{-5}$, $\vartheta_0 = 10^{-2}$ and $c = 0.5$.

Fig. 4.11; the dips become less deep and are sharper. Essentially, these electric and magnetic fields push the particle away from the minimum of the potential well.

4.7 Summarized Results

In this chapter, we have studied the simplest toy model of a homogeneous system of neutrinos and antineutrinos that shows fast conversions. We have found that, in the limit that the vacuum oscillation frequency ω is much smaller than the neutrino potential μ and there is no net neutrino-antineutrino asymmetry, the system is described by a particle moving in a quartic potential. Most importantly, the potential offers a barrier as opposed to a well, if the angle of intersection of the beams is larger than $\pi/2$, which explains the dependence of fast conversions on the angular distribution of the beams. Onset of fast conversions corresponds to the particle rolling down the potential, thereby causing an instability. Using the action variable and its adiabatic invariance, we have estimated the time-period of fast oscillation, both when μ is constant and when $\mu(t)$ varies with time. We have given numerical and semi-analytical evidence that the onset and waiting periods for the fast oscillations depend logarithmically on ϑ_0 and $\mathcal{O}(\omega/\mu)$. Finally, we have argued how our results generalize to a situation when the number of neutrinos and antineutrinos is not equal. In this case, the evolution may be interpreted as the motion of a particle in an external electric and magnetic field. Thus, under certain approximations, this simple classical mechanical problem can be

solved exactly.

The results in this chapter provide some useful insight of the flavor dynamics associated with fast oscillations, that has so far only been understood in the linear regime or explored numerically. Hopefully, these insights will be useful to understand the physics of fast oscillations in more realistic models of neutrino flavor conversions in core collapse supernovae.

Chapter 5

Non-standard neutrino self-interactions (NSSI) and collective oscillations

The analyses presented in the last two chapters have been performed within the context of the standard model (SM). However, extensions to the SM can give rise to new effective self-interactions of neutrinos. The presence of these non-standard self-interactions (NSSI) makes us reconsider many of the results of flavor evolutions of dense neutrino streams, which were calculated assuming standard interactions. In this chapter, we study the new effects of collective bipolar oscillations arising due to the presence of NSSI of neutrinos. We set up the formalism and analyze the evolution for a system of ν and $\bar{\nu}$ in the presence of NSSI. We highlight the presence of novel spectral splits during neutronization epoch as a result of NSSI, and its observable signatures in a liquid Argon detector. ¹

5.1 Introduction

We focus on NSSI that can be modeled by an effective four-Fermi operator of the form $G_F (G^{\alpha\beta} \bar{\nu}_{L\alpha} \gamma^\mu \nu_{L\beta}) (G^{\zeta\eta} \bar{\nu}_{L\zeta} \gamma_\mu \nu_{L\eta})$, where the coupling matrix G contains both standard

¹The results in this chapter are based on the paper: A. Das, A. Dighe and M. Sen, “ *New effects of non-standard self-interactions of neutrinos in a supernova*”, Journal of Cosmology and Astrophysics 1705 (2017) no.05, 051 [arXiv:1705.00468[hep-ph]].

and non-standard components [130]. When $\alpha = \beta$, the coupling $G^{\alpha\beta}$ is flavor-preserving and we call such interactions as flavor-preserving NSSI (FP-NSSI). Similarly, when $\alpha \neq \beta$, then $G^{\alpha\beta}$ would be flavor-violating and we refer to such interactions flavor-violating NSSI (FV-NSSI). Such NSSI of neutrinos within a core-collapse SN can have observable consequences on collective oscillations and thus are very important to analyze.

The framework for analyzing the effect of NSSI on collective oscillations was first developed in [130], which showed that FV-NSSI can cause complete flavor conversions even in the absence of any mixing. Motivated by this observation, we perform a detailed study of the effect of NSSI on supernova neutrino flavor evolution. We find that the presence of NSSI can change many of the earlier results significantly. We briefly outline these ideas below, before going into a more rigorous analysis in the following sections.

- It is well-known from previous literature that in a completely azimuthally symmetric ensemble of neutrinos and antineutrinos of a single energy, flavor conversions happen only in the inverted mass hierarchy (IH). In the case of the normal mass hierarchy (NH), only a breaking of these azimuthal symmetries can lead to conversions [114].

We will find that the presence of NSSI couplings can lead to conversions even in NH, without the need to break any of the symmetries of the initial setup. However, this will need couplings larger than the SM couplings. In the flavor-pendulum language discussed in 2.3.1, the NSSI act like an external force which can overturn the stable position of the pendulum, thereby making it unstable. Thus with a large enough NSSI, an NH scenario can mimic a standard IH scenario, and vice versa.

- Collective oscillations are known to conserve flavor lepton number, i.e., they always cause the pairwise conversions $\nu_e, \bar{\nu}_e \leftrightarrow \nu_x, \bar{\nu}_x$, where $x = \mu, \tau$ or any linear combination of both (see Chapter 1). This leads to spectral swaps developing around the zero crossing of the difference in neutrino spectra g_ω , which is defined as [106]:

$$\begin{aligned} g_\omega &\propto F_{\nu_e}(\omega) - F_{\nu_x}(\omega) && \text{for } \omega > 0, \\ &\propto F_{\bar{\nu}_x}(\omega) - F_{\bar{\nu}_e}(\omega) && \text{for } \omega < 0. \end{aligned} \quad (5.1.1)$$

We will find that FV-NSSI violates flavor lepton number, which may cause the swap to develop away from the zero crossing of the g_ω spectra. A spectral crossing is then no longer necessary for the development of swaps. This could give rise to collective

oscillations *during* the neutronization epoch, which are absent otherwise. Distinct observable splits in the neutrino spectra during this epoch can then be a signal of NSSI.

We expand on these ideas in the following sections.

5.2 Flavor evolution in presence of NSSI

We consider a two-flavor setup, consisting of ν_e and ν_x in the presence of NSSI. We first write down the entire formalism in terms of the occupation number matrices as illustrated in 2.2:

$$\partial_t \varrho_{\mathbf{p}} + \mathbf{v}_{\mathbf{p}} \cdot \nabla_{\mathbf{x}} \varrho_{\mathbf{p}} = -i[\mathcal{H}_{\mathbf{p}}, \varrho_{\mathbf{p}}] . \quad (5.2.1)$$

where the Hamiltonian matrix $\mathcal{H}_{\mathbf{p}}$,

$$\mathcal{H}_{\mathbf{p}} = \mathcal{H}_{\mathbf{p}}^{\text{vac}} + \mathcal{H}^{\text{MSW}} + \mathcal{H}_{\mathbf{p}}^{\nu\nu} , \quad (5.2.2)$$

contains the vacuum, matter and self-interaction terms. While the \mathcal{H}^{vac} and \mathcal{H}^{MSW} are the same as before, the $\mathcal{H}_{\nu\nu}$ get additional contributions due to the non-standard self-interactions. The most general form of the effective Hamiltonian due to self interactions is given by

$$\mathcal{H}_{\mathbf{p}}^{\nu\nu} = \sqrt{2}G_F \int \frac{d^3\mathbf{q}}{(2\pi)^3} (1 - \mathbf{v}_{\mathbf{p}} \cdot \mathbf{v}_{\mathbf{q}}) \{G(\varrho_{\mathbf{q}} - \bar{\varrho}_{\mathbf{q}})G + G \text{Tr}[(\varrho_{\mathbf{q}} - \bar{\varrho}_{\mathbf{q}})G]\} , \quad (5.2.3)$$

where the term $(1 - \mathbf{v}_{\mathbf{p}} \cdot \mathbf{v}_{\mathbf{q}})$ leads to multi-angle effects due to neutrinos moving on different trajectories. In the SM, the dimensionless coupling matrix G is an identity matrix. After including NSSI, the most general coupling matrix is given by

$$G = \begin{bmatrix} 1 + \gamma_{ee} & \gamma_{ex} \\ \gamma_{ex}^* & 1 + \gamma_{xx} \end{bmatrix} . \quad (5.2.4)$$

The bounds on $\gamma_{\alpha\beta}$ are very weak since processes involving neutrino self-interactions are rare and difficult to observe. Loose bounds on these four-neutrino contact interactions can be put from low-energy π^+ , K^+ decays [190] and from SN1987A data [191]. However, much stronger constraints on neutrino NSSI come from LEP data. The presence of non-standard neutrino coupling can give rise to a new decay channel $Z \rightarrow \nu\bar{\nu} \rightarrow \nu\bar{\nu}\nu\bar{\nu}$, which modifies

the invisible Z -width predicted by the SM [126]. Alternatively, such new interactions can contribute to loop corrections in a SM process, for example, in the $Z \rightarrow \nu\nu$ decay channel. The invisible Z -width is measured with an accuracy better than 1% and this can put more stringent bounds on the coupling [127, 129, 192]. Assuming the NSSI are due to the presence of a new gauge boson, these bounds directly translate into $|\gamma_{ee}|$, $|\gamma_{xx}|$ and $|\gamma_{ex}| \sim \mathcal{O}(1)$. Stronger bounds can come from primordial nucleosynthesis, however one needs to assume the presence of right-handed neutrinos [128]. Note that stringent bounds can be imposed on neutrino NSSI from $SU(2)_L$ gauge invariance [193]. However, these can be evaded in certain models, where active neutrinos mix with new Dirac fermions charged under a $U(1)'$ gauge group [194]. In this thesis, the couplings are restricted to $\mathcal{O}(0.01 - 0.1)$.

The coupling matrix G , being a 2×2 matrix, can be represented in the Pauli basis as

$$G = \frac{1}{2} (g_0 \mathbb{I} + \mathbf{g} \cdot \boldsymbol{\sigma}) . \quad (5.2.5)$$

The four-vector $g = \{g_0, \mathbf{g}\}$ is a measure of the net neutrino-neutrino coupling. The SM corresponds to $g_0 = 2$ and $|\mathbf{g}| = 0$. Thus, the vector \mathbf{g} indicates the strength of NSSI. Clearly, $g_0 = 2 + \gamma_{ee} + \gamma_{xx}$, $g_1 = 2 \operatorname{Re}(\gamma_{ex})$, $g_2 = 2 \operatorname{Im}(\gamma_{ex}^*)$ and $g_3 = \gamma_{ee} - \gamma_{xx}$. Thus, g_0 and g_3 are flavor-preserving NSSI (FP-NSSI) couplings while g_1 and g_2 are flavor-violating NSSI (FV-NSSI) couplings. Note that we can redefine the phase of ν_x such that $g_2 = 0$. The NSSI can thus be parameterized by g_0 , g_1 and g_3 .

There, using the polarization vector language, the EoMs take the form

$$\begin{aligned} \dot{\mathbf{P}}_{\mathbf{p}} &= (\omega_{\mathbf{p}} \mathbf{B} + \lambda \mathbf{L} + \mathcal{H}_{\mathbf{p}}^{\nu\nu}) \times \mathbf{P}_{\mathbf{p}}, \\ \dot{\bar{\mathbf{P}}}_{\mathbf{p}} &= (-\omega_{\mathbf{p}} \mathbf{B} + \lambda \mathbf{L} + \mathcal{H}_{\mathbf{p}}^{\nu\nu}) \times \bar{\mathbf{P}}_{\mathbf{p}}, \end{aligned} \quad (5.2.6)$$

where

$$\mathcal{H}_{\mathbf{p}}^{\nu\nu} = \mu \int \frac{d^3 \mathbf{q}}{(2\pi)^3} (1 - \mathbf{v}_{\mathbf{p}} \cdot \mathbf{v}_{\mathbf{q}}) \left\{ \frac{1}{4} (g_0^2 - |\mathbf{g}|^2) (\mathbf{P}_{\mathbf{q}} - \bar{\mathbf{P}}_{\mathbf{q}}) + [g_0 \boldsymbol{\xi} + \mathbf{g} \cdot (\mathbf{P}_{\mathbf{q}} - \bar{\mathbf{P}}_{\mathbf{q}})] \mathbf{g} \right\} . \quad (5.2.7)$$

and the other parameters are as described in 2.2.1. The variable ξ parameterizes the neutrino-antineutrino asymmetry such that $n_{\nu} = (1 + \xi)n_{\bar{\nu}}$. We further note that the parameter g_0 can be scaled away by the following redefinition in Eq. (5.2.7) :

$$\mu \rightarrow \mu (g_0/2)^2, \quad \mathbf{g} \rightarrow \mathbf{g} / (g_0/2). \quad (5.2.8)$$

This yields

$$\mathcal{H}_{\mathbf{p}}^{\nu\nu} = \mu \int \frac{d^3\mathbf{q}}{(2\pi)^3} (1 - \mathbf{v}_{\mathbf{p}} \cdot \mathbf{v}_{\mathbf{q}}) \left\{ \left(1 - \frac{|\mathbf{g}|^2}{4} \right) (\mathbf{P}_{\mathbf{q}} - \bar{\mathbf{P}}_{\mathbf{q}}) + [2\xi + \mathbf{g} \cdot (\mathbf{P}_{\mathbf{q}} - \bar{\mathbf{P}}_{\mathbf{q}})] \mathbf{g} \right\}. \quad (5.2.9)$$

Henceforth, we will work in terms of the rescaled \mathbf{g} and $\mathcal{H}_{\mathbf{p}}^{\nu\nu}$.

It is interesting to note that $\mathcal{H}_{\mathbf{p}}^{\nu\nu}$ in Eq. (5.2.9) has two types of terms: the first one is the SM neutrino-neutrino interaction term modified due to $|\mathbf{g}|$. If this were the only term present, the EoMs would represent a precessing top with a modified μ given by $\mu \rightarrow \mu(1 - |\mathbf{g}|^2/4)$. However, there is a subtle difference. The modified μ term can now change sign depending on the value of $|\mathbf{g}|$ and affect the motion of the top. The second term gives rise to a term of the form $\chi(t)\mathbf{g} \times \mathbf{P}$ (for neutrinos) or $\chi(t)\mathbf{g} \times \bar{\mathbf{P}}$ (for antineutrinos) in the EoMs [Eq. (5.2.6)]. It represents the equation of a precessing top around the direction \mathbf{g} with a time-dependent frequency $\chi(t)$. This allows us to interpret the NSSI vector as an external force on the precessing top.

In the further analysis, we work with a single-angle approximation, where the problem has a azimuthal symmetry and all neutrinos are emitted with the same ‘‘emission angle’’ [91]. As explained in 2.2, in this scenario the factor of $(1 - \mathbf{v}_{\mathbf{p}} \cdot \mathbf{v}_{\mathbf{q}})$ drops out of the integral.

5.2.1 The flavor pendulum

To understand the flavor evolution more clearly, we follow the analysis in [97], and rewrite our EoMs for a single momentum mode \mathbf{p} in terms of the new vectors $\mathbf{D} \equiv \mathbf{P} - \bar{\mathbf{P}}$, $\mathbf{S} \equiv \mathbf{P} + \bar{\mathbf{P}}$. The EoMs are exactly identical with

$$\mu \rightarrow \tilde{\mu} \equiv \mu(1 - |\mathbf{g}|^2/4), \quad \lambda\mathbf{L} \rightarrow \tilde{\lambda}\tilde{\mathbf{L}} \equiv \lambda\mathbf{L} + \mu(2\xi + \mathbf{D} \cdot \mathbf{g})\mathbf{g}, \quad (5.2.10)$$

where the vector $\tilde{\mathbf{L}}$ is defined such that it is normalized to unity. In terms of the vector

$$\mathbf{Q} \equiv \mathbf{S} - (\omega/\tilde{\mu})\mathbf{B} \quad (5.2.11)$$

the EoMs are

$$\begin{aligned} \dot{\mathbf{Q}} &= \tilde{\mu}\mathbf{D} \times \mathbf{Q} + \tilde{\lambda}\tilde{\mathbf{L}} \times \mathbf{S} \\ \dot{\mathbf{D}} &= \omega\mathbf{B} \times \mathbf{Q} + \tilde{\lambda}\tilde{\mathbf{L}} \times \mathbf{D}. \end{aligned} \quad (5.2.12)$$

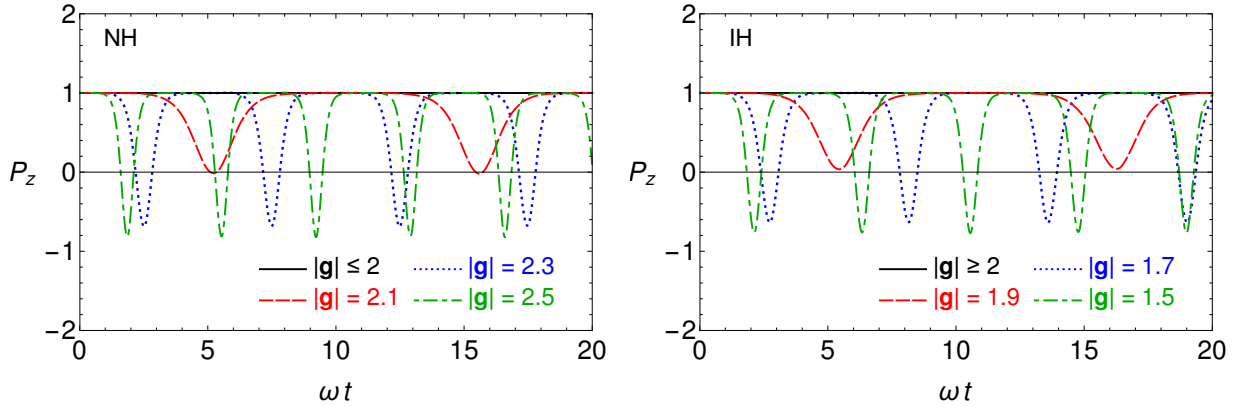


Figure 5.1: Time evolution of P_z and \bar{P}_z for four different values of $|\mathbf{g}|$, for NH (left) and IH (right). The other parameters are $\mu = 10\omega$, $\lambda = 0$, and $\vartheta_0 = 0.01$.

We observe that in the scenario $\tilde{\lambda} = 0$, $|\mathbf{Q}|$ is conserved. Thus \mathbf{Q} describes a spherical pendulum in the flavor space with length $|\mathbf{Q}|$, as in [97]. In the next sections, we study the motion of this pendulum for a constant as well as a realistic, decreasing neutrino density profile.

5.2.2 Constant neutrino-neutrino potential

5.2.2.1 Time evolution for a small mixing angle

In this section, we confine ourselves to a fixed neutrino density and study the flavor evolution of the system. In Fig. 5.1, we show the variation of P_z , i.e., z -component of the polarization vector \mathbf{P} , with time for three different values of $|\mathbf{g}|$. We consider zero asymmetry and for simplicity, put $g_1, g_2 = 0$, hence $|\mathbf{g}| = g_3$. Note that $\mathbf{D} \cdot \mathbf{g} = D_z g_3$ is almost conserved in this case, as the mixing angle ϑ_0 is small. Since $D_z(0) = 0$, we have $\mathbf{D} \cdot \mathbf{g} \simeq 0$ and hence $\tilde{\lambda} \simeq \lambda$. We choose the matter potential $\lambda = 0$ to start with.

In NH, there is no instability in the SM, i.e., $|\mathbf{g}| = 0$, since this is similar to a normal pendulum. With NSSI, since $\xi = 0$ and $\mathbf{D} \cdot \mathbf{g} \simeq 0$, the second term in Eq. (5.2.9) vanishes and μ is simply modified to $\tilde{\mu}$. The stability of the pendulum holds for $|\mathbf{g}| \leq 2$. However, if $|\mathbf{g}| > 2$, i.e., when the sign of $\tilde{\mu}$ reverses, collective oscillations start taking place. This can be clearly seen in the left panel of Fig. 5.1. As $|\mathbf{g}|$ is increased further, the frequency of collective oscillations also increases. The results in IH are complementary; for $0 \leq |\mathbf{g}| \leq 2$,

we observe an instability, whereas for $|\mathbf{g}| > 2$, the instability vanishes (Fig. 5.1, right panel).

In the absence of λ , Eq. (5.2.12) becomes,

$$\begin{aligned}\dot{\mathbf{Q}} &= \tilde{\mu} \mathbf{D} \times \mathbf{Q} \\ \dot{\mathbf{D}} &= \omega \mathbf{B} \times \mathbf{Q}.\end{aligned}\tag{5.2.13}$$

Clearly $\mathbf{B} \cdot \mathbf{D}$ is conserved. Moreover, with initial conditions $\mathbf{P}(0) = \bar{\mathbf{P}}(0) = (0, 0, 1)$, the scenario is equivalent to that of a pendulum whose oscillations are confined to a plane defined by \mathbf{B} and z -axis. In terms of $\mathbf{Q} = |\mathbf{Q}| (\sin \varphi, 0, \cos \varphi)$, we have

$$\ddot{\varphi} = -\omega \tilde{\mu} |\mathbf{Q}| \sin(\varphi + 2\vartheta_0).\tag{5.2.14}$$

For small ϑ_0 and φ , Eq. (5.2.14) corresponds to a harmonic oscillator for $\omega \tilde{\mu} > 0$ and an inverted pendulum for $\omega \tilde{\mu} < 0$. This is the reason why we observe collective oscillations in NH for $|\mathbf{g}| > 2$ when the sign of $\omega \tilde{\mu}$ becomes negative and we enter the inverted pendulum phase. Note that here the NSSI themselves have made the pendulum unstable, without breaking the spherical symmetry of the system. On the other hand, in IH, when $|\mathbf{g}| > 2$, the sign of $\omega \tilde{\mu}$ becomes positive and collective oscillations are suppressed.

Using the initial conditions $\varphi(0) \simeq -(\omega/\tilde{\mu}|\mathbf{Q}|) 2\vartheta_0$ and $\dot{\varphi}(0) = 0$, the solution to the above inverted pendulum ($\omega \tilde{\mu} < 0$) for small ϑ_0 and φ is

$$\varphi(t) = 2\vartheta_0 \left[1 - \left(1 + \frac{\omega}{\tilde{\mu}|\mathbf{Q}|} \right) \cosh \left(\sqrt{|\omega \tilde{\mu} \mathbf{Q}|} t \right) \right].\tag{5.2.15}$$

During the pendular oscillations, the time taken for $\varphi(t)$ to become of order unity is then

$$\tau \simeq \left| \frac{1}{|\omega \tilde{\mu} \mathbf{Q}|} \ln \left[\vartheta_0 \left(1 + \frac{\omega}{\tilde{\mu}|\mathbf{Q}|} \right) \right] \right|.\tag{5.2.16}$$

Thus, the frequency of collective oscillations is larger when $\omega \tilde{\mu}$ becomes more negative. This corresponds to $|\mathbf{g}|$ increasing beyond 2 in NH and $|\mathbf{g}|$ decreasing below 2 in IH, as observed in Fig. 5.1.

Now that we have demonstrated that instabilities in NH for $|\mathbf{g}| > 2$ are similar to IH for $|\mathbf{g}| < 2$, for further analysis we will confine ourselves to the scenario with IH and $|\mathbf{g}| < 2$.

Next we will show the effect of a non-zero $\tilde{\lambda} = \lambda$. This term is identical for both neutrinos and antineutrinos, and hence can be rotated away in a co-rotating frame, in the single-angle

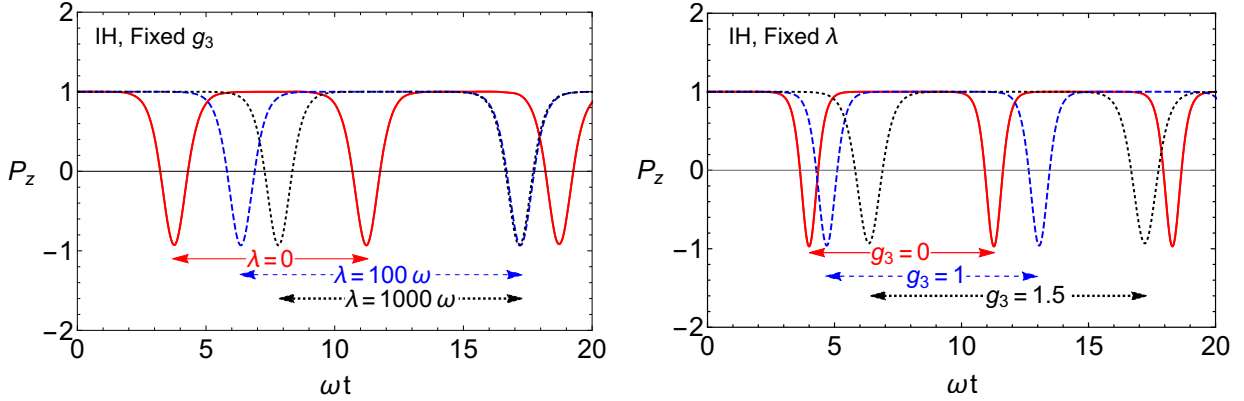


Figure 5.2: Left: Time evolution of P_z in IH with three different values of $\lambda = 0, 100\omega, 1000\omega$ for $g_3 = 1.5$. Right: Time evolution of P_z in IH with three different values of $g_3 = 0, 1, 1.5$ for $\lambda = 100\omega$.

approximation, as shown in [97]. Now $\mathbf{B} \cdot \mathbf{D}$ and $|\mathbf{Q}|$ are not exactly conserved, but exhibit fluctuations with a frequency of λ . These can average out to zero for large λ . We plot the time evolution of P_z with finite matter effect in Fig. 5.2 (left panel). It can be seen that the presence of matter effects does not change the qualitative nature of the plots, however, the value of τ increases with λ as has already been noticed [97]. The right panel of Fig. 5.2 shows the effect of changing g_3 in presence of a fixed matter density λ . We observe that changing g_3 also gives qualitatively similar results and leads to extension τ . Thus, a non-zero g_3 acts like an extra matter term in the system. This can also be discerned from Eq. 5.2.10.

5.2.2.2 Large mixing angle: double dip feature

If the vacuum mixing angle ϑ_0 is large (and $\lambda = 0$, so the effective mixing angle is not suppressed), the oscillations develop a doubly periodic pattern, as shown in Fig. 5.3. The oscillation wavelength remains the same, however a new “double-dip” structure is seen in the oscillation pattern.

This feature can be understood from the fact that when ϑ_0 is large, the initial misalignment angle $2\vartheta_0$ is large. The pendular motion of \mathbf{P} , which initially starts from the z -axis, is then symmetric about this initial misalignment axis. However the motion of \mathbf{P} is not exactly symmetric about the z -axis. This asymmetry becomes more prominent and visible when ϑ_0 increases and this leads to the double-dip feature. If we realign our axis from which φ

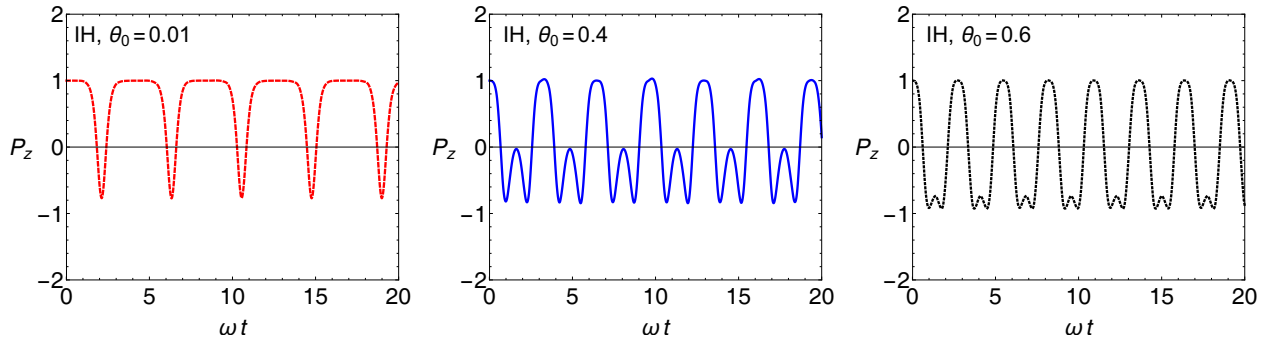


Figure 5.3: Time evolution of P_z and \overline{P}_z in IH for three different values of $\vartheta_0 = 0.01, 0.4, 0.6$. We take $g_3 = 1.5$ and $\mu = 10\omega$.

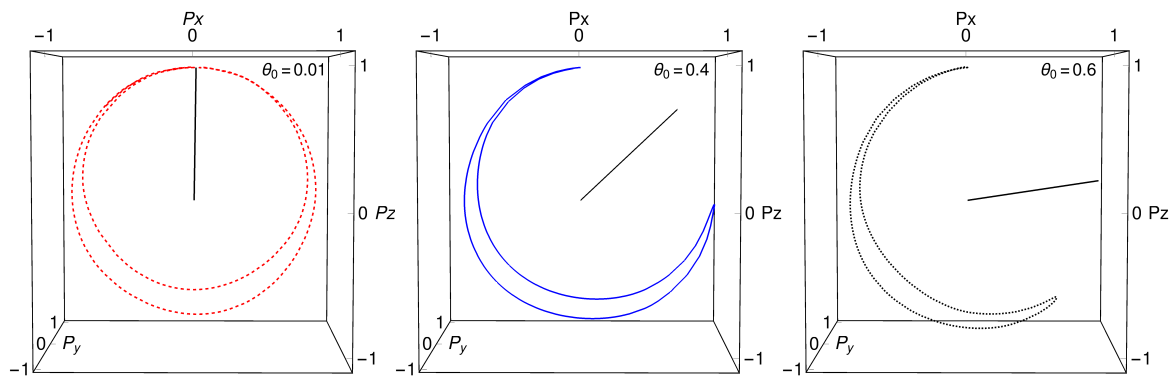


Figure 5.4: Parametric plot of $P_x(t)$, $P_y(t)$ and $P_z(t)$ in IH for three different values of $\vartheta_0 = 0.01, 0.4, 0.6$ (corresponding to those in Fig. 5.3). The pendular axis has also been shown. We take $g_3 = 1.5$ and $\mu = 10\omega$.

is measured with the pendular axis, then these features would vanish. In Eq. (5.2.14), this amounts to a shifting of $\varphi \rightarrow \tilde{\varphi} = \varphi + 2\vartheta_0$.

When the initial neutrino-antineutrino flux asymmetry is vanishing, and stays zero since $g_1 = 0$, we have $P_z(t) = \overline{P}_z(t) = S_z/2$, and Eq. (5.2.11) gives

$$P_z = \frac{1}{2} \left(|\mathbf{Q}| \cos \varphi + \frac{\omega}{\tilde{\mu}} \cos 2\vartheta_0 \right). \quad (5.2.17)$$

The maxima of P_z occur at $\varphi_{\max,1} = \sin^{-1} [-\omega \sin 2\vartheta_0 / (\tilde{\mu}|\mathbf{Q}|)]$ and $\varphi_{\max,2} = 2\pi - 4\vartheta_0 + \varphi_{\max,1}$, while both the minima are at $\varphi_{\min} = \pi$. Equation (5.2.17) then explains the double-dip feature. The heights of the two maxima are different, the larger maxima corresponding to $\varphi_{\max,1}$ and the smaller maxima corresponding at $\varphi_{\max,2}$.

A clearer idea may be obtained if we study the motion of \mathbf{P} in the 3-dimensional $[P_x(t), P_y(t),$

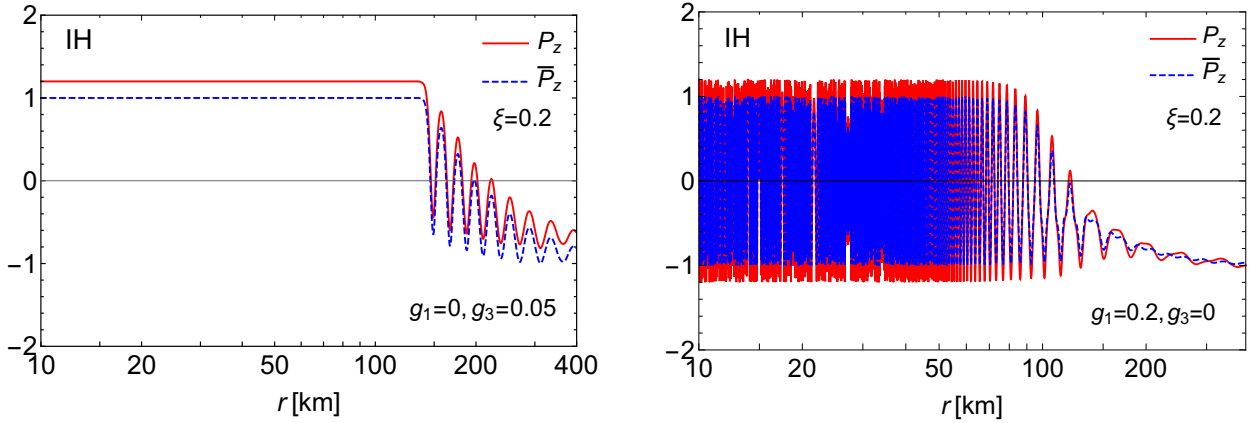


Figure 5.5: Time evolution of P_z and \bar{P}_z in IH with decreasing neutrino potential as in Eq. (5.2.18). The asymmetry is chosen to be $\xi = 0.2$ and $\omega = 0.3 \text{ km}^{-1}$. Left: $g_1 = 0, g_3 = 0.05$. Right: $g_1 = 0.2, g_3 = 0$.

$P_z(t)$] space as shown in Fig. 5.4 . When ϑ_0 is small, the motion is almost symmetric about the z - axis, tracing an almost complete circle in the $P_x(t) - P_z(t)$ plane. It is interesting to note that while the pendulum comes back to its initial position, it does not retrace its path. For larger ϑ_0 , the axis tilts significantly, and \mathbf{P} traces a trajectory symmetric about this new axis. The double-dip features are therefore a result of an initial large misalignment.

5.2.3 Flavor conversions with a varying neutrino potential in a supernova

Inside a core-collapse supernova, the neutrinos will experience a time-varying potential as they travel outwards from the neutrinosphere. Moreover, the initial neutrino flux is typically more than the antineutrino flux. To take into account these features, we consider the following spherically symmetric potential [106],

$$\mu = 7.5 \times 10^5 \text{ km}^{-1} \left(\frac{r_0}{r} \right)^4, \quad r > r_0, \quad (5.2.18)$$

where $r_0 = 10 \text{ km}$ is taken to be the radius of the neutrinosphere. We choose $\omega = 0.3 \text{ km}^{-1}$ corresponding to the atmospheric mass squared difference and $E \simeq 20 \text{ MeV}$, and a neutrino-antineutrino flux asymmetry of 20%. We take $\lambda = 0$ and study the effects of FP-NSSI and FV-NSSI through the rescaled couplings g_3 and g_1 (see Eq. (5.2.8)), respectively. We show

the evolution of P_z and \bar{P}_z in Fig. 5.5. The polarization vectors have been normalized such that $|\bar{\mathbf{P}}| = 1$. The following observations may be made from the figure.

- **FP-NSSI scenario:** When only g_3 is non-zero, the initial flux asymmetry is conserved, a result of $\mathbf{B} \cdot \mathbf{D}$ conservation. The initial flat values of P_z and \bar{P}_z denotes synchronized oscillations. It is important to note that the presence of g_3 leads to an extension of the time of onset of bipolar oscillations as explained in Section 5.2.2.1. The bipolar oscillations, which would have started at $r \simeq 100$ km at $g_3 = 0$, start at $r \simeq 130$ km now for $g_3 = 0.05$. Beyond that, almost complete flavor conversion takes place, while conserving the total flavor lepton number, hence retaining the flux asymmetry.
- **FV-NSSI scenario:** When only g_1 is non-zero, the flavor lepton number is not conserved. Rapid oscillations are observed to take place even at very low r values, due to the “transverse” NSSI term proportional to $\xi\mu g_1 \hat{\mathbf{x}}$. With increasing r , the value of μ decreases and so does the frequency of oscillation. During this evolution, the value of the flux asymmetry ξ keeps on changing. It is finally frozen at large r when $\xi\mu g_1 \rightarrow 0$. Even in this scenario, almost complete flavor conversion may take place.

Thus, we find that even in the simple single-angle approximation, the introduction of NSSI gives rise interesting results in the time evolution of system of neutrinos and antineutrinos of a single energy. In the next section, we will focus on a spectrum of neutrinos and antineutrinos, and study the effects of FP-NSSI and FV-NSSI on it.

5.3 Effects of NSSI on spectral swaps

Till now, we have studied the effects of NSSI on a single energy mode. In this section, we explore its effects on a toy spectrum, over a range of ω values. This will help us get a clear understanding of how NSSI can affect the spectral swaps. In this section, we explore the NSSI effects in the $g_1 - g_3$ plane and illustrate our results with a box spectrum g_ω^{in} (see Eq. (5.1.1)). The spectrum, shown in Fig. 5.6 (left panel), corresponds to a flat ω spectrum of neutrinos and antineutrinos, confined to $0 \leq |\omega| \leq 1$, with a $\nu - \bar{\nu}$ flux asymmetry of 10%. The neutrino flavors evolve while propagating through a medium with the neutrino-neutrino

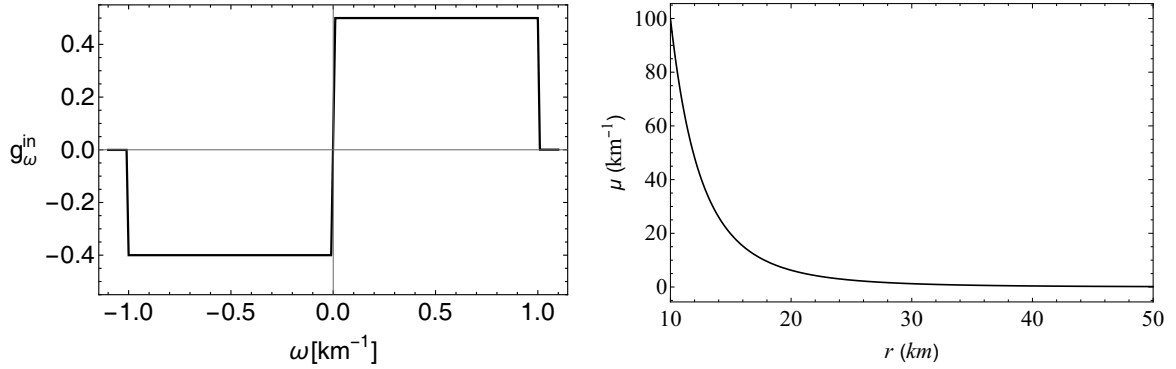


Figure 5.6: Initial spectrum and the background neutrino-neutrino potential for the analysis in Section 5.3. Left: Initial spectrum g_ω^{in} . Right: The neutrino-neutrino potential $\mu(r)$.

potential μ described by Eq. (5.2.18) and shown in Fig. 5.6 (right panel).

5.3.1 FP-NSSI scenario: pinching of spectral swaps

When $g_1 = 0$, $g_3 \neq 0$, the NSSI terms play the same role in the EoMs as the matter term, as we have seen in Sections 5.2.2.1 and 5.2.3. It is already known that presence of a matter term tends to suppress collective oscillations [195]. So we expect that increasing values of g_3 would lead to suppression of spectral swaps. In Fig. 5.7, we show the final spectrum g_ω^{final} (left panel) and the swap factor S_ω (right panel) for different values of g_3 , in IH.

It is observed that the swaps develop around the positive crossing at $\omega = 0$, with their relative extent on both sides of the crossing being fixed by approximate conservation of $\mathbf{B} \cdot \mathbf{D}$. The width of the swap is the greatest in the absence of g_3 (SM scenario). With increasing g_3 , the width of the swap is observed to decrease, i.e., the swaps get pinched. As g_3 approaches 2, the height of the swap also decreases till the swap finally vanishes when $g_3 \simeq 1.7$. Note that the value of g_3 at which the swap vanishes depends on initial spectrum, however our arguments in Section 5.2.2.1 have already indicated that for $g_3 > 2$ in IH, there would not be any collective oscillations.

It is important to mention that in this case, the conservation of $\mathbf{B} \cdot \mathbf{D}$ is approximately valid in the limit of small mixing angle ϑ_0 . From Eq. (5.2.12), we find

$$\frac{d}{dt} \mathbf{B} \cdot \mathbf{D} = \tilde{\lambda} [\mathbf{B} \mathbf{g} \mathbf{D}] , \quad (5.3.1)$$

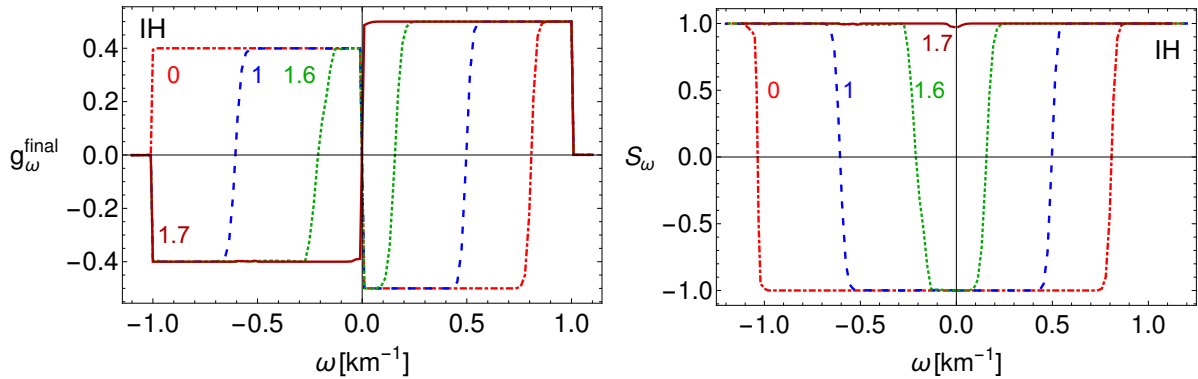


Figure 5.7: The final spectrum g_ω^{final} (left panel) and the swap factor S_ω (right panel) for $g_1 = 0$ and $g_3 = 0, 1, 1.6, 1.7$.

where $[\dots]$ represents the scalar triple product (box product). If $\vartheta_0 \simeq 0$, the vectors \mathbf{B} and $\mathbf{g} = g_3 \hat{\mathbf{z}}$ are nearly parallel, the box product vanishes, and the flavor lepton number conservation is valid.

The effect of the FP-NSSI coupling is thus to reduce both the height and width of the spectral swaps.

5.3.2 FV-NSSI scenario: flavor lepton number violation

The presence of a non-zero g_1 provides a more interesting scenario to study. The term $\xi\mu g_1 \hat{\mathbf{x}}$ essentially acts like an oscillation term between the two neutrino flavors. It causes flavor lepton number violation and can give rise to flavor conversions even with $\vartheta_0 = 0$ [130]. The variation of P_z, \bar{P}_z in Fig. 5.5 (right panel) also illustrate the non-conservation of flavor lepton number. Indeed with $\mathbf{g} = g_1 \hat{\mathbf{x}}$, Eq. (5.3.1) gives

$$\frac{d}{dt} \mathbf{B} \cdot \mathbf{D} = -\tilde{\lambda} g_1 D_y \cos 2\vartheta_0, \quad (5.3.2)$$

which is non-zero even for $\vartheta_0 = 0$. This non-conservation of $\mathbf{B} \cdot \mathbf{D}$ may have important observations. We illustrate the effect of g_1 on the same spectra as in Section 5.3.1 in Fig. 5.8.

The figure shows that the effect of g_1 is felt at very low values. With our particular spectrum, increasing g_1 increases the width for $\omega > 0$, while keeping the swap for $\omega < 0$ unchanged. Clearly this implies that $\mathbf{B} \cdot \mathbf{D} = \int d\omega g_\omega$ is not conserved. The width of the swap on both sides of the split is now governed by the variation in Eq. (5.3.2).

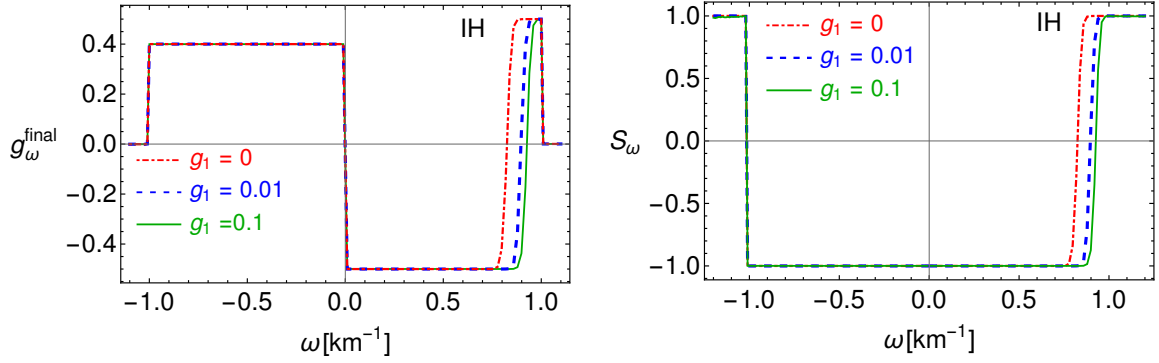


Figure 5.8: The final spectrum g_ω^{final} (left panel) and the final swap factor S_ω (right panel) for different values of $g_1 = 0, 0.01, 0.1$ and $g_3 = 0$.

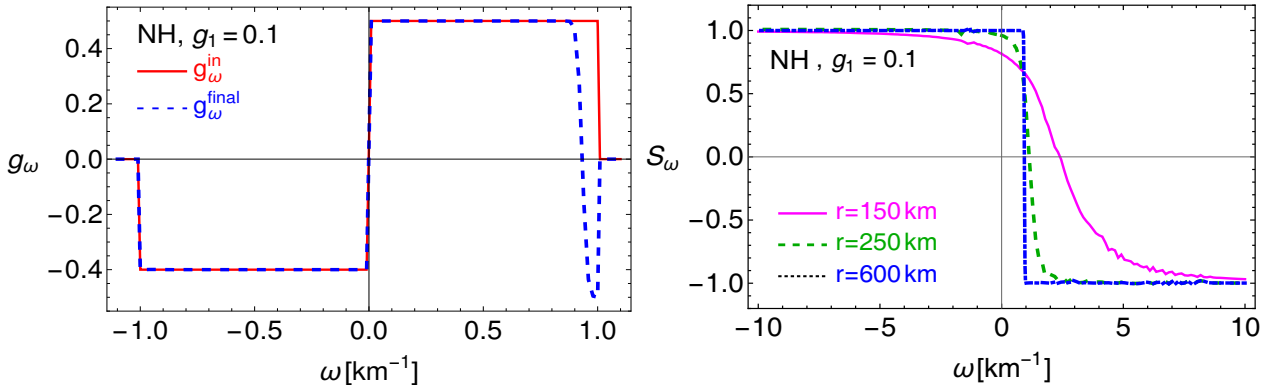


Figure 5.9: Left panel: The initial (red) and final (blue) spectrum in NH. Right panel: The development of the swap factor S_ω at different distances from the neutrinosphere for $g_1 = 0.1$.

An important observation may be made at this stage. When $\mathbf{B} \cdot \mathbf{D}$ is conserved, $\int d\omega g_\omega$ over the swapped region should vanish. This implies that the swapped region must contain at least one zero crossing in g_ω , by the intermediate value theorem. This is the essential reason for swaps to develop around a crossing. Therefore in the SM as well as in FP-NSSI, collective oscillations start taking place only when there is a g_ω crossing, which is the common wisdom. However, this notion breaks down when we have FV-NSSI. Now $\mathbf{B} \cdot \mathbf{D}$ is not conserved anymore and, depending on the evolution in Eq. (5.3.2), swaps may occur away from the zero crossing of g_ω .

We illustrate an interesting consequence of this observation in Fig. 5.9, where we take the same initial spectrum g_ω^{in} as in Fig. 5.6 (left panel), however consider the NH case. In the SM, we know that a swap cannot develop in such a case since the crossing at $\omega = 0$ is positive.

Even the discontinuity at $\omega = 1$ is not a real negative crossing and cannot lead to a swap as long as $\mathbf{B} \cdot \mathbf{D}$ is conserved. However, as the Fig. 5.9 (right panel) shows, in presence of g_1 , a swap starts developing for $\omega \simeq 1$, resulting in collective oscillations in that region. To understand the evolution of this swap further, we have added a $g_\omega = 10^{-5}$ (for $1 \leq \omega \leq 10$) and observed the development of the swap at different distances from the neutrinosphere. As the right panel of Fig. 5.9 shows, the swap clearly starts developing beyond the discontinuity at $\omega = 1$ where the spectrum virtually vanishes, a feature not seen in the case of the SM. Interestingly, the swap factor remains at $S_\omega = -1$ and does not change to $S_\omega = 1$ even for large enough ω .

Thus, introduction of an off-diagonal NSSI leads to unexpected swaps in the neutrino spectrum. This flavor number non-conservation can also lead to new spectral splits even in the neutronization burst epoch, as we will see in the next section.

5.4 Collective effects during neutronization burst

In the SM, collective effects cause pairwise conversions $\nu_e \leftrightarrow \nu_x$ and $\bar{\nu}_e \leftrightarrow \bar{\nu}_x$ due to flavor lepton number conservation. During the neutronization burst, only ν_e s are present. As a result, there is no zero-crossing in the spectrum g_ω and hence bipolar oscillations do not occur. However, as we have shown in Section 5.3, the presence of FV-NSSI can provide the necessary seed for collective oscillations to develop. As a result, spectral splits may be observed even during the neutronization burst. Note that during this epoch, none of the other collective effects, including the fast flavor conversions, can give rise to this phenomenon.

In Fig. 5.10, we demonstrate this novel phenomenon with an initial box spectrum consisting only of ν_e s. This spectrum is non-zero for $\omega_{\min} \leq \omega \leq \omega_{\max}$, which represents a cut-off in the ν_e spectra at low and high energies. We observe that

- In NH (left panels), the presence of a non-zero g_1 leads to the development of a swap around ω_{\max} , which corresponds to conversions of low energy ν_e s to ν_x s. With increasing value of g_1 , the swap becomes broader, thereby converting more of the ν_e s to ν_x s. For the spectrum used here, this phenomenon is visible for a non-zero FV-NSSI as low as 10^{-3} .

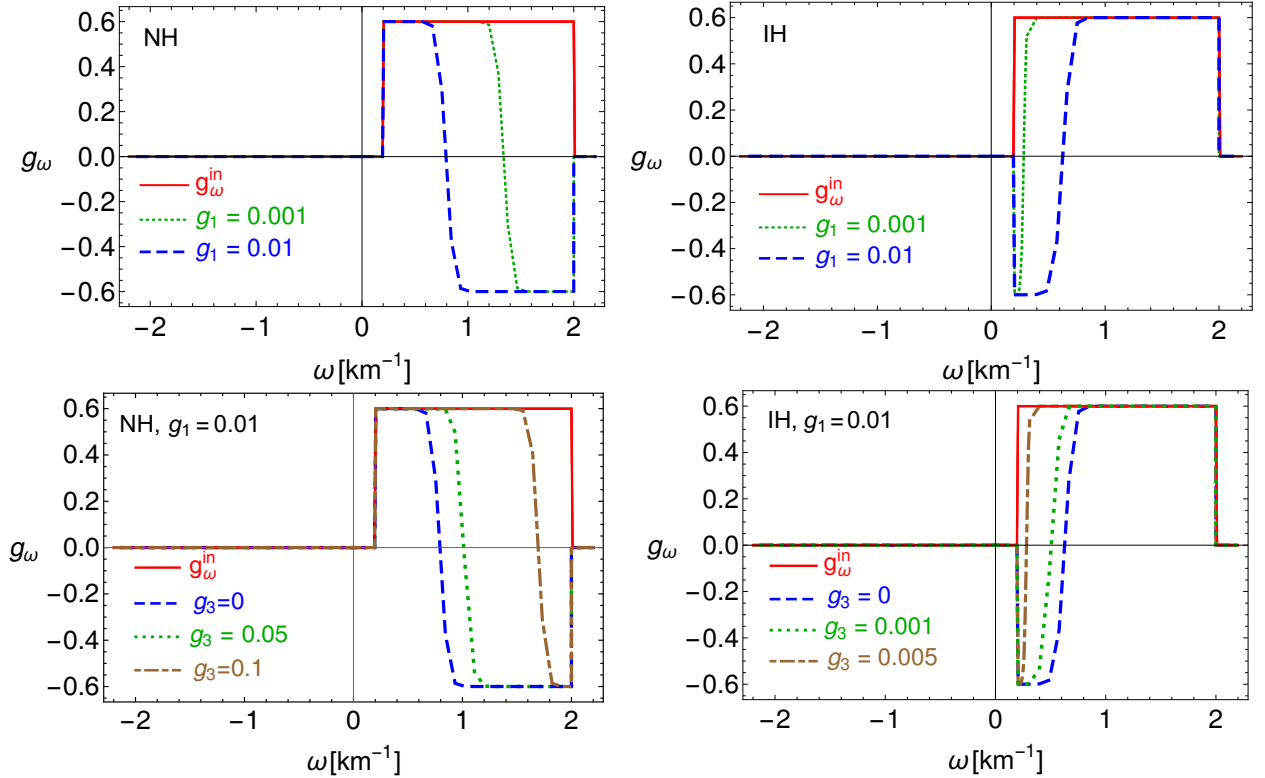


Figure 5.10: Effects of collective oscillations due to NSSI on a pure ν_e spectrum restricted to $0.2 \leq \omega \leq 2$, shown in solid line. Left Panels: NH, Right Panels: IH. Top Panels: The final spectra with $g_3 = 0$ (solid) and $g_1 = 0.001$ (dotted), and $g_1 = 0.01$ (dashed). Bottom Panels: The pinching of final spectra for $g_1 = 0.01$ with $g_3 = 0$ (dashed), $g_3 = 0.05$ (dotted) and $g_3 = 0.1$ (dotdashed) in NH (left). Similar plot in IH (right) for $g_1 = 0.01$ with $g_3 = 0$ (dashed), $g_3 = 0.001$ (dotted) and $g_3 = 0.005$ (dotdashed).

- In IH (right panels), the presence of a non-zero g_1 leads to the development of a swap around ω_{\min} , which corresponds to conversions of high energy ν_e s to ν_x s. With increasing value of g_1 , the swap becomes broader, thereby converting more of the ν_e s to ν_x s. For the spectrum used here, this phenomenon is visible for a non-zero FV-NSSI as low as 10^{-3} .
- If a non-zero g_3 is also present, the swap is pinched, as shown in the lower panels.

In order to see how the presence of FV-NSSI affects the neutrino spectrum during neutronization burst, we consider the following initial flux [79]

$$F_\nu^0(E_\nu) \propto \frac{E_\nu^3}{\langle E_\nu \rangle^4} e^{-4 \frac{E_\nu}{\langle E_\nu \rangle}}. \quad (5.4.1)$$

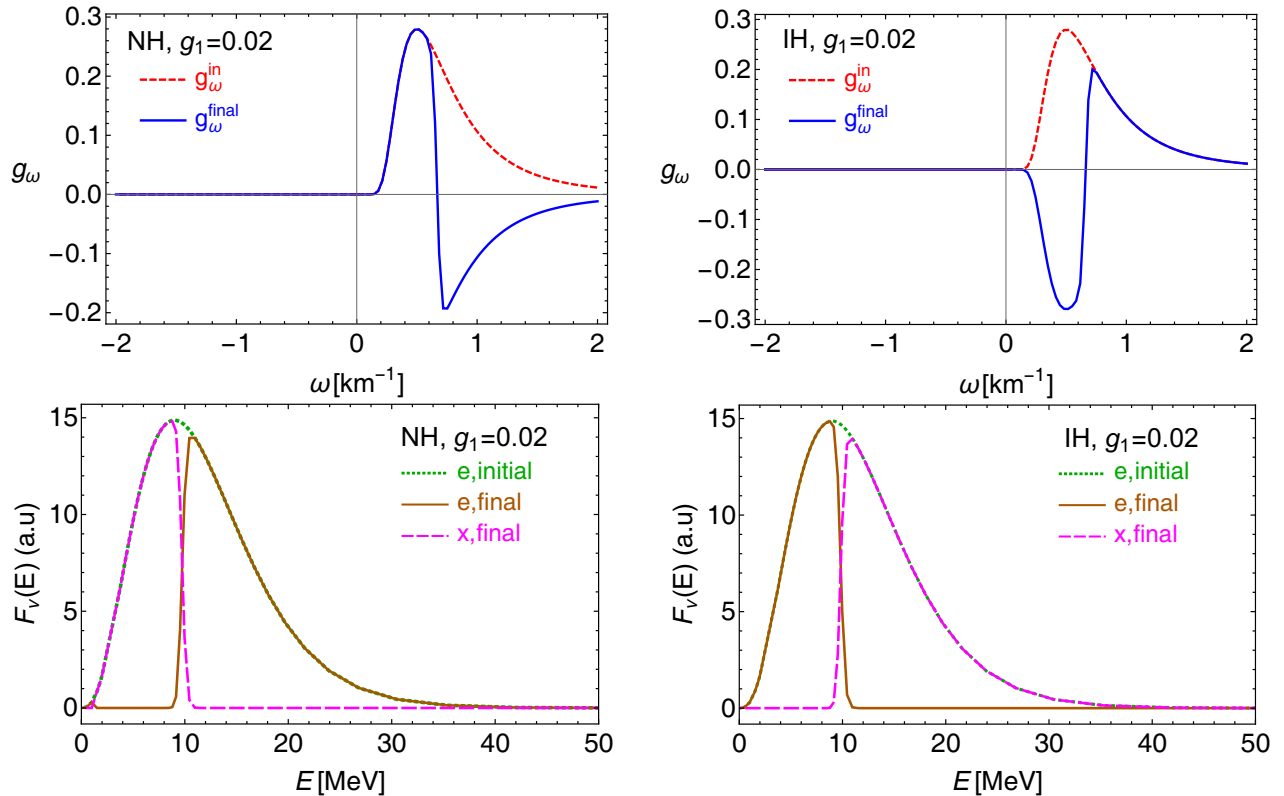


Figure 5.11: Effects of $\nu_e \leftrightarrow \nu_x$ collective oscillations on an initial ν_e spectrum during the neutronization burst, for $g_1 = 0.02$, $g_3 = 0$. Left panels: NH. Right panels: IH. We have taken $E = \Delta m_{\text{atm}}^2 / (2\omega)$.

We choose the average energy $\langle E_{\nu_e} \rangle = 12$ MeV. The fluxes for the $\bar{\nu}_e$, ν_x and $\bar{\nu}_x$ have all been taken to be zero during the neutronization epoch. With these parameters, the initial ν_e spectra g_ω^{in} , and the final ν_e spectra g_ω^{fin} , just after the $\nu_e \leftrightarrow \nu_x$ collective oscillations are over, are shown in Fig. 5.11 for both NH (left panel) and IH (right panel). Indeed, we observe a distinct split in the ν_e spectrum in both hierarchies.

- In NH, for high energies, the final spectrum is identical to the original ν_e spectrum, whereas at lower energies, all the ν_e s get converted to ν_x s. As a result, the average energy of the ν_e spectrum will increase and a sharp rise would be observed after a certain critical energy.
- In IH, the exact opposite behavior is observed. For low energies, the final spectrum is identical to the original ν_e spectrum, whereas at higher energies, all the ν_e s get converted to ν_x s. As a result, the average energy of the ν_e spectrum will decrease and

and its tail would be replaced by a sharp drop.

The analysis so far takes into account only two-flavor collective conversions. This could be followed further by another collective flavor conversion, in the stepwise process. In principle, collective conversions $\nu_e \leftrightarrow \nu_y$ and $\nu_e \leftrightarrow \nu_x$ may happen in a stepwise manner [95, 107, 109], where

$$\nu_y \equiv \cos \theta_{23} \nu_\mu + \sin \theta_{23} \nu_\tau, \quad \nu_x \equiv -\sin \theta_{23} \nu_\mu + \cos \theta_{23} \nu_\tau. \quad (5.4.2)$$

The spectra after these collective transformations will further be affected by MSW flavor conversions at the H and L-resonances [28, 77]. The final spectra arriving at the Earth would be

$$\begin{aligned} F_{\nu_e}^{\text{NH}} &= \left[|U_{e3}|^2 (1 - P_{ey} - P_{ex}) + |U_{e2}|^2 P_{ey} + |U_{e1}|^2 P_{ex} \right] F_{\nu_e}^0, \\ F_{\nu_e}^{\text{IH}} &= \left[|U_{e2}|^2 (1 - P_{ey} - P_{ex}) + |U_{e3}|^2 P_{ey} + |U_{e1}|^2 P_{ex} \right] F_{\nu_e}^0, \end{aligned} \quad (5.4.3)$$

where P_{ey} and P_{ex} are the collective flavor conversion probabilities for $\nu_e \leftrightarrow \nu_y$ and $\nu_e \leftrightarrow \nu_x$ respectively. We have taken the H and L-resonances to be adiabatic as is clear from the large values of the corresponding mixing angles [34, 35, 77]. In the absence of NSSI, $P_{ey} = P_{ex} = 0$ and hence

$$F_{\nu_e}^{\text{NH}} = |U_{e3}|^2 F_{\nu_e}^0, \quad F_{\nu_e}^{\text{IH}} = |U_{e2}|^2 F_{\nu_e}^0. \quad (5.4.4)$$

Since $|U_{e3}|^2 \simeq 0.025$, $|U_{e2}|^2 \simeq 0.3$ and the flux during the neutronization burst is well-predicted [131], the two hierarchies can be distinguished by observing the number of events during the first ~ 20 ms of a SN neutrino signal.

This picture changes with the introduction of NSSI. The non-zero values of P_{ey} and P_{ex} , combined with the sharp energy dependent spectral split features in these quantities will affect the final number of events as well as the ν_e spectral shape. For an illustration, we choose the scenario where $P_{ex} = 0$ and show the quantity (flux \times cross-section) for ν_e at a liquid Argon (LAr) detector in Fig. 5.12. Note that the exact position of the spectral split would depend on the initial flux as well as the values of NSSI parameters. In the scenario shown in the figure, increasing the value of g_1 tends to shift the split to higher energies in NH and lower energies in IH. On the other hand, the presence of a non-zero g_3 would cause pinching of the swap. This corresponds to shifting the split to lower energies in NH and to

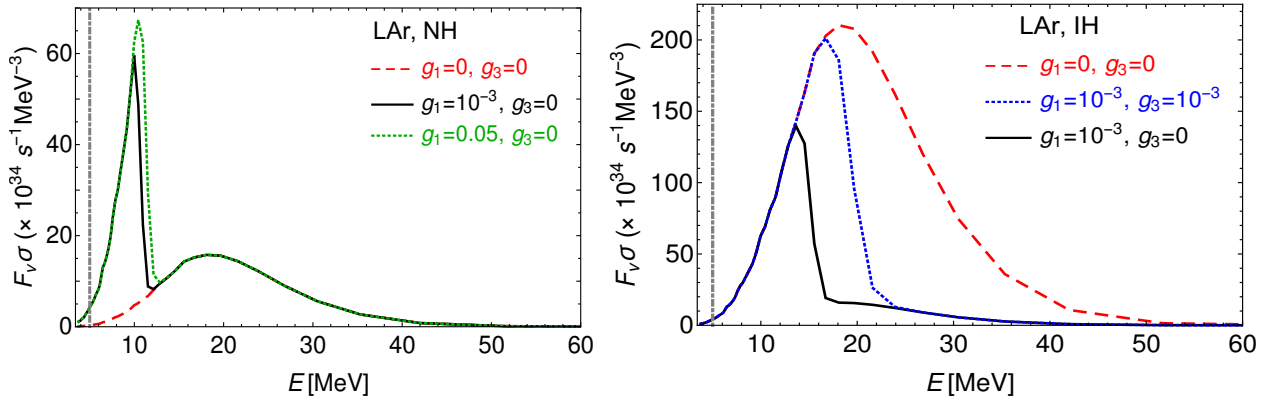


Figure 5.12: The quantity (flux \times cross-section) for charged-current events ($\nu_e + {}^{40}\text{Ar} \rightarrow {}^{40}\text{K}^* + e^-$) in a liquid Argon detector in different scenarios. The cross-sections have been taken from [196]. The threshold energy of the detector is taken to be $E = 5$ MeV [197], as shown in grey dotdashed lines. Left panel: NH. Right panel: IH.

higher energies in IH. If further $P_{ex} \neq 0$, it could give rise to multiple spectral splits. Since such features can be present in both hierarchies, the identification of mass hierarchy from the neutronization burst [77, 131] would become difficult.

The observation of such a spectral split during the neutronization epoch would indicate the presence of NSSI. This however would need a sufficiently large number of events and a very good resolution in time and energy to resolve these splits. With a neutrino flux of $\sim 10^{57}$ ν_e s during the neutronization burst of a SN at 10 kpc, one would expect up to $\mathcal{O}(100)$ events in a 40 kt liquid Argon detector. In water Cherenkov detectors, where ν_e flux will be detected through the elastic scattering $\nu_e + e^- \rightarrow \nu_e + e^-$ and the energy determination is not so good, the signals of NSSI may be discerned if the expected number of events are observed to be too high for the NH scenario and too low for the IH scenario. For the 500 kt Hyper-Kamiokande, one would expect up to $\mathcal{O}(100)$ of events during this neutronization burst.

Note that the above results are obtained under the single-angle approximation. Multi-angle effects and possible consequent effects of matter may modify the final spectra. However the distinctive effects of NSSI, in particular the formation of spectral splits where none would be present otherwise, could survive and are worth exploring further.

5.5 Summarized Results

In this work, we have investigated the effects of non-standard self-interactions (NSSI) on collective oscillations of supernova (SN) neutrinos. Using a flavor-pendulum picture to get an analytical understanding, we have performed a comprehensive study of the impact of flavor-preserving (FP-NSSI) as well as flavor-violating NSSI (FV-NSSI) on the flavor evolution of neutrinos. Indeed, many interesting results significantly distinct from the Standard Model (SM) expectations are seen to emerge with the addition of NSSI.

For an ensemble of neutrinos and antineutrinos of a fixed energy, we have showed that for large enough NSSI, the predictions for the two mass hierarchy interchange, i.e., flavor conversions can happen in NH, whereas they can vanish in IH. For a typical neutrino-neutrino potential in a SN, the FP-NSSI are observed to act like a matter term, causing a delay in the onset of flavor conversions. The FV-NSSI result in the violation of flavor lepton number, and hence do not preserve the initial neutrino-antineutrino flux asymmetry.

We have also analyzed the effects of NSSI on a box-spectrum of neutrinos and antineutrinos over a range of energy modes, in order to clarify how NSSI affects the spectral swaps. In the presence of FP-NSSI, spectral swaps develop around a spectral crossing. The FP-NSSI lead to the pinching of the spectral swaps, i.e., a decrease in their width and height. The flavor lepton number violation arising from FV-NSSI leads to interesting observations: while in the SM, the swaps have to develop around the zero crossing of the g_ω -spectra, the presence of FV-NSSI may cause swaps to appear away from spectral crossings, and even in the absence of spectral crossings.

An important consequence of such a flavor lepton violation with FV-NSSI is the presence of collective oscillations during the neutronization burst epoch of a SN leading to low (high) energy conversion of ν_e to ν_x in NH (IH). This would alter the neutronization burst signal. Using a realistic ν_e spectrum during the neutronization burst and taking into account the effect of MSW resonance inside the star, we have demonstrated the presence of spectral splits in the final spectra. Since collective effects would otherwise be absent during this epoch, the presence of such splits can be a clear indication of NSSI. This could also make the identification of hierarchy during neutronization burst harder.

Naturally, this motivates two questions:

- (i) Why do FP-NSSI lead to suppression of collective oscillations, while FV-NSSI seem to aid in collective oscillations even in situations where there would have been none in the SM?
- (ii) Can NSSI have any significant impact on fast flavor conversions?

In the next chapter, we provide an analytical understanding of the enhancement and suppression of collective oscillations by FV-NSSI and FP-NSSI respectively. We also study the effects of NSSI on fast flavor conversions in the simple intersecting 4-beam model, both analytically through a linear stability analysis as well as numerically.

Chapter 6

Analytical aspects of NSSI in a supernova and fast flavor conversions

In this chapter, we further explore the effects of non-standard self-interactions (NSSI) of neutrinos streaming out of a core-collapse supernova, in order to understand their features analytically. Using the standard linear stability analysis (LSA), we show that presence of NSSI gives rise to linearly as well as exponentially growing solutions. Using a simple toy models, we demonstrate analytically that flavor-preserving NSSI lead to a suppression of bipolar collective oscillations. We also study the impact of NSSI on fast flavor conversions using the simple intersecting 4-beam model as an example. We solve the full non-linear equations of motion in the 4-beam model numerically, and explore the interplay of fast and slow flavor conversions in the long-time behavior, in the presence of NSSI. ¹

6.1 Introduction

In the previous chapter, we made a detailed study of the effects of flavor-violating NSSI (FV-NSSI) and flavor-preserving NSSI (FP-NSSI) on collective oscillations. We demonstrated

¹The results in this chapter are based on the paper: A. Dighe and M. Sen, “ *Nonstandard neutrino self-interactions in a supernova and fast flavor conversions*”, Physical Review D97 (2018) no.4, 043011 [arXiv:1709.06858[hep-ph]].

using box spectra and single-angle analysis that FP-NSSI leads to the pinching of spectral swaps, hence the suppression of collective oscillations, whereas FV-NSSI may lead to the development of swaps away from (or even in the absence of) a spectral crossing. In particular, FV-NSSI can cause collective oscillations during the neutronization burst epoch for both hierarchies, leading to distinct features in the neutronization spectra. In this chapter, we will try to understand these effects analytically.

We perform a LSA in the two-neutrino flavor space to analytically understand the effects of NSSI on the onset of collective oscillation. As explained before, such an analysis typically leads to an eigenvalue equation [96], whose exponentially growing eigenvalues correspond to an instability. We find that when both FP-NSSI and FV-NSSI are present, one gets linearly increasing solutions along with the exponentially increasing ones. These linear solutions may lead to an earlier onset of flavor instability. Furthermore, presence of FV-NSSI may obviate the need for a seed to start collective oscillations.

In addition, note that the above study was performed assuming the absence of fast oscillations. This assumption was valid in the neutronization burst epoch, since only electron neutrinos are emitted in this phase and hence there can be no collective effects or fast oscillations in SM. It would be interesting to see how NSSI affects fast conversions, since these rapid conversions near the neutrinosphere might play an important role in SN explosion. In this chapter, we carry out a detailed study of the effects of NSSI on fast as well as slow collective flavor conversions.

We then proceed to analyze the effects of NSSI on fast oscillations. Using the intersecting 4-beam model of neutrinos and antineutrinos illustrated in Chapter 4, we demonstrate that fast oscillations are suppressed by FP-NSSI even for rapidly growing temporal solutions. This could not have been possible in the SM, where temporal instabilities are unsuppressed by matter effects [178, 180]. On the other hand, FV-NSSI enhance fast oscillations and also cause them to start even earlier than in the SM.

In the context of the 4-beam model, we had demonstrated in Chapter 4 that fast oscillations are absent when the angle between the neutrino and the antineutrino is obtuse. This corresponds to a potential barrier in terms of the classical analog presented earlier. However, we find that FV-NSSI allow fast oscillations to take place even when the angle between the

neutrino and the antineutrino is obtuse. An important consequence of the last result above is that FV-NSSI can induce fast oscillations in even simpler systems like a two back-to-back beams of neutrino-antineutrino. In such a system, it was shown that spatial inhomogeneities are necessary for an instability to exist [119]. However, this no longer remains a necessity in the presence of FV-NSSI, and fast oscillations take place even in absence of a spatial inhomogeneity.

Finally, we also study the effects of NSSI on the long-time flavor evolution of the 4-beam model by solving the fully non-linear equations of motion numerically. We demonstrate that the fast oscillations appear as modulations on the slow oscillations. The frequency and amplitude of the modulations are influenced by the values of the NSSI parameters.

We demonstrate these ideas in the following sections.

6.2 Linear Stability analysis with NSSI

We work in terms of the 2×2 occupation number matrices $\varrho_{\mathbf{p}}$. Following 5.2.3, the most general neutrino self-interaction Hamiltonian in presence of NSSI is

$$\mathcal{H}_{\mathbf{p}}^{\nu\nu} = \sqrt{2}G_F \int \frac{d^3\mathbf{q}}{(2\pi)^3} (1 - \mathbf{v}_{\mathbf{p}} \cdot \mathbf{v}_{\mathbf{q}}) \times \{G(\varrho_{\mathbf{q}} - \bar{\varrho}_{\mathbf{q}})G + G \text{Tr}[(\varrho_{\mathbf{q}} - \bar{\varrho}_{\mathbf{q}})G]\} , \quad (6.2.1)$$

Here G is the coupling matrix defined as (see Eq. (5.2.4))

$$G = \frac{1}{2} (g_0 \mathbb{I} + \mathbf{g} \cdot \boldsymbol{\sigma}) . \quad (6.2.2)$$

The parameter g_0 can be scaled away using the redefinitions

$$\mathbf{g} \rightarrow \mathbf{g}/(g_0/2), \quad \mu_{\mathbf{R}} \rightarrow \mu_{\mathbf{R}}(g_0/2)^2, \quad (6.2.3)$$

where $\mu_{\mathbf{R}}$ will be defined presently. Note that in this case, $\mu_{\mathbf{R}}$ is defined through Eq. (6.2.9).

Further simplification can be achieved by redefining the phase of ν_x such that $g_2 = 0$. This allows us to write the redefined coupling matrix as

$$G = \begin{bmatrix} 1 + g_3 & g_1 \\ g_1 & 1 - g_3 \end{bmatrix} . \quad (6.2.4)$$

Henceforth, we will work with this coupling matrix.

To understand the results of the previous chapter analytically, we perform an LSA to check for onset on an instability far away from the neutrinosphere. The formalism for the LSA has already been developed in 2.4. We redo the stability analysis in the presence of NSSI in this section.

We confine ourselves to a spherically symmetric setup, where neutrinos are emitted from a fiducial neutrinosphere of radius R . Following [96], we label them by the variable $u = \sin^2 \vartheta_R$, where ϑ_R is the emission angle of the neutrinos. For simplicity, we assume that the solution is stationary and has an axial symmetry. The radial velocity for a mode u at the radius r is $v_{r,u} = \sqrt{1 - uR^2/r^2}$.

In terms of the flux matrices F [96, 114]

$$F_{\omega,u} d\omega du = 2\pi r^2 v_{r,u} \varrho_{\mathbf{p}} \frac{d^3 \mathbf{p}}{(2\pi)^3}, \quad (6.2.5)$$

the EoMs, in presence of NSSI, become

$$i\partial_r F_{\omega,u} = [H_{\omega,u}, F_{\omega,u}], \quad (6.2.6)$$

where

$$H_{\omega,u} = (\omega + \lambda_r) v_{r,u}^{-1} + \mu_R \frac{R^2}{r^2} \int d\Gamma' \frac{1 - v_{r,u} v'_{r,u'}}{v_{r,u} v'_{r,u'}} \times \left\{ G F_{\omega,u} G + G \text{Tr} [F_{\omega,u} G] \right\}, \quad (6.2.7)$$

where the symbols have the usual meaning as 2.4. Following 2.4, the quantities λ_r (matter potential at a radius r) and μ_R (neutrino-neutrino potential at the neutrinosphere) are defined as

$$\lambda_r = \sqrt{2} G_F n_e(r), \quad (6.2.8)$$

$$\mu_R = \frac{\sqrt{2} G_F [F_{\omega,u}^{\bar{e}}(R) - F_{\omega,u}^{\bar{x}}(R)]}{4\pi R^2}, \quad (6.2.9)$$

The flux matrix can be written as a sum of a trace part, and a traceless part:

$$F_{\omega,u} = \frac{\text{Tr}(F_{\omega,u})}{2} + \frac{g_{\omega,u}}{2} \begin{pmatrix} s_{\omega,u} & S_{\omega,u} \\ S_{\omega,u}^* & -s_{\omega,u} \end{pmatrix}, \quad (6.2.10)$$

where

$$g_{\omega,u} = \begin{cases} F_{\omega,u}^e - F_{\omega,u}^x & \text{for } \omega > 0 \\ F_{\omega,u}^{\bar{x}} - F_{\omega,u}^{\bar{e}} & \text{for } \omega < 0 \end{cases}. \quad (6.2.11)$$

At $t = 0$, we have $s_{\omega,u} = 1$ and $S_{\omega,u} = 0$ in Eq. (6.2.10). As flavor evolution begins, $S_{\omega,u}$ starts developing a non-zero value. Since $s_{\omega,u}^2 + S_{\omega,u}^2 = 1$, a small amplitude expansion may be performed with the approximation $s_{\omega,u} \approx 1$, $S_{\omega,u} \ll 1$, and where terms of $\mathcal{O}(S^2)$ are dropped. This is equivalent to linearizing the equations in $S_{\omega,u}$.

We arrive at the linearized EoMs in presence of NSSI:

$$\begin{aligned}
i\partial_r S_{\omega,u} &= \left[(\omega + \lambda_r) v_{u,r}^{-1} + \mu_R \frac{R^2}{r^2} (1 - g_1^2 + 3g_3^2 + 4g_3) \times \int d\Gamma' \frac{1 - v_{u,r}v_{u',r'}}{v_{u,r}v_{u',r'}} g_{\omega',u'} \right] S_{\omega,u} \\
&- \mu_R \frac{R^2}{r^2} \int d\Gamma' \frac{(1 - v_{u,r}v_{u',r'})}{v_{u,r}v_{u',r'}} g_{\omega',u'} \times \left[(1 + g_1^2 - g_3^2) S_{\omega',u'} + 2g_1^2 S_{\omega',u'}^* + 4g_1g_3 \right].
\end{aligned} \tag{6.2.12}$$

Eq. (6.2.12) clearly is not an eigenvalue equation, as it would have been in the SM limit [96, 114]. This would lead to the following interesting consequences. (While describing these observations, we will drop the subscripts for simplicity of notation.)

(i) **Only FP-NSSI:** In this limit, Eq. (6.2.12) is an eigenvalue equation and the standard analysis of [96] holds. One can look for exponentially growing solutions of the form $S = Qe^{-i\Omega t}$, where $\Omega = \gamma + i\kappa$ is complex. A positive non-zero value of κ indicates an instability growing with a rate $e^{\kappa t}$.

(ii) **Only FV-NSSI:** The EoMs governing S are not simple eigenvalue equations in S anymore. However one may combine the pair of coupled differential equations for S and S^* to get an eigenvalue equation. This may be done by looking for solutions of the form $S = Ae^{\Gamma t}$, where A can be complex and Γ is real. Positive solutions of Γ indicate a runaway solution and hence signal an instability.

(iii) **Both FP-NSSI and FV-NSSI:** Eq. (6.2.12) cannot be converted to a simple eigenvalue equation. The term proportional to g_1g_3 would generate S even if it were vanishing at $t = 0$. As long as S is sufficiently small, the growth rate will be dominated by a linear rise owing to this term. However, as S grows, the exponential growth may take over. Hence one expects to find a linear rise, followed by an exponential one in the instability growth rates.

Using Eq. (6.2.12) we shall demonstrate these observations explicitly using a simple two-box spectrum in the single-angle approximation and far away from the neutrinosphere. This will also provide an analytical understanding of the numerical results presented in [198].

6.2.1 Analytical understanding of the evolution of a two-box spectrum

In the previous chapter, we showed that in the single-angle approximation and far away from the neutrinosphere, FP-NSSI can cause suppression of collective oscillations, leading to pinching of spectral swaps in a two-box spectrum. Conversely, presence of FV-NSSI leads to a gradual widening of spectral swaps. We will now try to explain these observations analytically using the formalism developed in the earlier section.

Far away from the neutrinosphere ($r \gg R$), we can drop terms of $\mathcal{O}(R^2/r^2)$ in Eq. (6.2.12). In this limit, the EoMs are given by

$$\begin{aligned}
i\partial_r S_{\omega,u} &= \left[\omega + \lambda_r + u\tilde{\lambda}_r + u\tilde{\mu}_r \epsilon (1 - g_1^2 + 3g_3^2 + 4g_3) \right] S_{\omega,u} \\
&- \tilde{\mu}_r (1 - g_3^2 + g_1^2) \int du' d\omega' (u + u') g_{\omega',u'} S_{\omega',u'} \\
&- 2\tilde{\mu}_r g_1^2 \int du' d\omega' (u + u') g_{\omega',u'} S_{\omega',u'}^* \\
&- 4\tilde{\mu}_r g_1 g_3 \int du' d\omega' (u + u') g_{\omega',u'} ,
\end{aligned} \tag{6.2.13}$$

where

$$\begin{aligned}
\tilde{\lambda}_r &= \sqrt{2} G_F n_e(r) \frac{R^2}{2r^2} , \\
\tilde{\mu}_r &= \frac{\sqrt{2} G_F}{4\pi R^2} \frac{R^4}{2r^4} [F_{\omega,u}^{\bar{e}}(R) - F_{\omega,u}^{\bar{x}}(R)] .
\end{aligned} \tag{6.2.14}$$

Here $\epsilon = \int d\omega' du' g_{\omega',u'}$ encodes the net neutrino-antineutrino asymmetry. This is the generalization of the multi-angle evolution equation derived for the SM, and reduces to it in the limit $g_1, g_3 \rightarrow 0$ [Eq. (31) in [96]].

For demonstrating the effects of NSSI, we consider the scenario where all the neutrinos have the same emission angle and hence may be labeled by a single angular mode u_0 . We take the initial spectrum to be the two-box spectrum, as shown in the left panel of Fig. 6.1:

$$g_\omega \equiv g_{\omega,u_0} = \begin{cases} -1 & -A < \omega < 0 , \\ +1 & 0 < \omega < B . \end{cases} \tag{6.2.15}$$

Such a simple box spectrum has the advantage of making the eigenvalues analytically tractable and hence the effects of NSSI become clear. Following [96], one can define

$$\bar{\lambda}_r \equiv \lambda_r + u [\tilde{\lambda}_r + \tilde{\mu}_r \epsilon (1 - g_1^2 + 3g_3^2 + 4g_3)] , \tag{6.2.16}$$

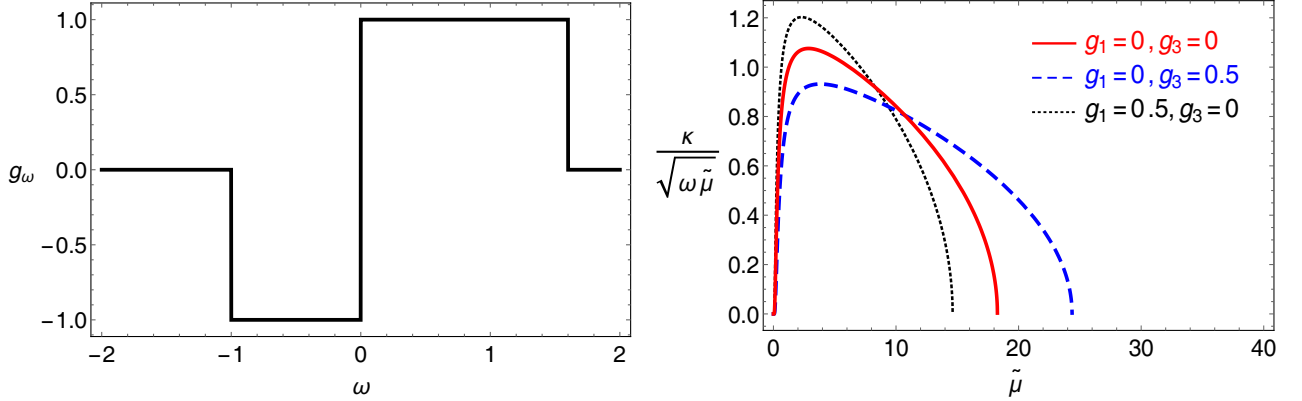


Figure 6.1: Left panel: a two-box spectrum [Eq. (6.2.15)] with $A = 1$ and $B = 1.6$. Right panel: Plot showing growth rates κ in units of $\sqrt{\omega\tilde{\mu}}$ for $u = 1/2$. Red (solid) indicates the SM, whereas blue (dashed) represents $g_1 = 0, g_3 = 0.5$ and black (dotted) shows $g_1 = 0.5, g_3 = 0$.

which acts as the effective matter term in the equations. In the following discussions in this section, we drop the subscript r of $\tilde{\mu}$ for simplicity of notation.

The suppression and the enhancement of collective oscillations can be characterized in terms of the change of the growth rate κ . The growth rates in this case are proportional to $\sqrt{\omega\tilde{\mu}}$, and hence come under slow collective oscillations. The right panel of Fig. 6.1 shows the growth rates in units of $\sqrt{\omega\tilde{\mu}}$ for $u = u_0 = 1/2$. For any other value of u_0 , the results will be identical with $\tilde{\mu}$ replaced by $2u_0\tilde{\mu}$. The effects of NSSI may be observed and interpreted as follows:

(i) **Only FP-NSSI:** As noted before, in this case Eq. (6.2.13) is a simple eigenvalue equation. The effective matter term can be rotated away by going to the appropriate co-rotating frame. The analytical results for SM [see Eq. (47) of [96]] then carry through with $\tilde{\mu}$ replaced by $\tilde{\mu}(1 - g_3^2)$, and hence the collective oscillations are suppressed due to g_3 .

(ii) **Only FV-NSSI:** In this scenario, Eq. (6.2.13) is not a simple eigenvalue equation. However, if the term $g_1^2 S_{\omega,u}^*$ can be neglected when compared to $(1 + g_1^2) S_{\omega,u}$, then Eq. (6.2.13) may be approximated by an eigenvalue equation, and the effective matter term can be co-rotated away. The numerical observation of enhancement of collective oscillations due to g_1 may be then qualitatively interpreted as a result of the $\tilde{\mu}(1 + g_1^2)$ factor. The effect of the neglected $g_1^2 S_{\omega,u}^*$ term is difficult to determine analytically, however.

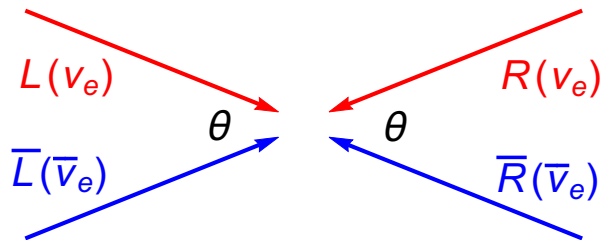


Figure 6.2: The intersecting 4-Beam Model, consisting of two left-going and two right-going neutrinos and antineutrinos.

When both FP-NSSI and FV-NSSI are present, Eq. (6.2.13) cannot be converted to an eigenvalue equation and hence an analytical understanding in terms of linear stability analysis seems elusive.

This provides us with a semi-analytical understanding of the effects of NSSI on collective bipolar oscillations. Now, we turn our attention to analyzing the impact of NSSI on fast flavor conversions.

6.3 Fast flavor oscillations: the 4-beam model

We demonstrate the effects of neutrino NSSI on a simple system that shows fast flavor oscillations, an intersecting 4-beam model consisting of two right-going and left-going neutrinos and antineutrinos each [119], as shown in Fig. 6.2 and considered earlier in Chapter 4. Since our understanding of the fast oscillations phenomenon is still in an exploratory phase, we have considered the simplest system showing such an effect [119, 183, 199], to analytically understand the phenomenon without delving deeper into a more realistic spectra.

Following [119], the amplitudes for the corresponding modes are denoted by Q_L ($Q_{\bar{L}}$) for neutrinos (antineutrinos) coming from left, and Q_R ($Q_{\bar{R}}$) for neutrinos (antineutrinos) coming from right. Their corresponding spectra are $g_L, g_{\bar{L}}, g_R$ and $g_{\bar{R}}$. The spectra here are taken to be left-right symmetric, i.e.,

$$\begin{aligned} g_R = g_L &= \frac{1}{2}(1 + a), \\ g_{\bar{R}} = g_{\bar{L}} &= -\frac{1}{2}(1 - a), \end{aligned} \tag{6.3.1}$$

where a gives the net neutrino-antineutrino asymmetry in the system. The range of a is

chosen to be $-1 \leq a \leq 1$. The angle at the intersection of the two beams is denoted by θ as shown in the figure.

Since we are interested in conversions taking place very close to the neutrinosphere, the effective neutrino-neutrino potential $\mu \approx \mu_R$, and the effective matter potential $\lambda \approx \lambda_R = \sqrt{2}G_F n_e(R)$. Also, it is more useful to label the modes using the velocity vector \mathbf{v} rather than the variable $u = \sin^2 \vartheta_R$. The EoM for the off-diagonal parameter $S_{\mathbf{p}}$ for each mode \mathbf{p} is given by

$$\begin{aligned}
i(\partial_t + \mathbf{v}_{\mathbf{p}} \cdot \nabla)S_{\mathbf{p}} &= \left[\omega + \lambda + \mu(1 - g_1^2 + 3g_3^2 + 4g_3) \times \sum_{\mathbf{q}} (1 - \mathbf{v}_{\mathbf{p}} \cdot \mathbf{v}_{\mathbf{q}})g_{\mathbf{q}} \right] S_{\mathbf{p}} \\
&\quad - \mu \sum_{\mathbf{q}} (1 - \mathbf{v}_{\mathbf{p}} \cdot \mathbf{v}_{\mathbf{q}})g_{\mathbf{q}} \times \left[S_{\mathbf{q}} + (g_1^2 - g_3^2)S_{\mathbf{q}} + 2g_1^2 S_{\mathbf{q}}^* + 4g_1g_3 \right]
\end{aligned} \tag{6.3.2}$$

where \mathbf{q} stands for the other three modes.

In the 4-beam model, $\lambda = 0$. For the linear stability analysis, we look for exponentially growing solutions of the form $S_q = Q_q e^{-i\Omega t}$, where $\Omega = \gamma + i\kappa$ is complex. A positive non-zero κ indicates an instability in the system and $\kappa \sim \mu$ indicates fast oscillations.

6.3.1 Linearized analysis of the model

The left-right symmetry of the intersecting 4-beam model can be used to combine the neutrino-antineutrino amplitudes into $Q_{\pm} \equiv (Q_L \pm Q_R)/2$ and $\bar{Q}_{\pm} \equiv (Q_{\bar{L}} \pm Q_{\bar{R}})/2$. This allows us to decouple the equations for four modes into two sets of two. Within the SM, the first set consists of (Q_+, \bar{Q}_+) , which is the left-right symmetric solution that undergoes slow collective oscillations, and the second set consists of (Q_-, \bar{Q}_-) , which is the left-right symmetry-breaking solution that undergoes fast oscillations [119].

We find that the narrative of fast oscillations changes significantly in the presence of NSSI.

(i) For the symmetry breaking solution, FV-NSSI (FP-NSSI) increases (decreases) the available parameter space for fast oscillations. In fact, for FV-NSSI, oscillations can happen even for $\cos \theta < 0$ which was not possible in the SM.

(ii) Within the SM, fast oscillations are possible for (Q_+, \bar{Q}_+) only if spatial homogeneity

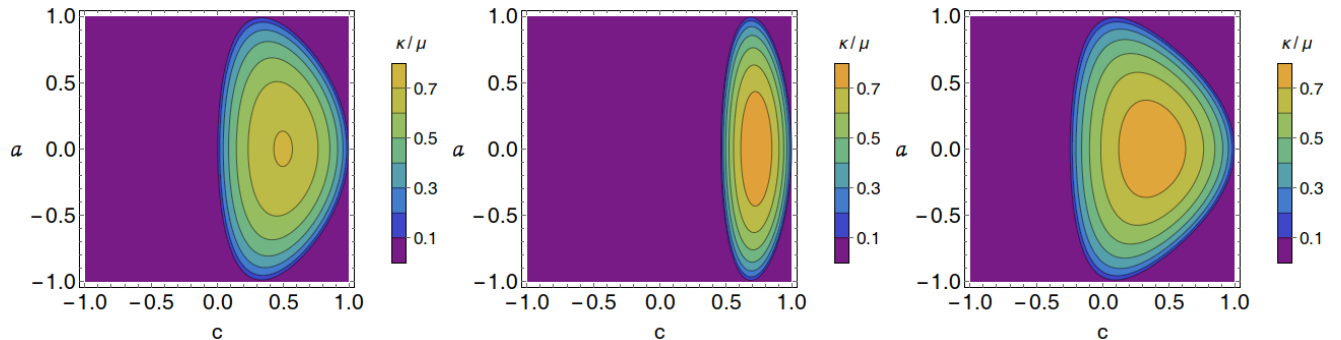


Figure 6.3: Dependence of growth rates on $c \equiv \cos \theta$ and the $\nu - \bar{\nu}$ asymmetry a , for the left-right symmetry-breaking solution (Q_-, \bar{Q}_-) . Left: $g_1, g_3 = 0$, Middle: $g_1 = 0, g_3 = 0.3$, Right: $g_1 = 0.3, g_3 = 0$.

of the beam is broken. However, the presence of FV-NSSI allows for fast oscillations even for homogeneous beams.

We now demonstrate the above features in the context of linear stability analysis. We work in the approximation where only either g_1 or g_3 is non-zero, and the $g_1^2 S_{\mathbf{q}}^*$ from Eq. (6.3.2) can be neglected. We have numerically checked that the latter is a good approximation for $g_1 \lesssim \mathcal{O}(0.5)$. It is now possible to understand the above features analytically, by writing down eigenvalue equations in the form

$$\Omega \begin{pmatrix} Q_{\pm} \\ \bar{Q}_{\pm} \end{pmatrix} = \begin{pmatrix} \mathcal{H}_{11} & \mathcal{H}_{12} \\ \mathcal{H}_{21} & \mathcal{H}_{22} \end{pmatrix} \begin{pmatrix} Q_{\pm} \\ \bar{Q}_{\pm} \end{pmatrix}, \quad (6.3.3)$$

where \mathcal{H}_{ij} 's and the corresponding eigenvalues are given in Appendix A. Note that in order to isolate fast oscillations, the eigenvalues are calculated in the limit $\omega/\mu \rightarrow 0$. This also automatically makes the analysis energy independent.

In the case of left-right symmetry breaking solution (Q_-, \bar{Q}_-) , non-zero complex eigenvalues are obtained for $\omega/\mu \rightarrow 0$, indicating the presence of fast oscillations. In Fig. 6.3, we show the growth rates in units of μ in the $a - \cos \theta$ plane, in the absence of NSSI (left panel), as well as in the presence of either FP-NSSI (middle panel) or FV-NSSI (right panel). The following observations can be made.

(i) In the absence of NSSI, one finds non-zero growth rates only for $\cos \theta > 0$. This can be easily understood from Eq. (A1) and Eq. (A2) for $g_3 = 0$ and $g_1 = 0$ respectively. In

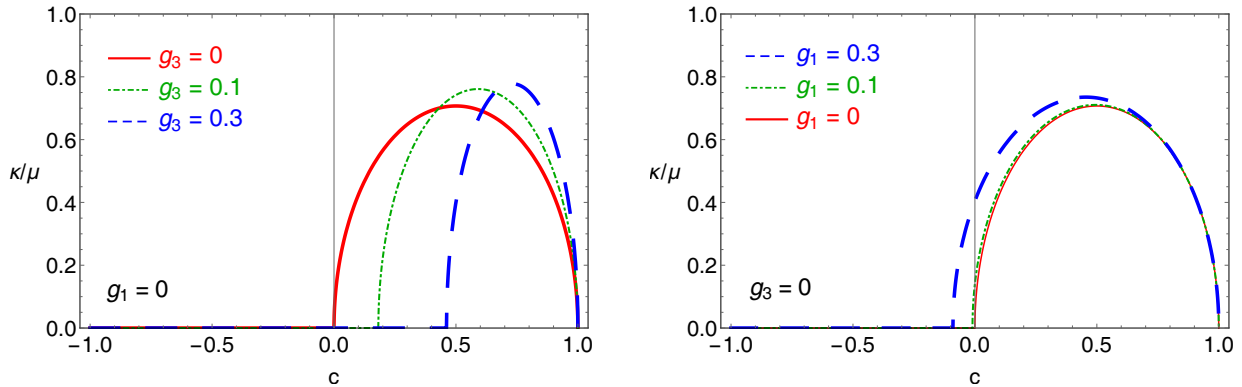


Figure 6.4: Growth rates at $a = 0$, as functions of $c \equiv \cos \theta$, for the left-right symmetry-breaking solution (Q_-, \bar{Q}_-) . Left: Only FP-NSSI. Right: Only FV-NSSI.

both cases, the argument of the square-root is never negative for $\cos \theta \leq 0$ and hence no instability occurs. In the scenario with instability, the growth rates do not depend on the sign of the neutrino-antineutrino asymmetry since the argument of the square-root depends on a^2 [119].

(ii) The presence of FP-NSSI suppresses fast oscillations, shifting the non-zero growth rates to higher values of $\cos \theta$. Larger values of FP-NSSI shift the domain of fast oscillations to more acute-angle modes. This results in the effective pinching of the allowed region in the $a - \cos \theta$ parameter space.

(iii) The presence of FV-NSSI, on the other hand, expands the domain of fast oscillations. As can be seen from the right panel of Fig. 6.3, FV-NSSI can lead to fast oscillations even with negative $\cos \theta$, i.e., the ν and $\bar{\nu}$ modes with obtuse intersection angles start showing fast oscillations. This effect becomes significant for $g_1 \sim \mathcal{O}(0.1)$.

In Fig. 6.4, we show the variation of the growth rates as a function of $\cos \theta$ for different values of g_3 (left) and g_1 (right). This gives a quantitative idea of the suppression and enhancement of the growth rate, with increasing g_3 and g_1 , respectively. Although both the plots are for zero neutrino-antineutrino asymmetry, we have checked that the features of the plot would remain unchanged with a non-zero asymmetry.

In the case of the left-right symmetric solution (Q_+, \bar{Q}_+) , the SM predicts no fast oscillations, since the eigenvalues in the limit $\omega/\mu \rightarrow 0$ are (see Appendix A)

$$\Omega_{\text{SM}}^{\pm} = \frac{\mu}{2} [a(3 - c) \pm \sqrt{a^2(3 - c)^2}], \quad (6.3.4)$$

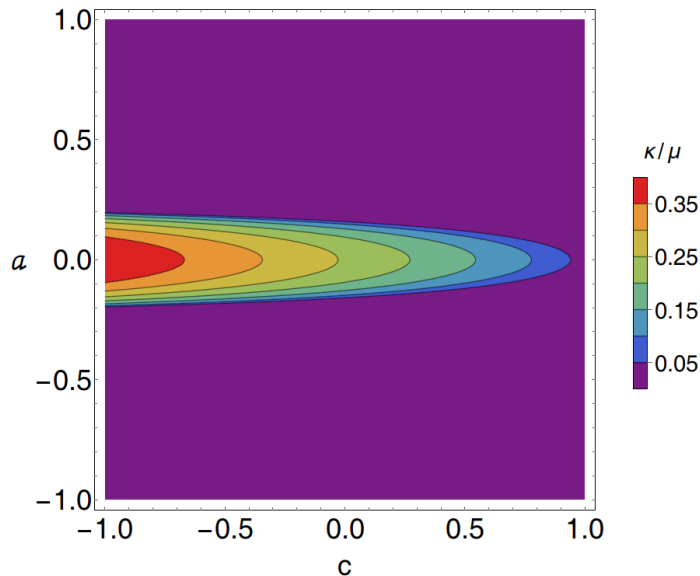


Figure 6.5: Dependence of growth rates on $c \equiv \cos \theta$ and the $\nu - \bar{\nu}$ asymmetry a , for the left-right symmetric solution (Q_+, \bar{Q}_+) , for $g_1 = 0.1$ and $g_3 = 0$.

which are always real. Also, in the presence of only FP-NSSI, the eigenvalues in Eq. (A3) can become complex only for $g_3 \gtrsim \mathcal{O}(1)$.

However, even with values of g_1 as small as 0.01, it is possible to get complex eigenvalues for Eq. (A4). In Fig. 6.5, we show the variation of the growth rates in the $a - \cos \theta$ plane for $g_1 = 0.1$. Clearly, large growth rates of $\mathcal{O}(\mu)$ are observed in the low-asymmetry region.

This opens up a new possibility for the back-to-back two-beam model, considered in [119], where spatial inhomogeneities were needed in order to start fast oscillations. In our intersecting 4-beam model, the scenario corresponds to the left-right symmetric solution (Q_+, \bar{Q}_+) with $c = -1$. In the presence of FV-NSSI, the eigenvalues are [see Eq. (A4)]

$$\Omega_{g_1}^+ = 2\mu \left[a (1 - g_1^2) \pm \sqrt{a^2 (1 + g_1^2)^2 - 4g_1^2} \right]. \quad (6.3.5)$$

Though $g_1 = 0$ would exhibit no instabilities, even for small values of g_1 , an instability would be developed for

$$|a| < \frac{2g_1}{(1 + g_1^2)}. \quad (6.3.6)$$

Thus, no spatial inhomogeneities would be needed for fast oscillations as long as the neutrino-antineutrino asymmetry a is sufficiently small. In Fig. 6.6, we show the growth rates as functions of a for different values of g_1 . Clearly larger g_1 values allow larger growth rates

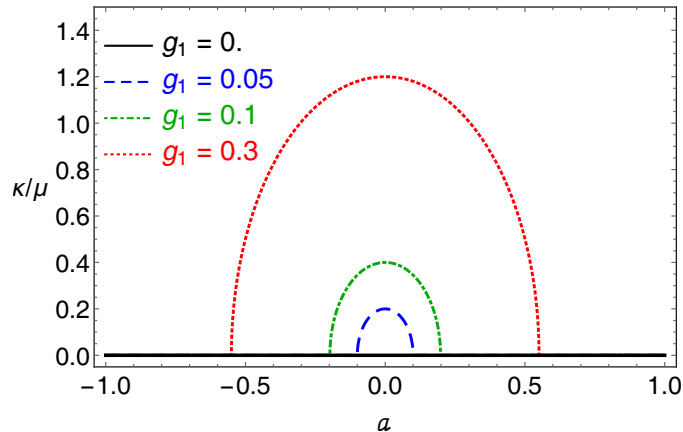


Figure 6.6: Growth rates in the effective two-beam scenario [the left-right symmetric solution (Q_+, \bar{Q}_+) with $c = -1$], as functions of neutrino-antineutrino asymmetry a .

and lead to instabilities even for larger asymmetries.

6.3.2 Interplay of fast and slow oscillations and NSSI

In this section, we demonstrate the effect of NSSI by numerically solving the fully non-linear equations of motion for the intersecting 4-beam system. The results relevant for the onset of fast oscillations are shown in Fig. 6.7. Note that the magnitude of the off-diagonal parameter $|S|$ is same for all the modes, and characterizes flavor conversions. The left panel shows the quantity $A_{e\mu} \equiv \log_{10}|S|$, which gives the amplitude of the flavor conversions, while the right panel shows $P_{e \rightarrow e}$, the ν_e survival probability. The following observations may be made.

(i) The time evolution of $A_{e\mu}$ in the SM shows an initial flat phase, followed by a sharp rise. This sharp rise corresponds to the onset of fast oscillations. The initial flat phase is an effect of non-zero ω . It does not succeed in causing large flavor conversions as can be seen from $P_{e \rightarrow e}$ in the left panel of Fig. 6.7.

(ii) As expected from the linear analysis, a non-zero g_3 delays the onset, whereas a non-zero g_1 reduces this initial waiting period. These effects start becoming appreciable when $g_1, g_3 \gtrsim \mathcal{O}(0.1)$.

(iii) The growth rate obtained from the numerical simulation is in good agreement with the calculations from the linear stability analysis.

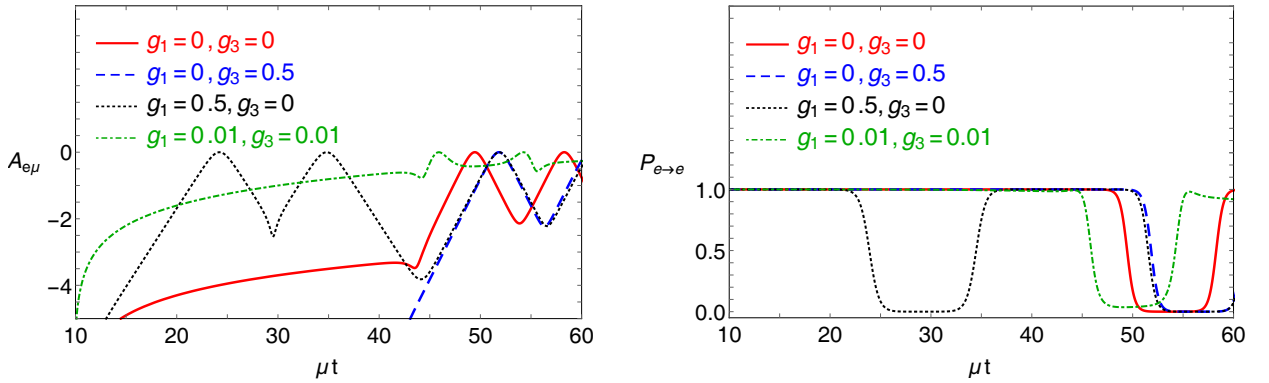


Figure 6.7: Onset of fast oscillations from the numerical solution of the fully nonlinear EoM, for $a = 0$ and $c = 0.5$. The other parameters are chosen to be $\omega/\mu_R = 10^{-5}$, and $\vartheta_0 = 10^{-2}$. The left panel shows quantity $A_{e\mu} = \log_{10}|S|$ which gives the extent of flavor conversion. The right panel shows the ν_e survival probabilities $P_{e \rightarrow e}$.

(iv) An eigenvalue equation was not possible when both FP-NSSI and FV-NSSI are present. However, the numerical solution verifies that the initial part of the dynamics is governed by a linear growth, as expected. As can be seen from $P_{e \rightarrow e}$, significant flavor conversion starts happening only when the exponential growth of oscillations takes over.

(v) Note that fast flavor oscillations are only sensitive to the asymmetries in the angular distributions of the neutrino-antineutrino beams, and energy only affects the onset, and not the rate. The subleading terms of order ω/μ act as a seed necessary for the onset of the oscillations. This does not affect the rate of oscillations, but only changes the initial waiting period [200].

This point is further elucidated in the left panel of Fig. 6.8, where we plot the quantity $|S|$. Small values of g_1 , in the absence of g_3 , do not affect the fast oscillations at all. On the other hand, when both g_1 and g_3 are non-zero, even when their values are $\mathcal{O}(0.01)$, an early linear rise as well as an early onset of exponential growth of oscillations may be observed. The fast oscillations seen at slightly later times seem to be riding on a slowly rising curve. This turns out to be a combined effect of slow oscillations and the early linear rise.

The right panel of Fig. 6.8 demonstrates the effect of NSSI on slow oscillations when fast oscillations are absent. Clearly, $g_1 \sim \mathcal{O}(0.01)$, even in the absence of g_3 , can shift the onset of slow oscillations to much earlier times. With the addition of a similar magnitude

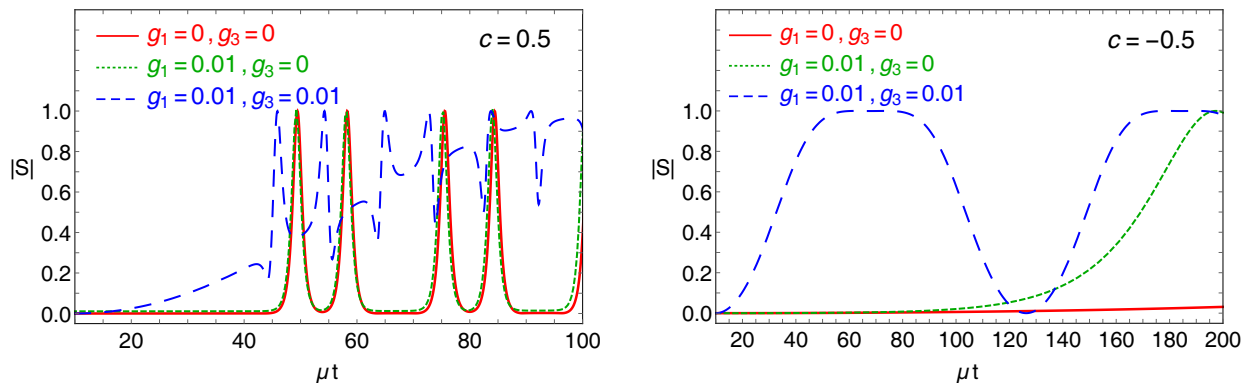


Figure 6.8: Onset of oscillation in terms of the off-diagonal parameter $|S|$ from the numerical solution of the fully nonlinear EoM for $a = 0$. The left panel shows the plot for $c = 0.5$ where we expect fast oscillations. The right panel shows the case $c = -0.5$, when fast oscillations are absent. The other parameters are chosen to be $\omega/\mu_R = 10^{-5}$, and $\vartheta_0 = 10^{-2}$.

of g_3 , the onset may be further hastened, bringing it in the domain of the onset of fast oscillations. Thus, it is possible for the oscillations to start deep inside the core, still keeping their frequencies small.

The long-time behavior of the non-linear oscillations would be an interplay of the fast and slow oscillations, influenced by NSSI. In Fig. 6.9, we show this long-time evolution of $|S|$ for different cases.

(i) In the SM ($g_1 = 0, g_3 = 0$), one can see fast oscillations with frequency $\sim \mu = 10^4 \text{ km}^{-1} = 0.03 \text{ s}^{-1}$, modulated by an envelope of slow oscillations with frequency $\sim \sqrt{\omega\mu} \approx 100 \text{ km}^{-1} = 0.0003 \text{ s}^{-1}$.

(ii) Small values of $g_1 \sim 0.005$ affect the slow oscillation frequency appreciably, while keeping the fast oscillations relatively unchanged. The modulating envelope increases in magnitude as well as frequency if g_1 is increased.

(iii) Non-zero values of g_3 does not affect the frequencies of fast and slow oscillation. However the modulating envelope decreases in amplitude. This is true both in the presence and absence of g_1 .

Larger values of NSSI also start affecting the frequency of fast oscillations. However, we will not explore such scenarios in this thesis.

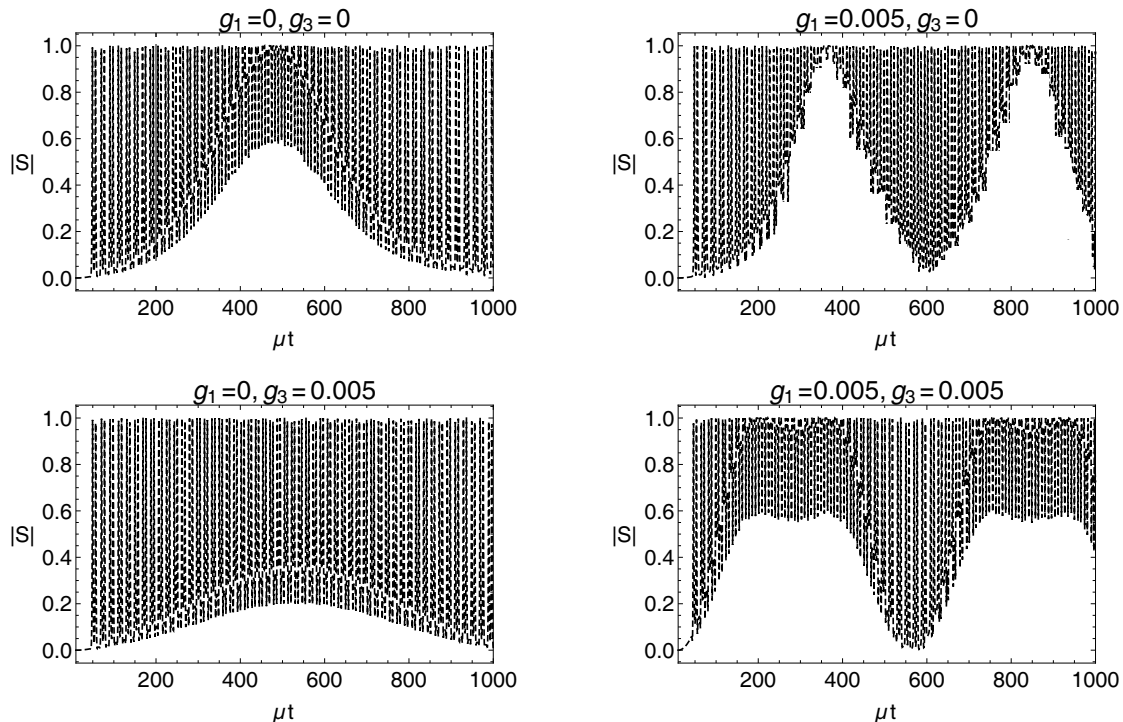


Figure 6.9: Long-time behavior of collective oscillations in terms of the off-diagonal parameter $|S|$ from the numerical solution of the fully nonlinear EoM for $a = 0$ and $c = 0.5$. The other parameters are chosen to be $\omega/\mu_R = 10^{-4}$, and $\vartheta_0 = 10^{-2}$. The rapid variations correspond to the fast oscillation frequency while the slowly changing envelope correspond to the slow oscillation frequency. The comparison of two columns indicates the effect of g_1 while the comparison of the rows indicates the effects of g_3 .

6.4 Summarized Results

We have investigated the effects of NSSI of neutrinos on collective flavor oscillations of neutrinos exiting a SN. Employing a linearized stability analysis, we have demonstrated how the exponentially growing flavor conversion modes are affected by the NSSI. While the linear stability analysis in SM leads to an eigenvalue equation, the most general EoM incorporating NSSI does not do so. Therefore, the problem of onset of oscillations, in complete generality, cannot be solved analytically. However, we have found that, if the system has only FP-NSSI, we get a straightforward eigenvalue equation, whose complex eigenvalue directly signals an instability. We have showed that if only FV-NSSI are present, an approximate eigenvalue equation can still be obtained, which motivates the enhanced growth rates observed in nu-

merical simulations. However, in the presence of both kinds of NSSI, we have found an additional linear contribution to $S_{\omega,u}$, which further complicates its evolution.

Using a simple two-box spectrum, we have analytically demonstrated the suppression of collective bipolar oscillations by FP-NSSI. This corresponds to the pinching of spectral swaps in presence of FP-NSSI, thereby explaining the results from previous literature. We have also shown that the presence of FV-NSSI increases the growth rate of flavor instabilities in the two-box spectrum.

We have also illustrated the NSSI effects on fast flavor oscillations, focussing on the intersecting 4-beam model, which is the simplest model where such effects can be analytically studied. For the symmetry-breaking modes, we have observed that the instability is restricted to a smaller region in the $a - \cos \theta$ plane with FP-NSSI, while FV-NSSI widens the corresponding region. Moreover, while the SM allows an instability only for $\cos \theta > 0$, the presence of FV-NSSI allows an instability even for an obtuse angle θ .

A striking corollary of the last result is that fast oscillations can take place for the two-beam system consisting of opposing neutrino and antineutrino beams, even in the absence of inhomogeneities. Indeed this scenario is equivalent to the left-right symmetric solution of the intersecting 4-beam model with $\cos \theta = -1$, where instability can be developed in the presence of FV-NSSI. This is in stark contrast to previous results in SM, where the two-beam system could exhibit fast oscillations only if spatial inhomogeneities were present. Clearly, the lepton flavor universality-breaking NSSI couplings now play the role of the symmetry-breaking seed required to give rise to an instability.

We have also solved the complete non-linear EoMs numerically for the 4-beam system, for the onset of oscillations as well as long-time behavior. It is observed that when both FP-NSSI and FV-NSSI are present, the extra linear contribution to S results in an initial linear growth, which may later be dominated by fast oscillations. However, in the situations where fast oscillations are absent, the same linear term helps in bringing the onset of slow collective oscillations to significantly earlier times. We have found that the long-time behavior of the system may be described by fast collective oscillations modulated by the slow ones. It is observed that FP-NSSI suppress the amplitude of these modulations while FV-NSSI enhance their amplitude and frequency.

Our main conclusion from this work is that NSSI can bring the fast as well as slow oscillations nearer to the core. Hence, they can have important consequences for the explosion mechanism and nucleosynthesis as flavor conversions can start occurring earlier. This indicates the importance of going beyond the approximation of a neutrinosphere and taking care of collisions in a neutrino oscillation analysis. Note that the effect of NSSI on the neutronization burst as calculated in [198] still stays valid.

Chapter 7

Conclusion

Neutrinos streaming through a dense media, like a core-collapse SN, may undergo non-linear flavor oscillations due to neutrino-neutrino forward scattering. Depending on the angular distributions of the emitted neutrinos, these oscillations can be “bipolar”, occurring with a rate proportional to $\sqrt{\omega\mu}$, or “fast”, occurring with a rate proportional to μ itself, where ω is a measure of the vacuum oscillation frequency, and μ is a measure of the neutrino density inside the supernova (SN). These oscillations are self-induced and collective. The work presented in this thesis aims to highlight some aspects of the collective flavor conversions of SN neutrinos, in the Standard Model (SM) and beyond.

While the bipolar oscillations have been a topic of intense research for more than a decade, fast oscillations are a relatively new topic. The study of fast oscillations has thus far been restricted to simple toy models of SN spectra. In these cases, the phenomenon was found to happen in physically less motivated scenarios for a SN, i.e., when the $\bar{\nu}_e$ s are in excess of ν_e s, but have a more forward peaked distribution [119]. It was also shown that fast conversions were suppressed by the background matter density. Ref. [118], on the other hand, found that these fast conversions were unaffected by the background matter. The results of these two groups were in contradiction. In [180], we made a detailed study of the presence fast flavor conversions in a SN, for realistic angular distributions of neutrinos, and a physically more plausible scenario, where ν_e s are in excess of $\bar{\nu}_e$ s. We focused on neutrino flavor dependent angular emission models, and studied flavor instabilities close to the neutrinosphere. Using a linear stability analysis, we categorized fast oscillations as temporal or spatial instabili-

ties. We found that while spatial instabilities are suppressed by ordinary matter, temporal instabilities are unaffected. This allowed us to resolve the contradictions among different groups in the existing literatures. We also performed a detailed numerical solution of the fully non-linear equations of motion for realistic angular emission spectra of neutrinos. We showed that an essential condition for the presence of fast oscillations is a crossing in the zenith angle spectra of neutrinos and antineutrinos. Using fluxes and angular distributions predicted by supernova simulations, we found that fast conversions can occur within tens of nanoseconds, only a few meters away from the neutrinosphere. If these fast flavor conversions indeed take place, they would have important implications for the supernova explosion mechanism and nucleosynthesis.

To get a more intuitive understanding of fast flavor conversions, in [200] we developed the analytical framework of the simplest system that exhibits fast flavor conversions: a set of four intersecting beams of neutrinos and antineutrinos. Under certain simplifying assumptions, we analytically demonstrated that a simple classical analog with a quartic oscillator can explain fast flavor conversions in this system. Fast oscillations correspond to inversion of this quartic potential, leading to an instability in the system. We identified that although the fast oscillations are governed mainly by the neutrino self-potential, the onset depends logarithmically on the subleading terms associated with the vacuum mixing. We provided a semi-analytical expression of the time period of fast oscillations. This vastly simplified our understanding of fast oscillations, and allowed us to associate an elegant classical picture with this quantum phenomenon.

Another fairly unexplored topic in collective oscillations was the impact of non-standard self-interactions (NSSI) of neutrinos on these self-induced flavor conversions. While the framework for studying such flavor-violating NSSI in the context of collective oscillations was developed a decade ago, much remains to be explored. Motivated by this, in [198] we redevelop the formalism to study the impact of both flavor-violating NSSI (FV-NSSI) and flavor-preserving NSSI (FP-NSSI) in the context of collective oscillations. Surprisingly, we found that the presence of NSSI questions many of the well-known results of flavor evolutions of dense streams. Numerically, we found that FP-NSSI suppresses collective oscillations, while FV-NSSI aids in flavor conversion. One of the most interesting and unexpected observations was that presence of FV-NSSI can allow for collective oscillations even during

the neutronization burst phase, which was not possible within the SM. This would result in distinct observable splits in the ν_e spectrum during the neutronization burst epoch, which would be a smoking-gun signal for the presence of NSSI. Using a realistic ν_e spectrum during the neutronization burst and taking into account the effect of MSW resonance inside the SN, we showed the observable effects of collective oscillations on the neutrino spectra in the upcoming liquid Argon based detectors. We found that large number of events are expected in next generation detectors, and therefore, it should be possible to distinguish these spectral splits, leading to identification of NSSI.

We realized that the behavior of collective oscillations in the presence of NSSI could be motivated analytically by the linear stability analysis. We redid the stability analysis in presence of NSSI in [201]. Using it, we demonstrated that indeed FP-NSSI suppresses collective oscillations, while FV-NSSI enhances them. Furthermore, we found that if both FP-NSSI and FV-NSSI are present, one encounters linearly increasing solutions, in addition to exponentially growing ones. Using simple toy models, we showed that such linear solutions may lead to an earlier onset of collective oscillations, leading to substantial flavor conversions behind the stalled shockwave.

Finally, we focused on the impact of NSSI on fast flavor conversions in simple toy models. In order to study their effects, we took resort to both numerical simulations as well as the stability analysis. We observed that for rapidly growing temporal solutions, FP-NSSI suppresses fast conversions. This is highly relevant, as within the SM, it is not possible to suppress fast-growing time instabilities even with a finite matter density. Furthermore, FV-NSSI increases the growth rate of fast oscillations, causing them to happen even deeper inside the neutrinosphere. This immediately calls for a study of fast oscillations, incorporating inelastic collisions into account. We also numerically studied the long-term behavior of the system in presence of FP-NSSI and/or FV-NSSI. We showed that typically the fast oscillations appear as rapid fluctuations modulated by the comparatively slower bipolar oscillations. This allowed for a clear demonstration of the different oscillation timescales associated with flavor conversion of dense neutrino streams.

However, note that all works on neutrino flavor conversions in this thesis neglect non-forward scatterings and collisions of neutrinos with the surrounding. This is justified because

the slow bipolar collective oscillations as well as the MSW flavor conversions take place far away from the neutrinosphere, and hence collisions are negligible in that domain. However, as we indicated in Chapter 6, presence of fast flavor conversions indicates the importance of going beyond the approximation of a neutrinosphere and taking care of collisions in a neutrino oscillation analysis. The study of flavor evolution in presence of collisions is a boundary value problem, where neutrinos of definite flavor stream out from the neutrinosphere. Therefore, given the initial conditions at an inner boundary, one can solve a system of coupled partial differential equations to study flavor evolution. However, the presence of very rapid flavor conversions deep inside a SN invalidates the concept of a sharp emission boundary, from where the unoscillated neutrino fluxes emerge. The boundary conditions become fuzzy and complete flavor averaging takes place within a few nanoseconds, leading to loss of flavor information. A consistent study of flavor evolution in presence of collisions is ongoing [202]. In Appendix B, we give a brief discussion of the effects of collision on fast flavor conversions.

Finally, all works in this thesis use a two-neutrino framework and a single-angle approximation. A more realistic treatment will require a detailed three flavor study, with the inclusion of multi-angle effects and matter effects. This will indeed be relevant in the formation of the neutrino spectra and dynamics of the SN core.

Thus, summarizing, the crux of the thesis broadly consists of two aspects of self-induced collective oscillations of neutrinos in dense environments. The first aspect focused on fast conversions, causing rapid flavor conversions immediately close to the neutrinosphere. The second aspect considered effects of NSSI of neutrinos on collective oscillations. Finally, we combined the two aspects and studied the effects of NSSI on fast flavor conversions. We hope that this thesis helps in a better understanding of the dynamics of neutrino flavor evolution in a core-collapse supernova.

Appendix A

Analytical aspects of NSSI and fast flavor conversions

A.1 The eigenvalues of the Hamiltonian in the 4-beam model

The expressions of the \mathcal{H} matrix elements in Eq. (6.3.3), for the L-R symmetric and symmetry breaking solutions, are given below. ¹

A.1.1 L-R Symmetric solution (Q_+, \bar{Q}_+)

For $g_1 = 0, g_3 \neq 0$, one has

$$\begin{aligned}\mathcal{H}_{11} &= \omega + \frac{\mu}{2} \left[(1 + g_3) \left(c - 3 + g_3(-5 + 7c) + a(3 - c + 13g_3 + cg_3) \right) \right], \\ \mathcal{H}_{12} &= \frac{\mu}{2} (1 - a)(3 - c)(1 - g_3^2), \\ \mathcal{H}_{21} &= -\frac{\mu}{2} (1 + a)(3 - c)(1 - g_3^2), \\ \mathcal{H}_{22} &= -\omega + \frac{\mu}{2} \left[(1 + g_3) \left((1 + a)(3 - c) + g_3(5 - 7c + 13a + ac) \right) \right].\end{aligned}$$

Similarly, for $g_1 \neq 0, g_3 = 0$, one has

¹This is relevant to Chapter 6 of this thesis.

Solution	Eigenvalue
(Q_-, \bar{Q}_-) $g_1 = 0, g_3 \neq 0$	$\Omega_{g_3}^- = \frac{\mu}{2} \left\{ a[5 + c + 16g_3 + (11 - c)g_3^2] \pm \sqrt{a^2(1+c)^2(1-g_3^2)^2 - 8(1-c)(1+g_3)^2(1+3g_3)[c(1+g_3) - 2g_3]} \right\} \quad (\text{A1})$
(Q_-, \bar{Q}_-) $g_1 \neq 0, g_3 = 0$	$\Omega_{g_1}^- = \frac{\mu}{2} \left\{ a[5 + c - g_1^2(3 - c)] \pm \sqrt{a^2(1+c)^2(1+g_1^2)^2 - 8(1-c)(1-g_1^2)(c+g_1^2)} \right\} \quad (\text{A2})$
(Q_+, \bar{Q}_+) $g_1 = 0, g_3 \neq 0$	$\Omega_{g_3}^+ = \frac{\mu}{2}(1 + g_3) \left\{ a[3 - c(1 - g_3) + 13g_3] \pm \sqrt{a^2(3-c)^2(1-g_3)^2 + 16g_3(1-c)[3 - c + g_3(1 - 3c)]} \right\} \quad (\text{A3})$
(Q_+, \bar{Q}_+) $g_1 \neq 0, g_3 = 0$	$\Omega_{g_1}^+ = \frac{\mu}{2} \left\{ -a[(c + 5)g_1^2 + c - 3] \pm \sqrt{a^2(c-3)^2(1+g_1^2)^2 - 8g_1^2(1-c)[(1+c)g_1^2 - c + 3]} \right\} \quad (\text{A4})$

Table A.1: Eigenvalues of Eq. (6.3.3) for the four cases described in this Appendix, with $\omega = 0$.

$$\begin{aligned} \mathcal{H}_{11} &= \omega + \frac{\mu}{2} \left[g_1^2 - 3cg_1^2 + c - 3 - a((c+5)g_1^2 + c - 3) \right], \\ \mathcal{H}_{12} &= \frac{\mu}{2}(1-a)(3-c)(1+g_1^2), \\ \mathcal{H}_{21} &= -\frac{\mu}{2}(1+a)(3-c)(1+g_1^2), \\ \mathcal{H}_{22} &= -\omega - \frac{\mu}{2} \left[(1+a)(c-3) + g_1^2(1-3c+a(c+5)) \right]. \end{aligned}$$

A.1.2 L-R Symmetry breaking solution (Q_-, \bar{Q}_-)

For $g_1 = 0, g_3 \neq 0$, one has

$$\begin{aligned}\mathcal{H}_{11} &= \omega + \mu \left[\frac{1}{2}(1+a)(1+c)(1-g_3^2) + (1+4g_3+3g_3^2)(2a+c-1) \right], \\ \mathcal{H}_{12} &= -\frac{\mu}{2}(1-a)(1+c)(1-g_3^2), \\ \mathcal{H}_{21} &= \frac{\mu}{2}(1+a)(1+c)(1-g_3^2), \\ \mathcal{H}_{22} &= -\omega + \mu \left[-\frac{1}{2}(1-a)(1+c)(1-g_3^2) + (1+4g_3+3g_3^2)(2a-c+1) \right].\end{aligned}$$

Similarly, for $g_1 \neq 0, g_3 = 0$, one has

$$\begin{aligned}\mathcal{H}_{11} &= \omega + \mu \left[\frac{1}{2}(1+a)(1+c)(1+g_1^2) + (1-g_1^2)(2a+c-1) \right], \\ \mathcal{H}_{12} &= -\frac{\mu}{2}(1-a)(1+c)(1+g_1^2), \\ \mathcal{H}_{21} &= \frac{\mu}{2}(1+a)(1+c)(1+g_1^2), \\ \mathcal{H}_{22} &= -\omega + \mu \left[-\frac{1}{2}(1-a)(1+c)(1+g_1^2) + (1-g_1^2)(2a-c+1) \right].\end{aligned}$$

The corresponding eigenvalues, in the limit $\omega/\mu \rightarrow 0$, are listed in Table A.1. We put $\omega = 0$ since we are only interested in the coefficient of μ for fast oscillations.

Appendix B

Collisions and flavor conversions

B.1 What role does collision play?

In this appendix, we study the effects of collisions on fast flavor conversions deep inside a SN core. Very close to the neutrinosphere, collisions might happen with a rate similar to the rate of fast oscillations and hence cannot be neglected. A typical back-of-the-envelope calculation, using a nucleon density $n_B = \rho_{\text{nuc}}/m_N \approx 1.8 \times 10^{38} \text{ cm}^{-3}$ and the neutrino-nucleon scattering cross-section $\sigma \sim G_F^2 E^2 \sim 10^{-42} \text{ cm}^{-2}$ for $E_\nu \sim 10 \text{ MeV}$, suggests that the scattering rate is $\Gamma = \sigma n_B \sim 10^7 \text{ s}^{-1}$. Thus, neutrinos produced inside a supernova undergo a number of collisions before they can finally free-stream. The stellar medium consists of protons, neutrons, electrons, positrons and neutrinos of all flavors. As explained in Chapter 1, a huge fraction of the emitted neutrinos is composed of electron neutrinos, while muon and tau neutrinos are much more scarce. These electron neutrinos are kept in thermal equilibrium due to charged current beta processes of the form $\nu_e + n \rightarrow e^- + p$ and $\bar{\nu}_e + p \rightarrow e^+ + n$. Beyond the neutrinosphere $\equiv R_{\text{NS}}$, these neutrinos can free-stream. Their spectrum is usually considered to be a quasi thermal spectrum with the temperature being that of the medium. While the electron flavor can undergo charged current(CC) interactions as well as neutral current (NC), the other flavors interact primarily by NC processes. The neutrinosphere might contain a few muons, however the emitted neutrinos do not carry enough energy to undergo CC interactions with muons.

Therefore, the neutrino interactions within a SN core can be classified into two main

Types of Scattering	Examples	Decouples at
Charged Current Number Changing (CCNC)	$\nu_e n \leftrightarrow p e^-$, $\bar{\nu}_e p \leftrightarrow n e^+$, $\nu_e \bar{\nu}_e \leftrightarrow e^+ e^-$.	R_{NS} R_{NS} R_{ES}
Charged Current Momentum Changing (CCMC)	$\nu_e e^- \leftrightarrow \nu_e e^-$, $\bar{\nu}_e e^+ \leftrightarrow \bar{\nu}_e e^+$,	R_{ES} R_{ES}
Neutral Current Number Changing (NCNC)	$NN \nu_{e,x} \bar{\nu}_{e,x} \leftrightarrow NN$, $\nu_e \bar{\nu}_e \leftrightarrow e^+ e^-$, $\nu_e \bar{\nu}_e \leftrightarrow \nu_x \bar{\nu}_x$.	R_{ES} R_{ES} R_{ES}
Neutral Current Momentum Changing (NCMC)	$\nu_{e,x} X \leftrightarrow \nu_{e,x} X$. $\nu_x e^- \leftrightarrow \nu_x e^-$, $\bar{\nu}_x e^+ \leftrightarrow \bar{\nu}_x e^+$,	R_{TS} R_{ES} R_{ES}

Table B.1: Table showing the different neutrino interactions within a SN core. The radii of the different decoupling regions follow $R_{\text{ES}} < R_{\text{TS}} < R_{\text{NS}}$.

categories: CC interactions and NC interactions. Furthermore, these processes can either conserve the number of neutrinos or modify it. The classification is shown in Table B.1. All these interactions occur at different rates and play an important role in keeping the neutrinos in local thermal equilibrium. For example, neutrino bremsstrahlung as well as pair production and absorption allow for exchange of energy with the medium, thereby keeping the neutrinos in thermal equilibrium up to the energysphere $\equiv R_{\text{ES}}$. Beyond this, the neutrinos can still undergo nucleonic collisions without exchanging energy and can diffuse upto the transportsphere $\equiv R_{\text{TS}}$, after which they can stream out freely. The different regions are shown in Fig.B.1.

In Fig.B.2, we plot the various interaction rates as a function of distance from the SN

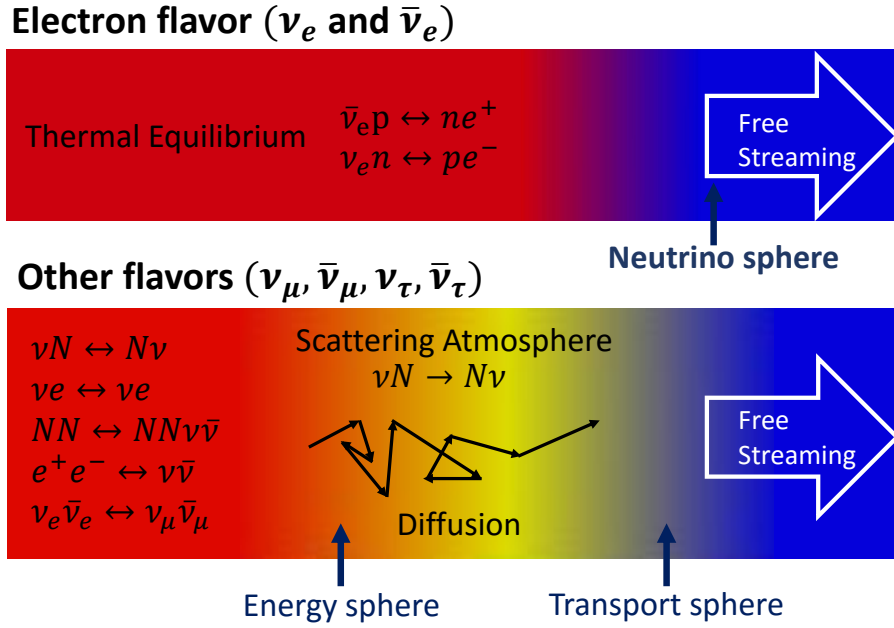


Figure B.1: Schematic plot showing the neutrinosphere, energysphere and transportsphere [68]. The different interaction channels decoupling at different radii are also shown.

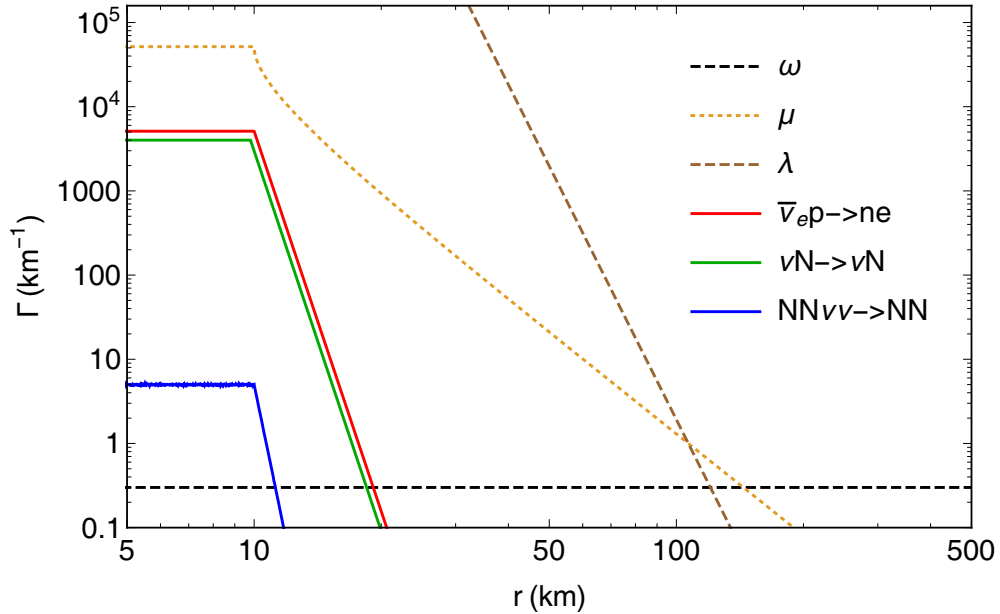


Figure B.2: Plot showing the different interaction rates as a function of the distance from the SN core. Processes occurring with rates smaller than bremsstrahlung are not shown.

core. We consider the density and temperature profiles given by [68] :

$$\rho = \begin{cases} 2 \times 10^{14} \text{ g cm}^{-3} & r \leq r_0 \\ 2 \times 10^{14} \text{ g cm}^{-3} \left(\frac{r_0}{r}\right)^{10} & r > r_0 \end{cases}$$

$$T = \begin{cases} 31.66 \text{ MeV} & r \leq r_0 \\ 31.66 \text{ MeV} \left(\frac{r_0}{r}\right)^{2.5} & r > r_0 \end{cases}$$

where $r_0 = 10$ km is taken to be the radius of the core. The profile for μ is taken from [91]. Our results indicate that very close to the neutrinosphere, the charged current interactions and neutrino-nucleon scatterings clearly dominate all other interaction rates, as indicated in Fig.B.2. In this case, these can be comparable to the neutrino self interaction potential μ . The rates involving neutrino pair-production are clearly much smaller (by a factor of $\mathcal{O}(10^3)$) because the neutrino density near the core is much smaller than the electron density. The other interaction rates are smaller and hence not shown in the figure. Hence, while studying fast conversions, one has to consider the impact of charged current processes and neutrino-nucleon scatterings. Note that we have considered that μ is also a constant immediately below the neutrinosphere. Strictly, this need not be the case. Certain simulations show that even below the neutrinosphere, μ can dominate over the collision rates [203].

B.1.1 Flavor evolution in presence of collisions

In presence of collisions, one cannot neglect the $\mathcal{C}[\varrho_{\mathbf{p},\mathbf{x},t}]$ term in Eq.[2.2.1]. The contribution to $\mathcal{C}[\varrho_{\mathbf{p},\mathbf{x},t}]$ can come from net neutrino number-preserving as well as net neutrino number-changing processes. As a result, $\text{Tr}[\varrho]$ (which measures the total number of neutrinos in the system) as well as $\text{Tr}[\varrho^2]$ (which is a measure of coherence) need not be preserved. This renders linearization of the problem difficult and one must work in the fully non-linear regime to have a correct understanding of the effect of collisions.

The collision term, including all types of relevant scattering terms, is given by [170]:

$$\begin{aligned}
\mathcal{C}[\varrho_{\mathbf{p},\mathbf{x},t}] = & \underbrace{\int d\mathbf{p}' \left(\mathcal{M}_{\mathbf{p}',\mathbf{p}}^{\nu X} G^{\text{NC}} \varrho_{\mathbf{p}'} G^{\text{NC}} (1 - \varrho_{\mathbf{p}}) - \mathcal{M}_{\mathbf{p},\mathbf{p}'}^{\nu X} \varrho_{\mathbf{p}} G^{\text{NC}} (1 - \varrho_{\mathbf{p}'}) G^{\text{NC}} + \text{h.c.} \right)}_{\nu X \text{ scattering}} \\
& + \underbrace{\int_{\omega' < 0} d\mathbf{p}' \left(\mathcal{M}_{\mathbf{p}',\mathbf{p}}^{Y \rightarrow \nu \bar{\nu} X} (1 - \varrho_{\mathbf{p}}) G^{\text{NC}} (1 - \varrho_{\mathbf{p}'}) G^{\text{NC}} - \mathcal{M}_{\mathbf{p},\mathbf{p}'}^{\nu \bar{\nu} X \rightarrow Y} \varrho_{\mathbf{p}} G^{\text{NC}} \varrho_{\mathbf{p}'} G^{\text{NC}} + \text{h.c.} \right)}_{\nu \text{ pair-creation/annihilation terms}} \\
& + \underbrace{\int d\mathbf{p}' \left(\left\{ \mathcal{M}_{\mathbf{p},\mathbf{p}'}^{\text{CC prod}} G^{\text{CC}}, 1 - \varrho_{\mathbf{p}} \right\} - \left\{ \mathcal{M}_{\mathbf{p},\mathbf{p}'}^{\text{CC ann}} G^{\text{CC}}, \varrho_{\mathbf{p}} \right\} \right)}_{\text{CCNC } \nu_e, \bar{\nu}_e \text{ terms}},
\end{aligned} \tag{B.1.1}$$

where $\mathcal{M}_{(\mathbf{p},\mathbf{p}')}^\alpha$ gives the matrix-amplitude squared for a particular process denoted by α ,

and $\{\cdot, \cdot\}$ denotes the anticommutator. The coupling matrices G^{NC} give the NC coupling of the different neutrino flavors to the SM particles. From Fig. B.2, one can see that among all possible NC inelastic scattering processes taking place, those with nucleons dominate, and we only consider them in our analysis. This simplifies the scenario since neutrinos have a flavor independent NC coupling to nucleons, and therefore G^{NC} is proportional to the identity matrix. It must also be remembered that within a SN, only the electron neutrinos have CC interactions and hence $G^{\text{CC}} \propto \text{diag}\{1, 0\}$.

Further simplifications may be achieved by assuming a dilute gas approximation and neglecting the Pauli blocking factors arising due to the fermionic nature of neutrinos. This leads to the following form for Eq. (B.1.1)

$$\begin{aligned}
\mathcal{C}[\varrho_{\mathbf{p},\mathbf{x},t}] &= \underbrace{-\Gamma_{\mathbf{p}}^{\nu X} [G^{\text{NC}}, [G^{\text{NC}}, \varrho_{\mathbf{p},\mathbf{x},t}]]}_{\nu X \rightarrow \nu X} \\
&+ \underbrace{2\Gamma_{\mathbf{p}}^{(Y \rightarrow \nu \bar{\nu} X)} G^{\text{NC}} G^{\text{NC}}}_{\nu \text{ pair production terms}} + \underbrace{2\Gamma_{\mathbf{p}}^{\text{CC}_{\text{prod}}} G^{\text{CC}}}_{\text{CCNC } \nu_e, \bar{\nu}_e \text{ production}} \\
&- \underbrace{\Gamma_{\mathbf{p}}^{(\nu \bar{\nu} X \rightarrow Y)} \{\varrho_{\mathbf{p},\mathbf{x},t}, G^{\text{NC}} \varrho_{\mathbf{p}',\mathbf{x}',t} G^{\text{NC}}\}}_{\nu \text{ pair annihilation terms}} - \underbrace{\{\Gamma_{\mathbf{p}}^{\text{CC}_{\text{ann}}} G^{\text{CC}}, \varrho_{\mathbf{p},\mathbf{x},t}\}}_{\text{CCNC } \nu_e, \bar{\nu}_e \text{ annihilation}},
\end{aligned} \tag{B.1.2}$$

where the quantity $\Gamma_{\mathbf{p}}^{\alpha} = \int d\mathbf{p}' \mathcal{M}_{(\mathbf{p},\mathbf{p}')}^{\alpha}$. We have also assumed that $\mathcal{M}_{(\mathbf{p},\mathbf{p}')}^{\alpha} = \mathcal{M}_{(\mathbf{p}',\mathbf{p})}^{\alpha}$. Note that since G^{NC} is proportional to the identity matrix, the terms that originate from neutrino-nucleon scattering ($\nu X \rightarrow \nu X$) drop out of the EoMs. Recently, an attempt to study the effect of collisions on neutrino flavor evolution in a dense media was made in [204]. The authors considered neutral current momentum changing processes of the form $\nu X \rightarrow \nu X$ and found that at small scales, flavor instabilities can be suppressed by collisions. Since the process considered preserves $\text{Tr}[\varrho]$, a linearized stability analysis can be performed in a straightforward manner. The authors, following [205], use a form of the collision kernel involving anticommutators of ϱ , which is more similar to the CC form. However, as outlined in [50], processes of the form $\nu X \rightarrow \nu X$ contribute to the EoM in the form $[G^{\text{NC}}, [G^{\text{NC}}, \varrho]]$, where G^{NC} is proportional to identity. As a result, such processes do not lead to damping. In this appendix, we follow the latter convention.

Working in the 2-neutrino flavor approximation, one can expand all the 2×2 matrices in

Eq. (B.1.2) in the Pauli basis (see Eq. (2.2.6)). However, since the total number of neutrinos is not conserved in the presence of collisions, we consider a different normalization for the polarization vectors than what is considered in Eq. (2.2.6). In particular, we consider

$$\begin{aligned}
\varrho_{\mathbf{p}} &= \frac{f_{\mathbf{p}}}{2} (\mathbb{I} + \mathbf{P}_{\mathbf{p}} \cdot \boldsymbol{\sigma}) , \\
\bar{\varrho}_{\mathbf{p}} &= \frac{\bar{f}_{\mathbf{p}}}{2} (\mathbb{I} + \bar{\mathbf{P}}_{\mathbf{p}} \cdot \boldsymbol{\sigma}) , \\
G^{\text{CC}} &= \frac{1}{2} (\mathbb{I} + \hat{\mathbf{z}} \cdot \boldsymbol{\sigma}) \\
G^{\text{NC}} &= \mathbb{I}
\end{aligned} \tag{B.1.3}$$

since now $f_{\mathbf{p}}$ and $\bar{f}_{\mathbf{p}}$ have dynamics of their own. The rest of the definition remains the same as Eq. (2.2.6).

Using Eq. (B.1.3), the corresponding polarization vector equations take the following form:

$$\begin{aligned}
\dot{\mathbf{P}}_{\mathbf{p}} &= \left[\omega_{\mathbf{p}} \mathbf{B} + \lambda \mathbf{L} + \mu \int d\mathbf{p}' (1 - \mathbf{v} \cdot \mathbf{v}') \mathbf{P}_{\mathbf{p}'} \right] \times \mathbf{P}_{\mathbf{p}} - \frac{\dot{f}_{\mathbf{p}}}{f_{\mathbf{p}}} \mathbf{P}_{\mathbf{p}} \\
&\quad - \Gamma_{\mathbf{p}}^{(\nu\bar{\nu}X \rightarrow Y)} \bar{f}_{\mathbf{p}'} \left(\bar{\mathbf{P}}_{\mathbf{p}'} + \mathbf{P}_{\mathbf{p}} \right) + 2 \left(\frac{\Gamma_{\mathbf{p}}^{\text{CCprod}}}{f_{\mathbf{p}}} \hat{\mathbf{z}} - \frac{\Gamma_{\mathbf{p}}^{\text{CCann}}}{2} (\mathbf{P}_{\mathbf{p}} + \hat{\mathbf{z}}) \right) ,
\end{aligned} \tag{B.1.4}$$

$$\begin{aligned}
\dot{f}_{\mathbf{p}} &= \left(4\Gamma_{\mathbf{p}}^{(Y \rightarrow \nu\bar{\nu}X)} - \Gamma_{\mathbf{p}}^{(\nu\bar{\nu}X \rightarrow Y)} \left[f_{\mathbf{p}} \bar{f}_{\mathbf{p}'} + f_{\mathbf{p}} \bar{f}_{\mathbf{p}'} \mathbf{P}_{\mathbf{p}} \cdot \bar{\mathbf{P}}_{\mathbf{p}'} \right] \right) \\
&\quad + 2 \left(\Gamma_{\mathbf{p}}^{\text{CCprod}} - \frac{f_{\mathbf{p}}}{2} \Gamma_{\mathbf{p}}^{\text{CCann}} - \frac{f_{\mathbf{p}}}{2} \Gamma_{\mathbf{p}}^{\text{CCann}} \hat{\mathbf{z}} \cdot \mathbf{P}_{\mathbf{p}} \right) .
\end{aligned} \tag{B.1.5}$$

Similar equations also hold for the antineutrinos with the following replacements, $\omega \rightarrow -\omega$, $\mathbf{P}_{\mathbf{p}} \rightarrow \bar{\mathbf{P}}_{\mathbf{p}}$ and $f_{\mathbf{p}} \rightarrow \bar{f}_{\mathbf{p}}$.

This is the most general EoM for neutrinos propagating in a dense medium and undergoing non-forward scatterings. As is clear from Fig.B.2, the only relevant processes which occur with a rate comparable to μ are the CC interactions. All the other processes have rates much smaller than μ and are neglected in this study. Although, the rates for production and annihilation can be different, we confine ourself to the regime of detailed balance and hence set $\Gamma_{\mathbf{p}}^{\text{CCprod}} = \Gamma_{\mathbf{p}}^{\text{CCann}} = \Gamma_{\text{CC}}$.

Ideally, one should perform a self-consistent study of the formation of neutrino angular distributions by collisions and then track the possible flavor changes due to fast oscillations. However, the relevant length scales for fast conversions are too small to be resolved by current SN simulations. Hence we do a parametric study of the effects of Γ_{CC} on fast flavor

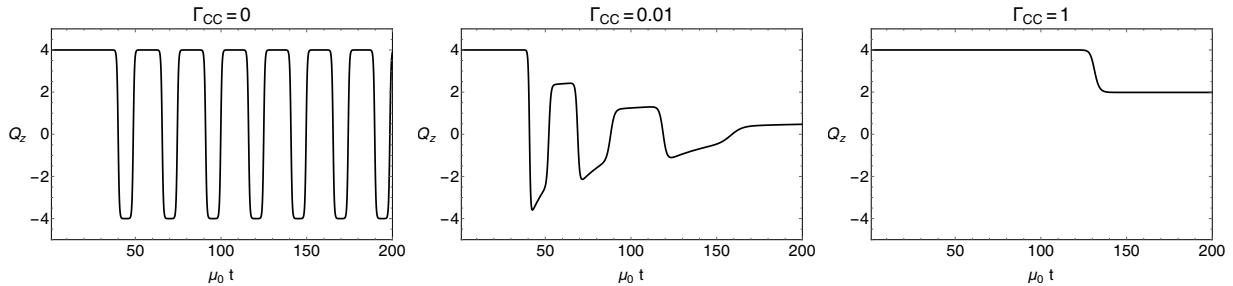


Figure B.3: Dynamics of the z -components of \mathbf{Q} , given by Q_z in presence of collisions. The parameters are chosen to be $\omega/\mu_0 = 10^{-5}$, $\vartheta_0 = 10^{-2}$ and $c = 0.5$. Here $\mu = \mu_0 = 10^5 \text{ km}^{-1}$ is the value of μ at the neutrinosphere. All the Γ_{CC} are chosen in units of μ_0 . Left: $\Gamma_{CC} = 0$. Middle: $\Gamma_{CC} = 0.01$. Right: $\Gamma_{CC} = 1$.

conversions in the simple intersecting 4-beam model considered in Chapters 4 and 6. We also confine ourselves to temporal evolution, and drop the spatial derivatives in Eq. (B.1.4).

In Fig. B.3, we plot the evolution of the ν_e flavor content in terms of the z -component of \mathbf{Q} (see Eq. (4.2.3) for the definition of \mathbf{Q}). We observe that in absence of collisions, for a small seed set by ω , we find an initial flat phase, followed by oscillations, which signals fast growths (left panel). However, as soon as CC interactions are switched on, they start suppressing flavor oscillations for values of Γ_{CC} as low as $\mathcal{O}(0.01)\mu$ (middle panel). As Γ_{CC} is increased, this suppression becomes stronger until for values of $\Gamma_{CC} \sim \mu$, the quantum Zeno regime is reached (right panel). Here, collisions are so rapid that the flavor content freezes in and does not change appreciably from its initial value.

Inclusion of NC pair production-annihilation interactions in this setup is more complicated as this couples the neutrino and antineutrino modes. Furthermore, with respect to the CC interactions, they are tiny, smaller by a factor of 10^3 . Typically, larger values of these interactions can lead to complete damping of oscillations. Since these processes produce and annihilate both the flavors at the same rate, they do not lead to any extra flavor asymmetry. Any $\nu_e \bar{\nu}_e$ excess is wiped out, leading to flavor equilibrium. We have checked that if both CC and NC interactions are present, an interplay between the two effects can happen.

Thus, using such a simple toy model involving four neutrino beams, one can conclude that while fast conversions take place in absence of collisions, introduction of collision terms with a rate similar to μ may tend to damp out the fast growths. However, note that recent

simulations [203] find that the neutrino potential is always larger by ~ 5 order of magnitude than the ν_e collisional rate. This latter is a factor ~ 3 larger than the $\bar{\nu}_e$ collisional term. Surprisingly, even in the deepest regions at $r \lesssim 10$ km, where these quantities flatten out, the neutrino dominance remains strong. These findings would imply that once fast conversions are generated above the neutrinosphere, they quickly propagate unimpeded.

Bibliography

- [1] “A translation of a machine-typed copy of a letter that Wolfgang Pauli sent to a group of physicists meeting in Tübingen in December 1930.”
<http://microboone-docdb.fnal.gov/cgi-bin/RetrieveFile?docid=953;filename=pauli%20letter1930.pdf>.
- [2] E. W. Kolb and M. S. Turner, *The Early Universe*, *Front. Phys.* **69** (1990) 1–547.
- [3] **Particle Data Group** Collaboration, C. Patrignani et al., *Review of Particle Physics*, *Chin. Phys.* **C40** (2016), no. 10 100001.
- [4] **SLD Electroweak Group, DELPHI, ALEPH, SLD, SLD Heavy Flavour Group, OPAL, LEP Electroweak Working Group, L3** Collaboration, S. Schael et al., *Precision electroweak measurements on the Z resonance*, *Phys. Rept.* **427** (2006) 257–454, [[hep-ex/0509008](#)].
- [5] B. Pontecorvo, *Inverse beta processes and nonconservation of lepton charge*, *Sov. Phys. JETP* **7** (1958) 172–173. [*Zh. Eksp. Teor. Fiz.*34,247(1957)].
- [6] Z. Maki, M. Nakagawa, and S. Sakata, *Remarks on the unified model of elementary particles*, *Prog. Theor. Phys.* **28** (1962) 870–880. [,34(1962)].
- [7] L. Wolfenstein, *Neutrino Oscillations in Matter*, *Phys. Rev.* **D17** (1978) 2369–2374.
- [8] S. P. Mikheev and A. Yu. Smirnov, *Resonance Amplification of Oscillations in Matter and Spectroscopy of Solar Neutrinos*, *Sov. J. Nucl. Phys.* **42** (1985) 913–917. [,305(1986)].
- [9] B. T. Cleveland, T. Daily, R. Davis, Jr., J. R. Distel, K. Lande, C. K. Lee, P. S. Wildenhain, and J. Ullman, *Measurement of the solar electron neutrino flux with the*

- Homestake chlorine detector, Astrophys. J.* **496** (1998) 505–526.
- [10] **GALLEX** Collaboration, M. Cribier, *Results of the whole GALLEX experiment, Nucl. Phys. Proc. Suppl.* **70** (1999) 284–291. [,284(1999)].
- [11] **SAGE** Collaboration, J. N. Abdurashitov et al., *Solar neutrino flux measurements by the Soviet-American Gallium Experiment (SAGE) for half the 22 year solar cycle, J. Exp. Theor. Phys.* **95** (2002) 181–193, [astro-ph/0204245]. [Zh. Eksp. Teor. Fiz.122,211(2002)].
- [12] **KamLAND** Collaboration, T. Araki et al., *Measurement of neutrino oscillation with KamLAND: Evidence of spectral distortion, Phys. Rev. Lett.* **94** (2005) 081801, [hep-ex/0406035].
- [13] **SNO** Collaboration, B. Aharmim et al., *Electron energy spectra, fluxes, and day-night asymmetries of B-8 solar neutrinos from measurements with NaCl dissolved in the heavy-water detector at the Sudbury Neutrino Observatory, Phys. Rev.* **C72** (2005) 055502, [nucl-ex/0502021].
- [14] **Super-Kamiokande** Collaboration, J. Hosaka et al., *Solar neutrino measurements in super-Kamiokande-I, Phys. Rev.* **D73** (2006) 112001, [hep-ex/0508053].
- [15] **Super-Kamiokande** Collaboration, Y. Fukuda et al., *Evidence for oscillation of atmospheric neutrinos, Phys. Rev. Lett.* **81** (1998) 1562–1567, [hep-ex/9807003].
- [16] **Super-Kamiokande** Collaboration, Y. Fukuda et al., *Neutrino induced upward stopping muons in Super-Kamiokande, Phys. Lett.* **B467** (1999) 185–193, [hep-ex/9908049].
- [17] **MACRO** Collaboration, M. Ambrosio et al., *Atmospheric neutrino oscillations from upward through going muon multiple scattering in MACRO, Phys. Lett.* **B566** (2003) 35–44, [hep-ex/0304037].
- [18] **Super-Kamiokande** Collaboration, Y. Ashie et al., *Evidence for an oscillatory signature in atmospheric neutrino oscillation, Phys. Rev. Lett.* **93** (2004) 101801, [hep-ex/0404034].
- [19] **Daya Bay** Collaboration, F. P. An et al., *Observation of electron-antineutrino*

- disappearance at Daya Bay, Phys. Rev. Lett.* **108** (2012) 171803, [arXiv:1203.1669].
- [20] **RENO** Collaboration, J. K. Ahn et al., *Observation of Reactor Electron Antineutrino Disappearance in the RENO Experiment, Phys. Rev. Lett.* **108** (2012) 191802, [arXiv:1204.0626].
- [21] **Double Chooz** Collaboration, Y. Abe et al., *Reactor electron antineutrino disappearance in the Double Chooz experiment, Phys. Rev.* **D86** (2012) 052008, [arXiv:1207.6632].
- [22] **K2K** Collaboration, E. Aliu et al., *Evidence for muon neutrino oscillation in an accelerator-based experiment, Phys. Rev. Lett.* **94** (2005) 081802, [hep-ex/0411038].
- [23] **MINOS** Collaboration, P. Adamson et al., *Measurement of the Neutrino Mass Splitting and Flavor Mixing by MINOS, Phys. Rev. Lett.* **106** (2011) 181801, [arXiv:1103.0340].
- [24] **T2K** Collaboration, K. Abe et al., *Measurement of Neutrino Oscillation Parameters from Muon Neutrino Disappearance with an Off-axis Beam, Phys. Rev. Lett.* **111** (2013), no. 21 211803, [arXiv:1308.0465].
- [25] A. Mirizzi, I. Tamborra, H.-T. Janka, N. Saviano, K. Scholberg, R. Bollig, L. Hudepohl, and S. Chakraborty, *Supernova Neutrinos: Production, Oscillations and Detection, Riv. Nuovo Cim.* **39** (2016), no. 1-2 1–112, [arXiv:1508.00785].
- [26] C. Giunti and C. W. Kim, *Fundamentals of Neutrino Physics and Astrophysics*. 2007.
- [27] S. M. Bilenky and B. Pontecorvo, *Lepton Mixing and Neutrino Oscillations, Phys. Rept.* **41** (1978) 225–261.
- [28] T.-K. Kuo and J. T. Pantaleone, *Neutrino Oscillations in Matter, Rev. Mod. Phys.* **61** (1989) 937.
- [29] J. Linder, *Derivation of neutrino matter potentials induced by earth, Submitted to: Am. J. Phys.* (2005) [hep-ph/0504264].
- [30] T.-K. Kuo and J. T. Pantaleone, *Nonadiabatic Neutrino Oscillations in Matter, Phys. Rev.* **D39** (1989) 1930.
- [31] J. T. Pantaleone, *Neutrino oscillations at high densities, Phys. Lett.* **B287** (1992)

- 128–132.
- [32] J. T. Pantaleone, *Neutrino flavor evolution near a supernova's core*, *Phys. Lett.* **B342** (1995) 250–256, [[astro-ph/9405008](#)].
- [33] **MINOS** Collaboration, P. Adamson et al., *Measurement of Neutrino and Antineutrino Oscillations Using Beam and Atmospheric Data in MINOS*, *Phys. Rev. Lett.* **110** (2013), no. 25 251801, [[arXiv:1304.6335](#)].
- [34] <http://www.nu-fit.org/?q=node/8>.
- [35] I. Esteban, M. C. Gonzalez-Garcia, M. Maltoni, I. Martinez-Soler, and T. Schwetz, *Updated fit to three neutrino mixing: exploring the accelerator-reactor complementarity*, *JHEP* **01** (2017) 087, [[arXiv:1611.01514](#)].
- [36] **JUNO** Collaboration, F. An et al., *Neutrino Physics with JUNO*, *J. Phys.* **G43** (2016), no. 3 030401, [[arXiv:1507.05613](#)].
- [37] **ICAL** Collaboration, S. Ahmed et al., *Physics Potential of the ICAL detector at the India-based Neutrino Observatory (INO)*, *Pramana* **88** (2017), no. 5 79, [[arXiv:1505.07380](#)].
- [38] F. Capozzi, E. Lisi, A. Marrone, and A. Palazzo, *Current unknowns in the three neutrino framework*, *Prog. Part. Nucl. Phys.* **102** (2018) 48–72, [[arXiv:1804.09678](#)].
- [39] **T2K** Collaboration, K. Abe et al., *Combined Analysis of Neutrino and Antineutrino Oscillations at T2K*, *Phys. Rev. Lett.* **118** (2017), no. 15 151801, [[arXiv:1701.00432](#)].
- [40] **NOvA** Collaboration, P. Adamson et al., *Constraints on Oscillation Parameters from ν_e Appearance and ν_μ Disappearance in NOvA*, *Phys. Rev. Lett.* **118** (2017), no. 23 231801, [[arXiv:1703.03328](#)].
- [41] **SNO** Collaboration, S. N. Ahmed et al., *Measurement of the total active B-8 solar neutrino flux at the Sudbury Neutrino Observatory with enhanced neutral current sensitivity*, *Phys. Rev. Lett.* **92** (2004) 181301, [[nucl-ex/0309004](#)].
- [42] **Super-Kamiokande** Collaboration, Y. Ashie et al., *A Measurement of atmospheric neutrino oscillation parameters by SUPER-KAMIOKANDE I*, *Phys. Rev.* **D71**

- (2005) 112005, [[hep-ex/0501064](#)].
- [43] **Borexino** Collaboration, C. Arpesella et al., *First real time detection of Be-7 solar neutrinos by Borexino*, *Phys. Lett.* **B658** (2008) 101–108, [[arXiv:0708.2251](#)].
- [44] **GALLEX** Collaboration, W. Hampel et al., *GALLEX solar neutrino observations: Results for GALLEX IV*, *Phys. Lett.* **B447** (1999) 127–133.
- [45] **T2K** Collaboration, K. Abe et al., *Search for CP violation in Neutrino and Antineutrino Oscillations by the T2K experiment with 2.2×10^{21} protons on target*, [arXiv:1807.07891](#).
- [46] **NOvA** Collaboration, M. A. Acero et al., *New constraints on oscillation parameters from ν_e appearance and ν_μ disappearance in the NOvA experiment*, Submitted to: *Phys. Rev. D* (2018) [[arXiv:1806.00096](#)].
- [47] F. Couchot, S. Henrot-Versill, O. Perdereau, S. Plaszczynski, B. Rouill d’Orfeuil, M. Spinelli, and M. Tristram, *Cosmological constraints on the neutrino mass including systematic uncertainties*, *Astron. Astrophys.* **606** (2017) A104, [[arXiv:1703.10829](#)].
- [48] A. Morales and J. Morales, *The Neutrinoless double beta decay: The Case for germanium detectors*, *Nucl. Phys. Proc. Suppl.* **114** (2003) 141–157, [[hep-ph/0211332](#)]. [,141(2002)].
- [49] J. D. Vergados, H. Ejiri, and F. Imkovic, *Neutrinoless double beta decay and neutrino mass*, *Int. J. Mod. Phys.* **E25** (2016), no. 11 1630007, [[arXiv:1612.02924](#)].
- [50] G. G. Raffelt, *Stars as laboratories for fundamental physics*. 1996.
- [51] H. A. Bethe, *Supernova mechanisms*, *Rev. Mod. Phys.* **62** (1990) 801–866.
- [52] A. Mezzacappa, *ASCERTAINING THE CORE COLLAPSE SUPERNOVA MECHANISM: The State of the Art and the Road Ahead*, *Ann. Rev. Nucl. Part. Sci.* **55** (2005) 467–515.
- [53] K. Kotake, K. Sato, and K. Takahashi, *Explosion mechanism, neutrino burst, and gravitational wave in core-collapse supernovae*, *Rept. Prog. Phys.* **69** (2006) 971–1144, [[astro-ph/0509456](#)].

- [54] S. Woosley and T. Janka, *The physics of core-collapse supernovae*, *Nature Phys.* **1** (2005) 147, [[astro-ph/0601261](#)].
- [55] H.-T. Janka, K. Langanke, A. Marek, G. Martinez-Pinedo, and B. Mueller, *Theory of Core-Collapse Supernovae*, *Phys. Rept.* **442** (2007) 38–74, [[astro-ph/0612072](#)].
- [56] H.-T. Janka, *Explosion Mechanisms of Core-Collapse Supernovae*, *Ann. Rev. Nucl. Part. Sci.* **62** (2012) 407–451, [[arXiv:1206.2503](#)].
- [57] Brown, G. E., *The fate of massive stars - Collapse, bounce and shock formation*, in *NATO Advanced Science Institutes (ASI) Series C* (M. J. Rees and R. J. Stoneham, eds.), vol. 90 of *NATO Advanced Science Institutes (ASI) Series C*, pp. 13–33, Nov., 1982.
- [58] Baade, W. and Zwicky, F., *On Super-novae*, *Proceedings of the National Academy of Science* **20** (May, 1934) 254–259.
- [59] G. E. Brown, H. A. Bethe, and G. Baym, *Supernova theory*, *Nucl. Phys.* **A375** (1982) 481–532.
- [60] S. W. Bruenn, *Neutrinos From SN1987A and Current Models of Stellar Core Collapse*, *Phys. Rev. Lett.* **59** (1987) 938–941.
- [61] S. A. Colgate and R. H. White, *The Hydrodynamic Behavior of Supernovae Explosions*, *Astrophys. J.* **143** (1966) 626.
- [62] H. A. Bethe and J. R. Wilson, *Revival of a stalled supernova shock by neutrino heating*, *Astrophys. J.* **295** (1985) 14–23.
- [63] A. Burrows, *Neutrinos From Supernova Explosions*, *Ann. Rev. Nucl. Part. Sci.* **40** (1990) 181–212.
- [64] Burrows, A., *On detecting stellar collapse with neutrinos*, *ApJ* **283** (Aug., 1984) 848–852.
- [65] A. Burrows and J. M. Lattimer, *The birth of neutron stars*, *Astrophys. J.* **307** (1986) 178–196.
- [66] T. Fischer, S. C. Whitehouse, A. Mezzacappa, F.-K. Thielemann, and M. Liebendörfer, *Protoneutron star evolution and the neutrino-driven wind in general*

- relativistic neutrino radiation hydrodynamics simulations*, *aap* **517** (July, 2010) A80, [arXiv:0908.1871].
- [67] A. Bandyopadhyay, P. Bhattacharjee, S. Chakraborty, K. Kar, and S. Saha, *Detecting supernova neutrinos with iron and lead detectors*, *Phys. Rev.* **D95** (2017), no. 6 065022, [arXiv:1607.05591].
- [68] G. G. Raffelt, *Muon-neutrino and tau-neutrino spectra formation in supernovae*, *Astrophys. J.* **561** (2001) 890–914, [astro-ph/0105250].
- [69] H.-T. Janka, F. Hanke, L. Hüdepohl, A. Marek, B. Müller, and M. Obergaulinger, *Core-collapse supernovae: Reflections and directions*, *Progress of Theoretical and Experimental Physics* **2012** (Dec., 2012) 01A309, [arXiv:1211.1378].
- [70] D. Vartanyan, A. Burrows, D. Radice, M. A. Skinner, and J. Dolence, *Revival of the Fittest: Exploding Core-Collapse Supernovae from 12 to 25 M_{\odot}* , *Mon. Not. Roy. Astron. Soc.* **477** (2018) 3091, [arXiv:1801.08148].
- [71] O. Just, R. Bollig, H.-T. Janka, M. Obergaulinger, R. Glas, and S. Nagataki, *Core-collapse supernova simulations in one and two dimensions: comparison of codes and approximations*, arXiv:1805.03953.
- [72] J. R. Wilson and R. W. Mayle, *Convection in core collapse supernovae*, *Physics Reports* **163** (1988), no. 1 63 – 78.
- [73] B. Mueller, *The Status of Multi-Dimensional Core-Collapse Supernova Models*, *Publications of the Astronomical Society of Australia* **33** (2016).
- [74] E. O’Connor and C. D. Ott, *The Progenitor Dependence of the Pre-explosion Neutrino Emission in Core-collapse Supernovae*, *Apj* **762** (Jan., 2013) 126, [arXiv:1207.1100].
- [75] E. P. O’Connor and S. M. Couch, *Two Dimensional Core-Collapse Supernova Explosions Aided by General Relativity with Multidimensional Neutrino Transport*, *Astrophys. J.* **854** (2018), no. 1 63, [arXiv:1511.07443].
- [76] I. Tamborra, F. Hanke, H.-T. Janka, B. Mueller, G. G. Raffelt, and A. Marek, *Self-sustained asymmetry of lepton-number emission: A new phenomenon during the*

- supernova shock-accretion phase in three dimensions*, *Astrophys. J.* **792** (2014), no. 2 96, [arXiv:1402.5418].
- [77] A. S. Dighe and A. Yu. Smirnov, *Identifying the neutrino mass spectrum from the neutrino burst from a supernova*, *Phys. Rev.* **D62** (2000) 033007, [hep-ph/9907423].
- [78] S. Horiuchi and J. P. Kneller, *What can be learned from a future supernova neutrino detection?*, *J. Phys.* **G45** (2018), no. 4 043002, [arXiv:1709.01515].
- [79] M. T. Keil, G. G. Raffelt, and H.-T. Janka, *Monte Carlo study of supernova neutrino spectra formation*, *Astrophys. J.* **590** (2003) 971–991, [astro-ph/0208035].
- [80] G. M. Fuller, R. W. Mayle, J. R. Wilson, and D. N. Schramm, *Resonant neutrino oscillations and stellar collapse*, *APJ* **322** (Nov., 1987) 795–803.
- [81] C. Lunardini and A. Yu. Smirnov, *Probing the neutrino mass hierarchy and the 13 mixing with supernovae*, *JCAP* **0306** (2003) 009, [hep-ph/0302033].
- [82] A. S. Dighe, M. T. Keil, and G. G. Raffelt, *Detecting the neutrino mass hierarchy with a supernova at IceCube*, *JCAP* **0306** (2003) 005, [hep-ph/0303210].
- [83] A. S. Dighe, M. T. Keil, and G. G. Raffelt, *Identifying earth matter effects on supernova neutrinos at a single detector*, *JCAP* **0306** (2003) 006, [hep-ph/0304150].
- [84] A. S. Dighe, M. Kachelriess, G. G. Raffelt, and R. Tomas, *Signatures of supernova neutrino oscillations in the earth mantle and core*, *JCAP* **0401** (2004) 004, [hep-ph/0311172].
- [85] V. Barger, P. Huber, and D. Marfatia, *Supernova neutrinos can tell us the neutrino mass hierarchy independently of flux models*, *Phys. Lett.* **B617** (2005) 167–173, [hep-ph/0501184].
- [86] G. L. Fogli, E. Lisi, A. Mirizzi, and D. Montanino, *Revisiting nonstandard interaction effects on supernova neutrino flavor oscillations*, *Phys. Rev.* **D66** (2002) 013009, [hep-ph/0202269].
- [87] Woosley, S. E. and Weaver, T. A., *The Evolution and Explosion of Massive Stars. II. Explosive Hydrodynamics and Nucleosynthesis*, *apjs* **101** (Nov., 1995) 181.
- [88] V. A. Kostelecky and S. Samuel, *Selfmaintained coherent oscillations in dense*

- neutrino gases*, *Phys. Rev.* **D52** (1995) 621–627, [[hep-ph/9506262](#)].
- [89] S. Samuel, *Bimodal coherence in dense selfinteracting neutrino gases*, *Phys. Rev.* **D53** (1996) 5382–5393, [[hep-ph/9604341](#)].
- [90] H. Duan, G. M. Fuller, and Y.-Z. Qian, *Collective neutrino flavor transformation in supernovae*, *Phys. Rev.* **D74** (2006) 123004, [[astro-ph/0511275](#)].
- [91] H. Duan, G. M. Fuller, J. Carlson, and Y.-Z. Qian, *Simulation of Coherent Non-Linear Neutrino Flavor Transformation in the Supernova Environment. 1. Correlated Neutrino Trajectories*, *Phys. Rev.* **D74** (2006) 105014, [[astro-ph/0606616](#)].
- [92] H. Duan, G. M. Fuller, J. Carlson, and Y.-Z. Qian, *Coherent Development of Neutrino Flavor in the Supernova Environment*, *Phys. Rev. Lett.* **97** (2006) 241101, [[astro-ph/0608050](#)].
- [93] C. W. Kim, J. Kim, and W. K. Sze, *On the Geometrical Representation of Neutrino Oscillations in Vacuum and Matter*, *Phys. Rev.* **D37** (1988) 1072.
- [94] A. Esteban-Pretel, S. Pastor, R. Tomas, G. G. Raffelt, and G. Sigl, *Decoherence in supernova neutrino transformations suppressed by deleptonization*, *Phys. Rev.* **D76** (2007) 125018, [[arXiv:0706.2498](#)].
- [95] B. Dasgupta and A. Dighe, *Collective three-flavor oscillations of supernova neutrinos*, *Phys. Rev.* **D77** (2008) 113002, [[arXiv:0712.3798](#)].
- [96] A. Banerjee, A. Dighe, and G. Raffelt, *Linearized flavor-stability analysis of dense neutrino streams*, *Phys. Rev.* **D84** (2011) 053013, [[arXiv:1107.2308](#)].
- [97] S. Hannestad, G. G. Raffelt, G. Sigl, and Y. Y. Y. Wong, *Self-induced conversion in dense neutrino gases: Pendulum in flavour space*, *Phys. Rev.* **D74** (2006) 105010, [[astro-ph/0608695](#)]. [Erratum: *Phys. Rev.* **D76**, 029901(2007)].
- [98] H. Duan, G. M. Fuller, J. Carlson, and Y.-Z. Qian, *Analysis of Collective Neutrino Flavor Transformation in Supernovae*, *Phys. Rev.* **D75** (2007) 125005, [[astro-ph/0703776](#)].
- [99] H. Duan, G. M. Fuller, and Y.-Z. Qian, *Collective Neutrino Oscillations*, *Ann. Rev.*

- Nucl. Part. Sci.* **60** (2010) 569–594, [arXiv:1001.2799].
- [100] S. Chakraborty, R. Hansen, I. Izaguirre, and G. Raffelt, *Collective neutrino flavor conversion: Recent developments*, *Nucl. Phys.* **B908** (2016) 366–381, [arXiv:1602.02766].
- [101] Y. Y. Y. Wong, *Synchronised neutrino oscillations from self interaction and associated applications*, *AIP Conf. Proc.* **655** (2003) 240–256, [hep-ph/0211045]. [240(2002)].
- [102] G. G. Raffelt and A. Yu. Smirnov, *Adiabaticity and spectral splits in collective neutrino transformations*, *Phys. Rev.* **D76** (2007) 125008, [arXiv:0709.4641].
- [103] G. G. Raffelt and A. Yu. Smirnov, *Self-induced spectral splits in supernova neutrino fluxes*, *Phys. Rev.* **D76** (2007) 081301, [arXiv:0705.1830]. [Erratum: *Phys. Rev.* **D77**, 029903(2008)].
- [104] G. L. Fogli, E. Lisi, A. Marrone, and A. Mirizzi, *Collective neutrino flavor transitions in supernovae and the role of trajectory averaging*, *JCAP* **0712** (2007) 010, [arXiv:0707.1998].
- [105] G. L. Fogli, E. Lisi, A. Marrone, A. Mirizzi, and I. Tamborra, *Low-energy spectral features of supernova (anti)neutrinos in inverted hierarchy*, *Phys. Rev.* **D78** (2008) 097301, [arXiv:0808.0807].
- [106] B. Dasgupta, A. Dighe, G. G. Raffelt, and A. Yu. Smirnov, *Multiple Spectral Splits of Supernova Neutrinos*, *Phys. Rev. Lett.* **103** (2009) 051105, [arXiv:0904.3542].
- [107] B. Dasgupta, A. Dighe, A. Mirizzi, and G. G. Raffelt, *Spectral split in prompt supernova neutrino burst: Analytic three-flavor treatment*, *Phys. Rev.* **D77** (2008) 113007, [arXiv:0801.1660].
- [108] A. Friedland, *Self-refraction of supernova neutrinos: mixed spectra and three-flavor instabilities*, *Phys. Rev. Lett.* **104** (2010) 191102, [arXiv:1001.0996].
- [109] S. Choubey, B. Dasgupta, A. Dighe, and A. Mirizzi, *Signatures of collective and matter effects on supernova neutrinos at large detectors*, arXiv:1008.0308.
- [110] A. Esteban-Pretel, A. Mirizzi, S. Pastor, R. Tomas, G. G. Raffelt, P. D. Serpico, and

- G. Sigl, *Role of dense matter in collective supernova neutrino transformations*, *Phys. Rev. D* **78** (2008) 085012, [[arXiv:0807.0659](#)].
- [111] R. F. Sawyer, *The multi-angle instability in dense neutrino systems*, *Phys. Rev. D* **79** (2009) 105003, [[arXiv:0803.4319](#)].
- [112] S. Chakraborty, T. Fischer, A. Mirizzi, N. Saviano, and R. Tomas, *Analysis of matter suppression in collective neutrino oscillations during the supernova accretion phase*, *Phys. Rev. D* **84** (2011) 025002, [[arXiv:1105.1130](#)].
- [113] S. Sarikas, D. d. S. Seixas, and G. Raffelt, *Spurious instabilities in multi-angle simulations of collective flavor conversion*, *Phys. Rev. D* **86** (2012) 125020, [[arXiv:1210.4557](#)].
- [114] G. Raffelt, S. Sarikas, and D. de Sousa Seixas, *Axial Symmetry Breaking in Self-Induced Flavor Conversion of Supernova Neutrino Fluxes*, *Phys. Rev. Lett.* **111** (2013), no. 9 091101, [[arXiv:1305.7140](#)]. [Erratum: *Phys. Rev. Lett.* **113**, no. 23, 239903 (2014)].
- [115] R. F. Sawyer, *Speed-up of neutrino transformations in a supernova environment*, *Phys. Rev. D* **72** (2005) 045003, [[hep-ph/0503013](#)].
- [116] N. Saviano, S. Chakraborty, T. Fischer, and A. Mirizzi, *Stability analysis of collective neutrino oscillations in the supernova accretion phase with realistic energy and angle distributions*, *Phys. Rev. D* **85** (2012) 113002, [[arXiv:1203.1484](#)].
- [117] A. Mirizzi and P. D. Serpico, *Flavor Stability Analysis of Dense Supernova Neutrinos with Flavor-Dependent Angular Distributions*, *Phys. Rev. D* **86** (2012) 085010, [[arXiv:1208.0157](#)].
- [118] R. F. Sawyer, *Neutrino cloud instabilities just above the neutrino sphere of a supernova*, *Phys. Rev. Lett.* **116** (2016), no. 8 081101, [[arXiv:1509.03323](#)].
- [119] S. Chakraborty, R. S. Hansen, I. Izaguirre, and G. Raffelt, *Self-induced neutrino flavor conversion without flavor mixing*, *JCAP* **1603** (2016), no. 03 042, [[arXiv:1602.00698](#)].
- [120] S. Bergmann, Y. Grossman, and D. M. Pierce, *Can lepton flavor violating*

- interactions explain the atmospheric neutrino problem?*, *Phys. Rev.* **D61** (2000) 053005, [hep-ph/9909390].
- [121] S. Bergmann, M. M. Guzzo, P. C. de Holanda, P. I. Krastev, and H. Nunokawa, *Status of the solution to the solar neutrino problem based on nonstandard neutrino interactions*, *Phys. Rev.* **D62** (2000) 073001, [hep-ph/0004049].
- [122] A. M. Gago, M. M. Guzzo, P. C. de Holanda, H. Nunokawa, O. L. G. Peres, V. Pleitez, and R. Zukanovich Funchal, *Global analysis of the postSNO solar neutrino data for standard and nonstandard oscillation mechanisms*, *Phys. Rev.* **D65** (2002) 073012, [hep-ph/0112060].
- [123] A. Friedland, C. Lunardini, and C. Pena-Garay, *Solar neutrinos as probes of neutrino matter interactions*, *Phys. Lett.* **B594** (2004) 347, [hep-ph/0402266].
- [124] M. M. Guzzo, P. C. de Holanda, and O. L. G. Peres, *Effects of nonstandard neutrino interactions on MSW - LMA solution to the solar neutrino problems*, *Phys. Lett.* **B591** (2004) 1–6, [hep-ph/0403134].
- [125] A. Esteban-Pretel, R. Tomas, and J. W. F. Valle, *Probing non-standard neutrino interactions with supernova neutrinos*, *Phys. Rev.* **D76** (2007) 053001, [arXiv:0704.0032].
- [126] M. S. Bilenky, S. M. Bilenky, and A. Santamaria, *Invisible width of the Z boson and 'secret' neutrino-neutrino interactions*, *Phys. Lett.* **B301** (1993) 287–291.
- [127] M. S. Bilenky and A. Santamaria, *Bounding effective operators at the one loop level: The Case of four fermion neutrino interactions*, *Phys. Lett.* **B336** (1994) 91–99, [hep-ph/9405427].
- [128] E. Masso and R. Toldra, *Constraints on neutrino-neutrino interactions from primordial nucleosynthesis*, *Phys. Lett.* **B333** (1994) 132–134, [hep-ph/9404339].
- [129] M. S. Bilenky and A. Santamaria, *'Secret' neutrino interactions*, in *Neutrino mixing. Festschrift in honour of Samoil Bilenky's 70th birthday. Proceedings, International Meeting, Turin, Italy, March 25-27, 1999*, pp. 50–61, 1999. hep-ph/9908272.
- [130] M. Blennow, A. Mirizzi, and P. D. Serpico, *Nonstandard neutrino-neutrino refractive*

- effects in dense neutrino gases*, *Phys. Rev.* **D78** (2008) 113004, [arXiv:0810.2297].
- [131] M. Kachelriess, R. Tomas, R. Buras, H. T. Janka, A. Marek, and M. Rampp, *Exploiting the neutronization burst of a galactic supernova*, *Phys. Rev.* **D71** (2005) 063003, [astro-ph/0412082].
- [132] A. Esmaili, O. L. G. Peres, and P. D. Serpico, *Impact of sterile neutrinos on the early time flux from a galactic supernova*, *Phys. Rev.* **D90** (2014), no. 3 033013, [arXiv:1402.1453].
- [133] S. Chakraborty, A. Mirizzi, and G. Sigl, *Testing Lorentz invariance with neutrino bursts from supernova neutronization*, *Phys. Rev.* **D87** (2013), no. 1 017302, [arXiv:1211.7069].
- [134] S. Ando, *Appearance of neutronization peak and decaying supernova neutrinos*, *Phys. Rev.* **D70** (2004) 033004, [hep-ph/0405200].
- [135] P. D. Serpico, S. Chakraborty, T. Fischer, L. Hudepohl, H.-T. Janka, and A. Mirizzi, *Probing the neutrino mass hierarchy with the rise time of a supernova burst*, *Phys. Rev.* **D85** (2012) 085031, [arXiv:1111.4483].
- [136] R. C. Schirato and G. M. Fuller, *Connection between supernova shocks, flavor transformation, and the neutrino signal*, astro-ph/0205390.
- [137] G. L. Fogli, E. Lisi, D. Montanino, and A. Mirizzi, *Analysis of energy and time dependence of supernova shock effects on neutrino crossing probabilities*, *Phys. Rev.* **D68** (2003) 033005, [hep-ph/0304056].
- [138] G. L. Fogli, E. Lisi, A. Mirizzi, and D. Montanino, *Probing supernova shock waves and neutrino flavor transitions in next-generation water-Cerenkov detectors*, *JCAP* **0504** (2005) 002, [hep-ph/0412046].
- [139] R. Tomas, M. Kachelriess, G. Raffelt, A. Dighe, H. T. Janka, and L. Scheck, *Neutrino signatures of supernova shock and reverse shock propagation*, *JCAP* **0409** (2004) 015, [astro-ph/0407132].
- [140] S. Galais, J. Kneller, C. Volpe, and J. Gava, *Shockwaves in Supernovae: New Implications on the Diffuse Supernova Neutrino Background*, *Phys. Rev.* **D81** (2010)

- 053002, [arXiv:0906.5294].
- [141] B. Dasgupta and A. Dighe, *Phase effects in neutrino conversions during a supernova shock wave*, *Phys. Rev.* **D75** (2007) 093002, [hep-ph/0510219].
- [142] J. P. Kneller, G. C. McLaughlin, and J. Brockman, *Oscillation Effects and Time Variation of the Supernova Neutrino Signal*, *Phys. Rev.* **D77** (2008) 045023, [arXiv:0705.3835].
- [143] E. Borriello, S. Chakraborty, H.-T. Janka, E. Lisi, and A. Mirizzi, *Turbulence patterns and neutrino flavor transitions in high-resolution supernova models*, *JCAP* **1411** (2014), no. 11 030, [arXiv:1310.7488].
- [144] H. Minakata, H. Nunokawa, R. Tomas, and J. W. F. Valle, *Parameter Degeneracy in Flavor-Dependent Reconstruction of Supernova Neutrino Fluxes*, *JCAP* **0812** (2008) 006, [arXiv:0802.1489].
- [145] B. Dasgupta and J. F. Beacom, *Reconstruction of supernova ν_μ , ν_τ , anti- ν_μ , and anti- ν_τ neutrino spectra at scintillator detectors*, *Phys. Rev.* **D83** (2011) 113006, [arXiv:1103.2768].
- [146] R. Laha, J. F. Beacom, and S. K. Agarwalla, *New Power to Measure Supernova ν_e with Large Liquid Scintillator Detectors*, arXiv:1412.8425.
- [147] H.-L. Li, Y.-F. Li, M. Wang, L.-J. Wen, and S. Zhou, *Towards a complete reconstruction of supernova neutrino spectra in future large liquid-scintillator detectors*, *Phys. Rev.* **D97** (2018), no. 6 063014, [arXiv:1712.06985].
- [148] A. Nikrant, R. Laha, and S. Horiuchi, *Robust measurement of supernova ν_e spectra with future neutrino detectors*, *Phys. Rev.* **D97** (2018), no. 2 023019, [arXiv:1711.00008].
- [149] F. Capozzi, B. Dasgupta, and A. Mirizzi, *Model-independent diagnostic of self-induced spectral equalization versus ordinary matter effects in supernova neutrinos*, arXiv:1807.00840.
- [150] “IAU Circular 4316 (1987).”
<http://http://www.cbat.eps.harvard.edu/iauc/04300/04316.html>.

- [151] **Kamiokande-II** Collaboration, K. Hirata et al., *Observation of a Neutrino Burst from the Supernova SN 1987a*, *Phys. Rev. Lett.* **58** (1987) 1490–1493. [,727(1987)].
- [152] R. M. Bionta et al., *Observation of a Neutrino Burst in Coincidence with Supernova SN 1987a in the Large Magellanic Cloud*, *Phys. Rev. Lett.* **58** (1987) 1494.
- [153] E. N. Alekseev, L. N. Alekseeva, I. V. Krivosheina, and V. I. Volchenko, *Detection of the neutrino signal from SN 1987A using the INR Baksan underground scintillation telescope*, in *European Southern Observatory Conference and Workshop Proceedings* (I. J. Danziger, ed.), vol. 26 of *European Southern Observatory Conference and Workshop Proceedings*, pp. 237–247, 1987.
- [154] A. Strumia and F. Vissani, *Precise quasielastic neutrino/nucleon cross-section*, *Phys. Lett.* **B564** (2003) 42–54, [astro-ph/0302055].
- [155] **Super-Kamiokande** Collaboration, M. Ikeda et al., *Search for Supernova Neutrino Bursts at Super-Kamiokande*, *Astrophys. J.* **669** (2007) 519–524, [arXiv:0706.2283].
- [156] K. Abe et al., *Letter of Intent: The Hyper-Kamiokande Experiment-Detector Design and Physics Potential*, arXiv:1109.3262.
- [157] N. Yu. Agafonova et al., *On-line recognition of supernova neutrino bursts in the LVD detector*, *Astropart. Phys.* **28** (2008) 516–522, [arXiv:0710.0259].
- [158] M. E. Monzani, *Supernova neutrino detection in Borexino*, *Nuovo Cim.* **C29** (2006) 269–280.
- [159] **KamLAND** Collaboration, K. Eguchi et al., *First results from KamLAND: Evidence for reactor anti-neutrino disappearance*, *Phys. Rev. Lett.* **90** (2003) 021802, [hep-ex/0212021].
- [160] **LENA** Collaboration, M. Wurm et al., *The next-generation liquid-scintillator neutrino observatory LENA*, *Astropart. Phys.* **35** (2012) 685–732, [arXiv:1104.5620].
- [161] J. F. Beacom and M. R. Vagins, *GADZOOKS! Anti-neutrino spectroscopy with large water Cherenkov detectors*, *Phys. Rev. Lett.* **93** (2004) 171101, [hep-ph/0309300].
- [162] F. Halzen, J. E. Jacobsen, and E. Zas, *Ultrasensitive Antarctic ice as a supernova detector*, *Phys. Rev.* **D53** (1996) 7359–7361, [astro-ph/9512080].

- [163] **IceCube PINGU** Collaboration, M. G. Aartsen et al., *Letter of Intent: The Precision IceCube Next Generation Upgrade (PINGU)*, [arXiv:1401.2046](#).
- [164] F. Halzen and G. G. Raffelt, *Reconstructing the supernova bounce time with neutrinos in IceCube*, *Phys. Rev.* **D80** (2009) 087301, [[arXiv:0908.2317](#)].
- [165] R. Abbasi, Y. Abdou, T. Abu-Zayyad, M. Ackermann, J. Adams, J. A. Aguilar, M. Ahlers, M. M. Allen, D. Altmann, K. Andeen, and et al., *IceCube sensitivity for low-energy neutrinos from nearby supernovae*, *aap* **535** (Nov., 2011) A109, [[arXiv:1108.0171](#)].
- [166] I. Gil Botella and A. Rubbia, *Decoupling supernova and neutrino oscillation physics with LAr TPC detectors*, *JCAP* **0408** (2004) 001, [[hep-ph/0404151](#)].
- [167] **LBNE** Collaboration, C. Adams et al., *The Long-Baseline Neutrino Experiment: Exploring Fundamental Symmetries of the Universe*, [arXiv:1307.7335](#).
- [168] **MicroBooNE** Collaboration, M. Soderberg, *MicroBooNE: A New Liquid Argon Time Projection Chamber Experiment*, *AIP Conf. Proc.* **1189** (2009) 83–87, [[arXiv:0910.3497](#)].
- [169] W. J. Marciano and Z. Parsa, *Neutrino electron scattering theory*, *J. Phys.* **G29** (2003) 2629–2645, [[hep-ph/0403168](#)].
- [170] G. Sigl and G. Raffelt, *General kinetic description of relativistic mixed neutrinos*, *Nucl. Phys.* **B406** (1993) 423–451.
- [171] A. D. Dolgov, *Neutrinos in the Early Universe*, *Sov. J. Nucl. Phys.* **33** (1981) 700–706. [[Yad. Fiz.33,1309\(1981\)](#)].
- [172] G. Raffelt, G. Sigl, and L. Stodolsky, *Quantum statistics in particle mixing phenomena*, *Phys. Rev.* **D45** (1992) 1782–1788.
- [173] G. Raffelt, G. Sigl, and L. Stodolsky, *NonAbelian Boltzmann equation for mixing and decoherence*, *Phys. Rev. Lett.* **70** (1993) 2363–2366, [[hep-ph/9209276](#)]. [Erratum: *Phys. Rev. Lett.* **98**,069902(2007)].
- [174] P. Strack and A. Burrows, *Generalized Boltzmann formalism for oscillating neutrinos*, *Phys. Rev.* **D71** (2005) 093004, [[hep-ph/0504035](#)].

- [175] A. Vlasenko, G. M. Fuller, and V. Cirigliano, *Neutrino Quantum Kinetics*, *Phys. Rev. D* **D89** (2014), no. 10 105004, [arXiv:1309.2628].
- [176] L. Stodolsky, *On the Treatment of Neutrino Oscillations in a Thermal Environment*, *Phys. Rev. D* **D36** (1987) 2273.
- [177] C. W. Kim, W. K. Sze, and S. Nussinov, *On Neutrino Oscillations and the Landau-Zener Formula*, *Phys. Rev. D* **D35** (1987) 4014.
- [178] B. Dasgupta and A. Mirizzi, *Temporal Instability Enables Neutrino Flavor Conversions Deep Inside Supernovae*, *Phys. Rev. D* **D92** (2015), no. 12 125030, [arXiv:1509.03171].
- [179] T. Morinaga and S. Yamada, *Linear stability analysis of collective neutrino oscillations without spurious modes*, *Phys. Rev. D* **D97** (2018), no. 2 023024, [arXiv:1803.05913].
- [180] B. Dasgupta, A. Mirizzi, and M. Sen, *Fast neutrino flavor conversions near the supernova core with realistic flavor-dependent angular distributions*, *JCAP* **1702** (2017), no. 02 019, [arXiv:1609.00528].
- [181] F. Capozzi, B. Dasgupta, and A. Mirizzi, *Self-induced temporal instability from a neutrino antenna*, *JCAP* **1604** (2016), no. 04 043, [arXiv:1603.03288].
- [182] S. Abbar and H. Duan, *Neutrino flavor instabilities in a time-dependent supernova model*, *Phys. Lett. B* **B751** (2015) 43–47, [arXiv:1509.01538].
- [183] F. Capozzi, B. Dasgupta, E. Lisi, A. Marrone, and A. Mirizzi, *Fast flavor conversions of supernova neutrinos: Classifying instabilities via dispersion relations*, *Phys. Rev. D* **D96** (2017), no. 4 043016, [arXiv:1706.03360].
- [184] A. Mirizzi and P. D. Serpico, *Instability in the Dense Supernova Neutrino Gas with Flavor-Dependent Angular Distributions*, *Phys. Rev. Lett.* **108** (2012) 231102, [arXiv:1110.0022].
- [185] <https://wwwmpa.mpa-garching.mpg.de/ccsnarchive/>. Results from an extended set of 1D core-collapse simulations.
- [186] S. Chakraborty, G. Raffelt, H.-T. Janka, and B. Mueller, *Supernova deleptonization*

- asymmetry: Impact on self-induced flavor conversion*, *Phys. Rev.* **D92** (2015), no. 10 105002, [arXiv:1412.0670].
- [187] M. Frensel, M.-R. Wu, C. Volpe, and A. Perego, *Neutrino Flavor Evolution in Binary Neutron Star Merger Remnants*, *Phys. Rev.* **D95** (2017), no. 2 023011, [arXiv:1607.05938].
- [188] M.-R. Wu and I. Tamborra, *Fast neutrino conversions: Ubiquitous in compact binary merger remnants*, *Phys. Rev.* **D95** (2017), no. 10 103007, [arXiv:1701.06580].
- [189] J. Y. Tian, A. V. Patwardhan, and G. M. Fuller, *Neutrino Flavor Evolution in Neutron Star Mergers*, *Phys. Rev.* **D96** (2017), no. 4 043001, [arXiv:1703.03039].
- [190] D. Yu. Bardin, S. M. Bilenky, and B. Pontecorvo, *On the ν - ν interaction*, *Phys. Lett.* **B32** (1970) 121–124.
- [191] E. W. Kolb and M. S. Turner, *Supernova SN 1987a and the Secret Interactions of Neutrinos*, *Phys. Rev.* **D36** (1987) 2895.
- [192] K. M. Belotsky, A. L. Sudarikov, and M. Y. Khlopov, *Constraint on anomalous 4ν interaction*, *Physics of Atomic Nuclei* **64** (2001), no. 9 1637–1642.
- [193] M. B. Gavela, D. Hernandez, T. Ota, and W. Winter, *Large gauge invariant non-standard neutrino interactions*, *Phys. Rev.* **D79** (2009) 013007, [arXiv:0809.3451].
- [194] Y. Farzan and J. Heeck, *Neutrinophilic nonstandard interactions*, *Phys. Rev.* **D94** (2016), no. 5 053010, [arXiv:1607.07616].
- [195] S. Chakraborty, T. Fischer, A. Mirizzi, N. Saviano, and R. Tomas, *No collective neutrino flavor conversions during the supernova accretion phase*, *Phys. Rev. Lett.* **107** (2011) 151101, [arXiv:1104.4031].
- [196] I. Gil-Botella, *Detection of Supernova Neutrinos*, in *Neutrino Cross section Future*, 2016. arXiv:1605.02204.
- [197] **DUNE** Collaboration, R. Acciarri et al., *Long-Baseline Neutrino Facility (LBNF) and Deep Underground Neutrino Experiment (DUNE)*, arXiv:1512.06148.
- [198] A. Das, A. Dighe, and M. Sen, *New effects of non-standard self-interactions of*

- neutrinos in a supernova*, *JCAP* **1705** (2017), no. 05 051, [arXiv:1705.00468].
- [199] I. Izaguirre, G. Raffelt, and I. Tamborra, *Fast Pairwise Conversion of Supernova Neutrinos: A Dispersion-Relation Approach*, *Phys. Rev. Lett.* **118** (2017), no. 2 021101, [arXiv:1610.01612].
- [200] B. Dasgupta and M. Sen, *Fast Neutrino Flavor Conversion as Oscillations in a Quartic Potential*, *Phys. Rev.* **D97** (2018), no. 2 023017, [arXiv:1709.08671].
- [201] A. Dighe and M. Sen, *Nonstandard neutrino self-interactions in a supernova and fast flavor conversions*, *Phys. Rev.* **D97** (2018), no. 4 043011, [arXiv:1709.06858].
- [202] F. Capozzi, B. Dasgupta, A. Mirizzi, M. Sen, and G. Sigl, *In Preparation*, .
- [203] I. Tamborra, L. Huedepohl, G. Raffelt, and H.-T. Janka, *Flavor-dependent neutrino angular distribution in core-collapse supernovae*, *Astrophys. J.* **839** (2017) 132, [arXiv:1702.00060].
- [204] V. Cirigliano, M. W. Paris, and S. Shalgar, *Effect of collisions on neutrino flavor inhomogeneity in a dense neutrino gas*, *Phys. Lett.* **B774** (2017) 258–267, [arXiv:1706.07052].
- [205] D. N. Blaschke and V. Cirigliano, *Neutrino Quantum Kinetic Equations: The Collision Term*, *Phys. Rev.* **D94** (2016), no. 3 033009, [arXiv:1605.09383].